Nearby Early-type Galaxies

A Dissertation
Submitted to the Faculty of Physics
at Ludwig-Maximilians-Universität München

by Mariangela Bernardi
of Breganze, Italy

München, 4 October 1999

1. Adviser: Prof. Dr. Ralf Bender
2. Adviser: Dr. Peter Schneider
Date of thesis defense:

Nearby Early-type Galaxies

Mariangela Bernardi, Ph.D.
Ludwig-Maximilians-Universität München 1999

The all-sky redshift-distance survey of nearby early-type galaxies (ENEAR) described in this thesis was constructed by combining about 1700 new spectra and R-band images of some 1200 galaxies with other previously published data. The ENEAR sample was drawn from a compilation of magnitude-limited ($m_B \leq 14.5$) redshift ($cz \leq 7000$ kms^{-1}) surveys, supplemented by some fainter or more distant galaxies in selected clusters. The database is extensive; it contains the redshifts, velocity dispersions, photometric parameters, and linestrengths of 1694 objects, all scaled to a uniform system.

Bright early-types are useful because they can be seen out to relatively large volumes. Furthermore, velocity dispersions of early-types are easier to measure than rotation curves of spirals and, because they tend to be located in groups, the errors in estimating distances to them can be reduced. Since the ENEAR database covers the whole sky, it is ideally suited for mapping the local peculiar velocity field, and measuring the amplitude and direction of the dipole motion.

To estimate peculiar velocities for the ENEAR galaxies we needed a distance indicator. Many of the ENEAR galaxies are in clusters, so we used these cluster galaxies (446 galaxies in 28 clusters) to build our own $D_n - \sigma$ relation. This required new, strict, objective criteria for assigning the galaxies to clusters, homogenization of our data with those from the literature, and correction for several systematic biases. The resulting $D_n - \sigma$ relation was used to estimate distances to, and so peculiar velocities for, about 1200 early-type galaxies in over 800 objects. The peculiar velocities were used to estimate the bulk flow (343 ± 53 kms^{-1} towards $l = 264 \pm 8, b = 33 \pm 5$), and to reconstruct the velocity and density fields of the matter within a sphere of 7000 kms^{-1} in radius around us.

Because it provides a set of data over a wide range of densities, the ENEAR sample is of great interest for stellar population studies, and for investigating environmental effects on scaling relations like $D_n - \sigma$ that are otherwise assumed to be universal. Moreover, early-type galaxies are particularly interesting because they are thought to have formed at some early epoch as smaller sub-systems merged with each other. Currently, a great effort is underway to pinpoint the epoch of their formation, especially because of the mounting evidence that early-types seen today form a remarkable homogeneous population. The end of this thesis presents a comparison of the $Mg_2 - \sigma$ relation of field and cluster galaxies which supports the hypothesis that most of the stars in early-types must have formed at high redshift ($z \geq 3$).

Life is not a problem to be solved
but a mystery to be revealed

Acknowledgments

It was a cold winter day when I arrived at ESO at the end of January 1996. I remember that day very well: I was shocked by the low temperature (-17 C), by how difficult it was to understand what people said, and by the impact of meeting Luiz da Costa. He has been my Ph.D. adviser at ESO during these years. He gave me the opportunity to join the ENEAR group since he believed I would have been a valuable addition to the team. I thank him for this and especially for the many hours we worked together. He had to put up with this "stubborn" woman, but I had to put up with that "slave driver"! More than three and a half years have passed since that day, and I still enjoy working with him!

None of this would have been possible without Roberto Saglia. He was my contact-point with ESO. I met him in March 1995 at the Sternwarte München, where I worked for a week. For that useful visit I must thank Francesco Bertola, my Master thesis adviser at the Padova University. I thank Roberto for the valuable advice and encouragement to carry out my Ph.D. at the Ludwig-Maximilians-Universität München. I have appreciated all his helpful discussions, critical comments, and suggestions during my time in Munich.

My thanks go also to Ralf Bender, my official Ph.D. thesis adviser. I thank the Sternwarte München and the Technische Universität München which partially contributed financial support for this work. I also acknowledge financial support from an ESO Studentship during 1997-1999 and travel support provided by the ESO Science Division.

Among my colleagues in the ENEAR team, first I thank Maria Victoria Alonso. We had very nice time together during her visits at ESO, both at work and outside. I found her a helpful collaborator and especially a very good friend. I thank Christopher Willmer for teaching me data reduction during his visit to ESO and my visit to the Observatório National in Rio de Janeiro. I thank also his wife and daughter, Vera and Aslife, for the nice time and hospitality I had at their place. I am grateful to Paulo Pellegrini for financial support during my visit to the Observatório National and for the nice weekend and tour around Rio de Janeiro. Thanks also to all the other collaborators of the Observatório National for helping with spectroscopic observations and data reduction. I am grateful to Gary Wegner for teaching me observing techniques and data reduction during my photometric and spectrocopic observing runs at the Michigan-Dartmouth-MIT Observatory at Kitt Peak. I thank Wolfram Freudling for companionship during my first observing run at MDM and helpful advice and encouragement during my first two years at ESO. I am grateful to Alvio Renzini for the many discussions and helpful suggestions he gave me during our collaboration. Thanks also to Saleem Zaroubi and Adi Nusser for putting up with countless versions of peculiar velocity tables. I became good friends with both of them. I thank Adi also for the nice red rose!

I am grateful to David Burstein for having provided the ENEAR team with the

updated 7S sample and for useful discussions and advice. I thank also Inger Jørgensen for having supplied some data tables in electronic form.

During my observing runs at the Kitt Peak and La Silla I became friends with several people, too numerous to name. I just mention the wonderful trip I had with Andrew Stephens to the Grand Canyon. We walked down the Hermit trail, on the west part of the Canyon. We pitched our tent close to the Hermit creek, about a 30 minute walk from the Colorado River. We spent a day and a half down in the Canyon. The following days we visited Monument Valley, Lake Powell, Bryce Canyon and the Meteor Crater. I enjoyed that trip very much. For the nice hospitality in Santiago I thank Alessandro, Chris, and all the others as well as Achim for the nice motorbike tour.

I thank all my old Italian friends from my childhood, high-school, and University who managed to keep in touch with me. My thanks go especially to Fabio Migliorini who was and will be forever one of my best friends.

At ESO I became friends with a lot of people. I thank all of them and mention only some by name: Anna, Elena, Simona, Piero, Marco, Francesco, Markus, Gerty, Marco, Joao, Jens, Nick, Hans, Lara, Mike, Franco, Barbara, Laura, Stefano, Fabio, Giorgio, Mauro, Michael, Claudine, Maurizio, Manuela. I also met nice people at the Max-Planck-Institut für Astrophysik in Garching: Roman, Rien, Tom, Antonaldo, Enzo, Beppi, Tony, Pierluigi, Valentina, Emanuela, and many others.

I have to thank separetly Martino Romaniello for the many suggestions and astronomical discussions (he wants absolutely to be mentioned in my acknowledgements).

I thank also Canio Dichirico for helping me at the beginning of my stay in Munich. During these years he has been a good friend; Reuben Cole for being a wonderful partner in Salsa dancing. I enjoyed dancing with him very much; and Tom Theuns for having been a good friend and for having lent me wonderful novels.

I thank Thomas Sykora for having improved my English; we shared many delightful experiences during my first two years in Munich.

I must of course thank my parents, Tiziano Bernardi and Maria Antonietta Alban. During all my life I have always felt your love. I thank also my sisters, Patrizia and Antonella, and my brother, Dino who always help me whenever I need. My thanks go also to Renato, Francesco and Cinzia. I am happy you are part of my family. A sweet thought goes also for my two nephews, Enrico and Alberto.

A special thank goes to my boyfriend, Ravi Sheth. His support, encouragement, and help have been unwavering and unconditional. I thank him especially because since I met him I have viewed the world through rose-tinted glasses.

Table of Contents

List of Tables

List of Figures

Chapter 1

Introduction

Empirical relations between structural properties of early-type galaxies are reviewed. The use of these relations for peculiar velocity analyses and stellar population studies, as well as recent results and unsolved issues are described. Special emphasis is placed on the necessity of constructing a homogeneous self-consistent catalog of peculiar motions by merging samples of early-type and spiral galaxies, and of assessing the universality of the scaling relations. These arguments provide the background to a number of issues which have been the primary reasons for carrying out the ENEAR redshift-distance survey.

This Chapter also describes the initial concept and primary goals of the ENEAR project, and the subsequent development and resulting collaborations that have led, over the last ten years, to the assembly of the ENEAR database.

1.1 Empirical relations

Correlations between the structural and dynamical properties of present-day early-type galaxies, such as their luminosity, size, metallicity, and stellar velocity dispersion, have been observed (e.g., Faber & Jackson 1976; Aaronson et al. 1981; Burstein et al. 1984; Dressler et al. 1987b; Djorgovski & Davis 1987; Bower et al. 1992; Saglia et al. 1993b; Jørgenson et al. 1996). Therefore, one might conclude that they are a remarkably homogeneous class of objects. However, comparisons between spectral synthesis models and observed integrated spectra show that early-type galaxies are not simple stellar populations: a population of stars that all have the same age and metallicity cannot reproduce the observed spectral energy distributions and line strenghts of these galaxies (e.g., Worthey 1994). Indeed, the observed correlations usually have a scatter that is larger than expected from the uncertainties of the measurements: this is most likely due to stellar population variations. In addition, although there are theoretical explanations for the physical origins of some of these correlations, they do not always describe the observations exactly. These discrepancies may also arise from stellar population differences between galaxies.

Fortunately, the dispersion around the observed correlations is usually small. This has two important consequences: these relations can be used

- to measure relative distances to early-type galaxies accurately, and
- to constrain models of their stellar populations.

Accurate distances allow one to quantify the large-scale, large-amplitude coherent motions in the nearby universe, and to reconstruct the mass density field. In turn, this allows one to constrain the cosmological parameter Ω_0. Constraints on the stellar population help further our understanding of the formation and evolution of early-types.

The amount of detailed information about the internal kinematics, global structural properties and stellar populations of elliptical galaxies has grown enormously over the last decade or so. This increase in data has allowed observers to propose relations that have a lower scatter than the correlation between luminosity and velocity dispersion, the $L-\sigma$ relation, that was first proposed by Faber & Jackson (1976). Amongst the empirical relations, those that have been most extensively used for early-type galaxies are the $D_n-\sigma$ relation (Dressler et al. 1987), the Fundamental Plane (FP) relation (Djorgovski & Davis 1987), and the $\mathrm{Mg}_2-\sigma$ relation (e.g., Jørgensen 1997; Colless et al. 1999; Bernardi et al. 1998). These are described briefly below.

1.1.1 The $D_n-\sigma$ and FP relations

It is now well-known that ellipticals do not uniformly populate the three-dimensional space defined by the central velocity dispersion (σ), the effective radius (r_e) which encloses half the luminosity of the galaxy, and the effective surface brightness ($\bar{\mu}_e$) which is the mean surface brightness within r_e. Rather, they are confined to a narrow Fundamental Plane (FP):

$$r_e \propto \sigma^{1.4}\,\bar{\mu}_e^{-0.85} \tag{1.1}$$

although the measured values of the exponents can differ by upto 15%.

Another photometric parameter that is correlated with σ is D_n. This is an isophotal diameter measured at a fixed (but somewhat arbitrary) isophotal level. This parameter can be thought of as a combination of r_e and μ_e, $D_n \propto r_e\,\mu_e^c$. The $D_n-\sigma$ relation can be used for almost all ellipticals. It also holds for S0 galaxies and for the bulges of early-type spirals (Dressler 1987). The FP and $D_n-\sigma$ relations show only a small dispersion, which makes them potentially useful both as distance indicators, and as strong constraints on models of galaxy formation.

The physical origin of these scaling relations is not fully understood. This reflects our limited understanding of galaxy formation and evolution. For example, the FP is naturally explained by combining the assumption of virial equilibrium with the assumption that the luminosity of an object depends on its mass. If M is the mass of a galaxy, L its luminosity, σ its velocity dispersion and r a suitably defined mean radius, e.g., that which encloses half the luminosity of the galaxy, then the virial equilibrium requires

$$\sigma^2 \propto M/r. \tag{1.2}$$

Substituting a smoothly varying mass to light ratio,

$$M/L \propto M^\gamma, \tag{1.3}$$

into the virial relation, and using the fact that the mean surface brightness μ within r is $\propto L/r^2$ yields

$$r\bar{\mu}^{1/(1+\gamma)} \propto \sigma^{2(1-\gamma)/(1+\gamma)}. \tag{1.4}$$

The empirical FP relation above requires that $\gamma \sim 0.18 \pm 0.05$. Since the expression on the left-hand side of equation (1.4) is just D_n, the model predicts that $D_n \propto \sigma^{1.4}$.

Including the effects of stellar population variations along the FP make such an analysis more complicated. Variations in age, metallicity, and the initial stellar mass function (IMF) probably contribute to the significant intrinsic scatter found for this relation (Jørgensen et al. 1993, 1996), which is about twice the value expected from the measurement errors. Before any further progress towards the understanding of the astrophysical origin of these scaling relations can be made, an improved knowledge of how to link astronomical observables like luminosity and stellar velocity dispersion to physical quantities like mass, mean potential and kinetic energy is required. Therefore, at the moment, we simply adopt the $D_n - \sigma$ relation as a useful empirical realization.

Since the angular size of a galaxy varies as $1/R$, where R is the distance to the galaxy, if d_n is the measured scale length of the galaxy (e.g., the angular size), then $1/d_n$ is a measure of its distance. Empirically, $d_n \propto \sigma^a$. Thus, the basic $D_n - \sigma$ distance indicator takes the form

$$\log D_n = a \log \sigma + b, \tag{1.5}$$

where $D_n \equiv d_n \times R$ and R is the estimated distance of the galaxy. The $D_n - \sigma$ or FP relations provide relative distances only. Therefore, these distance indicators must be calibrated. Since there are no luminous nearby elliptical galaxies which can be used to do this, an external condition must be imposed. For instance, to set the zero-point of the distance relation, one can require that "distant" clusters are at rest relative to the CMB, or that the Coma cluster itself is at rest. Once this is done, the $D_n - \sigma$ and the FP relations provide distance estimators with an accuracy of $\sim 19\%$.

Currently there are few techniques for measuring distances to galaxies on 100 h^{-1} Mpc scales. Other than the relations described above, the most common is the Tully-Fisher (TF) relation (Tully & Fisher 1977) for spiral galaxies. This is an observed correlation between the absolute magnitude of a galaxy and its maximum rotation velocity, as measured by the width of the HI 21 cm line. Since the rotational velocity of a galaxy is not expected to depend on how far it is from us, the TF relation allows one to compute the distance to a galaxy by simply measuring its apparent magnitude. This method has two primary advantages: spirals are more common than ellipticals, and the typical relative distance error of this method is smaller than for the FP/$D_n - \sigma$ methods ($\sim 15\%$ compared to $\sim 19\%$). On the other hand, as distance estimators, the FP/$D_n - \sigma$ relations have the advantage that early-type galaxies congregate in a cluster more strongly than spirals. By combining the results of the motions of several galaxies approximately at the same distance, the derived distance can be found $\sim \sqrt{N}$ (N is the number of galaxies considered) times more accuratly than for a single galaxy. Furthermore, because cores of early-types are reasonably bright, accurate velocity dispersions can be obtained optically for galaxies at redshifts even beyond 10000 kms^{-1}.

Which of the two relations, FP or $D_n - \sigma$, is more precise is still disputed. If the $D_n - \sigma$ relation is used, rather than the full FP treatment, a systematic error may be introduced (Phillips 1988), because the position of a galaxy in the FP depends on its effective surface brightness (Bender et al. 1992): galaxies with lower surface brightness have larger deviations. Jørgensen et al. (1993) concluded that the FP should be preferred, because the $D_n - \sigma$ relation has a larger scatter (17% compared to 11% using E galaxies in Coma) and suffers from the surface brightness bias. However, using a sample of 226 E and S0 galaxies in 10 clusters, the same authors found a different result: Jørgensen et al. (1996) found that the scatter in the FP and $D_n - \sigma$ relations are comparable. Van

Albada et al. (1993) found that the $D_n - \sigma$ relation has the same accuracy as the FP, provided that a proper surface brightness correction is applied. Davies et al. (1993) pointed out that, to avoid contamination, only galaxies in a restricted range of surface brightness should be used in the $D_n - \sigma$ relation. Finally, by using the $D_n - \sigma$ and FP relations to measure the relative distances of the Fornax and Coma clusters with respect to Virgo, D'Onofrio et al. 1997 argued that the $D_n - \sigma$ and FP relations have substantially the same accuracy, at least for nearby clusters.

We conclude that the $D_n - \sigma$ and FP relations are both potentially useful distance indicators because: 1) they are based on the correlation between photometric distance-dependent parameters (e.g., the galaxy size) and a spectroscopic, distance independent quantity (the stellar velocity dispersion); 2) they have small *rms* scatter, which results in an uncertainty in the predicted distance of a single galaxy of $\sim 19\%$; 3) they allow one to measure distances to galaxies on large, 100 h^{-1} Mpc, scales. On the other hand, the use of these relations as distance indicators is based on the assumption that they are universal: in all locations of the universe, the photometric and spectroscopic parameters of the early-type galaxies are assumed to follow the same relation, with no dependence on, e.g., the environment. Furthermore, because the surface brightness depends on the underlying stellar population, which in turn depends on metallicity, age, and IMF, the distances to early-type galaxies derived from these relations are sensitive to variations in how different galaxies evolved. For example, at lookback times of cosmological interest, younger elliptical galaxies could have had higher surface brightness compared to the present epoch. Scaling relations obtained at $z \lesssim 0.02$ would then lead to underestimates of their distances (e.g., Bershady 1996; van Dokkum & Franx 1996; Vogt et al. 1996).

Recently, several authors have found modest shifts with increasing redshift in the zero-point of the FP, $Mg_2 - \sigma$, and color-magnitude relations of cluster ellipticals (e.g., Bender et al. 1997; Dickinson 1995; Ellis et al. 1997; van Dokkum et al. 1998; Pahre et al. 1997; Stanford et al. 1998; Kodama et al. 1998). These results have important implications for models of galaxy formation and evolution (see Section 1.2.2). The availability of large aperture telescopes like the two 10m Keck telescopes, the two 8m Gemini telescopes, and the four 8m VLT telescopes will allow one to compare the scaling relations obtained for galaxies at different redshifts, leading to the possibility of studying the time-evolution of early-type galaxies.

To assess the universality of the $D_n - \sigma$ and FP relations, and to investigate stellar population differences between galaxies, one can use other correlations between measured global parameters of early-type galaxies, e.g., the $Mg_2 - \sigma$ relation. Since both σ and the Mg_2 line index are distance and reddening independent quantities, a comparison of the $Mg_2 - \sigma$ relations for early-types located in high and low density regions offers the best available way of demonstrating the significance, or otherwise, of environmental effects on galaxy populations.

1.1.2 The $Mg_2 - \sigma$ relation

The strong dependence of the stellar population on the structural parameters, implied by the existence of the FP or $D_n - \sigma$ relations, is confirmed further by the existence of the $Mg_2 - \sigma$ relation. This distance-independent relation can be used as an indicator of small population differences between galaxies that have the same velocity dispersion. Mg_2 is a molecular index (expressed in magnitudes) and measures both the MgI atomic

absorption and the broader MgH molecular absorption feature (the bandpass is 5154.1-5196.6 Å). This index has been widely used as a metallicity indicator for composite old stellar populations because it is sensitive to metallicity and insensitive to the shape of the IMF (Mould 1978). However, if the integrated light of the elliptical galaxy is due to a contribution of both giant and dwarf stars, Mg_2 also depends on the temperature of the main-sequence turn-off point (Burstein et al. 1984). This implies that Mg_2 is sensitive to differences in age of the stellar population. The effect of metallicity is to increase the strength of the index, while the a residual young stellar population tends to dilute the metal line index (probably leaving σ unaffected). Thus Mg_2 linestrength measurements can only supply constraints to combinations of age and metallicity, but cannot resolve the age/metallicity degeneracy. Indeed, for models of single stellar populations, which aim to predict the observables (linestrenghts, M/L and broad-band colours) given age, metallicity, and stellar initial mass function (IMF), the main problem in interpreting the observables is to break this degeneracy; It is difficult to determine unambiguously whether a spread in age rather than a spread in metallicity is required to reproduce the observations. Recent stellar population models (Worthey 1994; Vazdekis et al. 1996; Bressan et al. 1996) show that a change in age of a factor of ten, at fixed metallicity, produces a difference of ~ 0.11 mag in Mg_2, while a change of ten in $Z/Z_\odot$, at fixed age, results in a difference of ~ 0.18 mag (Jørgensen 1997; Colless et al. 1999). As a consequence, the measures of the Mg_2 linestrength must be very accurate if they are to be useful in the detecting stellar population differences. Although it is not entirely straightforward to use $Mg_2 - \sigma$ to constrain galaxy formation models, it has provided interesting results: it has been used to produce a FP corrected for subtle differences in stellar population (Jørgensen et al. 1996; Guzman & Lucey 1993), to place constraints on the global scatter in the ages, metallicities and M/L ratios for galaxies in clusters (Colless et al. 1999), and to investigate environment effects (Burstein et al. 1990; Guzman et al. 1992; Jørgensen et al. 1996; Jørgensen 1997; Colless et al. 1999; Bernardi et al. 1998).

1.2 Applications of empirical relations

1.2.1 Peculiar motions

The discovery of anisotropy in the Hubble flow on large scales from observations of spiral galaxies (Rubin et al. 1976), and the cosmic microwave background dipole (Smoot & Lubin 1979), interpreted as motion of our Local Group of 600 kms^{-1} toward ($l = 269^o$, $b = 28^o$), resulted in three vigorous pursuits: mapping of the peculiar velocity field of the local universe, mapping of large scale-structures, and searching for small-scale irregularities in the cosmic microwave background (CMB). It was hoped that the results would provide strong constraints on theories of the early universe, the formation of galaxies and the evolution of large-scale structure.

The finding by the "Seven Samurai" (7S) (Burstein et al. 1986) that the Local Group participates in a large streaming motion launched a high-intensity activity in this field. To construct a map of galaxy peculiar velocities in the nearby universe one needs to know the redshifts and distances of the galaxies. Indeed, the radial peculiar velocity of a galaxy is the difference between its total radial velocity as read from the redshift (cz)

and the Hubble velocity at its true distance (R)

$$v_p = cz - R \tag{1.6}$$

Furthermore, an absolute motion of the observer with respect to the CMB reference frame can be inferred, if the sky coverage of the galaxies considered is sufficiently uniform. Such a motion may in fact produce a dipole signature in the distribution of the positive and negative peculiar velocities. To build a uniform all-sky redshift-distance survey requires a significant effort since one needs high signal-to-noise spectra and images.

The 7S (Dressler et al. 1987a) reported a systematic variation in apparent velocity residuals of 423 ellipticals galaxies over the sky which, when interpreted as a bulk flow, implied that ellipticals in a large volume, out to ~ 6000 kms^{-1}, were moving with a bulk motion of ~ 600 kms^{-1} with respect to the CMB. The 7S computed distances using the $D_n - \sigma$ relation, and used the distance of the Coma cluster (7200 kms^{-1}) as their zero point. Even though it was obtained a decade ago, their sample remains one of the largest samples of elliptical galaxies in the literature; it extends out to 7000 kms^{-1}. Recent projects (EFAR, Wegner et al. 1996; SMAC, Hudson et al. 1999), comparable in size to that of 7S, have been undertaken to study the properties and peculiar motions of elliptical galaxies and clusters extending to larger volumes. While the SMAC survey covers the whole sky, the EFAR sample is confined to two volumes at distances between 6000 and 15000 kms^{-1}.

There is a general consensus that there are large scale flows in the nearby universe. Even though the "sources" of these motions are clearly associated to some mass concentrations, the properties and the spatial distribution of these concentrations are still hotly debated. At present, two different scenarios are still confronting each other. In one scenario (the small-scale motions scenario), peculiar motions are produced by local mass concentrations which can affect the motion of galaxies on scales of 40-50 h^{-1} Mpc. In the other (the large-scale motions scenario) it is assumed that big mass concentrations extend their influence over large regions, $\sim 100h^{-1}$ Mpc in extent.

The small-scale motions scenario agrees with the Great Attractor (GA) model of Lynden-Bell et al. (1988). This putative GA is a large, approximately spherical overdensity which influences the peculiar motions of galaxies on a scale of $\sim 50h^{-1}$ Mpc and is responsible for a large share of the Local Group's motion of 600 kms^{-1} with respect to the CMB. This model describes the basic picture of the bulk flow as follows: velocities rise outward from the Local Group towards the GA center, to approximately 2000 kms^{-1}, and decline beyond that point to zero (or near zero) at ~ 4500 kms^{-1}. From detailed modelling, these authors found that the peculiar motions of elliptical galaxies are best fitted by a flow towards an extremely large ($5 \times 10^{16} M_\odot$) mass concentration centered on $l = 307^o$ $b = 9^o$ at a redshift distance of 4350 kms^{-1}. They also reexamined the assumption, on which the large-scale flow interpretation is based, that the intrinsic properties of galaxies are the same everywhere. They found no evidence that systematic errors (Galactic absorption, cluster richness, different stellar populations) can either produce, or seriously affect, the large-scale motions that they saw. Both field and cluster ellipticals gave consistent bulk motion solutions, so they concluded that any environmental effect, although not excluded, must be rather subtle.

Other contemporary surveys produced galaxy distance estimates. Dressler et al. (1987b) provided two relations using six clusters, $D_n - \sigma$ and $D_n - Mg_2$, which gave distance estimators of 25% and 35% per galaxy respectively. Further analysis (Dressler &

Faber 1990; Faber & Burstein 1988; Burstein et al. 1990) largely confirmed the 7S result. The GA model created much speculation in the scientific community because, within the cold dark model of structure in the universe, it is difficult to explain the existence of such massive overdensities. More recent analyses, however, (e.g. Dekel 1998) suggest that the local motions are consistent with the COBE-normalized standard CDM model.

In contrast to these studies, an investigation of the peculiar motion of the Centaurus cluster by Lucey & Carter (1988) did not confirm the idea of a GA lying beyong the Hydra-Centaurus supercluster. They derived peculiar velocities to 5 nearby galaxy clusters, using the $D_n - \sigma$ relation, and concluded that the motions with respect to the CMB are not significantly different from zero. Indeed, the very existence of the GA is still questioned (Rowan-Robinson 1993), though some of the discussion in the literature simply reflects ambiguous definitions for this phenomenon (see reviews by Burstein 1990; Dekel 1994; Strauss & Willick 1995).

The large-scale motions scenario is supported by several other works. Mathewson et al. (1992a), from a survey of the peculiar velocities of 1355 spiral galaxies (657 in the GA region), found no back-side infall into the GA. This suggests that the GA does not exist. A similar result, also based on TF peculiar motion determinations, was found by Courteau (1992) and Courteau et al. (1993). Their main goal was to investigate the coherent motion (~ 350 kms^{-1}) of the Perseus-Pisces region (PP), directed towards the Local Group (Willick 1990, 1991). They claimed that the GA and the PP may both be part of a large-scale parallel streaming flow that includes all galaxies within a sphere of radius at least 6000 kms^{-1} around the Local Group, and that the motion might be due to very large-scale, low amplitude density fluctuations.

The main support for the existence of very large-scale peculiar motions comes from a result of Lauer & Postman (1994). Using brightest member galaxies as distance indicators, out to a distance of 15000 kms^{-1} , they found a bulk motion of 689 ± 178 kms^{-1} towards $l = 343^o$, $b = 52^o$ for an all-sky sample of 119 Abell clusters. Their result may imply that galaxies are being pulled by an extremely large concentration of mass, with much power in the peculiar velocity field arising from scales larger than 10000 kms^{-1}.

To a depth of ~ 6000 kms^{-1} , a rough consensus has emerged from recent peculiar velocity surveys of galaxies. For instance, Giovanelli et al. (1998) have found a flow of 200 ± 65 kms^{-1} towards $l = 295^o$, $b = 25^o$, from an I-band TF survey. The MarkIII velocity compilation yields 370 ± 110 kms^{-1} towards $l = 306^0$, $b = 13^o$ (Dekel et al. 1998). A similar amplitude for the bulk motion (420 ± 280 kms^{-1}) was found also by Hudson et al. (1997), who studied a sample of seven clusters in the Perseus-Pisces region and nine calibrating clusters from the literature, using FP distance determinations. Beyond this depth, however, the situation is much less clear.

In addition to the large motions found by Lauer & Postman (1994), other large motions have been obtained. Zehavi et al. (1998) have suggested that the volume within 7000 kms^{-1} is being subjected to a Hubble acceleration of $6.6\pm2.2\%$, resulting from a local underdensity of 20%, surrounded by an overdense shell. This result is based on the distances to 44 SNeIa. The bulk flow from the SMAC survey (Hudson et al. 1999) is also large: 630 ± 200 kms^{-1} towards $l = 260$, $b = -1$, though the direction of the motion does not agree with that found by others.

In contrast, Giovanelli et al. (1999) have found that, at small distances, the deviations from Hubble flow are dominated by the motions of nearby groups, comparable in amplitude to those of the Local Group. At distances larger than $35h^{-1}$ Mpc, the bulk flow

exhibits no significant change of value, anywhere up to 200 Mpc. Their dipole solution was drawn from a sample of 76 clusters of spiral galaxies (SCI+SCII). The bulk flow found by Müller et al. (1998), based on a sample of early-type galaxies covering three regions of the sky at $(-17^o.5 < \delta < +2^0.5)$ out to 15000 kms^{-1} , is also in disagreement with the Lauer & Postman (1994) result.

Currently favoured cosmological models are not able to produce coherent flows on such large scales (Feldman & Watkins 1994; Strauss et al. 1995; Jaffe & Kaiser 1995). A vast bulk flow over regions of $\sim 100h^{-1}$ Mpc, is discrepant with the CDM model, and the observed peculiar velocities disagree with the motion predicted from the galaxy density distribution observed with *IRAS* (Yahil 1988; Strauss et al. 1990). The *IRAS* data predict that the velocity flow should bifurcate towards the GA and PP, with an infall into PP.

The GA lies deep in the southern sky and in the brightest part of the supergalactic plane. Because spiral galaxies delineate the supergalactic plane much better than ellipticals, most of the large-scale peculiar velocity surveys have focused on spiral galaxies (Aaronson et al. 1982; Han & Mould 1990; Willick 1990, 1991, 1994; Willick et al. 1996; Mathewson et al. 1992a, b; Mould et al. 1993; Courteau et al. 1993, 1996, 1997). Most of these observational works, which used the TF distance estimator, have confirmed the 7S result of large-scale motions in the nearby universe. However, as described above, the nature of the mass concentrations that cause the flow remains controversial.

Given the computed distances and radial peculiar velocities, it is possible to extract the underlying three-dimensional velocity field and to reconstruct the mass density field (techniques used are, e.g., POTENT (Dekel et al. 1994); Wiener Fielter (Zaroubi et al. 1995); see also Chapter 8). These fields can provide useful constraints on the shape and amplitude of the mass power-spectrum, the relation between the galaxy and matter distributions, and the value of the cosmological density parameter Ω_0 (for reviews see Dekel 1994; Strauss & Willick 1995). To this end, several samples of galaxies, most with TF, and a few with $D_n - \sigma$/FP measurements, have been gathered over the last few years. If all galaxies trace the same velocity field, then analysis of large-scale motions greatly benefits from merging different samples into one self-consistent catalog. However, different observers differ in their selection procedures, the quantities they measure, the method of measurement, and the TF or $D_n - \sigma$/FP calibration techniques they use. These differences cause different systematic errors, and make merging of different datasets nontrivial.

A pioneering effort in merging two different datasets was carried out by D. Burstein, who compiled the MarkII catalog of 554 ellipticals and S0s (the 7S sample supplemented by data from Dressler et al. 1991 and Lucey & Carter 1988), and 429 spirals (mostly from Aaronson et al. 1982). This catalog was used in the first application of POTENT. Willick et al. (1997) combined spiral samples (Willick 1991; Mathewson et al. 1992b; Han & Mould 1990, 1992; Mould et al. 1991; Courteau 1996, 1997) with the MarkII ellipticals to form the MarkIII catalog of Galaxy Peculiar Velocities. The full MarkIII catalog consists of about 3300 galaxies ($\sim$ 2800 spirals and $\sim$ 500 early-types). Dekel (1994), using POTENT and a preliminary version of the Mark III catalog, and Dekel et al. (1998), using an improved version of the POTENT method and the final version of the MarkIII catalog, constructed maps of the velocity and associated density fields. They found a general resemblance between the fields recovered from spirals (S) with those reconstructed from the early-types (E). They argued that a 5% Hubble-like outflow has

to be added to the peculiar velocities of Es from MarkII to match the S data of MarkIII.

None of the projects mentioned so far have uniform sky coverage. Recently, Giovanelli et al. (1994-1997a,b) carried out a new survey of spiral galaxies that covered, essentially, the whole sky. Complementing their data set with measurements drawn from Mathewson et al. (1992b), they compiled a combined sample of about 1300 spiral galaxies in the field (SFI) and 500 spirals in clusters (SCI). The three-dimensional velocity and density fields were reconstructed using the SFI sample by da Costa et al. (1996). Compared to the earlier work of Dekel (1994), better sampling of the nothern hemisphere apparently led to significant differences in the density and velocity fields :

- the Perseus-Pisces (PP) region appears as a compact high density peak while the GA region is less prominent;
- the velocity field shows a region where the flow bifurcates towards the GA and toward the PP complex. An infall into PP is clearly seen (it was absent in Dekel's 1994 reconstruction)
- the density field is characterized by the existence of several voids sourrounded by tenuous structures. The existence of real voids in the matter distribution agrees with the picture obtained from galaxy redshift surveys (Pellegrini et al. 1990; da Costa et al. 1994).

All these findings are consistent with the velocity field predicted from the *IRAS* survey. From the more recent analysis of Dekel et al. (1998), the recovered mass distribution resembles, in its gross features, the results obtained in da Costa et al. (1996) from the SFI sample (Haynes et al. 1999a,b). The robust structures of the nearby universe are the two giant superstructures, the GA and the PP, each of mean mass density about twice the average, within regions of $\sim 50h^{-1}$ Mpc in diameter, and an extended underdense region between them.

More complete and homogeneous catalogs and improved bias-corrections to distance estimators will spread light on the several issues of large-scale motions that are still debated. Efforts to carry out galaxy surveys, to combine different data sets, and to analyze the associated three-dimensional velocity and mass density fields have been much more developed, both in size and in accuracy, for spirals than for early-types. Indeed, the only quantitative comparison of the velocities of early-type and spiral galaxies is shown in Dekel (1994) and in Dekel et al. (1998), using the MarkIII compilation. As seen before, most of this catalog consists of spiral galaxies ($\sim$ 2800 S compared to $\sim$ 500 E and S0). Although a general resemblance between the two fields was found, this E-S correlation cannot exclude the possibility that the inferred motions arise from environmental effects.

To verify that this E-S correlation is real and to test the results of da Costa et al. (1996) by using a complementary field, two fundamental issues must be overcome :

- the early-type sample must be enlarged
- the scatter in the distance indicators ($D_n - \sigma$, FP) must be reduced.

1.2.2 Stellar populations

The existence of the $D_n - \sigma$ and FP scaling relations indicate that early-type galaxies as a class, are homogeneous, and that their stellar populations vary smoothly and in

an orderly manner. Moreover, the tightness of these relations makes them extremely useful tools in computing galaxy distances. However, differences in age, metallicity or IMF, cause slope and zero-point shifts in the distance relations. For this reason, if their stellar populations differ, nearby early-type galaxies can yield spurious distances estimates (Gregg 1992). Indeed, early-types exhibiting "fine structures" (e.g., shells, arms, a bar) have systematically large positive and spurious peculiar velocities; these are probably due to current and/or recent star formation. Saglia et al. (1993b) argued that the scatter around both relations can be reduced by rejecting early-type galaxies with inner disk components. However, they concluded that the zero-point shift between the $D_n - \sigma$ relations of spheroidal and disky objects in Coma does not cause appreciable systematic differences in distances at smaller redshifts: for example, the 7S flow solution is not appreciably affected.

The most crucial assumption in using the $D_n - \sigma$ or FP relations as distance indicators is their "universality": a distance indicator derived using one sample must describe the galaxies in any other different sample. This topic and its implications is currently hotly debated.

If galaxies located in different environments had, on average, slightly different stellar populations, variations in the zero-point of the distances indicator would be observed. These shifts in the zero-point would introduce spurious peculiar velocities if the same distance indicator relations was applied indiscriminately. Therefore, it is clear that the universality of the $D_n - \sigma$ and FP distance indicators depends on the star formation and evolution history of early-type galaxies.

Great progress has been made in recent years towards charting and modeling galaxy formation and evolution. Yet, the origin of the galaxy morphologies, as illustrated by the Hubble classification, has so far defied a generally accepted explanation. This is especially the case for elliptical galaxies, with two quite different scenarios still confronting each other. One scenario is motivated by hierarchical clustering cosmologies: ellipticals form through a series of merging events that occur over a major fraction of cosmological time (e.g. Baugh et al. 1996; Kauffmann 1996). In hierarchical models, since clusters form from the highest peaks in the primordial density fluctuations, cluster ellipticals may complete most of their star formation at high redshifts (e.g. Kauffmann 1996; Kauffmann & Charlot 1998). On the other hand, in lower density environments, both star formation and merging are appreciably delayed to later times (Kauffmann 1996). The other scenario assumes, instead, that the whole baryonic mass of the galaxy was already assembled at early times in gaseous form, regardless of the mean density of the region; for this reason it is sometimes qualified as *monolithic*. Early examples of this latter scenario (Larson 1974; Arimoto & Yoshii 1987) stemmed from the Milky Way collapse model of Eggen et al. (1962); more recent incarnations include models by Bressan et al. (1994) and Matteucci (1994).

To investigate environments effects offers the opportunity for an observational test of the universality of the distance indicators as well as of the galaxy formation and evolution models.

Several studies in the literature show evidence that galaxies that are located in low-density environments have, on average, slightly younger stellar populations than those located in high density environments, in agreement with the prediction of the hierarchical scenario. The general idea behind all these works is that star formation and chemical enrichment terminated (on average) at a more recent epoch in field and poor-cluster

galaxies than in galaxies that are found in high density environments today.

Using 51 Coma ellipticals, Guzman et al. (1992) found that the $Mg_2 - \sigma$ relation for "halo" galaxies has a zero point of -0.017 ± 0.005 mag and larger scatter compared the "inner" ellipticals. They found similar effects for the D_n-Mg_2 relation. They explained the results as an "age offset". The differences between ellipticals located in low and high density environments agree with those found in the C-M diagrams: field ellipticals are bluer and show more scatter than those in clusters (Faber 1977; Burstein 1977; Larson et al. 1980).

De Carvalho & Djorgovski (1992) have analysed the (B-V) colour and Mg_2 correlations for a small subset (55 galaxies in clusters and 58 in the field) of 7S data set (Faber et al. 1989). They claimed to detect systematic differences between the field and cluster correlations: at a fixed luminosity, ellipticals in the field tend to be too blue, have too low Mg_2 or too high surface brightness. These effects fit naturally into the picture where the cluster ellipticals form early and in a more homogeneous way than the field ellipticals, which contain an admixture of younger stellar populations. However, at least part of the larger scatter for the field ellipticals can simply be a manifestation of the distances being more uncertain, which will also affect the FP relations. Pahre (1998) argues that most of the effect is due to reddening errors.

Two other studies, carried out by Bower et al. (1990) and Rose et al. (1994), investigated the environmental dependence of the stellar populations in early-type galaxies. They were particularly interested in determining the "age" differences of stellar populations. Their analysis is based on spectral indexes, in the 4000-4400 Åwavelength region, which can be used to evaluate the mean surface gravity of an integrated spectrum (Rose 1985). The age sensitivity results from the fact that the mean surface gravity effectively measures the luminosity of the main sequence turnoff relative to that of the giant branch: "integrated light of a young stellar system will contain a higher fraction of dwarf-star light in the blue than an older one". They used six composite spectra in high density clusters and three composite plus fourteen individual galaxy spectra in low density environments. They claimed that their results indicate the presence of a large intermediate-age stellar population in low density environments while it is almost negligible in dense clusters.

It is worth noting that all the above mentioned works are based on small samples of early-type galaxies.

In constrast, by comparing the observed peculiar motions to cluster richness for the 7S sample, Burstein et al. (1990) found no environmental effects on the slope or zero point of the $D_n - \sigma$ relation. However, they found a marginal difference in the effects of stellar population variations (indicated by the residuals ΔMg_2 of the $Mg_2 - \sigma$ relation) on the zero point of $D_n - \sigma$ relation for galaxies in clusters and those in the field. In low density environments, singly observed galaxies appear to have values of ΔMg_2 that decrease as the predicted distance decreases. This effect is weak, but it is in the sense of the effect that star formation would have on both D_n and Mg_2. The same behaviour is not seen for cluster galaxies. However, Burstein et al. showed that in order to understimate the distances derived using $D_n - \sigma$ by ~ 0.2 dex, the change in Mg_2 should be at least ~ 0.15 mag. Because such a large effect on Mg_2 is not observed, they concluded that this effect is weak, and simply contributes to noise in the measured velocity field. Guzman & Lucey (1993) disagree; using Bruzual's models, they argued that the change produced in Mg_2 would be only ~ 0.05 mag, which is consistent with

ΔMg_2.

Jørgensen et al. (1996) and Jørgensen (1997) claim a weak trend in $Mg_2 - \sigma$ offsets with "local density" $\log \rho_{cluster} = 2 \log \sigma_{cluster} - \log R$, where R is the projected distance of the galaxy from the cluster center. The offsets scale as $0.009 \log \rho_{\rm cluster}$, with $4 \leq \rho_{\rm cluster} \leq 7$. Thus, the highest difference in Mg_2, at a given σ, is ~ 0.008 mag. To test further the reality of environment effects, these authors compared $Mg_2 - \sigma$ for 100 field galaxies with that for 143 cluster galaxies using the large homogeneous 7S data set. They found a difference in the median zero points for the two samples of 0.009 ± 0.003 mag. Using stellar population models, the changes in age/metallicity corrisponding to such offset can be evaluated. One finds that the changes are small compared the values usually assumed by models which support the idea of an intermediate-age stellar population. Therefore, the 7S sample and the dataset of Jørgensen et al. give the same result: variations in age and metallicity are not significant enough for stellar populations of early-type galaxies to show environmental effects clearly.

Recently, in their study of EFAR galaxies, Colless et al. (1999) arrived at the same conclusion. They do not detect a significant correlation of the $Mg_2 - \sigma$ zero point with cluster dispersion $\sigma_{cluster}$, X-ray luminosity or X-ray temperature. In addition, Bernardi et al. (1998) (see also Chapter 8) found that cluster, group and field early-type galaxies follow almost identical $Mg_2 - \sigma$ relations, with a luminosity-weighted age difference of at most ~ 1 Gyr between the corresponding stellar populations.

Finally, several works have found a modest shift, with increasing redshift, in the zero-point of the fundamental plane, $Mg_2 - \sigma$, and color-magnitude relations of cluster ellipticals (e.g., Bender et al. 1997; Dickinson 1995; Ellis et al. 1997; van Dokkum et al. 1998; Pahre et al. 1997; Stanford et al. 1998; Kodama et al. 1998). All these studies agree in concluding that most stars in ellipticals formed at $z \gtrsim 3$.

The results reported above, of no significant evidence of environmental effects, together with the existing evidence for the majority of stars in cluster early-type galaxies having formed at very high redshift, have important implications. They argue in favour of

- the universality of the $D_n - \sigma$ and FP distance relations,
- the proposition that most stars in galactic spheroids had to form at high redshifts ($z \gtrsim 3$), whether or not the spheroids now reside in low or high density regions.

1.3 The ENEAR project

From the review given in Section 6.1.4, it is clear that some important results on the peculiar motions have been obtained from the available redshift-distance surveys. However, progress in the last few years has been slow. To build a uniform all-sky redshift-distance survey requires a significant effort, because one needs high signal-to-noise spectra as well as images. Until recently, the largest data sample suitable for peculiar velocity studies was that of the 7S. Since then, most peculiar velocity data has come from measurements of Tully-Fisher distances of spiral galaxies. Studies of early-type galaxies have, instead, concentrated primarily on galaxies in clusters, so as to study the properties of the Fundamental Plane and its possible dependence on environment. Currently, there are two major catalogs of peculiar velocity data: the Mark III catalog and the SFI-SCI sample

of spirals. No equivalent sample is currently available for elliptical galaxies. Therefore, the primary goal of our program has been to measure distances for an all-sky magnitude and redshift limited ($m_B \leq 14.5$ and $cz \leq 7000$ kms^{-1}) sample of early-type galaxies (ENEARf sample), to extend the 7S data in depth and complement the SFI survey of spiral galaxies. Thus, for the past several years, our team has carried out spectroscopic and photometric observations of early-type galaxies in the nearby universe.

Our sample also complements recent work on early-type galaxies in clusters; it provides a set of data over a wide range of densities. This is of great interest for stellar population studies, and for investigating environmental effects. In contrast to earlier work, clusters in the ENEAR database (ENEARc sample) were selected based on complete redshift surveys of magnitude-limited samples. Groups, identified by an objective algorithm, were used to assign galaxies to clusters using well-defined criteria. This procedure is considerably superior to those utilized in the past when only incomplete redshift information was available. The identification of groups also permits a much improved grouping of galaxies, which is critical when studying early-type galaxies. A strict assignment of galaxies to different environments is crucial for finding evidence for or against systematic differences between cluster and field early-types.

Cluster galaxies are used to derive the $D_n - \sigma$ relation. Although, such relation has been obtained by a number of groups, it was derived from different sets of data, in different passbands, with a variety of instrumental setups, and with different techniques for removing various biases and making membership assignments. This has prompted us to build our own scaling relation. To do so, we have combined our new data with those of previous authors suitably converted to a common system. This conversion was possible by making observations of a representative number of galaxies that had already been observed by other authors, thereby allowing us to use as much as possible data already avaliable in the literature.

At the moment, the ENEAR redshift-distance all-sky sample consists of over 1600 galaxies with measurements of central velocity dispersion and photometric parameters. Since ENEAR is an ongoing project, more data will be included in the database as they become available.

1.3.1 Development and collaborations

Due to the enormous bookkeeping work and collaborations that go into a project of this size it is worth reporting the initial conception, the subsequent development, and the individual and collective efforts of everyone who has participated in the project. This section is offered in recognition of the efforts of all those involved in the project so far; it is meant to give a clear view of everyone's contributions and responsibilities.

The ENEAR project was conceived as a spin-off of the Southern Sky Redshift Survey (SSRS, da Costa et al. 1988) which started back in 1982. From the very beginning the SSRS collaborators decided to integrate early-type galaxies longer than necessary for redshift determinations, with the intention of complementing the Faber-Jackson work carried out in the northern hemisphere by Tonry & Davis (1981). For that purpose, early-type galaxies were integrated to an average S/N of about 20 close to the NaD absorbtion line. Some 300 galaxies satisfied this criteria and, in 1988, da Costa, de Carvalho, Rité & Latham submitted a paper on the spectroscopic data. At that time there were few homogeneous datasets available and they found some systematic effects

relative to the 7S data. Since they were insecure about the origin of those effects they decided to withdraw the paper and wait until things could be sorted out better. This has taken another ten years.

By 1987, the results of the 7S and Djorgovski & Davis (1987) made it clear that one would have to go beyond the Faber-Jackson relation, which meant that to continue the project would require a major effort of imaging in order to use the $D_n - \sigma$ or FP scaling relations as distance indicator. Furthermore, the controversial results of the 7S, with a sample going roughly to 13.5, demonstrated the need to go deeper in order to probe structures like Perseus-Pisces which were absent in the 7S sample. In a meeting in Balatonfured in Hungary in the summer of 1987, L. N. da Costa, R. Giovanelli, M. P. Haynes, and D. S. Mathewson had taken the first steps for the SCI TF project. The ENEAR was therefore a nice complement to the TF project as it probes denser regions than the spirals. The first team of collaborators to the ENEAR project was formed by people working at the Observatório National (ON, Rio de Janeiro, Brazil): L. N. da Costa, P. S. Pellegrini and C. N. A. Willmer.

Until 1988 the sample was based exclusively on the SSRS data, and the idea of the ENEAR collaborators was to eventually use the measured CfA1 Redshift Survey data (Huchra et al. 1983) to produce an all-sky sample. At that time, in an effort led by P. S. Pellegrini, the collaborators attempted to create an all-sky magnitude limited sample (m_B=14.5). In the north they used the CfA1 galaxy sample; in the south they defined conversion relations between diameters and magnitudes to derive a magnitude-limited sample comparable to the CfA1. An all-sky sample was created (Pellegrini et al. 1990) by merging the CfA1, the SSRS and the equatorial sample (Huchra et al. 1990) for which complete redshift information were available. At that time they also decided to select galaxies only out to 7000 kms^{-1} . This limit was chosen so that the sample depth would be comparable to the SFI, and so that the sample size would remain manageable. In retrospect, because this redshift cut means that our sample is no longer truly magnitude-limited, this was a poor decision that we are now trying to correct.

About the same time the first imaging observations were carried out at CTIO (Cerro Tololo Interamerican Observatory, Chile) and at SAO (Smith Sonian Astronomic Observatory, Mount Hopkins USA) in the northern hemisphere with the full-time participation of M. V. Alonso who began her thesis work on this project in 1988 and who has given, for the past ten years, an enormous contribution to the development of the ENEAR project. To overcome several difficulties in Brazil, M. V. Alonso spent two long periods at the CfA visiting L. N. da Costa and trying to reduce the data from SAO. Unfortunately, in 1990 IRAF was in its infancy, there was a migration to SUNs, and basically nothing worked very well. In Brazil problems with spectroscopic data observed with Reticon in CASLEO (Complejo Astronomico el Leoncito, San Juan Argentina) and with the data reduction packages delayed the analysis of the spectroscopic data. In addition, the redshift survey time at CTIO and ESO (European Southern Observatory, La Silla Chile) was being used to extend the sample in depth, which prevented from restricting the sample to m$\leq$ 14.5. The financial and political situation at the ON also created a chaotic situation which dramatically affected the performance of the group in Rio de Janeiro. In addition, key people such as C. N. A. Willmer were absent for two years during their postdocs.

In 1990-1992 the group had problems getting time at CTIO for imaging partially because some of the collaborators were also part of the SFI project, and the TAC (Tele-

scope Acquisition Commitee) was unwilling to grant more time before some publication in that program. In the north they were trying to use the SAO imager but they could not compete with the ongoing CfA2 Redshift Survey (Huchra et al. 1995) for time at the 60 inches for spectroscopy. To overcome the lack of telescope time the group in Rio tried to enlarge the collaboration in order to have some access to the ESO telescopes, but for reasons beyond their control this attempt bore no fruits.

For all these reasons the progress of the project slowed down in the period 1990-1992. Only in 1993 was the team able to continue this effort, thanks to a spin-off of the SFI and EFAR project (Wegner et al. 1996). G. Wegner and W. Freudling joined the team, thus giving the project significant time at the two telescopes at MDM (Michigan-Dartmouth-M.I.T. Observatory, Arizona USA) and access to photometric time at ESO's telescopes. Recently, a major boost has been the ON-ESO agreement giving the project generous time at the 1.52m telescope at La Silla for spectroscopy. With these new possibilities the project has made enormous progress.

Thus, along the years the team increased in number. At the beginning of 1996, I joined the group (providing them, as some of them said, with fresh blood). I found suitable conditions for carrying out my PhD thesis: a huge amount of data collected in the past years was ready for analysis. Furthermore, I would have access to the MDM and ESO telescopes. I would also have the opportunity to use the most update data reduction facilities, to work in an international environment, and especially to collaborate with experts from all over the world.

Since my arrival, I have contributed to the development of this project as follows: observing and reducing part of the data; adapting the photometric procedure described by Saglia et al. (1997) to suit our requirements, which was then used by M. V. Alonso and myself to measure all the photometric parameters; obtaining the velocity dispersion and line indices of all the available spectra using the software installed by G. Wegner and C. N. A. Willmer during their 1997 visit to ESO (they have kept the spectroscopic data reduction up-to-date); keeping the database up-to-date.

My main contribution has been to make statistical analyses of the sample and of the derived photometric and spectroscopic parameters. Since the sample is compiled from our new data and from the literature, it was crucial to insure that data from different sources was combined homogeneously; if this is done incorrectly, systematic effects would seriously compromise the whole effort. Therefore it was necessary to bring all the photometric and spectroscopic measurements, from all the various sources, to a uniform system. Once the sample was assembled, missclassified galaxies or galaxies with peculiar features in their spectra or images were identified. Thereafter, careful checks of the quality of the data, the reliability of the measured parameters, and the nature of the errors were necessary. A special effort was made to assign galaxies to groups/clusters using well-defined criteria, since this is important both for mapping the peculiar velocity field and for studying the environmental effects. The groups/clusters identified in this way were used to define the ENEARc cluster sample. This sample was used to determine the $D_n - \sigma$ relation, which was used as distance indicator, and the $Mg_2 - \sigma$ relation. Both relations are useful for stellar populations studies. Finally, distances and peculiar velocities for the whole sample were obtained, and analyses of the velocity field and determination of the bulk motion carried out.

Recently, S. Zaroubi has used the peculiar velocities derived from the ENEARc cluster sample and the ENEARf all-sky magnitude-distance limited sample, to recon-

struct the velocity and mass density field using the Wiener Filter technique. The reconstruction of the mass power spectrum and estimates of the parameter β is still ongoing.

I would like to point out that the scope of the project has also broadened. ENEAR is not just a velocity-distance sample of galaxies but a large database of spectroscopic and photometric information useful for different studies of early-type galaxies in the nearby universe. In the future, it may be enriched by new photometric measurements derived from near-IR CCD images. For example, in collaboration with R. P. Saglia and R. Bender, I have observed ~ 200 cluster galaxies in the K and H bands. Unfortunately, due to the large amount of optical data I had to deal with, reduction of the near-IR data is still incomplete; therefore they are not included in this thesis.

The main results I obtained using the data of the ENEAR sample are: a determination of the $D_n - \sigma$ distance indicator using the cluster sub-sample; a computation of the bulk-flow using field galaxies, groups and clusters; and a determination of the $\mathrm{Mg}_2 - \sigma$ relation which gives some clues on early-type galaxies formation, environmental effects, and on the universality of the $D_n - \sigma$ relation.

One should realize the enormous bookkeeping work and collaborations that go into a project of this size. As one can imagine it has been a daunting task to coordinate these various efforts. Thanks to L. N. da Costa, who persisted with this project through all the problems which arose during these years, the ENEAR database is now giving its first results which tell us more about the mysteries of the vast and mostly unknown space around us.

1.4 Outline of thesis

This thesis is organized as follows: Chapter 2 gives a description of the ENEAR sample, its completeness, and an overview of the available photometric and spectroscopic data. Our observations and data reduction for photometry and spectroscopy are described in Chapter 3 and 4, respectively. The cluster sample selection, the membership assignement, and the data available for those cluster galaxies suitable for the determination of a distance relation are reported in Chapter 5. The method used to derived the $D_n - \sigma$ distance indicator with its selection bias corrections, the peculiar velocities of the cluster sample, and the determination of the $\mathrm{Mg}_2 - \sigma$ relation are decribed in Chapter 6. The first results on the large-scale motions obtained using the ENEAR database are presented in Chapter 7, where we report: the determination of the distances for the complete magnitude-redshift limited sample; the bulk motion derived from this complete-limited sample and from clusters; and a Wiener Filter reconstruction of the velocity and density fields. Finally, in Chapter 8 we present the comparison of the $\mathrm{Mg}_2 - \sigma$ relations derived from galaxies belonging to different environments and its interpretation, which is another valuable result obtained from an application of the ENEAR database. Chapter 9 gives a summary and conclusions about this work and future prospects.

Chapter 2

The ENEAR redshift-distance survey

The ENEAR redshift-distance survey consists of early-type galaxies selected from an all-sky magnitude-limited sample of galaxies brighter than $m_B = 14.5$ with complete redshift information as well as a sample of 28 clusters. These two samples are complimeted by fainter galaxies in the field, and by early-type spirals that were misclassified in the original catalogs from which our sample was drawn. By combining our new observations with data available in the literature we have constructed a homogeneous database. It has a total of 2027 galaxies with measured velocity dispersions, 1891 galaxies with photometric information and 1694 galaxies with measured distances.

The primary goal of this chapter is to describe the sample and to give an overview of the photometric and spectroscopic data obtained during the ENEAR survey. From this data set, well-defined and homogeneous samples that are suitable for analysing the peculiar velocity field and, more generally, for studying the properties of present-day early-type galaxies, can be drawn.

2.1 ENEARf: The magnitude-limited sample

2.1.1 Selection

The primary goal of the ENEAR project has been to extend the volume probed by the 7S, who sampled the peculiar velocity field of early-type galaxies within a volume $\sim$ 4000 kms^{-1} in radius. Their sample included early-type galaxies brighter than $m_B \sim$ 13.5, where m_B is roughly in the Zwicky $B(0)$ system, adopted for instance in the Center for Astrophysics Redshift Survey (CfA1, Huchra et al. 1983). We also wanted to complement the SFI TF redshift-distance survey of late spirals (e.g., da Costa et al. 1996; Haynes et al. 1999a,b) out to $\lesssim$ 7000 kms^{-1} which was initiated immediately after the results of 7S.

To achieve this goal our team assembled all the complete redshift surveys available at the beginning of this project (in 1988) to build up an all-sky sample. Originally the following samples were used: 1) the CfA1 Redshift Survey sample (Huchra et al. 1983), covering the regions $b > 40°$ and $\delta > 0°$ in the northern galactic cap, and $b < -30°$ and $\delta > -2.5°$ in the southern hemisphere; 2) the sample of galaxies used in the Southern Sky Redshift Survey (da Costa et al. 1988) covering the regions $b < -30°$ and $\delta \leq -17.5°$

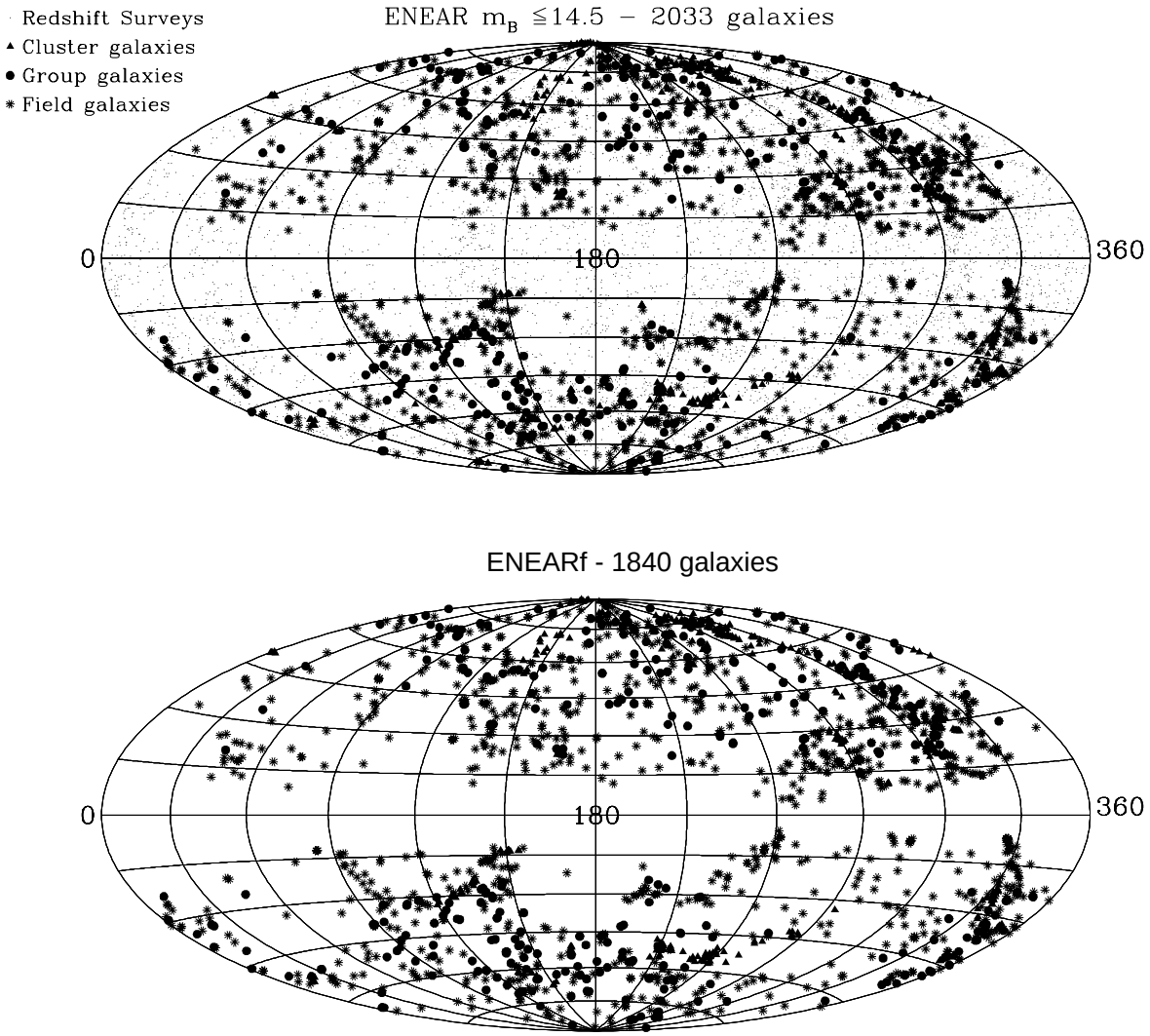

Figure 2.1 The projected distribution in galactic coordinates of (upper panel) the magnitude-limited sample of early-type galaxies ($T \leq -2$) and (lower panel) the ENEARf sample. Small dots refer to galaxies included in the magnitude-limited redshift surveys, as described in the text. The other symbols indicate ENEAR galaxies belonging to different environments.

in the southern galactic cap, and $b > 40°$ and $\delta < -17.5°$ in the northern galactic cap; 3) the equatorial survey sample of Huchra et al. (1990) filling in the gaps between the first two samples near the equator. Magnitudes for the SSRS galaxies were assigned based on magnitude-diameter relations derived by Pellegrini et al. (1990) who made the first attempt to build up a uniform magnitude-limited sample for the whole sky. More recently, we have added galaxies drawn from the Optical Redshift Survey (Santiago et al. 1995). This is the second attempt at constructing an all-sky sample of optical galaxies that is comparable to those extracted from *IRAS*, and at extending the sample towards lower galactic latitudes to further increase the sky coverage to match that of the SFI and to properly cover the region of the Great Attractor. The projected distribution of the whole m_B=14.5 magnitude-limited sample is shown in the upper panel of Figure 2.1.

Magnitudes used in the different catalogs were converted into an approximately homogeneous system using statistical corrections between the various systems as described in Pellegrini et al. (1990) and da Costa et al. (1998). However, as discussed in these papers the individual magnitudes can have errors as large as 0.5 mag.

The morphological types adopted are those from Lauberts & Valentijn (1989). The types given in the CfA1 catalog were converted according to the following prescription. CfA1 types -6, -4 and -1 were assigned types -7, -3, -2, respectively, while -5, -3 and -2 remained unchanged to roughly conform with the the ESO system. In the equatorial region we used the RC3 classification (Corwin & Skiff 1995) also transformed to our system. Some of the morphological classifications in the parent samples were wrong. This means that, although we have converted all classifications to a single system, objects that were wrongly classified initially will still be wrongly classified. Therefore, we removed some objects from the sample in the course of the program as discussed below.

From the all-sky sample we have drawn 2033 galaxies brighter than $m_B = 14.5$ and $T \leq -2$ and considered those 1840 galaxies with $cz < 7000$ kms^{-1} as our primary targets. This sample is hereafter refer to as ENEARf. The redshift cutoff was adopted for two main reasons: so that the sample depth would be comparable to the SFI; as a compromise between the number of objects to be observed in the time available, and the desire to have a high level of completeness in the nearby volume. It is our hope in the future to extend the present sample to make it a truly magnitude-limited sample. The redshift distribution of the sample as a whole is shown in Figure 2.2, from which we find that the redshift-limited sample corresponds to 90% of the magnitude-limited sample. Also note that at $cz \sim 7000$ kms^{-1} the selection function shows a sharp decline which means that the neglect of high-redshift galaxies should not lead to a very strong selection bias in the peculiar velocity.

The ENEARf sample consists of 466 galaxies with $T \leq -5$, 305 galaxies with $T = -3$ and 1069 with $T = -2$. The projected distribution of this selected sample is shown in the lower panel of Figure 2.1. Comparison between the two panels shows that the sample being considered is a fair representation of the main structures probed by the magnitude-sample as a whole. Clearly, our sample is sufficiently deep and dense to probe the most prominent large-scale structures in the nearby universe including Virgo, the Great Attractor region and its extension to the Telescopium-Pavo-Indus complex, Perseus-Pisces and Coma.

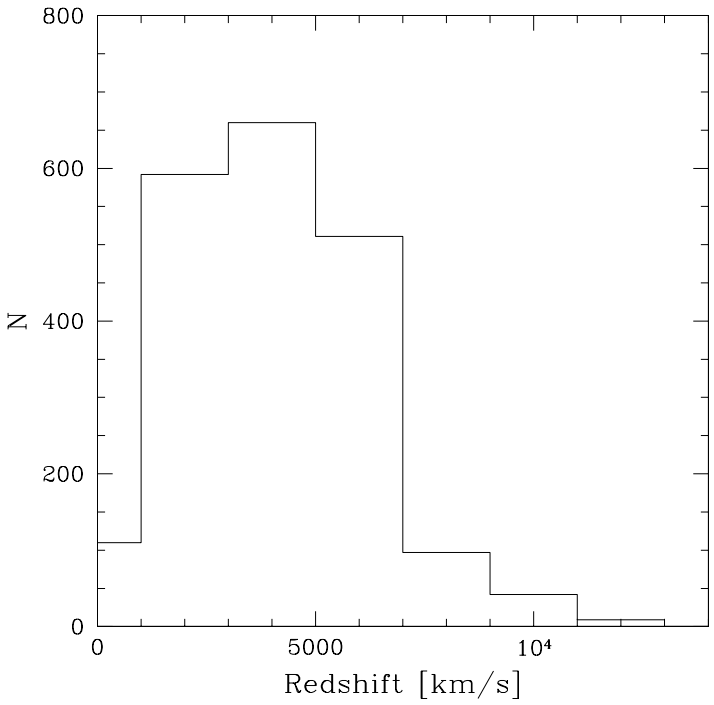

Figure 2.2 The redshift distribution of the ENEAR sample of early-type galaxies ($T \leq -2$) brighter than $m_{\rm B} = 14.5$.

2.1.2 Pruning the sample

Because the ENEARf sample was extracted from different catalogs (Zwicky, ESO, MCG), it is not surprising that some pruning of the sample is required both before and after the observations. Galaxies in very crowded fields, obvious cases of misclassifications, superposed galaxy images, and bright stars very close to the target galaxy were among the most obvious reasons for removing a galaxy from the sample prior to the observations. We also discarded galaxies after observations due to the presence of strong emission lines in their spectra, small S/N spectra for low surface brightness galaxies, low σ galaxies observed at low-resolution (most of which have been re-observed at high-resolution) with large errors, galaxies observed in non-photometric nights or under poor seeing conditions. A complete description of these cases will be presented in Chapter 3 and 4. In the final sample of peculiar velocities we have also removed galaxies which are either misclassified (e.g., with $D/B > 10$ or showing shells, arms, dust lane, large bar) or are contaminated by the light of nearby objects, as described in Chapter 7. The pruning of the parent sample is still ongoing.

2.1.3 Grouping galaxies

In contrast to late-type galaxies, early-types tend to reside in virialized clumps and in regions of high density. Therefore, in order to use early-type galaxies to map the peculiar velocity field it is important to assign them to groups and clusters. This is a major advantage of using early-types to map the peculiar velocity field. Indeed, even though

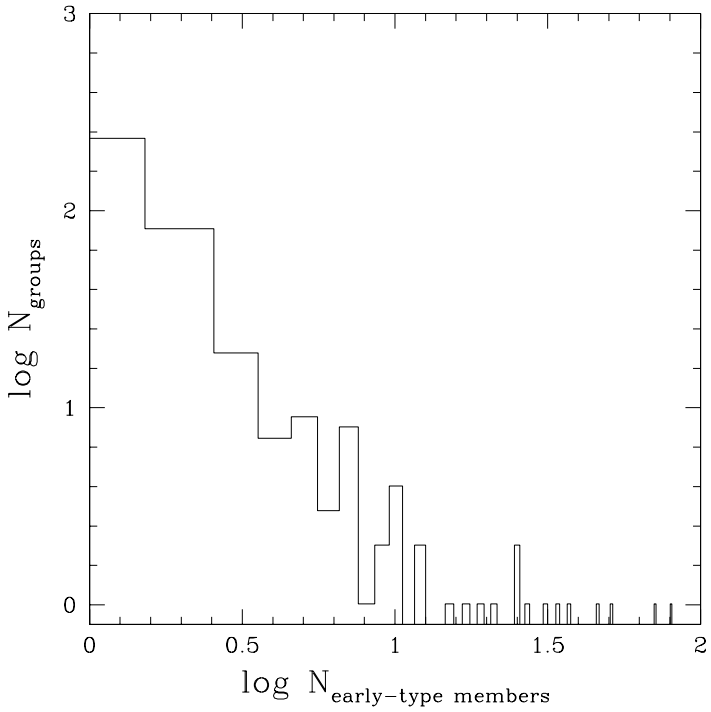

Figure 2.3 Multiplicity function of early-type galaxies in groups.

the number of groups may be relatively small, the distances to them are considerably more accurately determined, because the distance errors are decreased by a factor of $\sqrt{N}$, where N is the number of early-type galaxies in the group.

Since our sample is drawn from complete redshift surveys the assignment of galaxies to groups can be done in a systematic way, greatly improving on earlier work. This is done by searching groups in the original magnitude-limited catalog using objective friends-of-friends algorithms (e.g., Huchra & Geller 1982; Maia et al. 1989).

To assign galaxies to groups we have used the group catalogs of Maia et al. (1989) for the SSRS and of Huchra & Geller (1982) for the CfA1. These groups were defined as associations with a density contrast $\delta\rho/\rho > 40$. These catalogs have been used as they provide the largest sky coverage. In regions covered by CfA2 and SSRS2 we have replaced these groups by those recently compiled by Ramella et al. (1997) for the CfA2 and by Ramella et al. (1999) for the SSRS2. These surveys cover a slightly smaller area but extend to fainter magnitudes and consider groups with larger density contrast $\delta\rho/\rho > 80$ (numerical simulations suggest that these are less contaminated by spurious groups). Groups have also been identified at low galactic latitudes using the data from the ORS kindly provided by B. Santiago and M. Davis.

In assigning galaxies to groups we have adopted the following prescription. First, if more than one early-type galaxy is assigned to the same group it is called a group galaxy. Second, we assign galaxies to a group if their projected separation is $\leq 1.5R_p$ and $cz_{\rm gal} - cz_{\rm gr} \leq 1.5\sigma_{\rm gr}$, where R_p is the mean projected separation of the group, $cz_{\rm gal}$ is the radial velocity of the early-type galaxy, $cz_{\rm gr}$ is the mean group velocity and $\sigma_{\rm gr}$ is the *rms* velocity of galaxies in the group. We thus allow some early-type galaxies in the vicinity of high-density groups to be included.

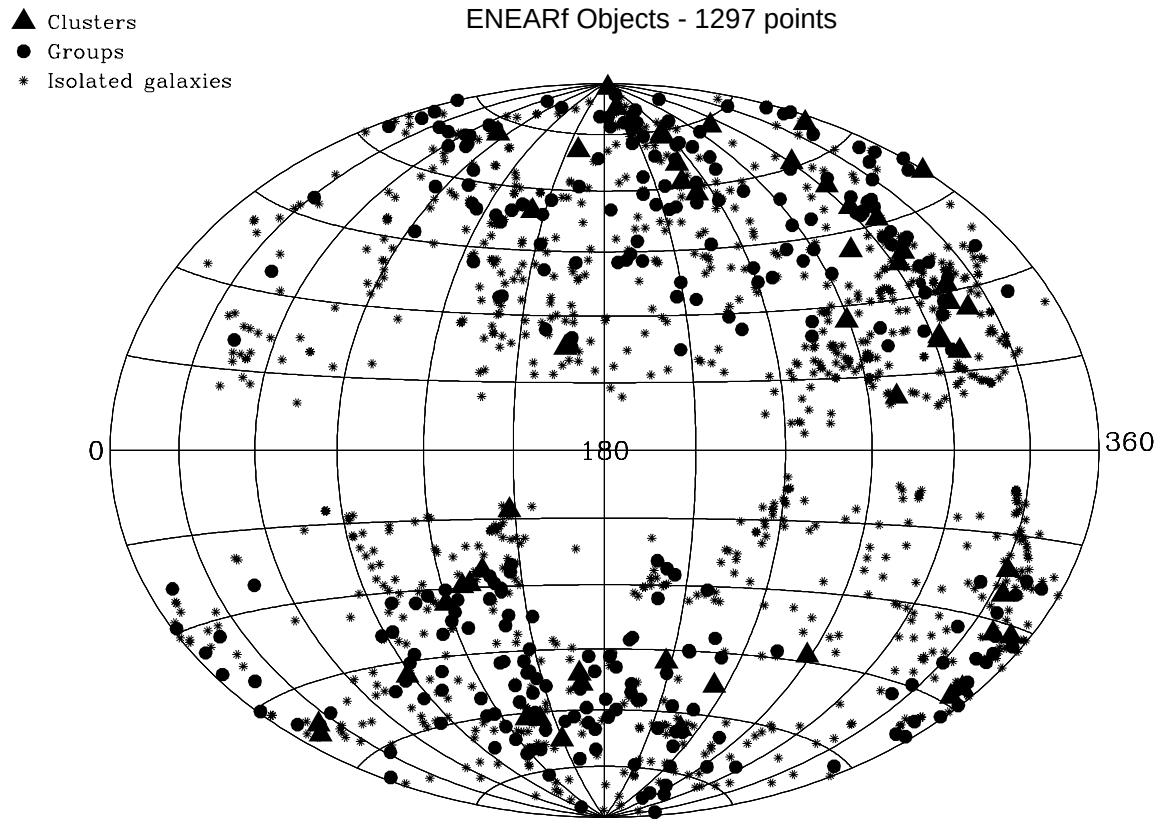

Figure 2.4 The projected distribution, in galactic coordinates, of the ENEARf objects. Filled triangles, circles and asterisks represent clusters, groups and isolated galaxies, respectively.

In regions where group catalogs are not available we adopt mean values for R_p and $\sigma_{\rm gr}$ and look for early-type companions satisfying the same criteria from other early-type galaxies.

In the ENEARf sample we find that 51% of the early-type galaxies are isolated, 45% are assigned to groups according the first criteria and 4% are peripheral group members. Also, 15% of the early-type galaxies are associated with groups in which the other members are late-type galaxies. For these cases the galaxy is effectively isolated as far as its distance error is concerned, except that the group redshift, instead of the individual galaxy redshift, is used when computing its peculiar velocity. All other groups containing at least two early-type galaxies are treated as single objects with the redshift corresponding to the mean redshift of the group and the distance as the error-weighted mean distance of the early-type galaxies in the group. Figure 2.3 shows the number of groups obtained in this way as a function of the number of early-type galaxies in the group.

Figure 2.4 shows the projected distribution of 1297 objects in the ENEARf sample; there are 971 isolated galaxies and 239 groups with more than 4 early-type members. In Chapter 5 we also make a somewhat arbitrary division of the sample into field and cluster objects, where a cluster is defined as a system with more than 15 members, of which at least 5 are early-type galaxies. This cluster sample is used to define a template distance relation in Chapter 6. Chapter 8 describes how the ENEAR assignment to

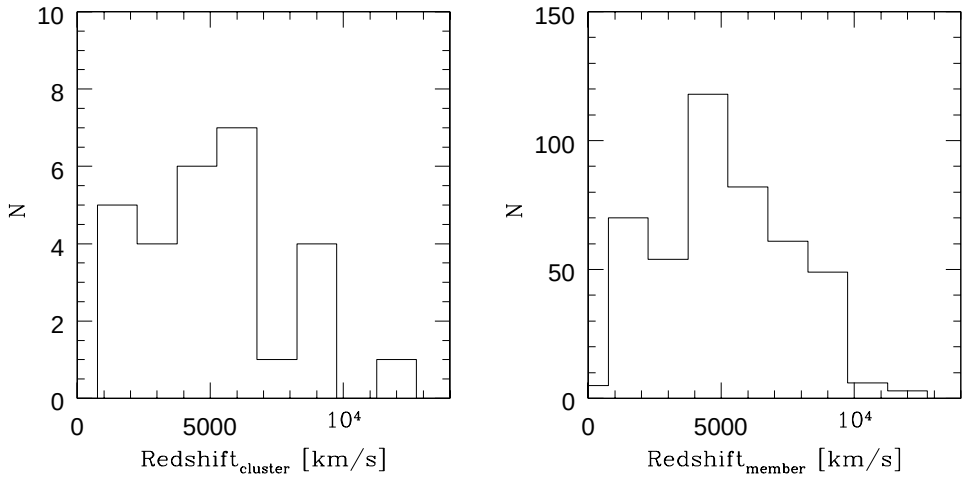

Figure 2.5 Redshift distibution of clusters (left panel) and cluster members (right panel).

field, groups and clusters can be used to investigate the properties of early-type galaxies in different environments.

2.2 ENEARc: The cluster sample

The ENEARf sample was complemented by a cluster sample, hereafter ENEARc which has been used to define a self-consistent template distance relation (Chapter 6) combining all the cluster data. The sample consists of groups identified in ENEARf with more than 5 early-type galaxies to which were added clusters selected from the literature. The latter were not identified as groups because either most of the member galaxies were fainter than the $m_B = 14.5$ limiting magnitude or because they lie beyond our redshift limit of 7000 kms^{-1} or outside the surveyed region at very low galactic latitudes. In addition to the clusters identified as groups, fainter members have been added according to well-defined membership criteria (discussed in greater detail in Chapter 5). A total of 58 groups were identified satisfying our criteria, i.e., more than 15 cluster members and more than 5 early-type galaxies; most of these objects are in the Abell or the ACO cluster catalogs. However, we have used only 28 candidates, for which a substantial number of observations were already available in the literature; this allowed us to concentrate our efforts on the field galaxies. We hope, in the future, to observe all 58 clusters.

Currently, the ENEARc sample consists of 446 galaxies in 28 clusters/groups. Figure 2.5 shows the redshift distribution of the clusters which span a range of redshifts up to $cz \sim 10,000$ kms^{-1} with an approximately uniform number per redshift bin. Also

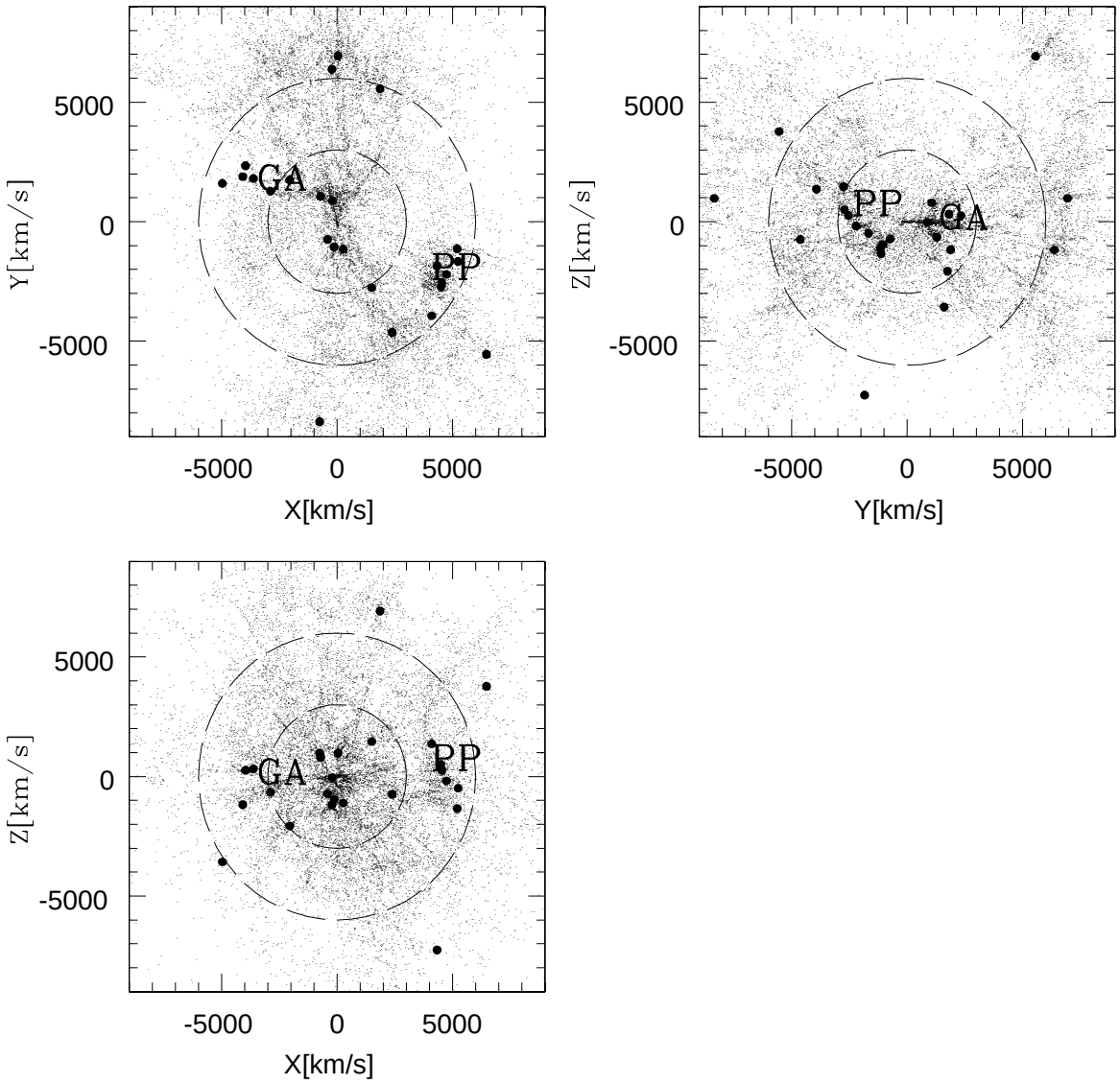

Figure 2.6 The spatial distribution of the 28 clusters in Cartesian supergalactic coordinates (X, Y, Z), expressed in kms^{-1} in the CMB reference frame. The two dominant concentrations of galaxies, the Great Attractor (GA) and the Perseus-Pisces (PP) superclusters, are indicated on the three panels. Small dots show the objects in the parent magnitude-limited redshift survey samples from which our catalog is drawn.

Table 2.1 Main samples in the ENEAR catalog

Source (1)	N_σ (2)	N_{Mg_2} (3)	N_{D_n} (4)	N_{FP} (5)
Our	1103	1036	1294	1294
LC	114	–	78	–
7S	543	533	499	179
D	158	151	175	–
JFK	159	119	200	194
Lc	85	–	84	–
S	88	81	98	98

Notes: N is the number of galaxies observed by us and by other authors for spectroscopy and photometry. The references are: LC: Lucey & Carter (1988); 7S: Faber et al. (1989); D: Dressler (1987), Dressler et al. (1991); JFK: Jørgensen, Franx & Kjaergaard (1992,1995a,1995b); Lc: Lucey et al. (1997); S: Smith et al. (1997).

shown is the redshift distribution of all the cluster members identified using the criteria above. The spatial distribution of these clusters is shown in Figure 2.6, where the supergalactic cartesian coordinates of the clusters in three orthogonal projections are shown. The figure shows that the clusters are distributed nearly uniform across the sky; they delineate all the major structures in the nearby universe.

2.3 Data

2.3.1 Other sources

To estimate distances, both kinematical and structural parameters of the galaxies are required. These include measurements of the central velocity dispersion from high-quality spectra and photometric parameters such as the half-light radius, r_e, the surface brightness within this radius, $\bar{\mu}_e$, and the angular diameter, d_n, within which the mean surface brightness is equal to a pre-specified value, following Dressler et al. (1987a). In addition, other parameters of interest such as total magnitudes, disk-to-bulge ratios and ellipticities are also computed.

To minimize the observational effort we have compiled spectroscopic and photometric parameters from the literature. This database stores the following information: galaxy identification, coordinates, radial velocity, magnitude, morphological type, major and minor-axis lengths, velocity dispersion measurements, line indices and a whole range of photometric parameters obtained in different passbands. Measurements from different authors or different observations conducted by us are stored separately to allow for intercomparison. Although extensive, the compilation is not complete as preference was given

to data in the redshift range of interest. We hope to make all this information publicly available soon.

The bulk of the data still comes from the all-sky sample of "elliptical" galaxies of Faber et al. (1989), as distributed in electronic form by Burstein (the Mark II catalog), although several more recent observations from other authors are included. The original ENEAR database also included the earlier compilations of Tonry & Davis (1981) and Whitmore et al. (1985), some of which was based on old data. However, comparison with modern CCD data showed that the errors in the measurements were large ($\sim 30\%$) and required large zero-point shifts. Therefore, these old compilations have been excluded from our sample.

The samples cover different regions of the sky, were selected in a variety of ways, and were observed in different resolutions or passbands. With the exception of the 7S, most of the data refer to galaxies in clusters. Table 2.1 lists the datasets that are currently included in our database and the number of galaxies available from each. In total there are 2826 measurements of velocity dispersion and 2570 values of photometric parameters, corresponding to 2027 galaxies with velocity dispersion, 1891 galaxies with photometry and 1694 with the required information to compute their distance. From these data, distances to 68% of the ENEARf galaxies and 89% of the ENEARc sample can be estimated.

Note, however, that the parameters cannot be used as listed; they must first be transformed into a common scale. There is a sufficient overlap between our different runs to ensure the uniformity of our internal data. Furthermore, observations of galaxies in our ENEARc sample provided enough overlaps with other authors to allow the conversion of the measurements of other authors into our system, thus allowing us to optimize the use of publicly available data.

2.3.2 New photometric observations

Since 1988, photometric observations in R-band have been made using different telescopes in the northern and southern hemispheres. Over 1500 galaxies have been observed of which 1294 now have measured photometric parameters. Most of the data were taken with large format CCDs, allowing for good sky subtraction, and occasionally for observing more than one galaxy per frame, especially for galaxies in groups. Some galaxies had to be discarded from the early-type sample because: 1) bright stars close to the galaxy were present; 2) the field was very crowded; 3) images were superposed; and 4) the morphological type was incorrect.

Because the imaging observations were conducted over an extended period of time, an attempt was made to conduct repeated observations in different runs to provide the necessary data for run-to-run corrections which would allow us to transform all of our measurements into a common internal system. As a result, 356 observations of 321 galaxies are available for assessing these statistical corrections.

All images were reduced using standard *IRAF* tools, and surface photometry was carried out by fitting elliptical and circular apertures to the two-dimensional light distribution of each galaxy. Profiles of the light distribution were fitted by a de Vaucouleurs' $r^{1/4}$ law sometimes in combination with an exponential profile to represent the light distribution of a disk. The fits used the algorithm developed by Saglia et al. (1997), which also corrects for the smearing effects due to seeing and provides information about the

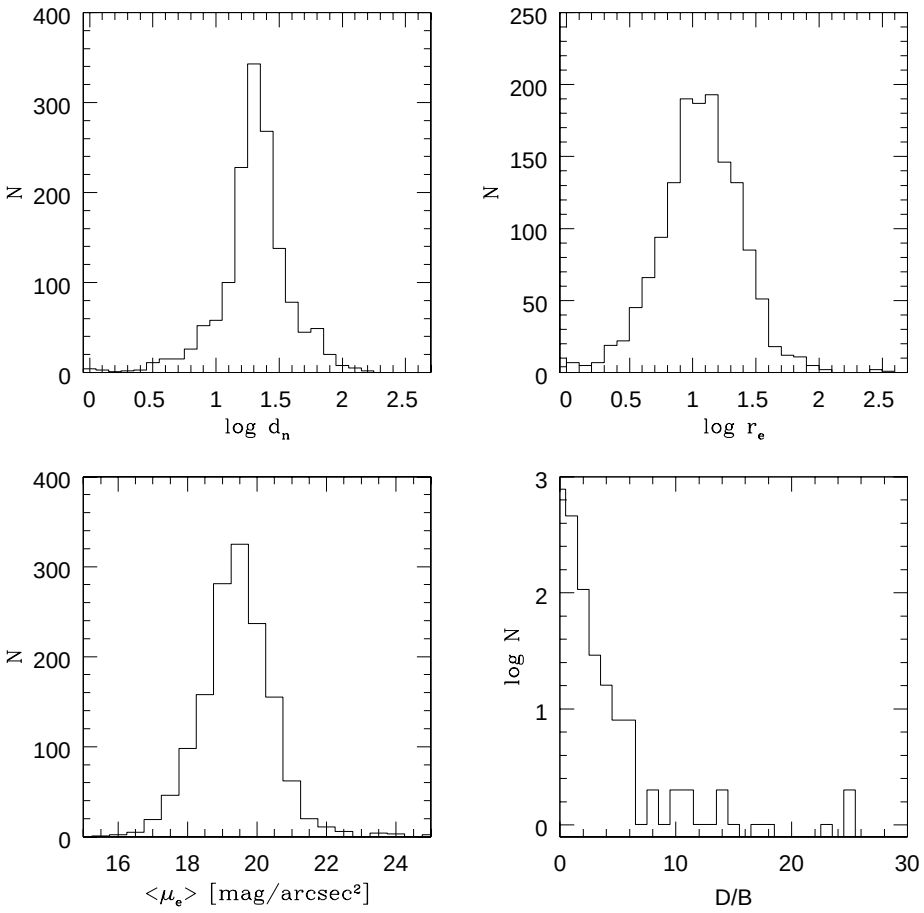

Figure 2.7 Distribution of observed photometric parameters: $\log d_n$, $\log r_e$ (d_n and r_e in arcsec), $\bar{\mu}_e$, and the D/B ratio.

quality of the fit. The main photometric parameters derived are the angular diameter d_n (as defined by the 7S), the half-light radius, r_e, the mean surface brightness within this radius, $\bar{\mu}_e$, as well as global quantities such as total magnitudes, m_R, the disk-to-bulge ratio, D/B, ellipticity, position angle and parameters which can be used to characterize the overall image shape (e.g., boxy, disky). Details of the observations, data reduction, and analysis and tables listing the photometric parameters are given in Chapter 3.

To illustrate the characteristics of the observed samples Figure 2.7 shows the distribution of values for $\log d_n$, $\log r_e$, $\bar{\mu}_e$ and the disk-to-bulge ratio D/B of the observed galaxies. The first three parameters are used in defining the distance relations. The D/B ratio has also been used as an indicator of late-type galaxies, which have been removed from the sample. Finally, to characterize the population as a whole, Figure 2.8 shows Kormendy's law, which is a projection of the Fundamental plane of early-type galaxies in the $\bar{\mu}_e - M_R$ plane. To derive the absolute magnitude M_R from the observed total magnitude m_R we used galaxy distances as computed from the $D_n - \sigma$ relation presented in Chapter 6. The two symbols in the figure show the morphological type (elliptical or lenticular) assigned to the object in the original catalogs.

As mentioned above our derived values of photometric parameters $\log d_n$, r_e and

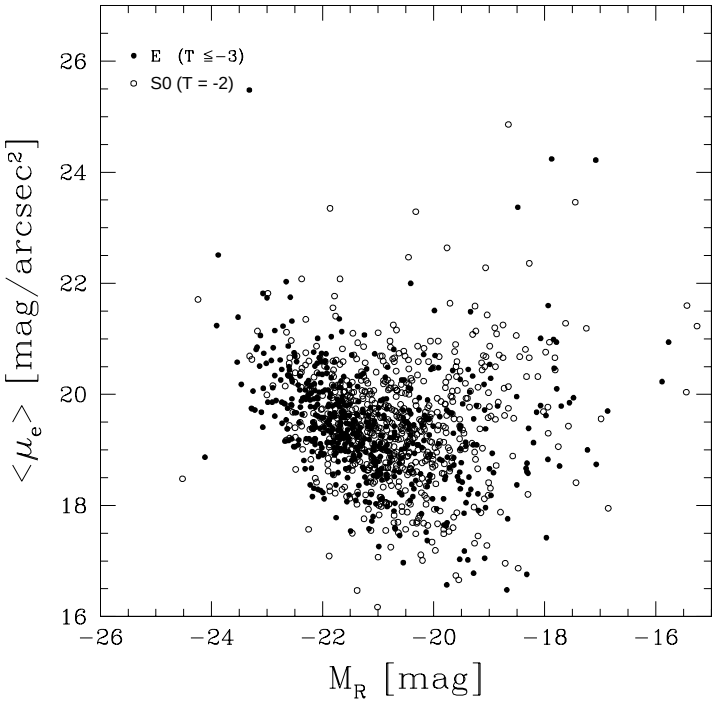

Figure 2.8 Distribution of observed $\bar{\mu}_e$ versus M_R (Kormendy's law).

$\bar{\mu}_e$ were transformed into an internally consistent system using repeated observations. Even though not all possible combinations have enough data for a direct comparison, a uniform system can be built using our own observations and data from other authors. By careful examination of all multiple observations available internal conversion relations were derived for each photometric parameter of interest. These were used to create a uniform internal system. In addition, we used measurements of 337 galaxies that we had in common with other sources to derive corrections to scale the data in the public domain to our system. From the comparison between our measurements and those of other authors we estimate that the typical errors in $\log d_n$, $\log r_e$, and $\bar{\mu}_e$ are 0.017 dex, 0.08 dex, and 0.3 mag arcsec^{-2}, respectively. This is consistent with our internal estimates. Even though photon-statistics, sky subtraction, seeing corrections and fitting errors all contribute to the errors of the photometric quantities, we find that the main source of error is the uncertainty in the photometric zero-point.

98 galaxies originally observed by the 7S using photoelectric photometers have now been re-observed using CCDs. Because more complete information about these galaxies is now available, their distance can now be estimated using the FP. Finally, it is also worth mentioning that some ∼150 galaxies have also been observed in the B-band and ∼200 in the H and K near-IR bands.

In the ENEARc sample there are currently 588 galaxies with d_n, 452 with r_e and $\bar{\mu}_e$, and 592 with σ. Thus it is possible to determine both a FP and a $D_n - \sigma$ relation. On the other hand, whereas $D_n - \sigma$ distances are available for 581 galaxies, while only 445 galaxies have FP distances. Furthermore, we found that the parameters involved in computing FP distances are more sensitive to seeing effects and also to the procedure used in fitting the surface brightness profile. For all these reasons, in this work we

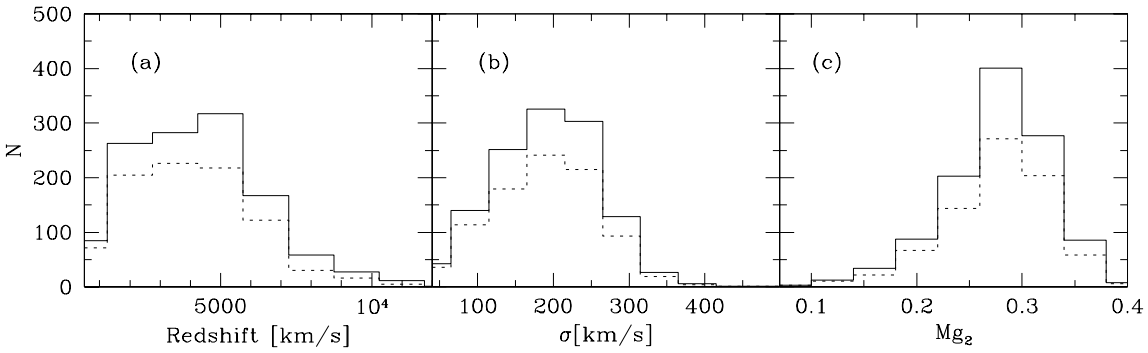

Figure 2.9 Distribution of (a) the redshift, (b) the velocity dispersion, and (c) the Mg_2 line index for the observed galaxies. Dotted histograms represent observations at high-resolution ($\lesssim$2.5Å). The plots show the total number of observations including multiple observations of the same object.

compute distances primarily based on the $D_n - \sigma$ relation. In fact, the $D_n - \sigma$ results that follow are based on 446 of the 581 galaxies.

2.3.3 New spectroscopic observations

Our spectroscopic observations have been conducted over a long period of time, using a variety of sites, detectors and gratings, with the spectral resolution ranging from 2 to 5 Å. Some of the data date back to the mid-80s and were obtained using the intensified photon-counting Reticon detector used for the Southern Sky Redshift Survey (SSRS, da Costa et al. 1991). Because the errors in these earlier observations were considerably larger than those that can be currently attained, we have excluded them from our database. All of these galaxies have since been reobserved.

A total of 1679 spectra of early-type galaxies have been obtained, including 533 multiple spectra of 406 galaxies. The number of repeated observations range from two to more than 10 for a few comparison galaxies. The multiple observations were used to compare: 1) new CCD to older Reticon spectra; 2) low to high resolution spectra; 3) spectra taken at different telescopes or with different setups. These repeated observations have been used to make our measurements internally consistent and to calibrate our internal error estimates as described in Chapter 4, where the details of the observations, data reduction, uniformization of the data and corrections applied to the raw data can be found. We have also observed several galaxies with previous measurements to derive statistical corrections and bring data available in the literature into a uniform system (see Chapter 5 for details).

By analysing these spectra using standard techniques we have measured redshifts, velocity dispersions and the Mg_2 line index. Figure 2.9 shows the distribution of redshifts, velocity dispersions and Mg_2 line indices of the observed galaxies. Over 60% of the spectra were obtained at high-resolution ($\lesssim$2.5Å) allowing more us to make more accurate measurements, especially for galaxies with $\sigma \lesssim 100$ kms^{-1}. Since most of the observed galaxies had previously measured redshifts we can compare them to our new measurements. Figure 2.10 shows the distribution of radial velocity differences.

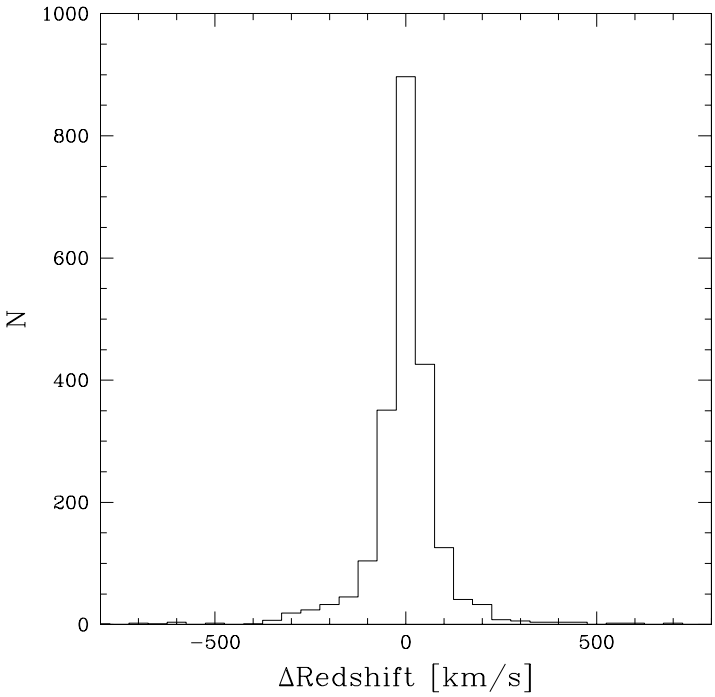

Figure 2.10 Distribution of the differences between our new redshifts and those previously available in the literature.

A detailed description of the observations, data reduction, and derived spectroscopic parameters is given in Chapter 4.

Our spectroscopic parameters have been brought into a uniform system using the many repeated observations we have in different runs at the same, and from different, sites. Our fiducial system is defined by our high-resolution spectra ($\sim$ 2 Å). Using observations of galaxies in common with other authors we were also able to transform published data into our system. From these external comparisons we also find that our errors are typically 8% in σ and 0.01 mag in Mg_2.

Galaxies with more than one measurement were combined using an error-weighted mean of the different observations, eliminating outliers whenever possible, to prevent biasing our results. About 3% of the observed galaxies exhibit emission lines. Some of these cases are obvious misclassifications in the original catalog, while others may indicate the presence of residual star-formation. We have recorded all such emission line galaxies.

2.4 The redshift-distance survey

2.4.1 Completeness

To measure the radial component of the peculiar velocity of a galaxy $v_p = cz - R$ we need to know the redshift of the galaxy (cz) and the redshift independent galaxy distance (R). This distance must be measured from a secondary distance indicator like the $D_n - \sigma$ or FP relation. The former requires values of the characteristic angular size of the galaxy,

d_n, while the latter requires parameters such as the half-light radius, r_e, and the mean surface brightness, $\bar{\mu}_e$, derived from profile fitting (so it can only be derived for galaxies with imaging data). Moreover, reliable values of r_e and $\bar{\mu}_e$ require observations with relatively good seeing. Therefore, when analyzing the completeness of the sample, it is important to distinguish between distances determined using the $D_n - \sigma$ relation from those which use the FP relations. In this section, we estimate the completeness of our sample considering only $D_n - \sigma$ distances because, as discussed above, the number of galaxies that can have distances estimated by these relations are larger than those with FP distances.

Since our parent sample has complete redshift information (see Section 2.1.1), completeness here refers to galaxies for which we have both velocity dispersion and d_n measurements and thus are able to compute $D_n - \sigma$ distances. Figure 2.11 shows the completeness function of the ENEARf redshift-distance survey as a function of: (a) the galaxy redshifts, (b) the total magnitude m_B, (c) the galactic longitude, and (d) the galactic latitude. This information is useful for producing realisitic mock samples for analysis of the peculiar velocity field. We find no strong dependence with the redshift, magnitude, galactic longitude or latitude. In general, the sample completeness is a nearly constant 70%. This demonstrates that our dataset, though not 100% complete, is remarkably uniform both in depth, and in sky coverage; both are essential for allowing unbiased analyses. This is in marked contrast to other catalogs assembled from different sources (e.g., Mark III) which show large sampling variations in different directions of the sky. We have not investigated the completeness of the sample as function of morphological types since analysis of our images shows that the morphological classification available from the original catalogs is not reliable and that it should not be used to define sub-types of the early-type population in any detailed analysis of their properties.

To underscore the uniformity of the observed sample Figure 2.12 compares the projected distribution, in galactic coordinates, of all galaxies of the ENEARf sample that have measured distances (filled circles) with galaxies for which distances are still not available (open circles). Clearly, the sample with measured distances, although sparser, is a fair representation of the ENEARf sample as a whole; all major structures in the nearby universe are well sampled. We also find that the distribution of missing galaxies does not reveal any particularly under-sampled region.

So far, we have shown all galaxies individually. However, as we discussed earlier, early-type galaxies are found predominantly in clusters/groups. Therefore Figure 2.13 shows the distribution of independent objects defined by the grouping procedure described in section 2.1.3 (and in more detail in Chapter 5). Currently, we have distances for 1238 galaxies in 849 independent objects. This catalog of grouped objects is the final sample which we will use for peculiar velocity analyses.

2.4.2 Comparison with other surveys

The ENEARf sample shown in Figure 2.12 is the largest and most homogeneous sample of nearby early-type galaxies currently available for cosmic flow studies. To highlight this, Figure 2.14 compares the projected distributions, in redshift slices, of the ENEARf and the 7S samples. Note the obvious differences both in the total number of galaxies, and in the structures probed by the two samples. In particular, in the most distant redshift shell, Perseus-Pisces is clearly visible in out ENEARf catalog but is completely

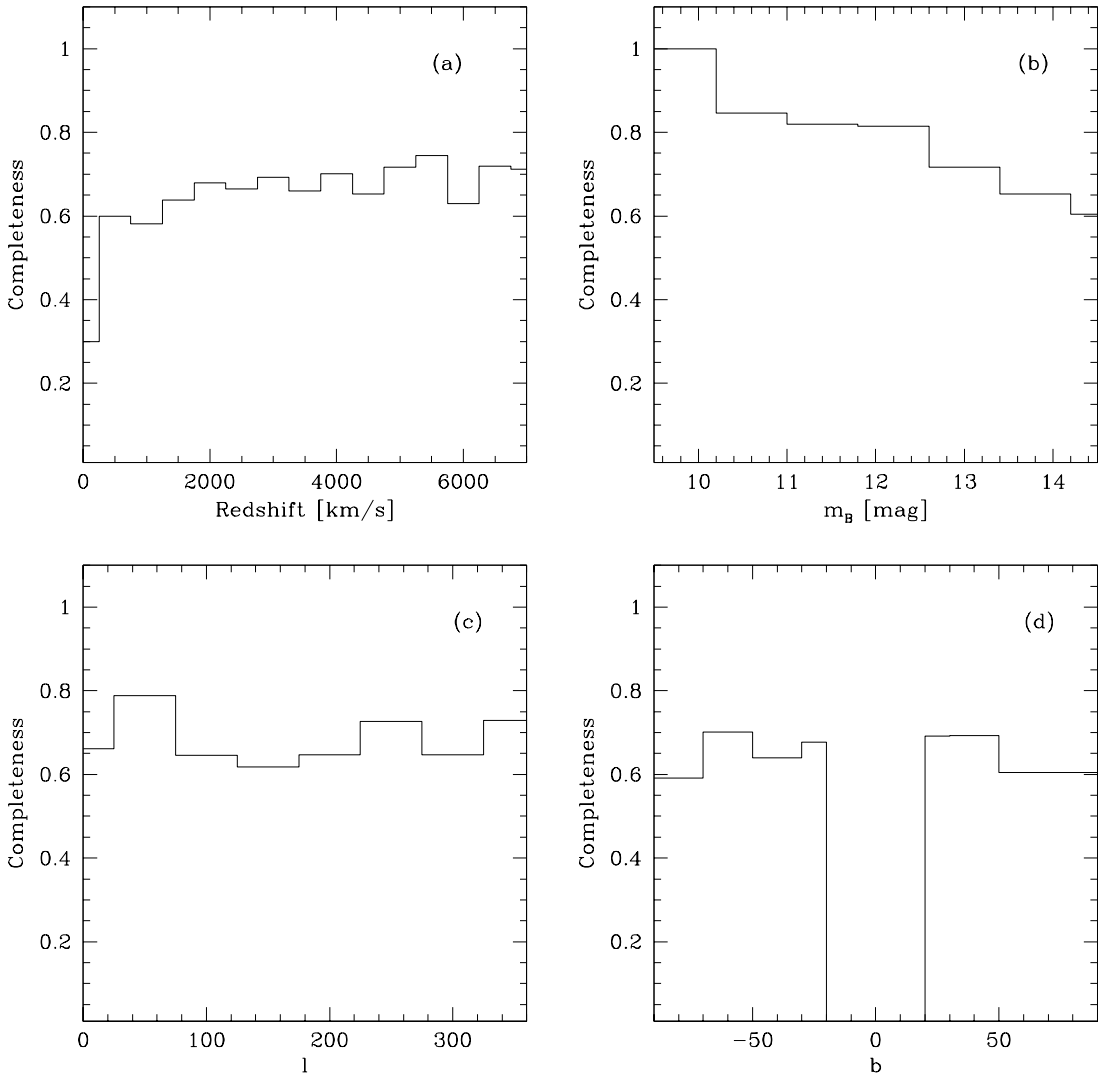

Figure 2.11 The completness of the ENEARf sample as function of (a) redshift, (b) total magnitude, m_B, (c) galactic longitude, and (d) galactic latitude.

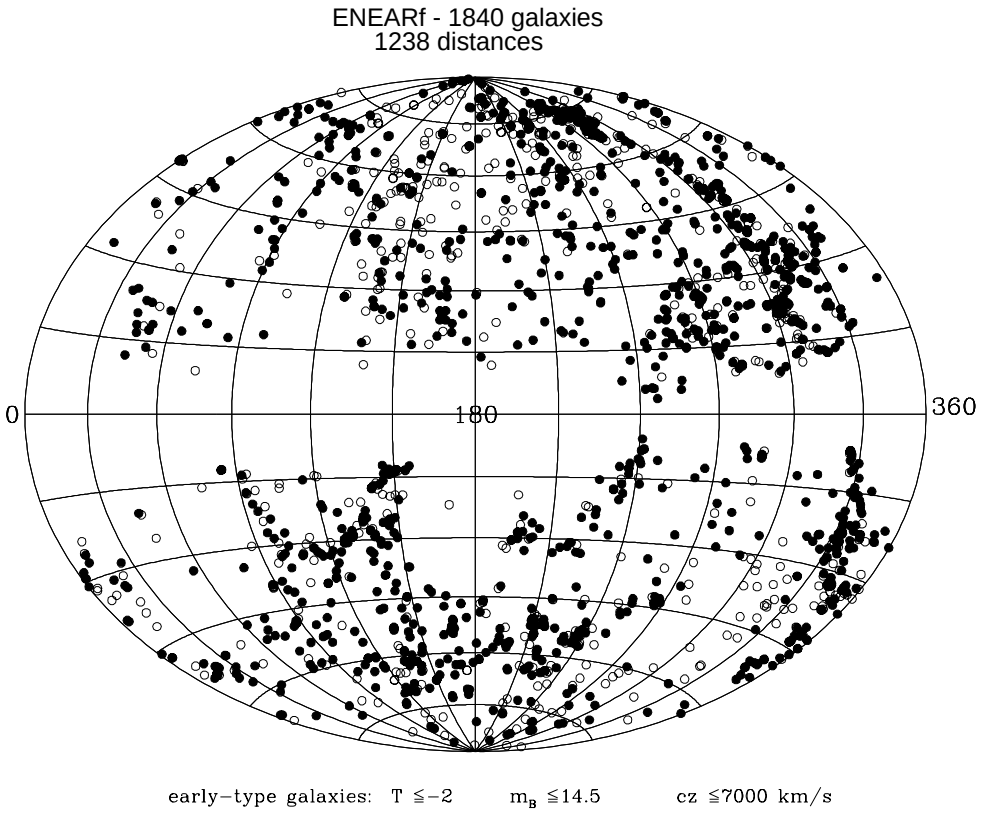

Figure 2.12 Projected distribution, in Galactic coordinates, of all ENEARf galaxies with (filled circles) and without (open circles) measured distances.

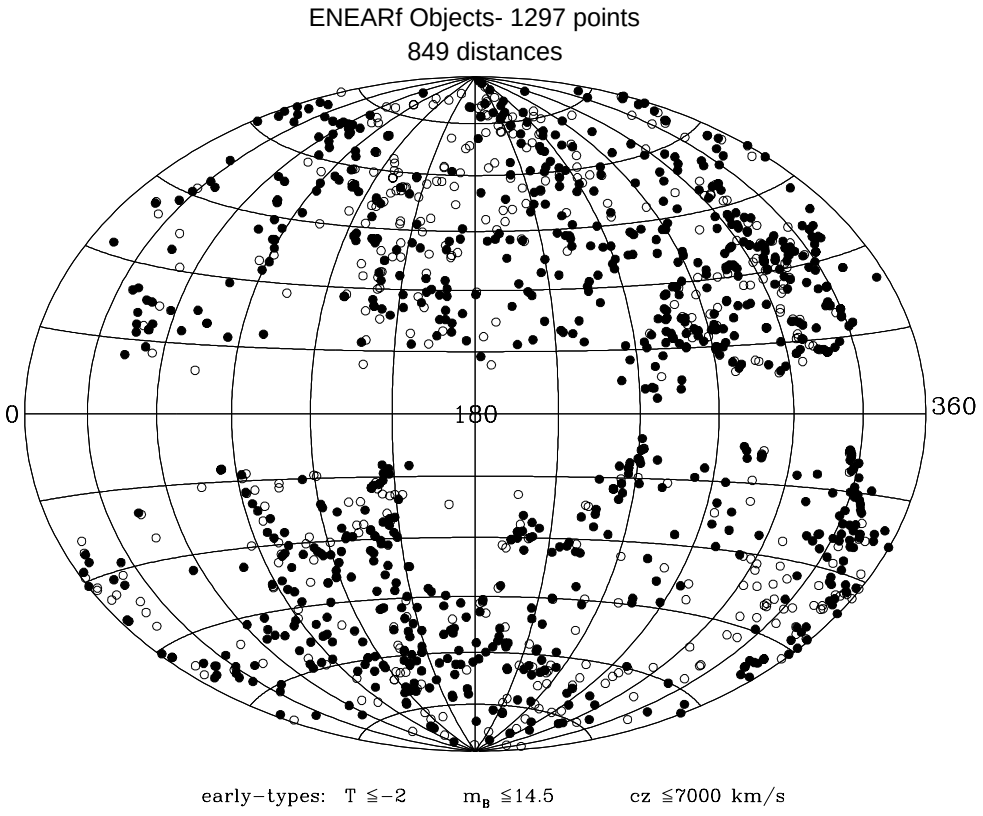

Figure 2.13 Projected distribution, in galactic coordinates, of ENEARf "objects" useful for peculiar velocity analyses. Filled and open circles represent objects with and without measured distances.

absent in the shallower 7S sample. This accounts for some of the surprises encountered in earlier (7S-based) reconstructions.

It is also worth comparing our sample with other recently completed TF surveys. Figure 2.15 compares the projected distribution of individual galaxies having measured distances in our ENEARf catalog with the recently completed SFI TF survey of spiral galaxies. As expected, the ENEARf early-types delineate the structures more sharply than do the more spread out spirals. For this reason, combining the two samples is highly desirable, and is the subject of future work.

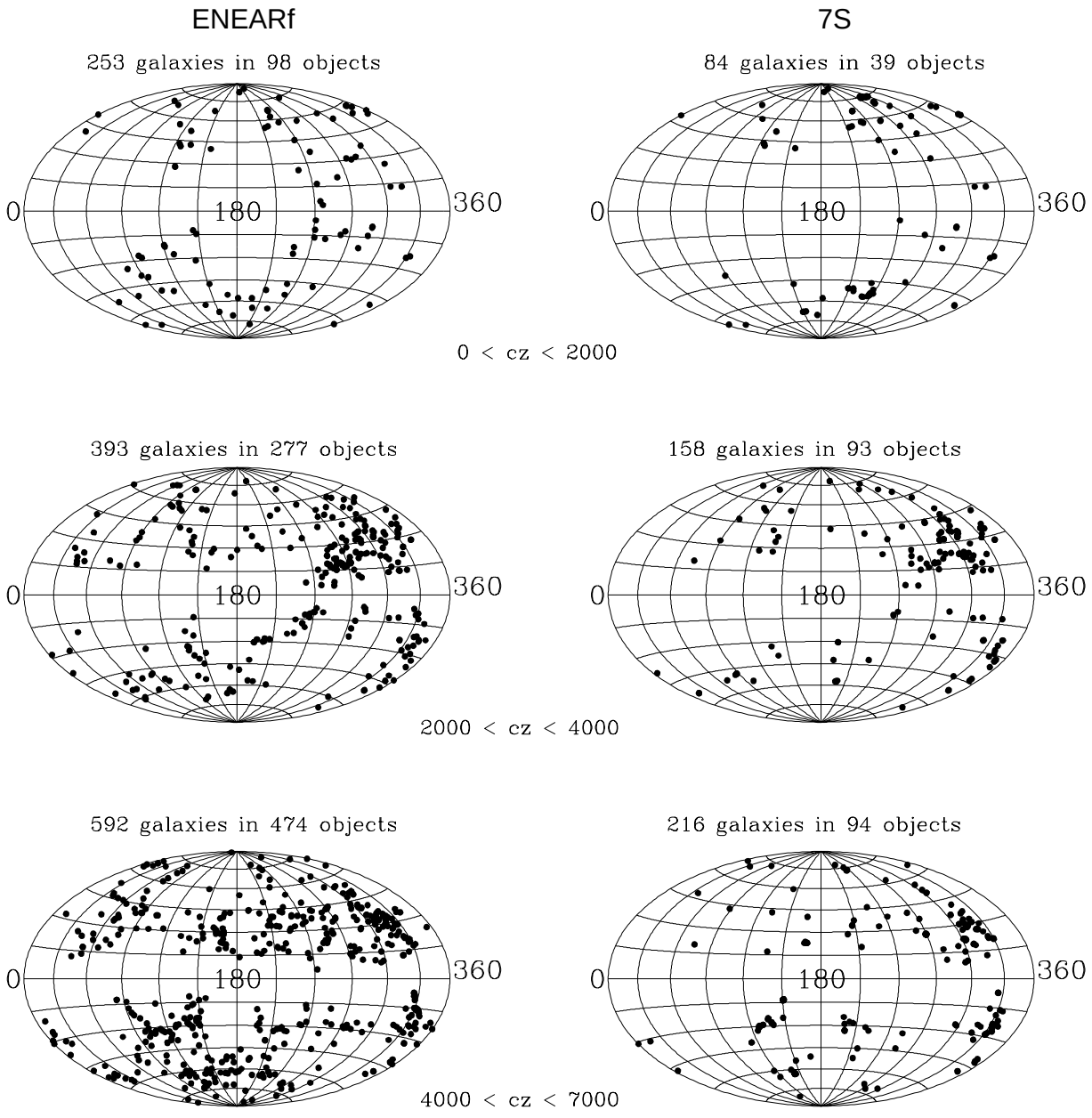

Figure 2.14 Comparison of the projected distribution, in galactic coordinates, of ENEARf and 7S objects in different redshift slices. The number of galaxies and the number of objects in which they are grouped are reported.

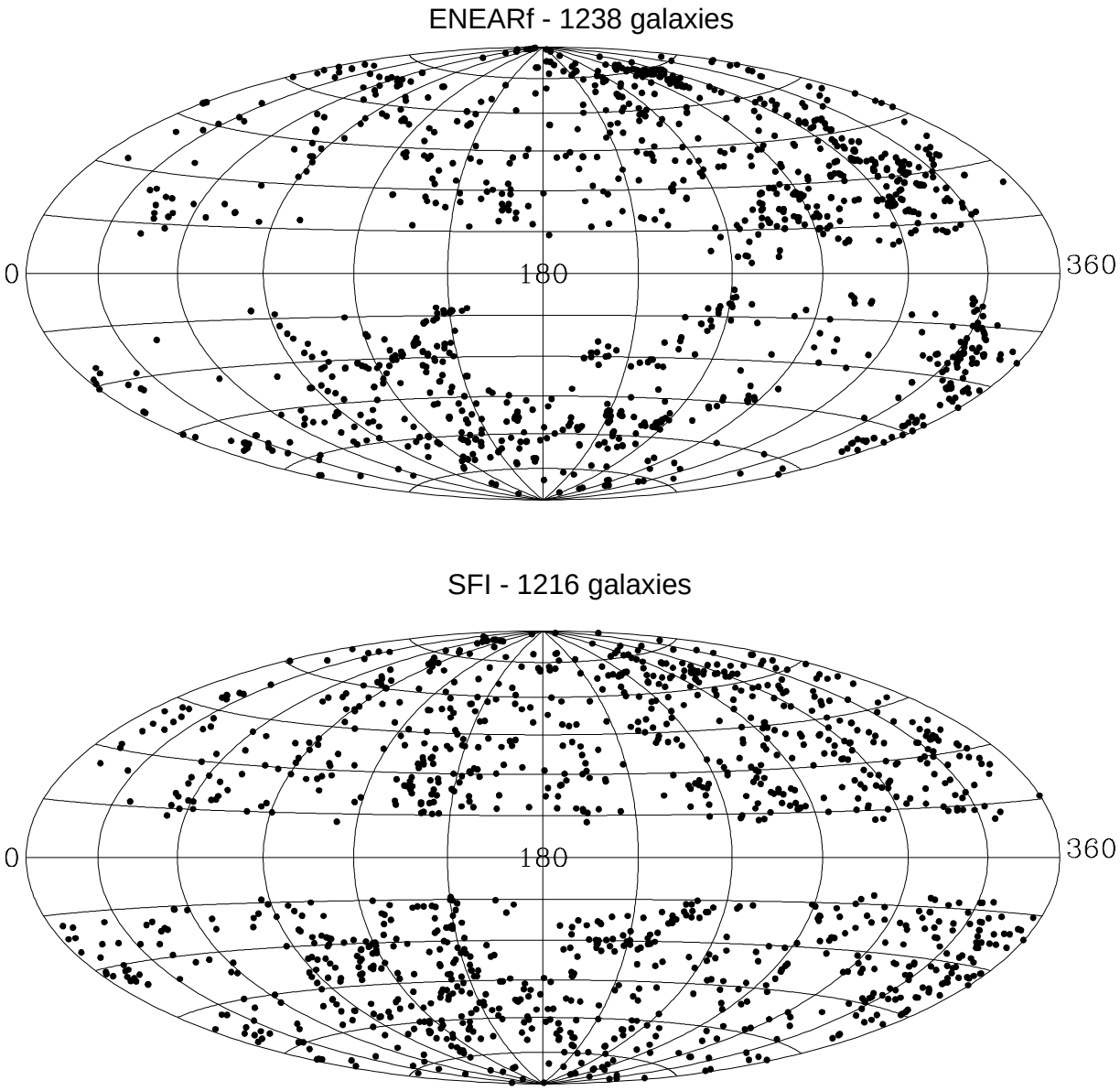

Figure 2.15 Comparison of the projected distribution of galaxies, in galactic coordinates, from the ENEARf sample (upper panel) and the SFI catalog of spiral galaxies (lower panel).

Chapter 3

Photometry

This chapter reports on results derived from the photometric analysis of $R-$band imaging observations of over 1500 galaxies carried out for the ENEAR project. Here we present the photometric measurements of 1294 mostly early-types selected from an all-sky magnitude-limited sample (ENEARf) as well as fainter galaxies in the field or in selected clusters and early-type spirals misclassified in the original catalogs from which our sample was drawn. Out of the total 946 galaxies had no previous photometric measurements. New observations and data reduction are still ongoing.

Ellipses and circular apertures have been used to derive surface brightness profiles. Ellipse fitting is used to study the shape of the isophotes and derive profiles for the ellipticity, the position angle, and the parameters which measure the deviation of isophotes from pure ellipses. The surface brightness profiles determined from circular aperture photometry are fitted by a two-component disk-bulge model to derive seeing-corrected global parameters such as the angular size (as measured by the effective radius, r_e and the characteristic diameter, d_n) and mean surface brightness $\bar{\mu}_e$, which are needed to estimate galaxy distances. The uncertainties in the derived parameters have been evaluated from the quality of the fitted model, the zero-point calibration error, and the internal comparison of the light profiles and the derived global parameters obtained from multiple observations of the same galaxy. These uncertainties have been further tested by comparing our results with those obtained by other authors. Multiple observations are also used to bring photometric parameters into a common internal system. In total there are 356 repeated observations of 321 galaxies and 337 galaxies in common with other authors. Comparison of our light profiles obtained from different observations of the same galaxy show, in general, good agreement in both shape and photometric zero-point. The mean differences in zero-point are insignificant and for a given galaxy is $\lesssim$0.1 mag. Errors in the global parameters estimated from the scatter of internal comparisons are: 0.017 dex in $\log d_n$, 0.08 dex in $\log r_e$, 0.3 mag arcsec^{-2} in $\bar{\mu}_e$, 0.019 in FP $= \log r_e$- 0.30 $\bar{\mu}_e$, and 0.09 mag in the total magnitude. These values are, in general, consistent with those estimated from the comparison with other authors.

3.1 The data

3.1.1 Observations

Optical $R-$band photometric imaging have been conducted since 1988 using the Danish 1.54m and the Dutch 0.9m telescopes at European Southern Observatory (ESO), the

Table 3.1 Photometry Observing Runs

Run (1)	Date (2)	N_p (3)	Setup (4)	Notes (5)
CTIO-701	Nov 87	3	9	
FLWO-201	Dec 88	0	7	
FLWO-202	Apr 89	8	7	
FLWO-203	Sep 89	6	7	
ESO-601	Nov 89	2	1	
CTIO-702	sep 90	0	9	
FLWO-204	Nov 91	0	8	
ESO-602	Sep 92	0	1	
FLWO-205	Oct 92	2	8	
MDM-551	Jan 93	0	10	
FLWO-206	Mar 93	3	8	
ESO-603	Jul 93	3	2	
ESO-604	Nov 93	2	2	
ESO-605	May 94	5	2	
MDM-552	Mar 95	5	11	
ESO-606	Aug 95	2	3	
MDM-553	Nov 95	6	12	
ESO-611	Dec 95	15	6	
MDM-555	May 96	3	12	
ESO-607	Oct 96	0	4	
MDM-554	Nov 96	3	12	
ESO-608	Feb 97	3	4	
MDM-556	Feb 97	3	12	
ESO-609	Apr 97	4	5	
MDM-557	Jun 97	4	12	
ESO-610	Nov 97	1	5	
MDM-558	Nov 97	0	12	
ESO-613	Mar 98	3	5	still reducing
MDM-559	May 98	3	12	still reducing
MDM-560	Nov 98	1	12	still reducing
CTIO-703	Feb 99	6	10	

Notes: In column (3) the number of photometric nights for the corrisponding run are reported. Information about the setup indicated in column (4) are given in Table 3.2

Table 3.2 Photometry Observing Setups

Setup	Telescope	N_m	N_r	Detector	Field of view arcmin× arcmin	Scale arcsec/pixel	Gain e^-/ADU	RON [e^-]
(1)	(2)	(3)	(4)	(5)	(6)	(7)	(8)	(9)
1	ESO 1.54	23	8	RCA 5264-7-3	4.0 x 2.5	0.47	20	15
2	ESO 1.54	273	61	Tek #28	6.5 x 6.5	0.38	3.5	8.0
3	ESO 1.54	110	44	CCD #17	8.5 x 8.5	0.51	2.0	3.7
4	ESO 1.54	91	17	LORAL/LESSER W11-4	13.3 x 13.3	0.39	1.31	7.2
5	ESO 1.54	196	54	LORAL/LESSER C1W7	13.3 x 13.3	0.39	1.31	7.2
6	ESO 0.9	50	21	Tek	3.8 x 3.8	0.44	3.56	8.0
		743	205					
7	FLWO 0.61	80	8	Tek	5.5 x 5.5	0.65	3.8	12
8	FLWO 1.30	186	45	Tek	11.2 x 11.2	0.65	2.5	13
		266	53					
9	CTIO 0.9	44	26	RCA # 5	4.2 x 2.6	0.49	6.5	–
10	CTIO 0.9	214	42	Tek2K	13.5 x 13.5	0.396	3.2	4.0
		258	68					
11	MDM 1.3	25	4	Willbur2x2 STIS	20.5 x 20.5	0.63	2.25	4. 73
12	MDM 1.3	344	26	Nellie LORAL	15.0 x 15.0	0.44	2.94	4.28
		369	30					
Total		1636	356					

0.9m telescope at Cerro Tololo Interamerican Observatory (CTIO), the 0.61m and 1.3m telescopes at Fred Lawrence Whipple Observatory (FLWO) and the 1.3m telescope at Michigan–Dartmouth–MIT Observatory (MDM). During these years 31 observing runs have been carried out; 177 full and partial nights were assigned to the ENEAR project for photometric observations, out of which 96 had photometric conditions. The basic information about each run is summaried in Table 3.1 which gives: in column (1) the identification number of the run; in column (2) the date; in column (3) the number of the available photometric nights; in column (4) the corrisponding reference number of the setup used, which is described in Table 3.2; and in column (5) we identify the runs for which the data reduction is still ongoing. A total of 12 different setups were used corresponding to different telescope-detector combinations as summarized in Table 3.2 which gives: in column (1) the setup reference number; in column (2) the observatory and the telescope; in column (3) the number of images N_m; in column (4) the number of images N_r taken of the same galaxy in that run or in any other of our runs, which are used as calibrators to homogenize our observations; and in columns (5)-(8) information about the detector which includes identification, the size of the detector, pixel scale, gain and read out noise.

The observations of the galaxies were carried out in the R Cousins band with exposures varing 120 to 600 seconds depending on the telescope used and the brightness of the galaxy. A total of 2163 images taken in photometric nights were analyzed. Currently, a sample consisting of 1636 images of 1294 galaxies has been constructed discarding 153 frames for a variety of reasons among which: galaxies too close to the edge of the CCD, low signal-to-noise, inappropriate for analysis due to stellar contamination, superposed images and crowded fields. In addition, about 374 frames obtained in recent runs or with identification problems are still being analyzed and are not discussed here.

It is important to point out that the total number of galaxies with photometric information could increase significantly with a more detailed analysis of the available frames which we intend to carry out in the future. This is because in several frames other early-type galaxies not satisfying our strict selection criteria (Chapter 1) are present, especially in the direction of groups/clusters, which have not been yet identified and no light profiles were derived. It is our intention in the future to re-analyze the available frames to search for other early-type galaxies, especially those brighter than 14.5 but $cz > 7000$ kms^{-1} or in clusters.

A total of 321 galaxies have multiple observations, from two to ten times using either the same or different setups. Figure 3.1 shows the distribution of repeated images, from

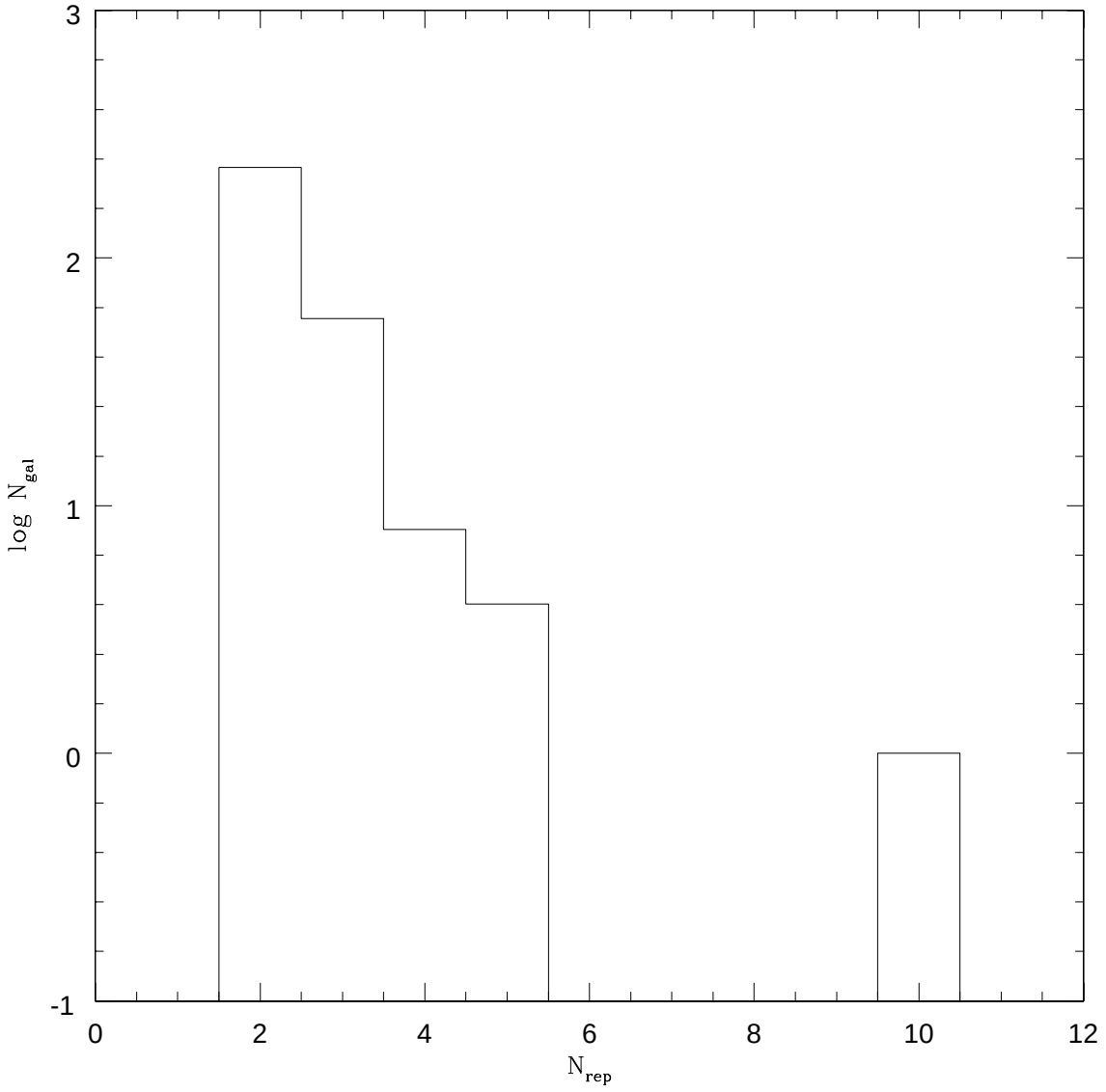

Figure 3.1 The distribution of the internal repeated observations.

which we find that ~ 70 galaxies have more than two observations. Given the large number of setups used and the long duration of the program, these repeated observations are of paramount importance to ensure the overall uniformity of our data. These multiple observations are used below to make our measurements of photometric parameters internally consistent and to estimate their errors. Finally, it is worth mentioning that $B-$band images have also been obtained and analyzed for ~ 178 early-type galaxies.

Flat-field images were taken as a series of exposures of the the twilight sky in the R and, depending on the site, in a second passband mostly V but also in B and I. In addition, for each night 10-20 bias frames were taken.

About 4-5 fields of Landolt (1983, 1992) stars were observed each night in the R in a second passband, depending on the site. In general, standards were observed at intervals of $\sim 1-2$ hours depending on the photometric conditions, and covering a wide range of airmass up to a value of 2.5. These images are used to provide estimates of the photometric zero-point, atmospheric extinction coefficient, and color term. Typically, about 30 stars were observed during each night, frequently with the telescope slightly defocused so as to allow for high signal-to-noise integration without saturating the center of stars.

During the several observing runs the seeing, measured as the FWHM of the stellar light profile, varied from 0.9 to 3 arcsec with a median value of 1.4 arcsec. The distribution of the ration between the FWHM of the point-spread function as measured on all galaxy frames obtained in photometric nights and the galaxy angular size as measured by the effective radius r_e is shown in Figure 3.2. The median value of the distribution is ~ 0.1 but shows an extended tail to larger values. Therefore, measurements of the photometric parameters must be corrected for seeing effects.

3.1.2 Data reduction

The standard reduction of the data was performed using IRAF[1] routines. All images of standard stars and galaxies were trimmed, bias-subtracted and divided by a flat-field. The images were processed at each step of the basic data reduction using the task **ccdproc** in the IRAF **imred.ccdred** package.

For each night overscan subtracted bias frames were median combined and 3σ clipped using the tasks **ccdred.combine**. If the bias stayed consistent from night to night, the median of all the overscan subtracted bias frames for the entire run was subtracted from all images.

Sky flats over one or more nights in R and other passbands used for the standards were also median combined and 3σ clipped to create master frames. Sky flats have short exposure time (5-30 s) compared the integration time used for a galaxy (~ 300 s). Since the response of the CCD might depend on the exposure time the best solution is to build a "superflat". This is done combining a large number of galaxy frames taken over an interval of time of relative constancy of the camera and CCD setup. These frames can be observations of the same object taken moving systematically the telescope from exposure to exposure or images of different galaxies but with the main object placed in different regions of the frame. The final "superflat" is obtained by smoothing the median

[1]IRAF (Image Reduction and Analysis Facility) is distributed by the National Optical Astronomy Observatories

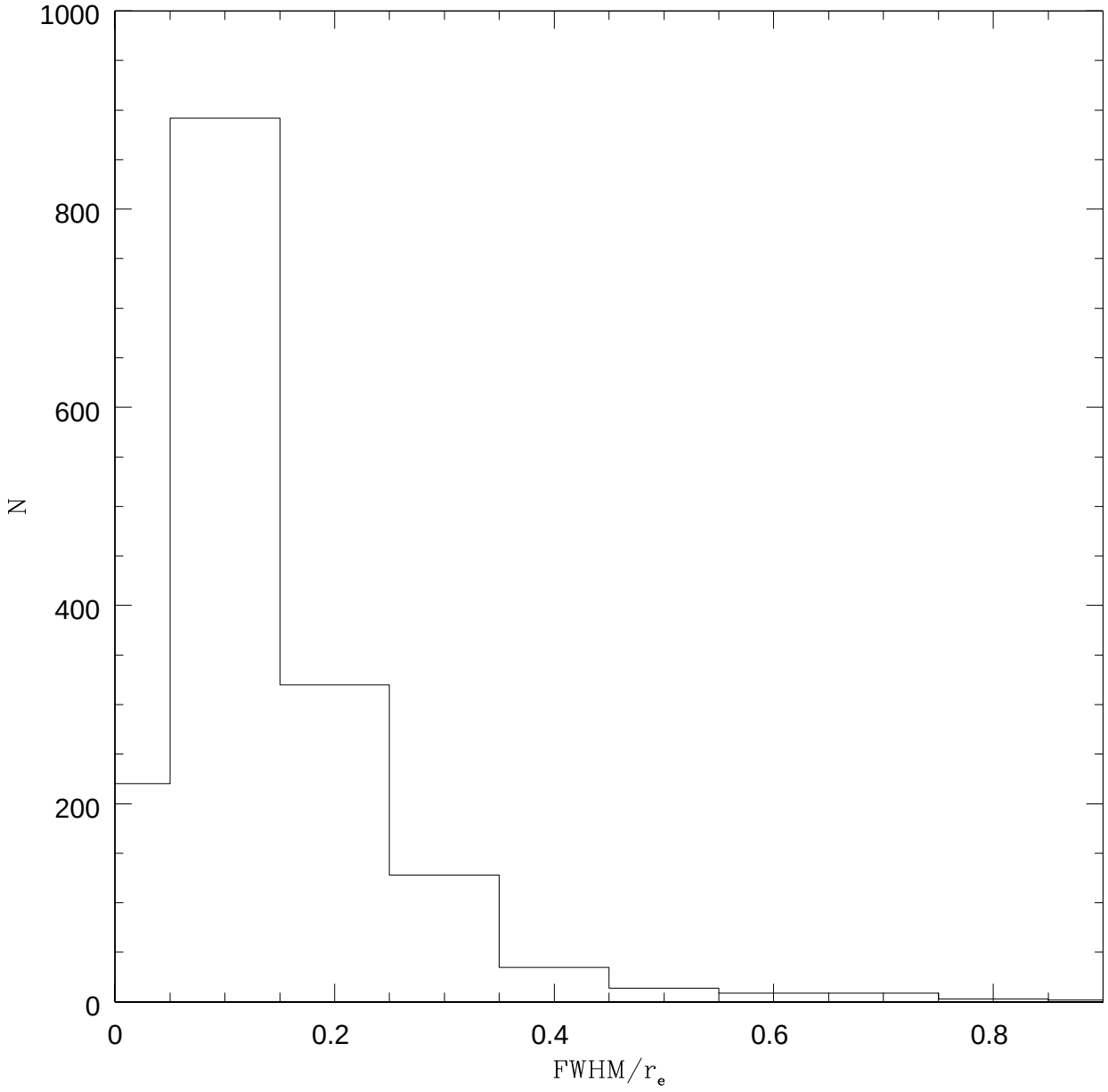

Figure 3.2 Histogram of the ratio between the FWHM of the PSF as measured from stars on the images of the observed galaxies and their angular size as measured by the effective radius r_e. The median value of the ratio is 0.1.

combined frame using the task **mkillumcor**. The "superflat" has also the advantage to remove the problem of the color difference between the twilight sky and the night sky. However, it is possible to build the "superflat" only when the CCD used has a field of view large enough so that the extent of the galaxy is small compared with the total frame size, and most of the galaxies observed are in low density field. Because a significant fraction of the observed galaxies were relatively large in most cases the sky flat was used. We estimate the uncertainty in the residual large–scale response of the CCD to be less than 1%.

Cosmic rays were removed using the task **ccdred.cosmicrays** on all the galaxy image frames. These were identified and removed for those pixels deviating more than 5σ from the surrounding pixels. The rms deviation σ is given by $\sigma = \sqrt{(\sigma^2(P) + RON^2)/gain}$, where RON is the readout noise in e^-, $gain$ is in e^- per ADU, and $\sigma(P)$ is the poisson noise $\sqrt{sky * gain}$ (sky is the mean background level count).

The final reduction steps of the galaxy images were performed using the GALPHOT package developed for similar work on spiral galaxies (Haynes et al. 1999a and references therein). Estimates for the background were obtained from "sky boxes" placed in regions free of bright stars, around the galaxy but far enough not to be contaminated by light from the outer parts of the galaxy. For each "sky box" the mean intensity was computed after automatically masking faint stars and galaxies within the box. The adopted sky value was computed as the mean of the values of each sky box, since the images were sufficiently flat not to require a higher order surface fit. Finally, the resulting mean sky value was subtracted from the image. Typically the scatter of the mean sky intensity as determined in each sky box was $\lesssim$1%.

Finally, in preparation for carrying out galaxy surface photometry a rectangular region about twice the size of the galaxy image was marked using the task **markgal** and cosmic rays, bad columns, and stars outside this box were automatically masked using **clean**. Additional undesirable features (eg. stray light still visible form stars, low-level and multiple-pixel cosmic rays) both inside and outside the marked box were masked interactively using the task **images.imedit**. All the image reductions were carried out by myself and M. V. Alonso thereby assuring the uniformity of the procedure.

3.1.3 Photometric calibration

Photometric calibration was carried out by nightly observations of the Landolt standards observed in the R and, depending on the site, in a second passband mostly V but also in B and I. About 30 stars were typically observed along each night, covering a wide range in colors and airmass, in order to obtain values of the atmospheric extinction coefficient, the color transformation coefficient, and the photometric zero-point.

Instrumental magnitudes for the stars were obtained using a suitable circular aperture, large enough to measure the total flux without significantly increasing the error due to the sky noise. The sky level was determined as the median of the counts distribution within an annular ring around the star but far enough to avoid contribution from the stellar wing. The zero-point, extinction coefficient and color term were determined fitting the difference between the derived instrumental magnitude (e.g. R) and the standard magnitude (e.g. R_o) as a function of airmass (X) and color (e.g. $V - R$):

$$R_o = R + k_R X + C_R(V - R) + Z_R \tag{3.1}$$

Table 3.3 Photometric Solutions

Run (1)	N_{stars} (2)	Filters (3)	C_R (4)	Z_R (5)	k_R (6)	σ_{stars} (7)	Notes (8)
CTIO-701	6-10	$V-R$	0.056	20.677	0.054-0.057	0.013-0.031	not in Figure A.1
FLWO-202	21-30	$V-R$	0.026	19.681	0.101-0.145	0.26-0.035	not in Figure A.1
FLWO-203	9-29	$V-R$	-0.014	19.703	0.078-0.097	0.017-0.031	not in Figure A.1
ESO-601	9-10	$V-R$	0.012	21.529	0.065-0.074	0.032-0.035	
FLWO-205	23-49	$V-R$	-0.127	22.384	0.151-0.440	0.026-0.029	
FLWO-206	28-41	$V-R$	-0.110	22.296	0.176-0.199	0.012-0.015	
ESO-603	18-30	$V-R$	0.080	23.362	0.115-0.128	0.009-0.016	
ESO-604	63-129	$V-R$	0.080	23.365	0.060-0.066	0.012-0.017	
ESO-605	21-44	$V-R$	0.075	23.330	0.025-0.035	0.010-0.016	
MDM-552	8-38	$B-R$	0.028	22.491	0.003-0.014	0.009-0.024	
ESO-606	51-60	$V-R$	0.047	22.937	0.047-0.090	0.022-0.023	
MDM-553	30-57	$V-R$	-0.005	22.184	0.096-0.112	0.011-0.013	
ESO-611	9-41	$V-R$	0.048	22.087	0.084-0.102	0.008-0.023	
MDM-555	12-38	$V-R$	0.087	21.927	0.022-0.043	0.007-0.023	
MDM-554	27-42	$I-R$	-0.023	22.051	0.048-0.060	0.010-0.019	
ESO-608	39-46	$V-R$	0.064	23.578	0.037-0.086	0.011-0.015	
MDM-556	27-36	$I-R$	0.061	22.222	0.010-0.016	0.013-0.019	
ESO-609	32-43	$V-R$	0.015	23.585	0.001-0.004	0.022-0.024	
MDM-557	24-62	$I-R$	0.004	22.075	0.082-0.118	0.018-0.023	
ESO-610	38	$V-R$	0.016	23.836	0.039	0.022	
ESO-613	60-81	$V-R$	0.059	23.784	0.075-0.088	0.013-0.034	still reducing
MDM-559	30-44	$V-R$	0.012	24.034	0.172-0.223	0.013-0.019	still reducing
MDM-560	32	$V-R$	-0.136	23.594	0.0689	0.018	still reducing
CTIO-703	27-44	$V-R$	0.005	22.635	0.064-0.086	0.011-0.021	

$$V_o = V + k_V X + C_V(V-R) + Z_V \tag{3.2}$$

The zero-point Z_R and color term C_R were taken as the mean value of the photometric solution determined for each photometric night, since they only depend on the instrument, filter and telescope. The value of the extinction coefficient k_R was then determined on a nightly basis using the previously calculated zero-point and color term. Since colors are not available for our galaxies, in the photometric calibration of our objects we have assumed a mean color typical of early-type galaxies (Frei & Gunn 1994; Fukugita et al. 1995) for which we assume: $(B-R) = 1.48$, $(V-R) = 0.56$, and $(R-I)$=0.70 mag. The error introduced by this assumption is negligible since the color-term coefficient is typically small.

The uncertainty in the photometric zero-point was estimated from the dispersion of the differences between the estimated magnitudes of the standards obtained by applying the photometric solution for each night and the listed Landolt magnitudes. Nights were considered photometric if the zero-point error was $\lesssim$0.03 mag. Based on this criterium out of a total of 177 nights allocated to the project, 96 were photometric. Figure A.1 in Appendix A shows for each photometric night the transformation from instrumental magnitudes to calibrated magnitudes of the observed standard stars as function of the airmass (left panel), the color (middle panel), and the universal time (right panel). The identification number of the run and the date of the night are also reported on the top of the left panel, while the number of stars and the uncertainty in the photometric calibration are given on the top of the middle panel. Unfortunatly, Figure A.1 does

not show the results for the three oldest runs because it was not possible to recover the tables with the instrumental magnitudes of the standard stars. Table 3.3 gives the coefficients of the photometric solution of all the analyzed runs, listening: in column (1) the identification number of the run; in column (2) the range covered by the number of standards; in column (3) the passband used; in column (4) the color term; in column (5) the zero-point calibration; in column (6) the range covered by the extinction coefficient during the nights assigned to the run; and in column (7) the range covered by the uncertainty in the photometric calibration.

Whenever possible, galaxy images obtained in non-photometric nights were calibrated using short exposure frames of the same object obtained in photometric conditions. This was done measuring the instrumental magnitude of the stars in common in the photometric and non-photometric frames, computing the difference between the mean magnitude of the two frames, and adding this difference to the photometric zero-point of the non-photometric image.

3.2 Surface brightness profiles

Surface brightness profiles were obtained from elliptical and circular apertures, using GALPHOT. The light profiles obtained from ellipse fitting (e.g., Jedrzejewski 1987) were used to derive information about the shape of the objects and to compare our light profiles with those of other authors which by and large use the same methodology. The circularly averaged profiles were used to derive global parameters of the galaxies following the procedure described by Saglia et al. (1993a).

3.2.1 Ellipse fitting

An initial guess of ellipse fitting routine was provided by marking on the image points corresponding to the major- and minor-axis at a bright isophotal level but beyond $\sim$ 4 arcsec to avoid a major contribution of the point-spread function. Successive ellipses were fitted, both inwards and outwards, discarding pixels within masked regions, varying the semi-major axis by about 10% at each step. The surface brightness profiles derived from the ellipse fits were terminated at a radius, r_{max} where the galaxy light profile counts drop below 2-σ level of the sky background, which corrisponds for our data to $\sim$ 3% of the sky level.

The errors in the surface brightness profiles are determined taking into account the contribution of the Poisson noise and the error in the sky determination, the latter being the dominant source at the faint isophotal levels:

$$\delta\mu = 2.5 \log \left[1 + \frac{\frac{area}{gain} \times (meanint + sky) + (area \times skyerr)^2}{area \times meaint} \right] \qquad (3.3)$$

where $area$ is the area (in square pixels) of the annulus on the contour at which the intensity is measured, $gain$ is the gain (in e^-/ADU) of the CCD used, $meaint$ is the mean intensity (in counts per pixel) within the annulus, sky is the mean sky level (in counts per pixel), and $skyerr$ is determined multiplying sky by the percentages of the sky uncertainty estimated as described in Sec. 3.1.2. The uncertainty in the determination of the mean sky value could influence significantly the accuracy of the derived surface

brightness. For our sample, the size of any given galaxy was usually small compared with the size of the CCD, so the sky subtraction is usually accurate ($\lesssim$1%). However, since sky errors are scaled by the area of the annulus, even though they are small, the effect of sky errors are important especially at large radii where the surface brightness of the galaxy is low while the sky level remains constant.

Besides the surface brightness, for each fitted ellipse the magnitude, the center of the ellipse, the ellipticity (defined as $\epsilon = 1 - b/a$, where b and a are the semi-minor and semi-major axes respectively), and the position angle of the major axis (N through E) were computed and recorded as a function of the semi-major axis including the errors in each of these quantities. The residuals of the ellipse fitting were expanded in a Fourier series and the third and fourth order Fourier coefficients, for the sine (s_3 and s_4) and cosine terms (c_3 and c_4) were computed. These coefficients were normalized by dividing by $aI'(a)$, the product between the semi–major axis a and the local intensity gradient I'. These Fourier coefficients are useful to quantify the deviation of the isophotes from perfect ellipses. In particular, the coefficient c_4 has been extensively used to characterize the shape of the object as disk-like ($c_4 > 0$) and box-like ($c_4 < 0$) (e.g., Lauer 1985; Jedrzejewski 1987; Bender & Möllenhof 1987; Peletier et al. 1990).

Next, a two-dimensional galaxy model was created from the fit and integrated magnitudes, as a function of the semi-major axis, were computed from the galaxy model. The errors in the total integrated magnitude are computed as the errors in the surface brightness using Equation 3.3, except in this case *meanint* is the mean intensity within the aperture and *area* is the total area enclosed within the contour.

The instrumental values obtained for the surface brightness and magnitudes were calibrated for atmospheric extinction, color, and magnitude zero-point calibration using Eq. 3.1. In addition, the K-correction were applied and the effects of Galactic extinction and cosmological surface brightness dimming were accounted: a) the K-correction is needed because the amount of galaxy luminosity observed in the R-band decreases with increasing redshift. This correction was computed as $K_R(z) = 2.5log(1+z)$ assuming that $F_\nu \sim \nu^0$ (early-type galaxies have nearly a flat spectral shape in this wavelength range). The value of K_R ranges from 0.01 to 0.04 mag; b) our estimates for galactic extinction in the R-band are based on estimates of Burstein & Heiles (1984). We adopt $A_R = 2.40E(B-V)$ where $E(B-V)$ is the redenning values of the visual color excess. For the observed galaxies this correction is $\lesssim$0.13 mag. We have compared our corrections with those obtained using the extinction maps of Schlegel et al. (1998) and we find no significant differences; c) finally, the surface brightness was corrected by the $(1+z)^4$ cosmological dimming. This correction accounts for the dimming with redshift of 1) the energy of the flux individual photons; 2) the flux number of photons ; 3) the dimension of the source (angular area).

Figure 3.3 shows an example of the results derived from the elliptical isophote fitting for a typical early-type galaxy (548 G 62). The panels show, from top to bottom: the R-band surface brightness, the ellipticity, the position angle, and the normalized c_4 Fourier coefficient, all plotted as function of the semi-major axis length ($a^{1/4}$). In this Figure we present data out to r_{max}, corresponding to $\sim$ 3% of the sky level. Table 3.4 gives the values of these profiles, listing: in column (1), the semi–major axis in arcsec; in columns (2) and (3), the R-band surface brightness in mag arcsec^{-2} and error; in columns (4) and (5) the ellipticity and its error; in columns (6) and (7) the position angle and its error; and in columns (8) and (9) the normalized c_4 Fourier coefficient and its error.

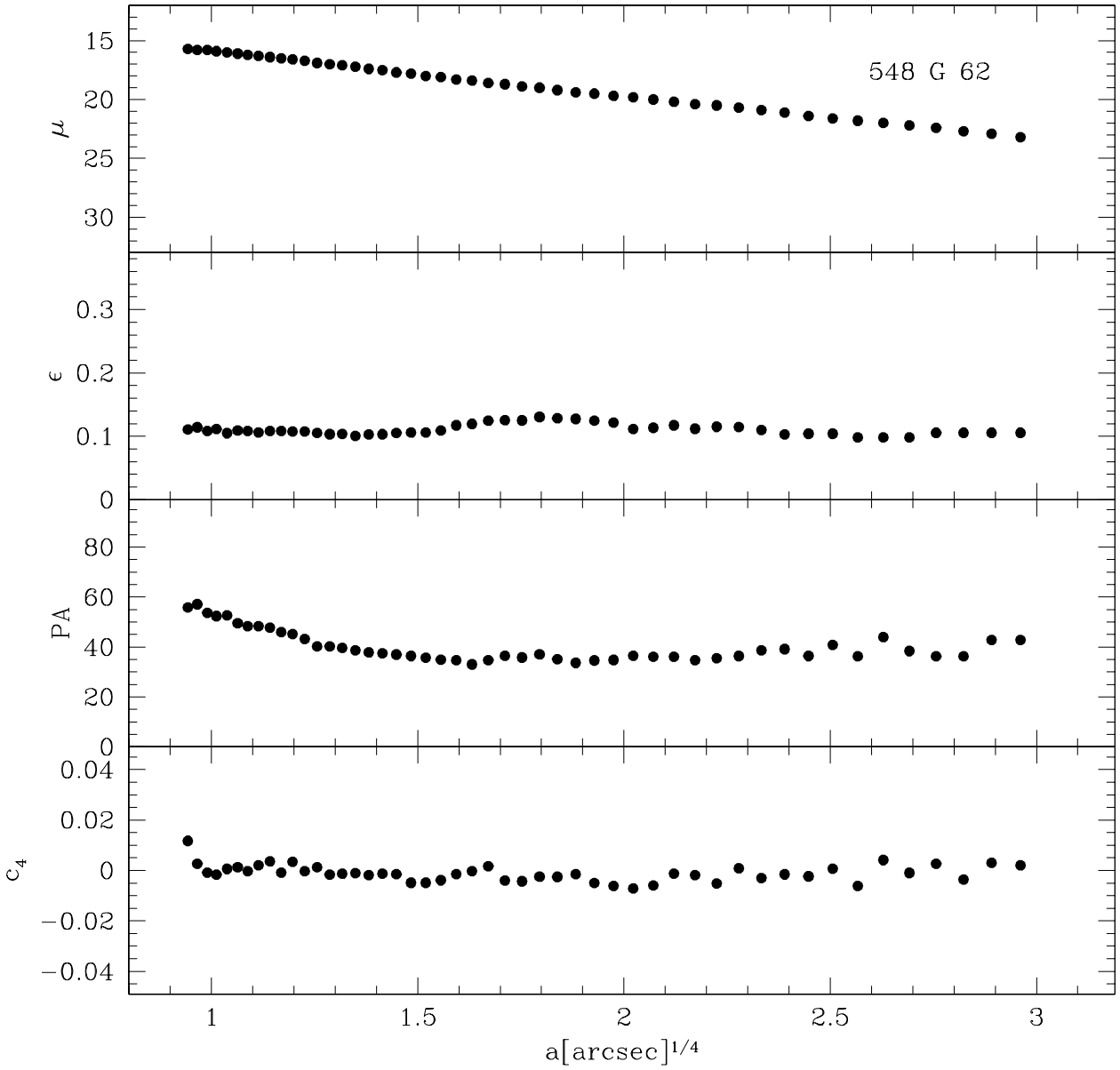

Figure 3.3 Results derived from the ellipse fitting (from top to bottom): the surface brightness (in magnitude/arcsec^2), the ellipticity, the position angle and the normalized c_4 Fourier coefficient are shown versus the semi-major axis ($a^{1/4}$, where a is in arcsec).

Table 3.4 Ellipse Fitting Profiles for 548 G 62

a arcsec (1)	μ mag/arcsec^2 (2)	ϵ_μ mag/arcsec^2 (3)	ϵ (4)	ϵ_ϵ (5)	PA degree (6)	ϵ_{PA} degree (7)	c_4 (8)	ϵ_{c_4} (9)
0.79	15.715	0.006	0.110	0.015	55.82	4.28	0.0117	0.0113
0.87	15.809	0.004	0.114	0.009	57.11	2.46	0.0026	0.0071
0.96	15.810	0.006	0.108	0.010	53.69	3.00	-0.0008	0.0049
1.05	15.907	0.005	0.111	0.007	52.36	1.98	-0.0016	0.0042
1.16	16.007	0.006	0.105	0.007	52.67	2.28	0.0006	0.0044
1.28	16.108	0.007	0.109	0.008	49.55	2.28	0.0012	0.0024
1.40	16.206	0.006	0.108	0.006	48.36	1.84	-0.0002	0.0018
1.54	16.306	0.007	0.106	0.006	48.35	1.93	0.0021	0.0033
1.70	16.406	0.007	0.108	0.006	47.80	1.85	0.0035	0.0042
1.87	16.504	0.005	0.108	0.004	45.92	1.26	-0.0008	0.0034
2.05	16.605	0.007	0.107	0.005	45.21	1.61	0.0034	0.0034
2.26	16.705	0.006	0.107	0.005	43.25	1.44	-0.0003	0.0033
2.49	16.904	0.005	0.105	0.004	40.22	1.21	0.0012	0.0037
2.74	17.004	0.006	0.103	0.004	40.29	1.42	-0.0016	0.0038
3.01	17.104	0.006	0.103	0.004	39.62	1.23	-0.0013	0.0031
3.31	17.204	0.007	0.100	0.004	38.72	1.47	-0.0010	0.0041
3.64	17.403	0.005	0.102	0.003	37.81	0.98	-0.0018	0.0030
4.00	17.504	0.007	0.103	0.004	37.47	1.36	-0.0012	0.0045
4.40	17.705	0.008	0.105	0.005	36.97	1.43	-0.0015	0.0051
4.85	17.805	0.009	0.105	0.005	36.41	1.66	-0.0048	0.0052
5.33	18.050	0.009	0.105	0.005	35.71	1.63	-0.0048	0.0049
5.86	18.106	0.010	0.109	0.006	34.91	1.74	-0.0038	0.0063
6.45	18.305	0.009	0.117	0.005	34.71	1.41	-0.0014	0.0058
7.09	18.406	0.011	0.119	0.006	33.04	1.68	-0.0002	0.0068
7.80	18.607	0.012	0.124	0.007	34.75	1.90	0.0017	0.0072
8.58	18.708	0.013	0.125	0.008	36.44	2.02	-0.0039	0.0068
9.44	18.909	0.015	0.125	0.009	35.81	2.29	-0.0043	0.0089
10.39	19.090	0.015	0.130	0.009	37.01	2.11	-0.0024	0.0099
11.42	19.210	0.017	0.128	0.010	35.17	2.38	-0.0025	0.0109
12.57	19.410	0.019	0.127	0.010	33.65	2.56	-0.0014	0.0121
13.82	19.513	0.021	0.124	0.013	34.59	3.21	-0.0049	0.0141
15.21	19.715	0.023	0.121	0.015	34.82	3.78	-0.0061	0.0163
16.73	19.814	0.024	0.111	0.014	36.54	4.03	-0.0071	0.0157
18.40	20.120	0.023	0.113	0.012	36.15	3.39	-0.0059	0.0134
20.24	20.212	0.023	0.117	0.012	36.13	3.24	-0.0012	0.0140
22.26	20.417	0.034	0.111	0.017	34.73	4.78	-0.0018	0.0195
24.49	20.516	0.033	0.115	0.016	35.51	4.22	-0.0051	0.0176
26.94	20.715	0.032	0.114	0.015	36.39	4.11	0.0008	0.0173
29.63	20.922	0.046	0.110	0.022	38.69	6.11	-0.0029	0.0242
32.60	21.125	0.056	0.103	0.025	39.14	7.45	-0.0015	0.0282
35.86	21.427	0.055	0.104	0.027	36.41	7.85	-0.0023	0.0297
39.44	21.636	0.087	0.104	0.036	40.88	10.47	0.0007	0.0391
43.39	21.838	0.086	0.098	0.038	36.28	11.81	-0.0060	0.0424
47.73	22.450	0.102	0.098	0.045	43.93	13.84	0.0041	0.0493
52.50	22.249	0.116	0.098	0.049	38.38	15.06	-0.0009	0.0542
57.75	22.457	0.142	0.105	0.057	36.25	16.53	0.0026	0.0641
63.52	22.763	0.160	0.105	0.063	36.25	18.07	-0.0036	0.0703
69.87	22.981	0.218	0.105	0.081	42.83	23.39	0.0030	0.0910
76.86	23.284	0.267	0.105	0.084	42.83	24.17	0.0020	0.0939
84.55	23.403	0.300	0.105	0.103	42.83	29.60	0.0021	0.1150

In Appendix B, we present the profiles derived from the ellipse fitting for the whole sample of observed galaxies. Figures B.1 - B.3 show the variation of the measured surface brigthness, ellipticity, position angle and the normalized c_4 Fourier coefficient, as a function of the semi-major axis splitting the observed galaxies into the three subsamples: 1) galaxies in the ENEARf magnitude and redshift limited sample; 2) galaxies in clusters but fainter or more distant than the limits of the ENEARf sample; 3) early-type galaxies not associated to our clusters and not satisfying the ENEARf selection criteria and galaxies of morphological types $T > -2$. The profiles are shown out to a radius $rmax$. We show these samples separately because they represent different pupulations with different overall properties.

Whenever more than one profile for the same galaxy is available they are over-plotted. There is a very good agreement between the profiles derived from multiple observations of the same object, for all the above parameters. Significant discrepancies are seen only for the ellipticity and the position angle mainly at small radii due to the seeing effects which tend to degenerate the determination of the major and minor axes of the galaxy. As expected, galaxies affected by the light contamination of nearby objects, tracking problems, presence of dust-lane, and other intrinsic peculiarities which are sensitive to exact position of the center of the apertures show differences even more evident in the ellipticity, position angle, and c_4 profiles than in that of the surface brightness. We note that in few cases the position angle profiles obtained from different observations present small offsets, which could be partially caused by an innacurate orientation of the image.

In these Figures, the most notable trend is a gradual change in the position angle and ellipticity. These gradual variations are more evident for galaxies with well-defined sub-components, such as a spheroid and a disk, which usually are also singled out by the variation of the c_4 parameter. In some cases, one finds abrupt variations in these profiles, clearly indicating the presence of other structures such as arms, rings, bar, or dust lane. Other features can be associated to the presence of stars, crowded backgrounds, interacting galaxies, residual contamination from nearby galaxies, significant differences in seeing conditions and/or tracking problems, extended galaxies reaching the edge of the detector, and other intrinsic peculiarities. We found that galaxies showing large or abrupt variations in the profiles derived by ellipses are usually identified with objects showing large deviations between the surface brightness profile measured from circular aperture photometry and a two-component model used to parametrize the real light profile of early-type galaxies (see Section 3.3.3). These objects are identified and flagged in the photometric catalog presented at the end of this Chapter and a description of the causes for the features is given in Table 3.12.

3.2.1.1 Light profile comparisons

In order to evaluate the results of our surface photometry we have carried out comparisons of light profiles obtained by us from different observations as well as with those published by other authors. While the accuracy of our surface photometry can be evaluated by comparing either circularized light profiles or those derived from ellipse fitting for galaxies with multiple observations, comparison with published results is only possible using surface brightness profiles obtained by ellipse fitting which has been more generally used. Since the internal comparisons of the light profiles based on the ellipse fitting yield similar results as those using the circularized profiles and our primary goal

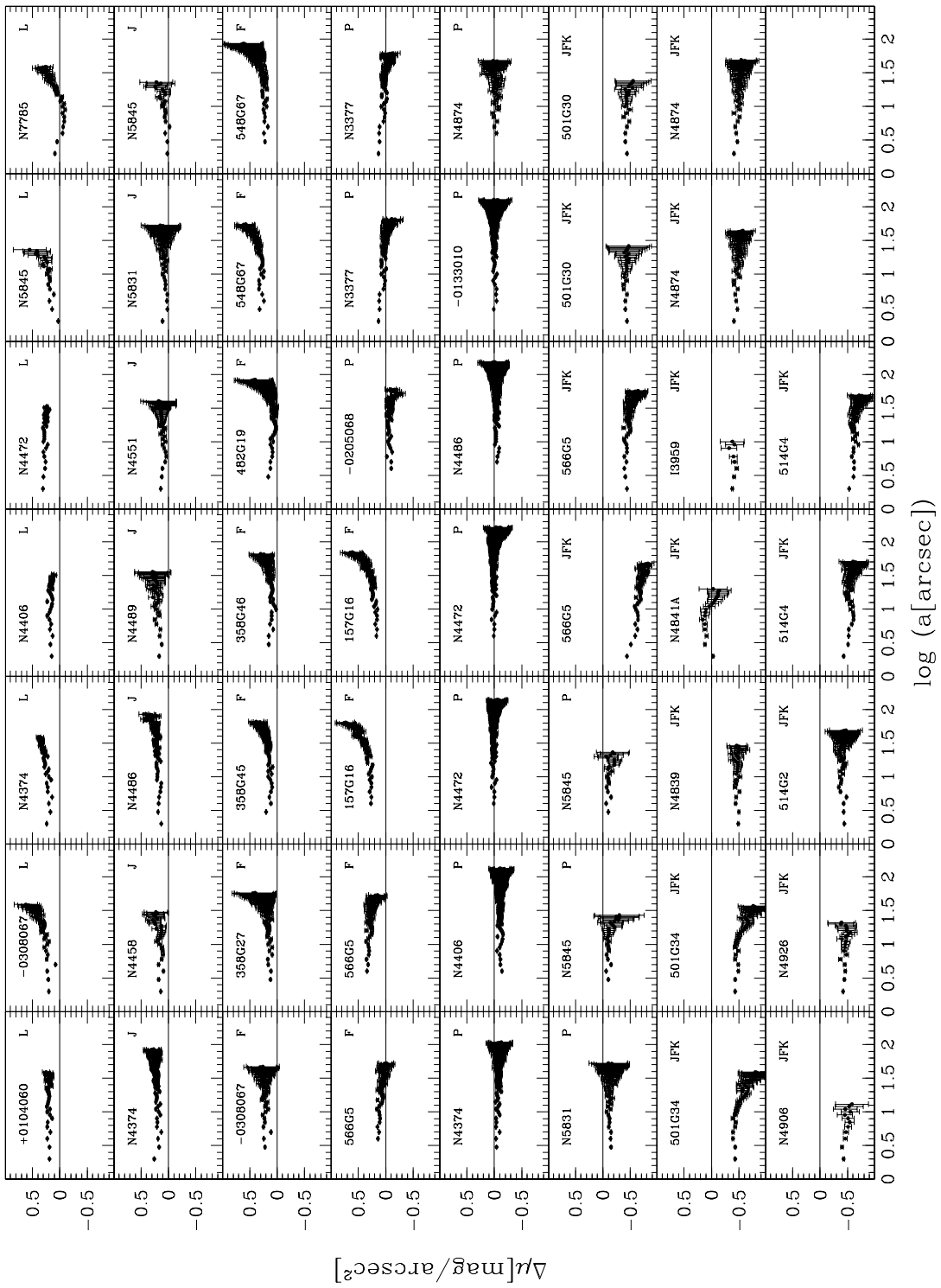

Figure 3.4 Comparison of luminosity profiles between our measurements and those of: (L) Lauer (1985); (J) Jedrzejewski et al. (1987); (F) Franx et al. (1989); (P) Peletier et al. (1990); (JFK) Jørgensen et al. (1992). The name of the galaxy is shown in the left corner while the identification of the different authors in the right corner.

Table 3.5 External Comparisons of the Light Profiles

Reference	N_c	Filter	Field of view arcmin × arcmin	$\Delta\mu$ mag/arcsec^2	σ_μ mag/arcsec^2
(1)	(2)	(3)	(4)	(5)	(6)
Lauer (1985)	7	R	3.6 × 3.6 - 2.6 × 1.7	0.23 ± 0.02	0.07
Jedrzejewski et al. (1987)	7	R	2.6 × 4.2	0.16 ± 0.02	0.06
Franx et al. (1989)	11	R	1.8 × 3.0 - 4.5 × 7.3	0.23 ± 0.03	0.09
Peletier et al. (1990)	13	R	5.0 × 7.0	-0.05 ± 0.02	0.05
Jørgensen et al. (1992)	16	Gunn-r	2.5 × 4.0 - 6.4 × 6.4	-0.48 ± 0.02	0.07

Notes: All differences are "our measurement" - "literature measurement".

is to derive global photometric parameters using the latter, a more detailed discussion is given in Section 3.2.2.1 (see Table 3.6). Therefore, in this section we compare our profiles with those of other authors.

Figure 3.4 shows the comparisons of our light profiles with those obtained by Lauer (1985), Jedrzejewski et al. (1987), Franx et al. (1989), Peletier et al. (1990) and Jørgensen et al. (1992), as indicated in each panel. The light profile differences were computed as a function of the semi–major axis (a) or equivalent radius ($r = \sqrt{(ab)}$) of the ellipses, as appropriate. Galaxies with close companions or surrounded by fainter galaxies, and very small galaxies were not included in the comparison, with the exception of NGC 4841A. The surface brightness profile of this galaxy is affected by the light of the nearby galaxy NGC 4841. Here, we show this comparison as an example of the effects caused by light contamination. The error bars were calculated as a combination of our internal errors and those given by the authors, whenever available. No zero-point shift was applied to take into account the different filters used by the different authors, which explains the relative offsets observed in the figures. The largest observed offset is seen in the comparison with Jørgensen et al. (1992) who used a Gunn-r filter. We also point out that with the exception of Jørgensen et al. (1992) galaxies, most galaxies shown in the figure are bright nearby galaxies.

The comparison between our light profiles and those obtained by other authors show, in general, a good agreement. Besides the zero-point shifts due to the different pass-bands considered, the main differences occur at large radii where the uncertainties in the background subtraction are important. These differences are particularly strong in the comparisons with Lauer (1985) and Franx et al. (1989), who have used small CCDs. In those cases where galaxies were larger than the field-of-view of the CCDs used (e.g., NGC 4406, NGC 4472, MCG -02-05-068), only the light profiles of the inner regions of the galaxies are presented. For all other authors even these differences are within the error estimates. Only the comparison between the light profiles of NGC 4841A measured by us and the result obtained by Jørgensen et al. shows a zero-point shift which is not consistent with those found from the comparison of the other galaxies in common. This

is due to the contamination of the light from the close companion. It should be noted that most of the older data were obtained with smaller detectors making the determination of the sky intensity particularly difficult for large galaxies. It is interesting that comparing profiles obtained with different filters and even in different passbands (in the case of Jørgensen et al.), no significant gradients are seen in the light profile differences. The comparisons with Peletier (1990) are particularly good. These data use a larger CCD and are the closest to our photometric system, thereby the comparisons are free of possible color-gradient effect.

The quantitative results from the above comparisons are summarized in Table 3.5 which gives: in column (1) the reference; in column (2) the number of galaxies in common with other authors; in column (3) the filter used by these authors; in column (4) the field-of-view of the published data; in columns (5) and (6) the mean difference in surface brightness and the scatter. Considering only the comparison with Peletier et al. (1990), closest to our photometric system, we find a mean difference in surface brightness of -0.05 $\pm$ 0.02 mag arcsec^{-2} with a dispersion of 0.05 mag arcsec^{-2}. These values are consistent with our estimates of the zero-point error and the errors in surface brightness. The mean values obtained for the other authors are consistent with the expected differences in zero-point shift between the different filters. In general, the scatter of the residual difference in the surface brightness profiles of the external comparisons is small $\sim$ 0.05 mag showing quantitatively the good agreement between our photometry and previous results.

3.2.2 Circularly averaged profiles

While ellipse fitting provides information on the shape and orientation of the galaxy, the derivation of global photometric parameters was conducted using the procedure developed by Saglia et al. (1997) based on the circularly averaged radial surface brightness profiles. One advantage of using the circularly averaged profiles is that all photometric parameters of interest in deriving scaling relations (d_n, r_e and $\bar{\mu}_e$) can be obtained from them. As discussed by Saglia et al. (1993a) for most elliptical galaxies the circularly averaged growth curve does not differ significantly from that derived by following the elliptical isophotes. Even though most of the early-type galaxies are a combination of a bulge and disk components the difference introduced by using circular isophotes is small. In cases of galaxies showing flattened bulges or an evident disk component, especially if it is seen edge-on, the values of the global parameters are less accurate. Figure 3.5 show the distribution of the ellipticity of the ENEARf sample (left panel) and the faint/distant cluster galaxies (right panel). Most of the objects have ellipticity < 0.5.

The circularly averaged light profiles were determined using circular apertures in diameter steps of 1 pixel from 1 arcsec out to an upper radius limit, r_{max}, as previously defined. The center for the aperture photometry was assumed to be that obtained from the smallest ellipse derived from the two-dimensional isophotal fit. At each radius, the mean surface brightness within a ring one pixel wide was determined as well as the total integrated magnitude within that radius. The instrumental values obtained for the surface brightness and magnitudes were calibrated using the photometric solution and were corrected for galactic extinction and K-corrected. The surface brightness was also corrected for the $(1+z)^4$ cosmological dimming. The light profiles for all the observed galaxies are shown in Figures C.1 - C.3 of Appendix C (see also Section 3.3.3), together with best model fits.

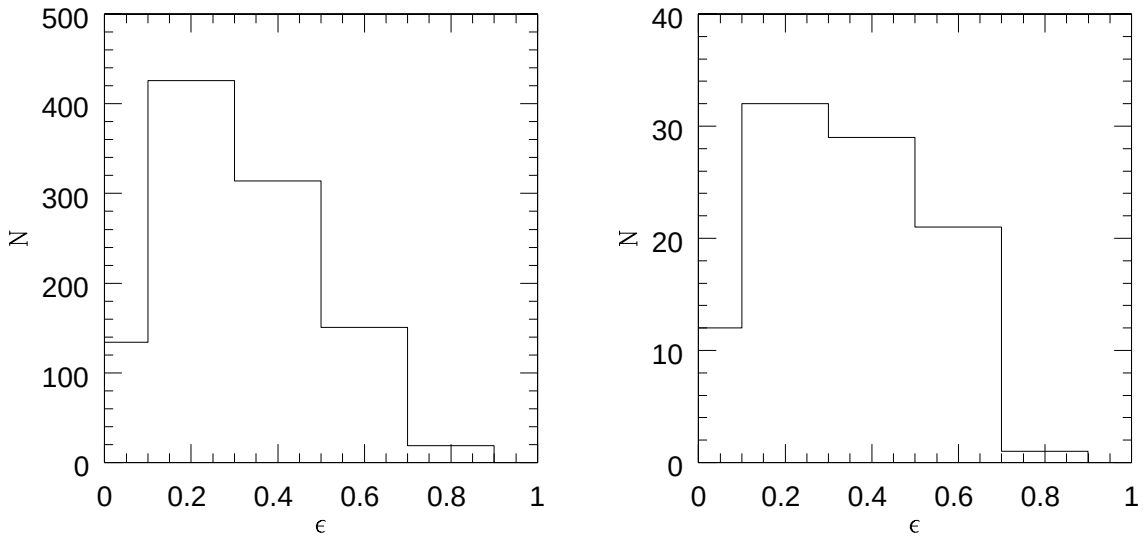

Figure 3.5 The distribution of the ellipticity for galaxies in the ENEARf sample (left panel) and for faint and/or distant cluster galaxies (right panel).

3.2.2.1 Internal comparisons of the light profiles

We have used multiple observations of the same galaxy to estimate the accuracy of our derived surface brightness profiles. For this purpose we compare profiles for galaxies with multiple observations splitting them into three sets of frames, those observed: (i) in the same night; (ii) in different nights but with the same setup; and (iii) with different setups. By splitting the comparisons in this way it is possible to separately evaluate the contribution to the errors due to the reduction procedure, seeing variations and zero-point calibration. In these comparisons galaxies close to other galaxies of comparable size or close to bright stars were discarded.

Figure 3.2.2.1 shows the difference of surface brightness profiles of galaxies observed in the same night. We show 185 independent comparisons. The resulting residual profile has been truncated when the error in the intensity is 30%, even though the galaxy light profiles extend much further out, to minimize the crowding of the plots due to the large error bars. The same criteria is adopted in the subsequent figures. In general, the comparison shows very good agreement over a wide range of radii. Some differences are noticeable near the center and at large radii. The former are primarily due to significant

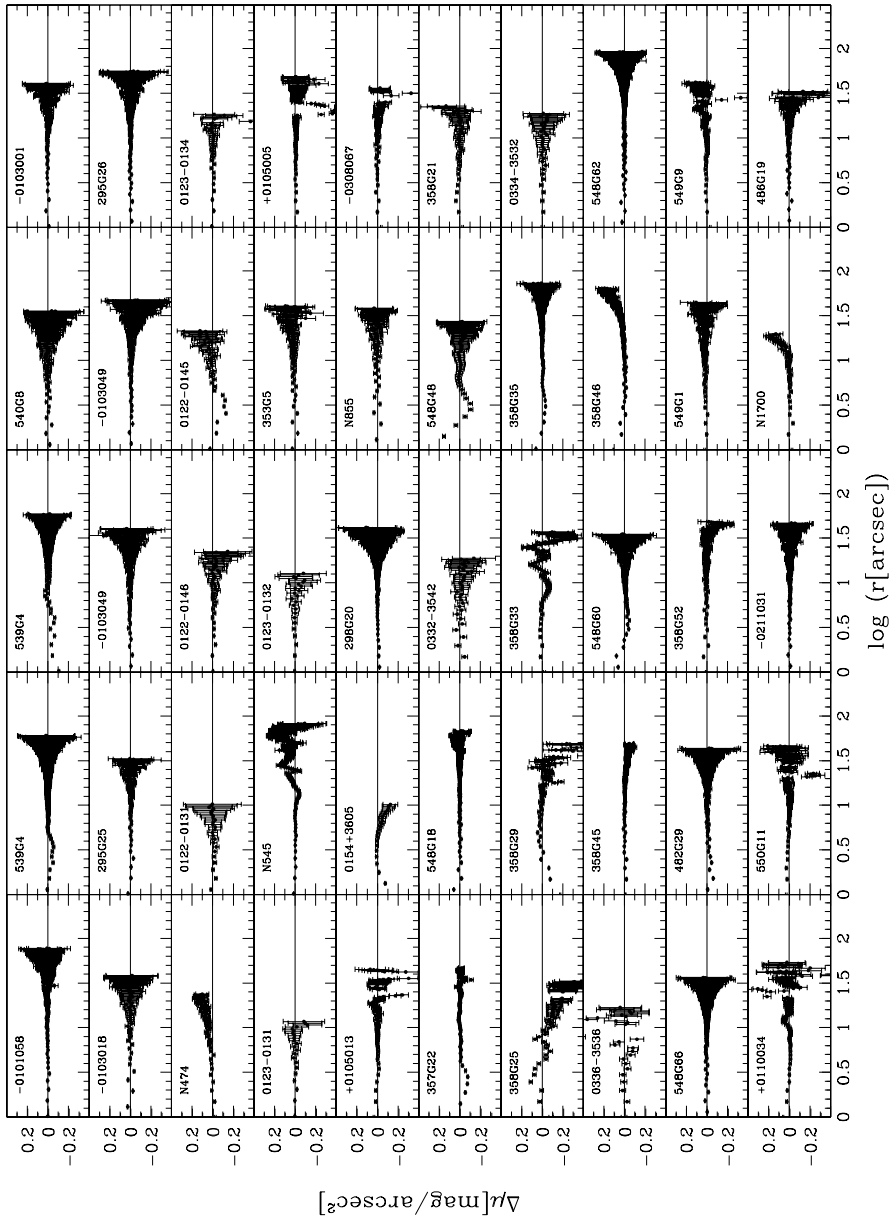

Figure 3.6 Surface brightness comparison of our internal measurements obtained with the circular apertures. The panels show differences in surface brightness in the R band for galaxies observed during the same night.

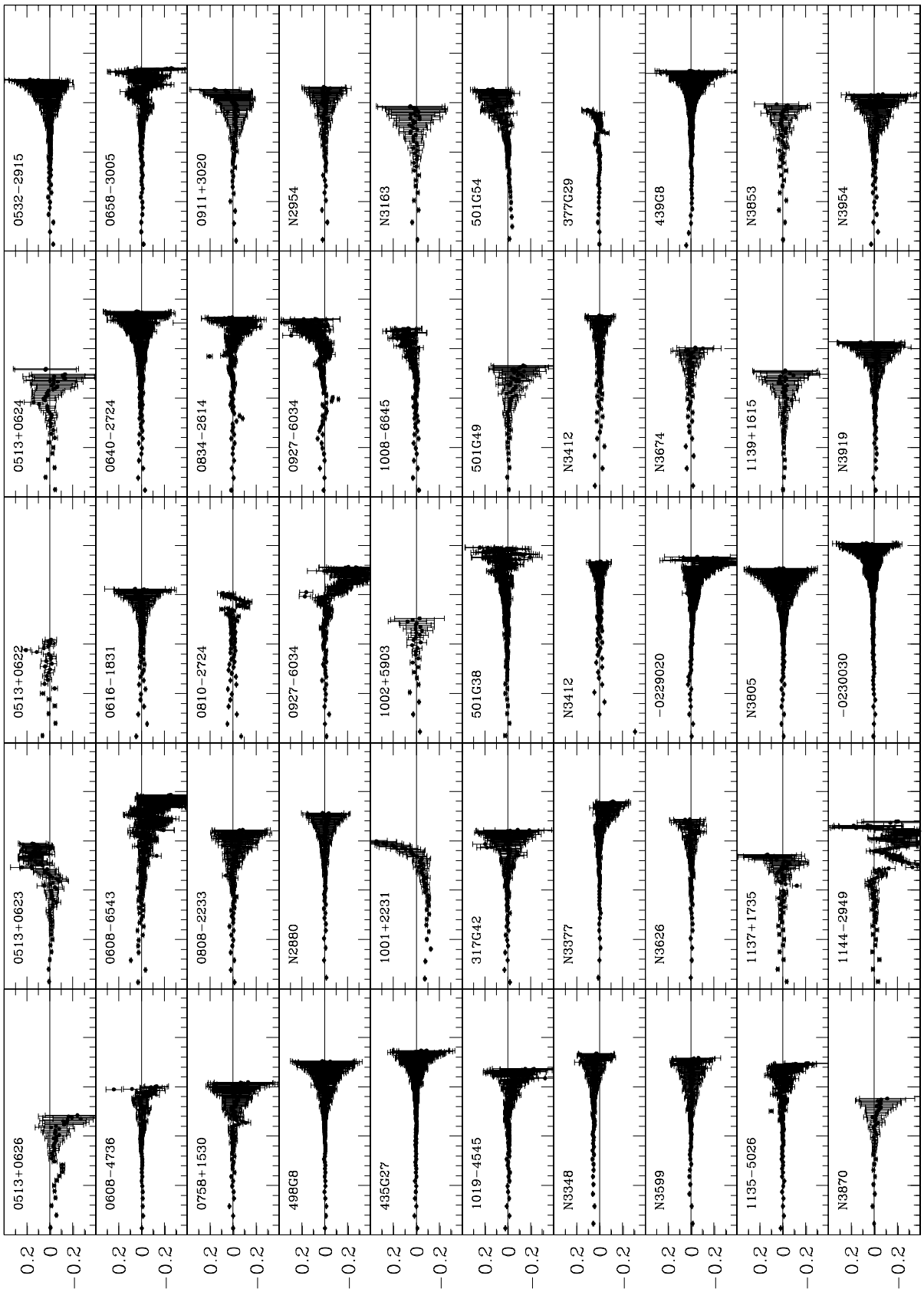
0513+0626
0513+0623
0513+0622
0513+0624
0532−2915
0608−4736
0608−6543
0616−1831
0640−2724
0658−3005
0758+1530
0808−2233
0810−2724
0834−2614
0911+3020
498G8
N2880
0927−6034
0927−6034
N2954
1019−4545
1001+2231
1002+5903
1008−6645
N3163
N3348
N3377
N3412
N3412
377G29
N3599
N3626
−0229020
N3674
439G8
1135−5026
1137+1735
N3805
1139+1615
N3853
N3870
1144−2949
−0230030
N3919
N3954
317G42
501G38
501G49
501G54
0.2
0
−0.2
0 0.5 1 1.5 2
Δμ[mag/arcsec²]
log (r[arcsec])

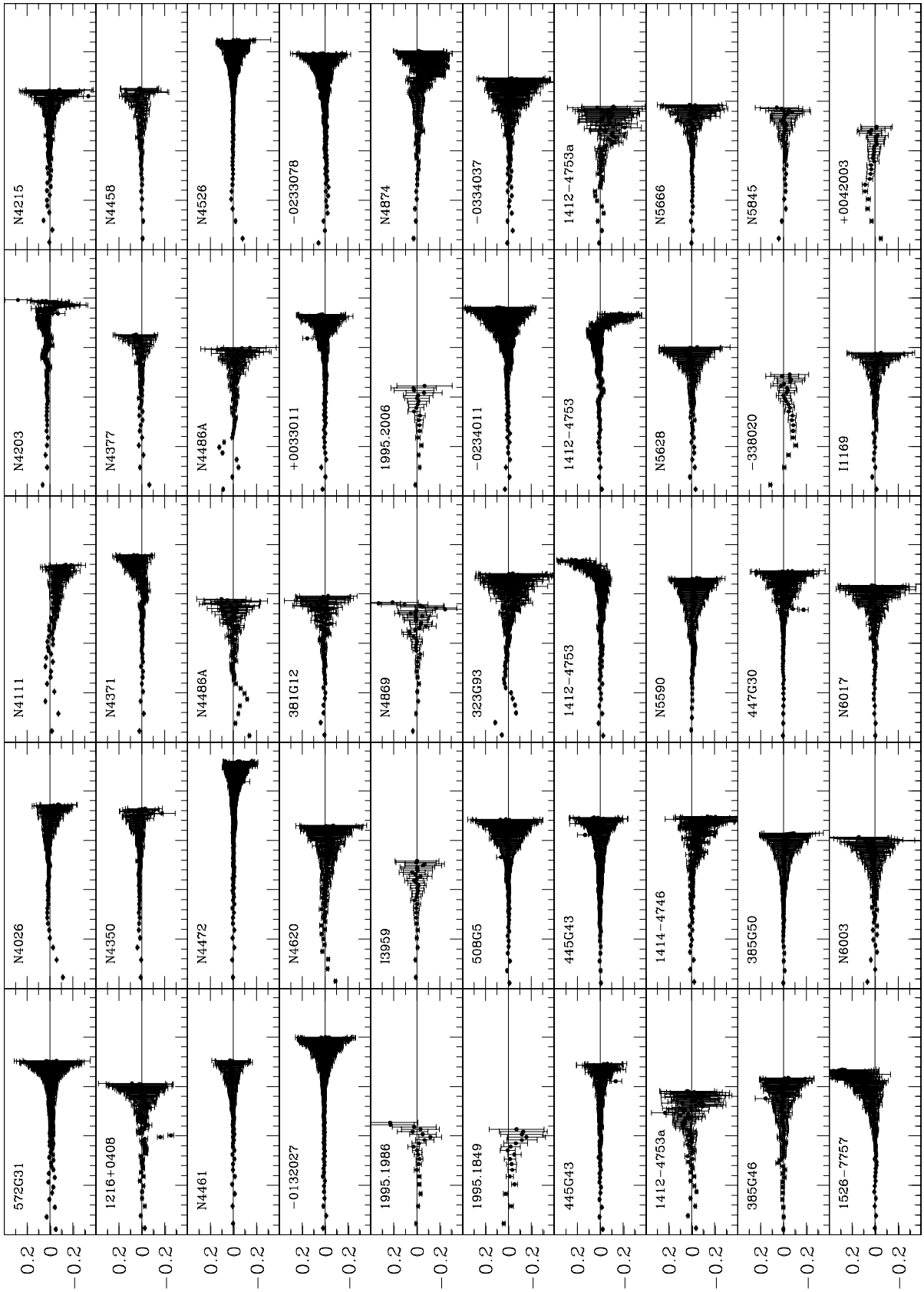
572G31
N4026
N4111
N4203
N4215
1216+0408
N4350
N4371
N4377
N4458
N4461
N4472
N4486A
N4486A
N4526
−0132027
N4620
381G12
+0033011
−0233078
1995.1986
I3959
N4869
1995.2006
N4874
1995.1849
508G5
323G93
−0234011
−0334037
445G43
445G43
1412−4753
1412−4753
1412−4753a
1412−4753a
1414−4746
N5590
N5628
N5666
385G46
385G50
447G30
−338020
N5845
1526−7757
N6003
N6017
I1169
+0042003
0.2
0
−0.2
0 0.5 1 1.5 2
log (r[arcsec])
Δμ[mag/arcsec²]

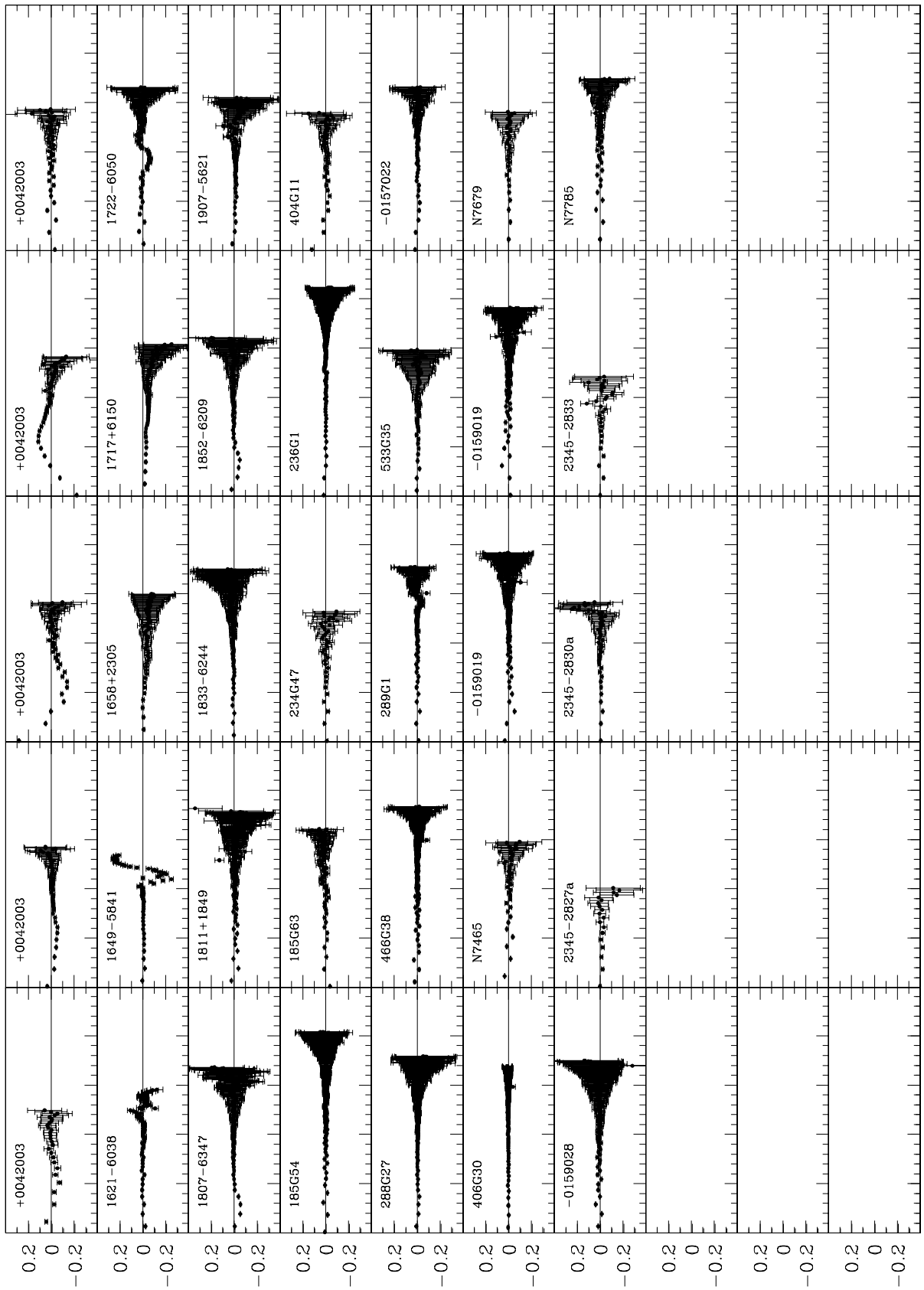
+0042003
1621−6038
1807−6347
185G54
288G27
406G30
−0159028
+0042003
1649−5841
1811+1849
185G63
466G38
N7465
2345−2827a
+0042003
1658+2305
1833−6244
234G47
289G1
−0159019
2345−2830a
+0042003
1717+6150
1852−6209
236G1
533G35
−0159019
2345−2833
+0042003
1722−6050
1907−5621
404G11
−0157022
N7679
N7785
Δμ[mag/arcsec²]
log (r[arcsec])

variations of the seeing during the night. This is especially important in the case of very small galaxies such as IC3957. Another problem of a different nature is illustrated by the galaxy NGC 4486A which shows a bad comparison near the center. It turns out that from the inspection of our images we can see that there is a relatively bright star very close to the center of the galaxy which compromised the light profile in the inner parts of the galaxy. The effect of the star is also noticeable in the position angle profile shown in Figure C.1 in Appendix C. Another cause for poor comparisons is illustrated by the galaxy 323 G 93 which, in addition of a relatively bright star near the center, one can see the presence of a dust lane. Both of these features lead to inaccurate centering and to the discrepancy seen at the inner parts of the residual profile. Differences at large radii, such as seen in the comparison of galaxies 0927-6034 and 1649-5841, are due to both a crowded stellar field, making the determination of the mean sky level difficult, and the presence of relatively bright stars superposed onto the outer parts of the galaxy image. A particular case of discrepancies at large radii is shown by 1144-2949, which has a large D/B and in the outer region there are weak features. A more subtle problem is that of galaxy 1722-6050 which shows a small depression in the residual profile in the radii interval 5-10 arcsec. Close inspection of the image shows a pair of apparently interacting galaxies. In a few cases there are small zero-point shifts such as in the case of NGC 3348, which is, however, consistent with zero-point error estimated for the night. For each pair of profiles we compute the mean weighted difference between them within the radii range r_{min} and r_{max}. Using these mean values a final mean was obtained yielding 0.004 ± 0.003 mag arcsec^{-2} with a scatter of 0.042 mag arcsec^{-2}, consistent with the estimated uncertainties of the photometric calibration.

The residual profiles presented in Figure 3.2.2.1 are between profiles derived from images of 53 galaxies obtained in different nights using the same setup. Such comparisons are useful since they reflect the more general cases of combining observations under different atmospheric conditions without introducing issues related to color-terms, field-of-view and other instrument-telescope dependent quantities. From the inspection of Figure 3.2.2.1 one finds that, in general, the observed discrepancies are similar to those described earlier from comparison of objects observed in the same night. The worst comparison is that for the galaxy NGC 5596, which is due to either poor tracking or strong wind leading to distorted images in one of the frames. The good agreement shown in Figure 3.2.2.1 provides an additional verification of the accuracy of our photometric solutions. In this case we find that the mean difference is 0.001 ± 0.007 mag arcsec^{-2} and the scatter is 0.052 mag arcsec^{-2}, consistent with the values obtained above.

Finally, comparisons of the surface brightness profiles extracted from images taken with different setups are shown in Figure 3.2.2.1 for a total of 114 galaxies. Our images have been inspected for all galaxies showing significant features in the residual profiles. As before, these features are associated to the presence of stars, crowded backgrounds, dust lanes, interacting galaxies, residual contamination from nearby galaxies, significant differences in seeing conditions and/or tracking problems, extended galaxies reaching the edge of the detector, and other intrinsic peculiarities which are sensitive to exact position of the center of the apertures. The most notable examples are: NGG 936 (large galaxy near the edge); 0733+1800 (star near the center); MCG -02-22-008 and 0959+1356 (significant seeing differences); 1649-5841 (crowded background); 1722-6050 (apparently interacting galaxy). Some of these cases have already been discussed above. Note that in the case of 1722-6050 the differences are now much more dramatic which

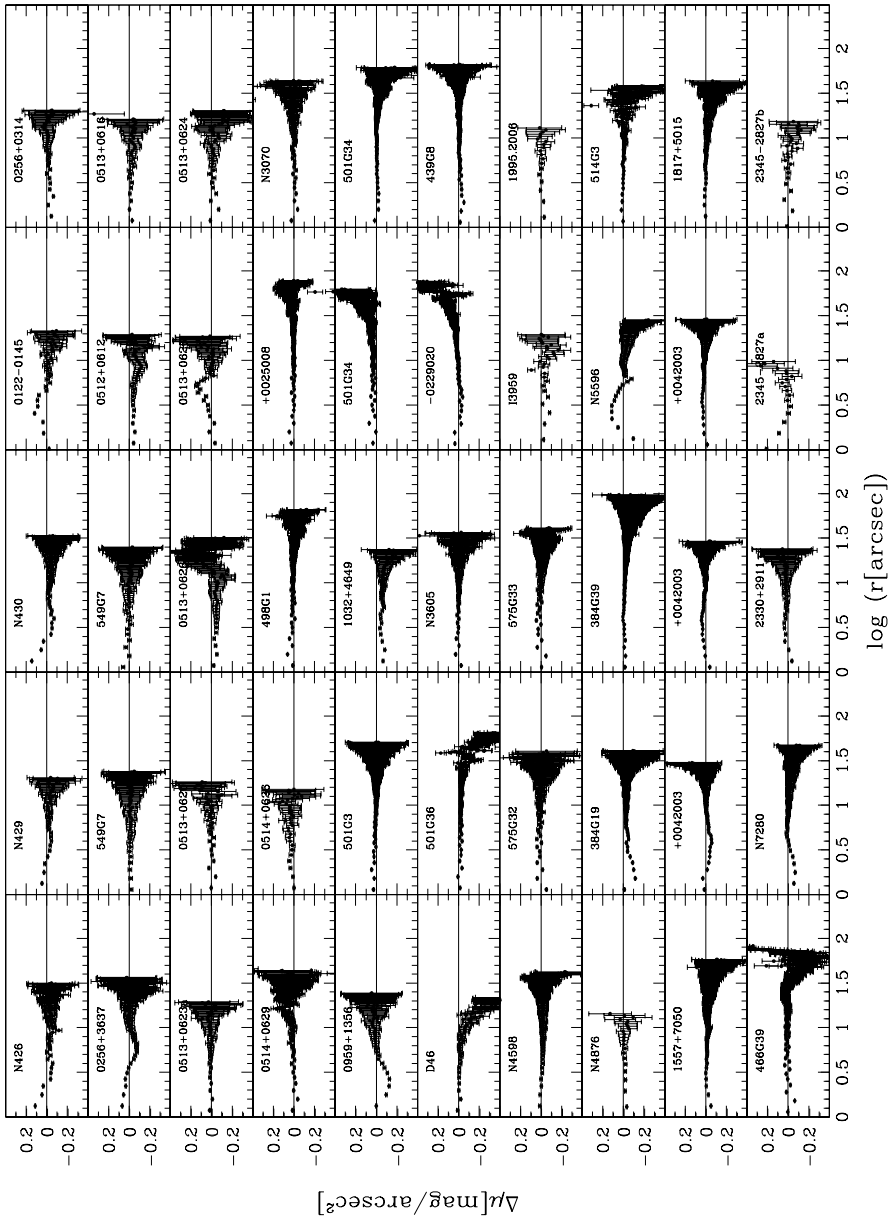

Figure 3.7 Surface brightness comparison of our internal measurements obtained with the circular apertures. The panels show differences in surface brightness in the R band for galaxies observed during different nights but using the same setups.

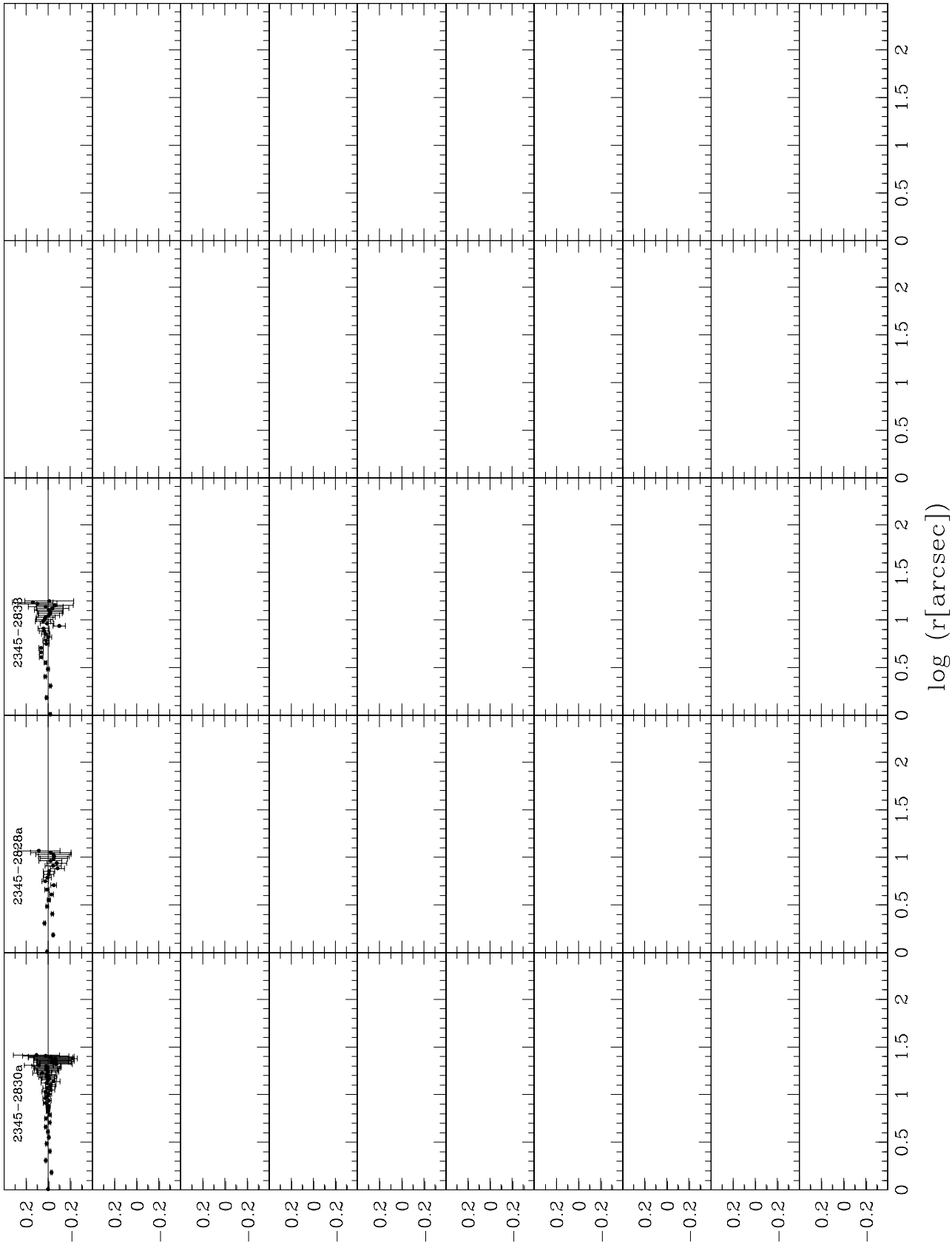
2345−2830a
2345−2828a
2345−2833
Δμ[mag/arcsec²]
log (r[arcsec])

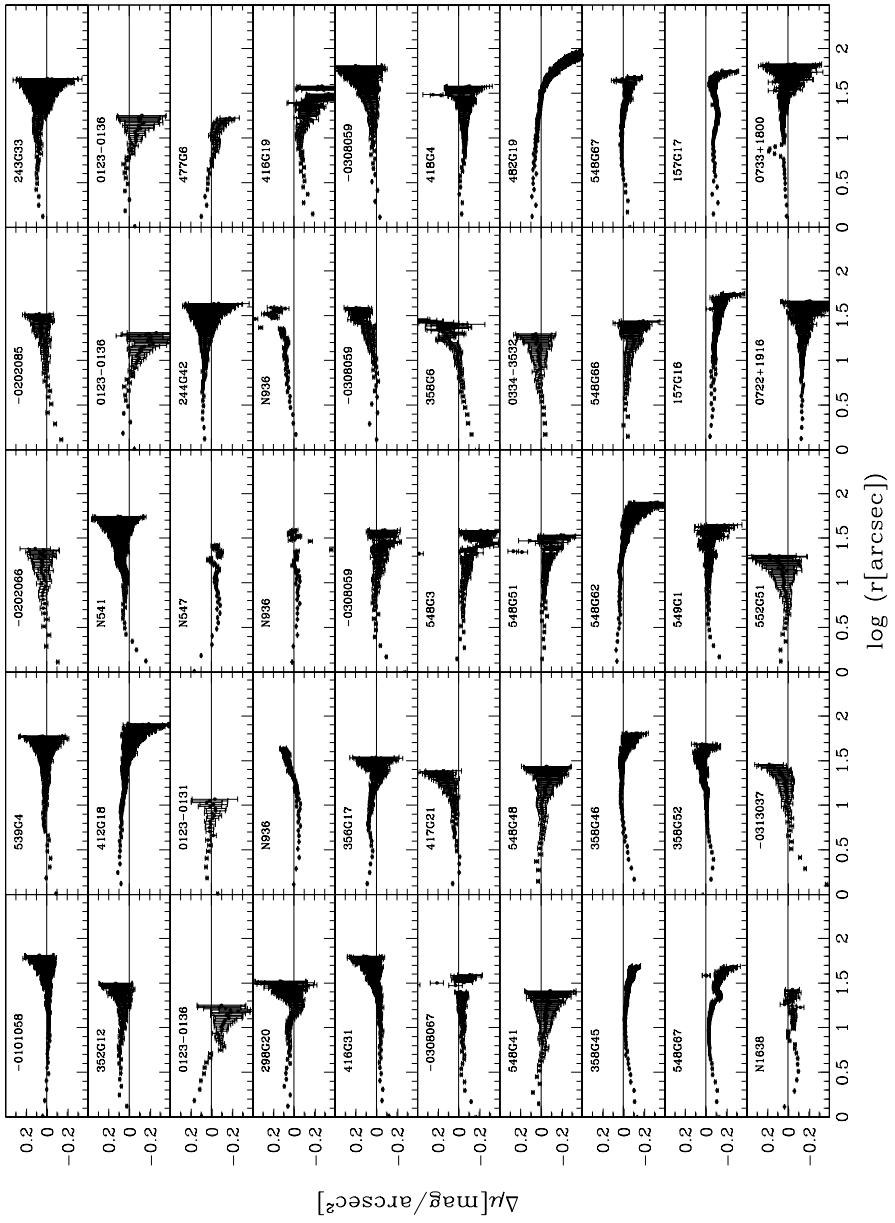

Figure 3.8 Surface brightness comparison of our internal measurements obtained with the circular apertures. The panels show differences in surface brightness in the R band for galaxies observed using different setups.

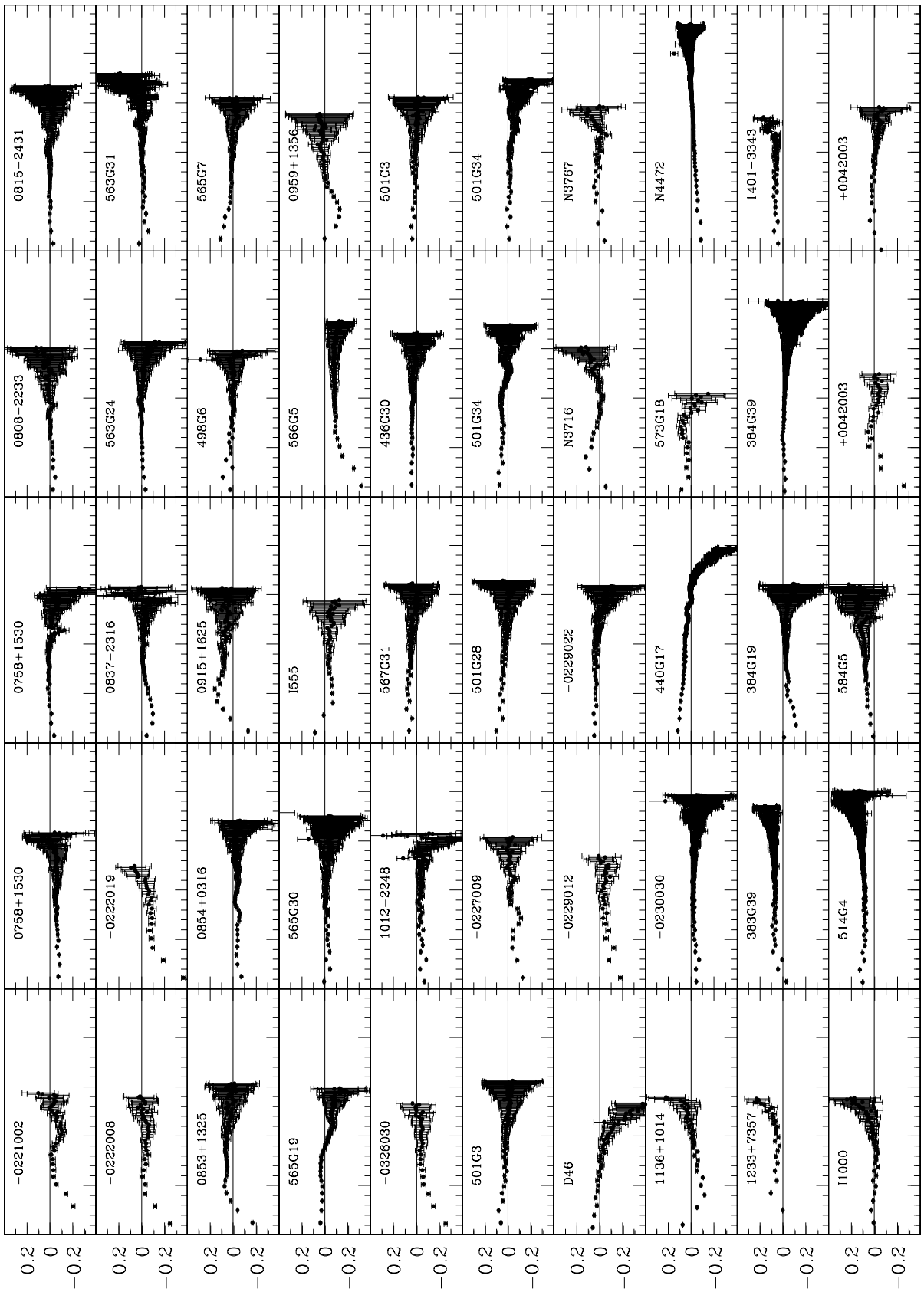
−0221002
0758+1530
0808−2233
0815−2431
−0222008
−0222019
0837−2316
563G24
563G31
0853+1325
0854+0316
0915+1625
498G6
565G7
565G19
565G30
I555
566G5
0959+1356
−0326030
1012−2248
567G31
436G30
501G3
D46
−0229012
−0229022
N3716
N3767
1136+1014
−0230030
440G17
573G18
N4472
1233+7357
383G39
384G19
384G39
1401−3343
I1000
514G4
584G5
+0042003
+0042003
0
0.5
1
1.5
2
−0.2
0
0.2
Δμ[mag/arcsec²]
log (r[arcsec])

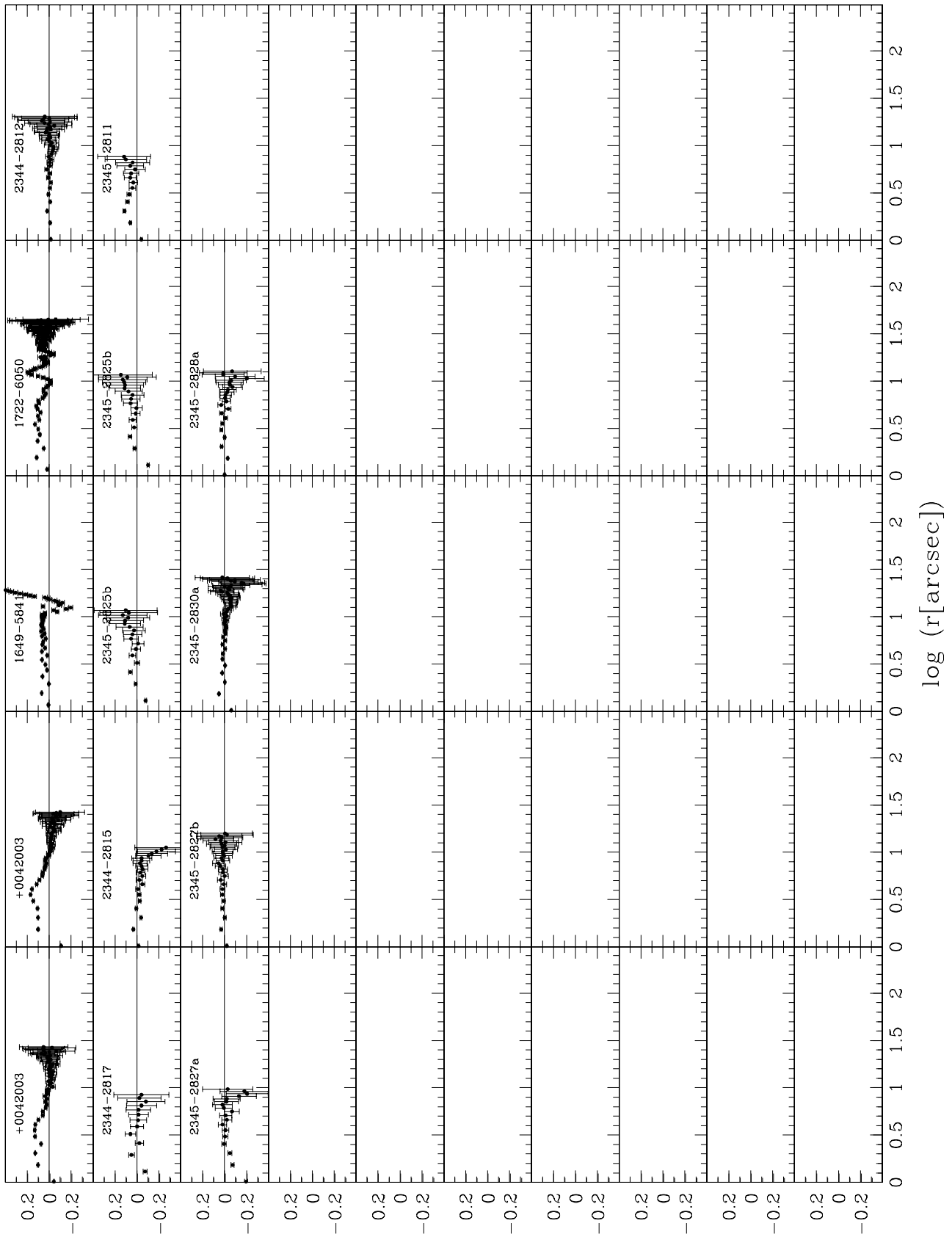
+0042003
+0042003
1649−5841
1722−6050
2344−2812
2344−2817
2344−2815
2345−2825b
2345−2825b
2345−2811
2345−2827a
2345−2822b
2345−2830a
2345−2828a
Δμ[mag/arcsec²]
log (r[arcsec])

Table 3.6 Internal Comparisons of the Light Profiles

Comparison	N_c	$\Delta\mu$ mag/arcsec^2	σ_μ mag/arcsec^2
(1)	(2)	(3)	(4)
same night	172	0.004 ± 0.003	0.042
same setup	53	0.001 ± 0.007	0.052
different setups	114	0.002 ± 0.009	0.094

can be accounted for by differences in the choice of the center. Another case of interest is MCG +00-42-003 for which four pairs of profiles with different setup are presented. While some of them are in excellent agreement others show differences on scales $<$ 5 arcsec which are due to variable seeing conditions. Also more noticeable are relative offsets which can be as large 0.1 mag in the comparison of a given pair of profiles, which is consistent with our estimated error in the photometry. From these comparisons we find a mean difference of 0.002 ± 0.009 mag arcsec^{-2} and a scatter of 0.094 mag arcsec^{-2}. The larger scatter is likely due to the additional uncertainties in the photometric calibration introduced by color terms of different setups. These residuals differences are further investigated in Section 3.4.2 in our attempt to construct a homogeneous set of global photometric parameters.

The above results are summarized in Table 3.6 which gives: in column (1) the set considered; in column (2) the number of galaxies in common; in columns (3) the mean difference in surface brightness and its error; and in column (4) the scatter. We point out that these values are consistent with those obtained from a similar comparison of profiles determined by the ellipse fitting method.

3.3 Light profile fitting

3.3.1 Photometric parameters

The goal of our imaging survey has been to determine photometric quantities that enter in the empirical redshift independent distance relations such as the $D_n - \sigma$ and the FP as well as other global parameters such as the total magnitude and the the disk-to-bulge ratio which characterizes lenticular galaxies. Furthermore, since our sample was chosen to explicit include lenticular galaxies it is important to examine how the parameters that enter the scaling relation should be determined in the case of a two-component system. Therefore, following the work of Saglia et al. (1997) the surface brightness profiles obtained in the previous section were fitted, as described below, using a two-component model comprising a bulge and a disk. Here we point out that the $(1+z)^4$ correction described in Section 3.2.1 is applied only when computing the surface brightness and not the total magnitude.

We parametrize the spheroidal component using the de Vaucouleurs' $r^{1/4}$ law given by $I_B(r) = I_{eB} \exp(-7.67[(r/r_{eB})^{1/4} - 1])$, where the effective radius r_{eB} is the radius of the isophote which encloses half the total luminosity of the bulge component, and I_{eB} is the surface brightness at that radius. Therefore, to the observed profiles we fit the analytical expression

$$\mu_B(r) = -2.5 \log I_B(r) = 8.325[(r/r_{eB})^{1/4} - 1] + \mu(r_{eB}) \tag{3.4}$$

where $\mu(r_{eB}) = -2.5 \log I_{eB}$ is the value of the surface brightness at r_{eB}. Integrating Eq. 3.4 from zero to infinity, one obtains the total flux of the spheroidal component of the galaxy $F_{B-tot} = 7.214\pi r_{eB}^2 I_{eB}$ and the flux inside the radius r_{eB}, $F_B(< r_{eB}) = F_{B-tot}/2 = 3.608\pi r_{eB}^2 I_{eB}$.

Hence, since the mean surface brightness within r_{eB} is $\bar{\mu}_{eB} = -2.5 \log(F_B(< r_{eB})/(\pi r_{eB}^2))$ and $m_{totB} = -2.5 \log F_{B-tot}$, one obtains that

$$\bar{\mu}_{eB} = m_{totB} + 1.995 + 5 \log r_{eB} \tag{3.5}$$

The disk component is parametrized by the usual exponential law

$$I_{exp}(r) = I_o exp(-r/\alpha) \tag{3.6}$$

where α is the exponential scale length and I_o is the central surface brightness of the disk. Integrating this equation to infinity we get the total magnitude of the disk component which is given by

$$m_{totD} = \mu_o - 5 \log(\alpha) - 2.5 \log(2\pi) \tag{3.7}$$

where $\mu_o = -2.5 \log(I_o)$.

The total magnitude of the galaxy is then given by $m_{tot} = -2.5 \log F_{tot}$ where $F_{tot} = F_{B-tot} + F_{D-tot}$ and $F_{D-tot} = 10^{(-m_{totD}/2.5)}$ is the total flux of the disk component. The disk-to-bulge ratio is given by $D/B = F_{B-tot}/F_{D-tot}$. Since most of our galaxies are fitted by a combination of the $r^{1/4}$ and the exponential laws, it is convenient to also define the radius which encloses half of the total light of the galaxy r_e and the corresponding mean surface brightness $\bar{\mu}_e$ which differ from r_{eB} and $\bar{\mu}_{eB}$ as determined from the bulge component alone.

The global parameters $\bar{\mu}_e$, r_e, m_{tot}, and D/B are the measured quantities presented in the following of this work. Possible correlations between these global parameters and those of the sub-componets will be investigated in a future work.

Finally, we also compute the characteristic angular diameter d_n, as originally defined by the 7S, of a circular aperture within which the average surface brightness of the galaxy corrected for galactic extinction, K–dimming and cosmological effects is equal to a given value. Here we adopt the isophotal level $\mu_R = 19.25$ mag arcsec^{-2} in the $R-$band regardless of the morphological type, which corresponds to $\mu_B = 20.75$ mag arcsec^{-2} in B assuming a mean value for $(B - R)$=1.5 (e.g., Lucey and Carter 1988; Lucey et al. 1991; Jørgensen et al. 1992).

Our choice of using a two-component model in fitting the surface brightness profile of early-type galaxies contrasts with most previous work which have by and large used a single-component fit to determine the photometric parameters that are used in defining, for instance, the FP (eg. Jørgensen et al. 1995a; Scodeggio et al. 1998). In addition, if

one is to explore possible effects of different morphology in the distance relation it is essential to be able to characterize the relative contributions of the spheroidal and disk components, dynamically distinct systems. One expects that for a lenticular galaxy only the spheroidal component should satisfy the scaling relation obeyed by pure ellipticals. Therefore, ignoring the presence of the disk could bias the results. Saglia et al. (1997) points out that by ignoring the presence of a disk component lead to errors of $\sim 20\%$ in the radius r_e which encloses half of the total light of the galaxy. Smith et al. (1997), on the other hand, argue that the important quantity is the combination of the effective radius with the mean surface brightness ($\log r_e$-0.30 $\bar{\mu}_e$) which is not significantly affected by the presence of a disk, since the errors in r_e and $\bar{\mu}_e$ are correlated.

Similar concerns apply to the proper choice of the isophotal level at which the d_n parameter should be defined. The diameter at a faint isophotal level may be contaminated by the disk component with different dynamical properties while defining it at a brighter isophotal level makes it sensitive to seeing effects, especially for more distant galaxies. Following Dressler (1987) suggestions of measuring d_n at 20.75 mag arcsec^{-2} for lenticular galaxies, we found very small values probably affected by seeing. Moreover, in recent works (e.g., Jørgensen et al. 1995; Lucey et al. 1991) the diameters have been measured at the same level independently of morphological types. For these reasons we decided to measure d_n for both lenticular and elliptical galaxies at the same level for the whole sample presented in this work. As shown by Dressler (1987), the $D_n - \sigma$ relation also applies to lenticular and spirals (not later than Sb). Alternatively, one should consider possible residuals in the $D_n - \sigma$ relation as a function of the D/B ratio. We will return on these issues in Chapter 6.

3.3.2 Fitting procedure

The circularly average profiles were fitted using the procedure developed by Saglia et al. (1997) which simultaneously fits a $r^{1/4}$ and exponential profiles, convolved with a PSF to take into account the effects due to the seeing. Seeing effects can be significant out to a radius of 5-10 FWHM, and thus lead to substantial errors when FWHM is comparable to $2r_e$. Since the median seeing of our observations was $\sim$ 1.4 arcsec and the median value for the effective radius of the galaxies in the ENEARf sample is $\sim$ 15 arcsec, seeing effects are significant for $\lesssim$25% of the galaxies. On the other hand, for faint galaxies in clusters seeing effects are important for at least half of the observed galaxies.

Values for r_e, α, I_o, D/B, and the FWHM are determined by minimizing the weighted sum of the squared magnitude differences between the observed galaxy surface brightness profile and the model profile with respect to these parameters. The weights are the statistical errors in the values of the surface brightness at each radius computed as described earlier. Each galaxy profile is fitted three times using: (i) a pure $r^{1/4}$ law ($D/B = 0$); (ii) an exponential disk profile ($B/D = 0$); (iii) the sum of a bulge and a disk component. In all cases these profiles are convolved with a PSF characterized by a FWHM which is also left as a free parameter of the fit. For each of those cases one can either assume a fix mean sky value, for instance as determined from the "sky boxes" or allow it to be a free parameter of the fit. Therefore, the procedure produces six sets of parameters. The χ^2 is computed for each of the six fits, and the one with the smallest reduced χ^2 is chosen as the best fit. Examination of the fits to the observed light profiles shows that in most cases the choice of the fit with the smallest χ^2 leads to

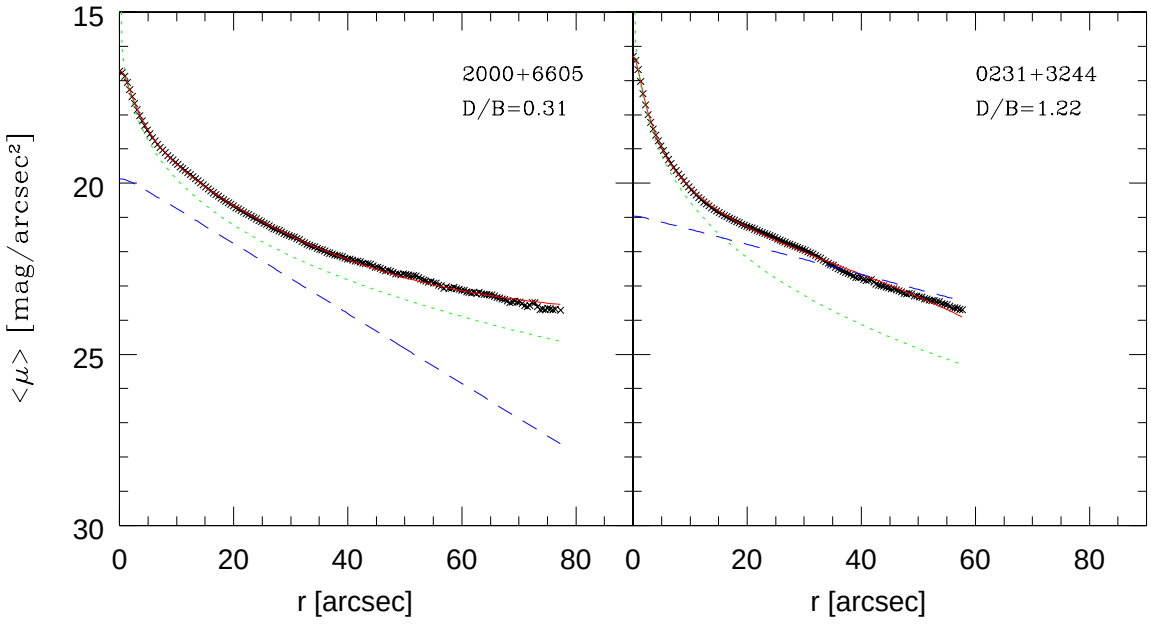

Figure 3.9 Examples of the light profile fitting for two galaxies with different D/B ratio. The $r^{1/4}$ fit is indicated with a dotted line, the exponential fit with a dashed line, and the combination of the two fits with a solid line.

reliable fits. However, in about 10% of the cases it was found that the best fit would involve large extrapolations ($\gtrsim$40%), probably due to the adopted conservative cutoff of the surface brightness profile at $\sim$ 3% of the sky level. In these cases, the best fit was usually replaced by the fit obtained fixing the mean sky value and more physically meaningful results were derived.

Figure 3.9 illustrates the results of the profile-fitting procedure showing the three fits considered for two galaxies (as indicated in each panel) in our sample with different D/B ratios. The left panel shows the fits obtained for the light profile measured for a round elliptical galaxy while the right panel shows the light profile of an S0 galaxy. As can be seen both fits are excellent (both are high-quality fits as defined below) once a combination of bulge+disk profile is considered leading to the values of D/B shown in the figure. The FWHM determined from the fits are in reasonable agreement with those measured from stellar profiles on the respective galaxy frames.

In Figure 3.10 we show the distribution of the difference between the FWHM inferred by the best-fit model of the galaxy and the FWHM as measured from stellar profiles on the image devided by this last quantity. The distribution is peaked around zero

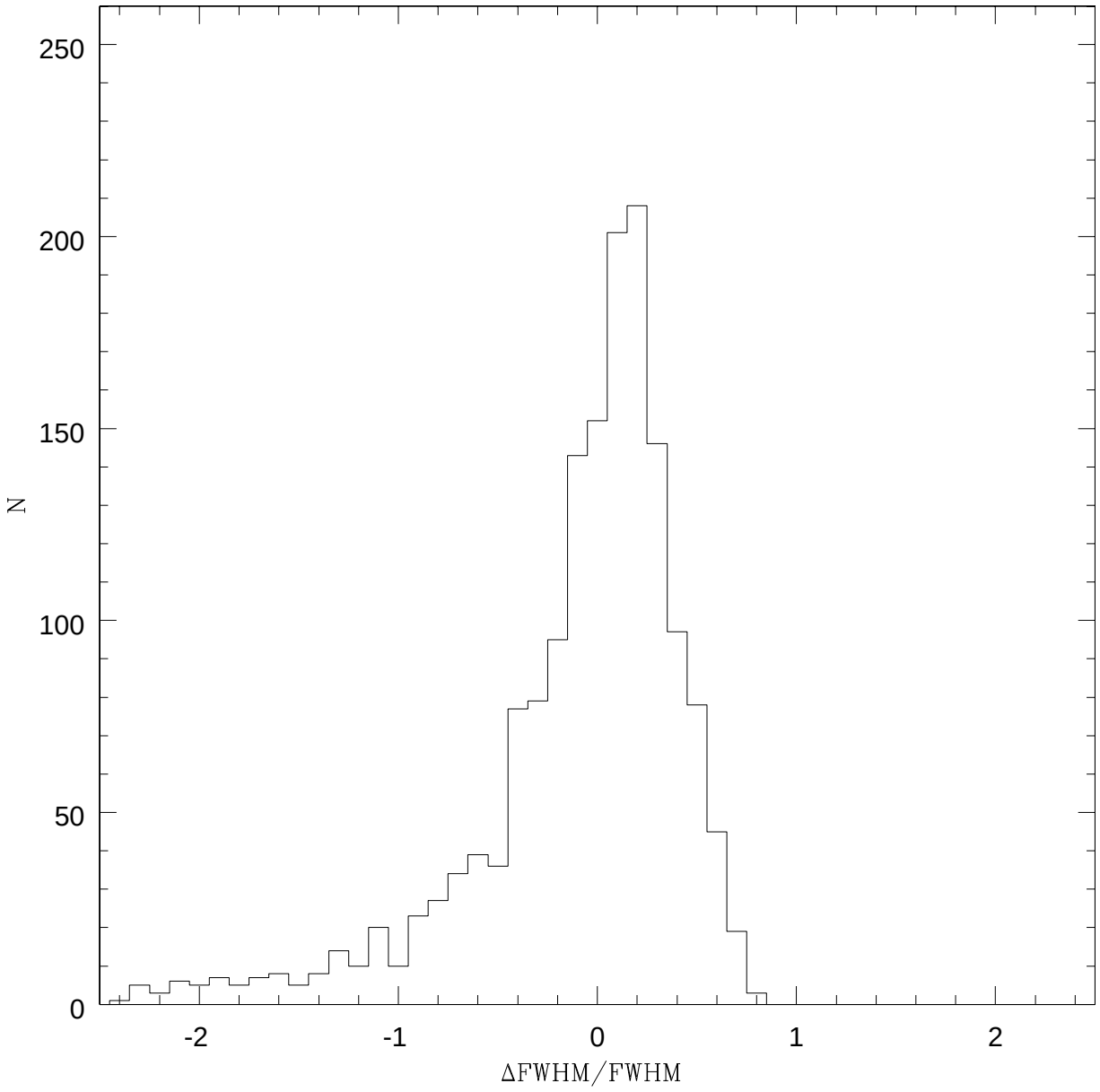

Figure 3.10 The distribution of the difference between the FWHM derived from the fit and the value measured on the frame devided by the measured FWHM.

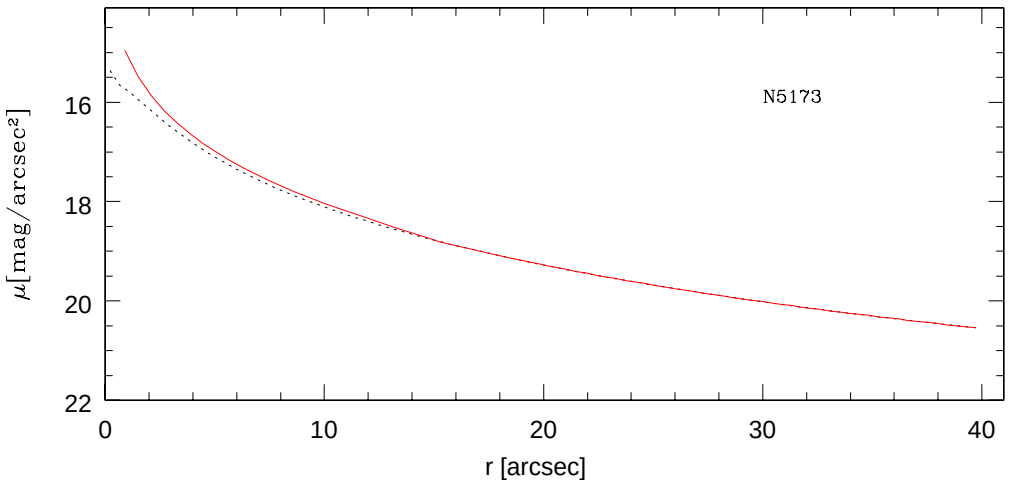

Figure 3.11 Comparison of the mean surface brightness as function of the radius obtained: (dotted line) without taking into account the effects of the seeing; (solid line) using Saglia et al. (1993a) method.

but is skewned towards negative values indicating that, in general, the fitting procedure overestimates that measured on the frame. We note that there is no apparent correlation between difference of the estimated and measured FWHM with the observed FWHM.

The impact of the seeing correction is illutrated in Figure 3.11 which shows the circularized integrated magnitude obtained with and without taking into consideration the effects due to the seeing. In this particular case the galaxy was observed with a seeing of $\sim$ 1.5 arcsec. The effect of the seeing correction is to make the integrated light profile brighter and steeper in the innermost region and as a consequence increase the value of d_n. This correction yields brighter values of $\bar{\mu}_e$ and smaller values of r_e. The effect on d_n can be seen in Figure 3.12 which plots the seeing-corrected values of d_n against those measured in the original profile. As can be seen the correction for the seeing increases the value of d_n but the effect is only important for galaxies with $d_n \sim 10$ arcsec, which in the case of ENEARf affects only very few galaxies. For values of $d_n >$ 10 arcsec it increases by about 2%. Of course, the effect for fainter galaxies in clusters is important with corrections being as large 20%.

A quality parameter Q has been assigned to the resulting fits according to the following criteria (e.g., Saglia et al. 1997): (i) the maximum extent of the profile (r_{max}) compared to r_e; (ii) the influence of the seeing on the galaxy (the FWHM compared

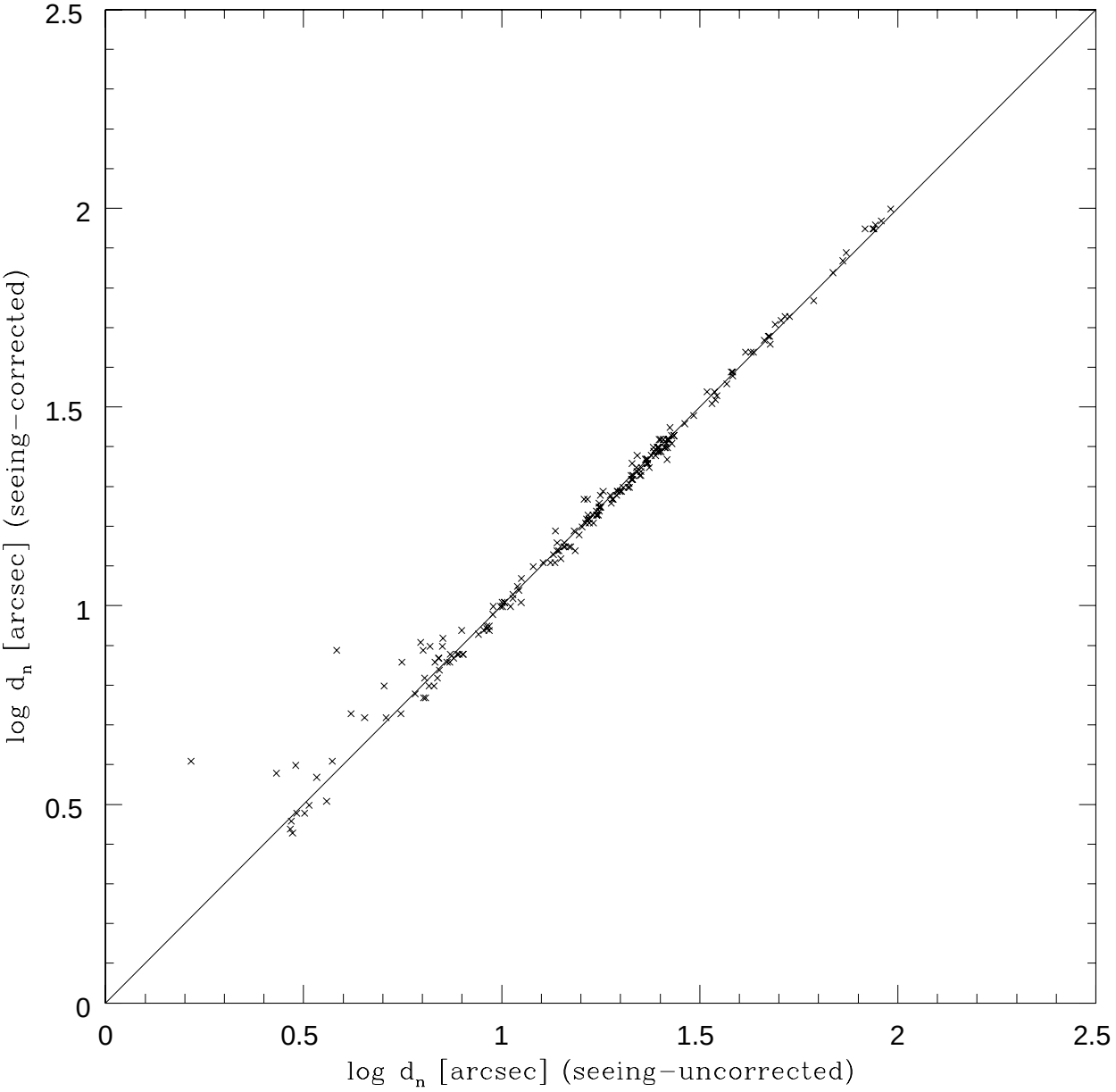

Figure 3.12 Effects of the seeing correction in our $\log d_n$ values. It is shown a comparison between $\log d_n$ uncorrected and corrected by seeing effects.

to r_e); (iii) the value of the integrated galaxy S/N; (iv) the galaxy surface brightness relative to the sky level; (v) the uncertainty of the sky determination; (vi) the amount of extrapolation (the fraction of the total light derived by the extrapolation of the profile beyond the r_{max} of the data points) used to compute the total magnitude m_{tot}; (vii) the goodness of the fit as measured by the reduced χ^2. The overall quality of the fit ranges from excellent (1) to adequate (3) and it is determined from the relative importance of the various criteria described above. Using Monte-Carlo simulations of model observations, with the characteristics of the EFAR sample, Saglia et al. (1997) were able to relate the values of Q to the errors of the global photometric parameters. Profile fits with $Q = 1$ lead to the following errors: 1) m_{tot} of $\lesssim$0.05 mag; 2) $r_e \lesssim 10\%$; $\log d_n$ and FP defined as $\log r_e$-0.30$\bar{\mu}_e$ $\lesssim 0.005$. For $Q = 2$ the errors in these quantities are: $\lesssim$0.15 mag, $\lesssim 25\%$ and $\lesssim 0.01$. For $Q = 3$ the errors are large and the results should be considered tentative. In our case we have adopted the same definition for all Q parameters except that associated to the χ^2 of the fit which had to be renormalized to the S/N of our data to benefit from Saglia et al. simulations.

While we use the Q-parameter as an indication of the quality of the fits and of the global photometric parameters the errors associated to these parameters have been estimated also taking into account the scatter of the comparisons of our repeated observations of the same galaxy. The accuracy of these errors are then assessed by comparison with data of other authors.

To illustrate fits of different qualities in Figure 3.13 we show the observed light profile of four galaxies together with their two-component fits. Note that evident differences between the observed light profile and the fit is seen only in the case of Q=3. This shows the stringent criteria adopted in qualify the fitting profiles. We also show the poor quality fit ($Q = 3$) obtained for a galaxy classified as an S0 (T=-2) but which shows, from the inspection of the image, clear evidence of the presence of spiral arms and a huge bar therefore being a case of misclassification. This galaxy as well as other similar cases showing large deviations from the fits are indicated in the final photometric catalog presented below. These cases represent, in general, galaxies which have wrong morphological types assigned to them in the original catalogs.

3.3.3 Results

Figures C.1 - C.3 in Appendix C show the results of the profile-fitting analysis for the three sub-samples considered in this work: the magnitude and redshift-limited ENEARf (1044 galaxies); faint and/or more distant cluster galaxies (96 galaxies); and the remaining observed galaxies which include early-type galaxies not in clusters and not satisfying the selection criteria of the ENEARf sample (129 galaxies). This set includes misclassified spirals and interacting galaxies. We show these samples separately because they represent different pupulations with different overall characteristics for the fits. For this reason, below we only consider the first two "homogenous" sub-samples to characterize the results of the fit in terms of the type of profile and quality of the fit.

In these figures we show for each galaxy: (i) in the upper panel the observed light profile (small dots) and the best-fit bulge and/or disk model (solid lines) as function of $r^{1/4}$. The large vertical line marks the derived value of r_e, while the small vertical line the maximum extent of the profile, r_{max}. The horizontal dashed line is the intensity corresponding to 1% of the sky. In the case of multiple observations the sky value is

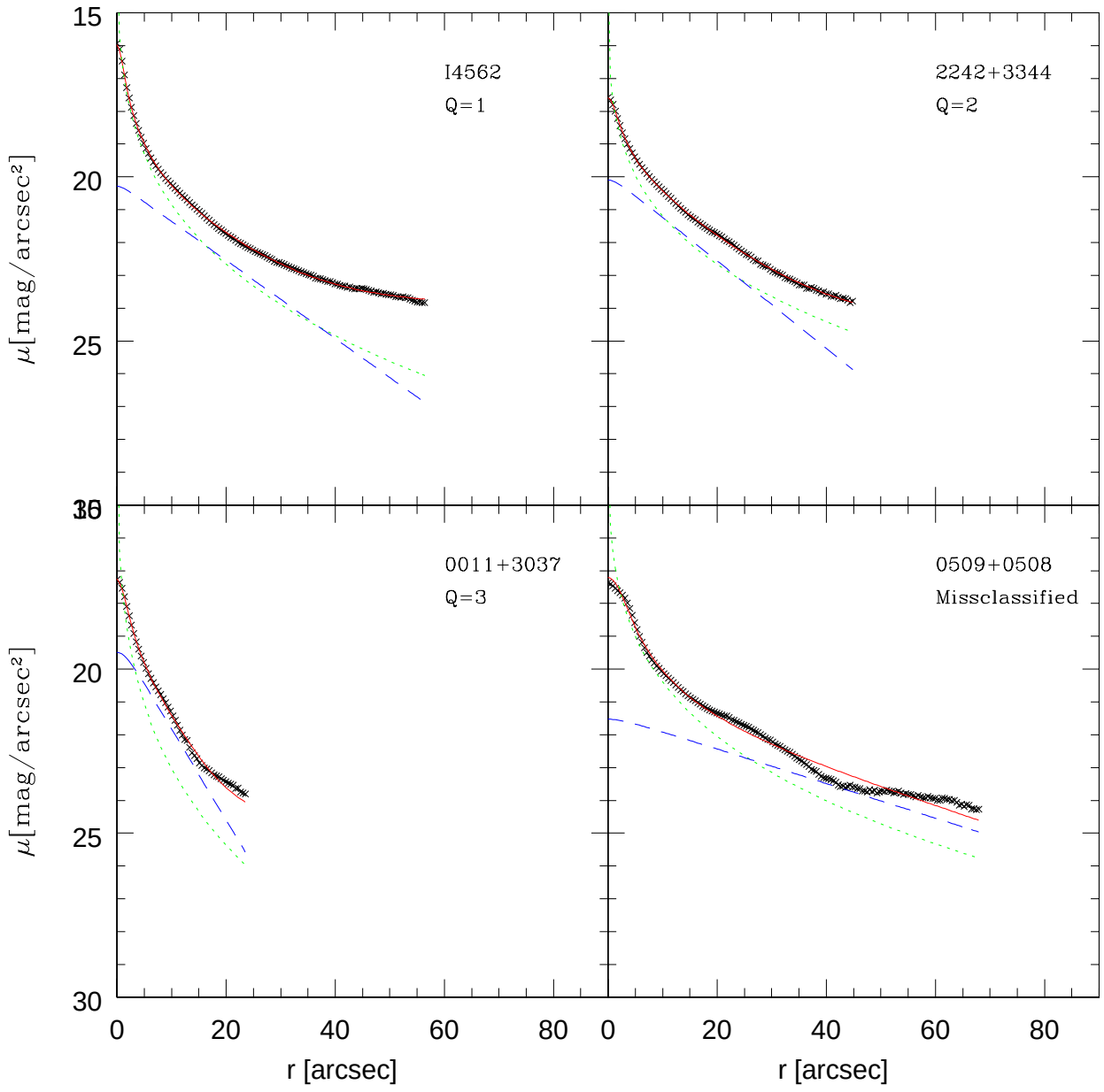

Figure 3.13 Examples of the light profile fitting of different quality. Q=1 is the best quality while Q=3 is the worst. The light profile of a galaxy (0509+0508) classified S0 (T=-2) but showing presence of arms and a bar is also shown. In these plots, the $r^{1/4}$ fit is indicated with a dotted line, the exponential fit with a dashed line, and the combination of the two fits with a solid line.

taken from the image where the profile reaches the largest distance from the center. The value of r_e (in arcsec), the total $R-$band magnitude, and the D/B ratio are also given in lower left corner of each panel, while in the upper right corner we give the name of the galaxy; (ii) in the lower panel the difference $\mu_{obs}(r) - \mu_{fit}(r)$ (small dots) and the difference in the total magnitudes within a radius r (solid line) as computed from the image and from the fitted profile. The observed profiles were calibrated, K-corrected, corrected for galactic extinction and for the cosmological surface brightness dimming. For galaxies with multiple observations all the available profiles are presented.

For the ENEARf sample we find that $\sim 10\%$ of the galaxies are well represented by a pure $r^{1/4}$ law while 89% are best fitted by a two-component model, with 75% of the cases having $D/B < 1$. These results are in contrast with the original morphological classification of the galaxies, for which about 26% of them are ellipticals. This is a further indication that the classification available from the original catalog is not reliable and that it should not be used to define sub-types of the early-type population in any detailed analysis of their properties. Furthermore, we note that the sample also includes disk-dominated galaxies, with 8 galaxies having $D/B > 20$ and at least one case, the edge-on galaxy 358 G 25, for which the best fit is a pure exponential disk. For this sample about 24% of the fits to the galaxy profiles have a quality $Q = 1$, 30% $Q = 2$ and 46% $Q = 3$. The main cause for the $Q = 3$ fits are associated to the isophotal level the profiles were truncated for analysis, which impacts the Q of the sky correction and the Q of the correction required in computing the total magnitude of the galaxy due to the large extrapolation in radius. If these two Qs were discarded, from all the other conditions over 60% of the fits would have $Q = 1$. We expect in the future to re-analyze all the available profiles relaxing the condition imposed in the maximum extent of the light profile, for which we have adopted a conservative cutoff at an error of $\sim 3\%$ of the sky. Other poor fits ($\lesssim 30\%$) are caused by the presence of features in the light profiles in excess to the bulge-disk models. In some cases, this is an indication either for the presence of dust lanes, bars, rings and spiral arms or contamination by nearby galaxies or stars. In particular, Q_{χ^2} serves as an indicator of significant deviations of the light profile from the model fits which may impact the derivation of global parameters and its value is listed in the final photometric table presented below (Section 3.5).

For the sample of cluster galaxies not in the ENEARf we find a higher percentage (36%) of elliptical galaxies. For about 15% of the galaxies the fits have $Q = 1$, for 32% $Q = 2$ and the remaining $Q = 3$.

The parameters that characterize the quality of the fits to the observed early-type galaxies light profiles and the galaxy population as a whole are summarized in Figure 3.14 for the two homogenous populations described above, namely ENEARf (solid line) and faint/distant cluster galaxies (dashed line). The figure shows the cumulative distribution for: (a) the quality parameter Q of the fit; (b) the quantities Q_{χ^2} associated to goodness of the fit as measured by the reduced χ^2; (c) the logarithm of the disk-to-bulge ratio; (d) the maximum extent of the profile (r_{max}) compared to r_e; (e) the ratio between the half-luminosity radius and the seeing FWHM; (f) the logarithm of the reduced χ^2 of the fit; (g) the ratio of the galaxy to the sky flux within the effective radius; and (h) the logarithm of the total signal-to-noise ratio of the profiles.

From the figure one finds significant differences between the ENEARf and the faint cluster galaxies. The quality of the light profiles of the ENEARf galaxies is more affected by the cutoff we have applied to the profiles (panel a and b). Indeed, the percentage

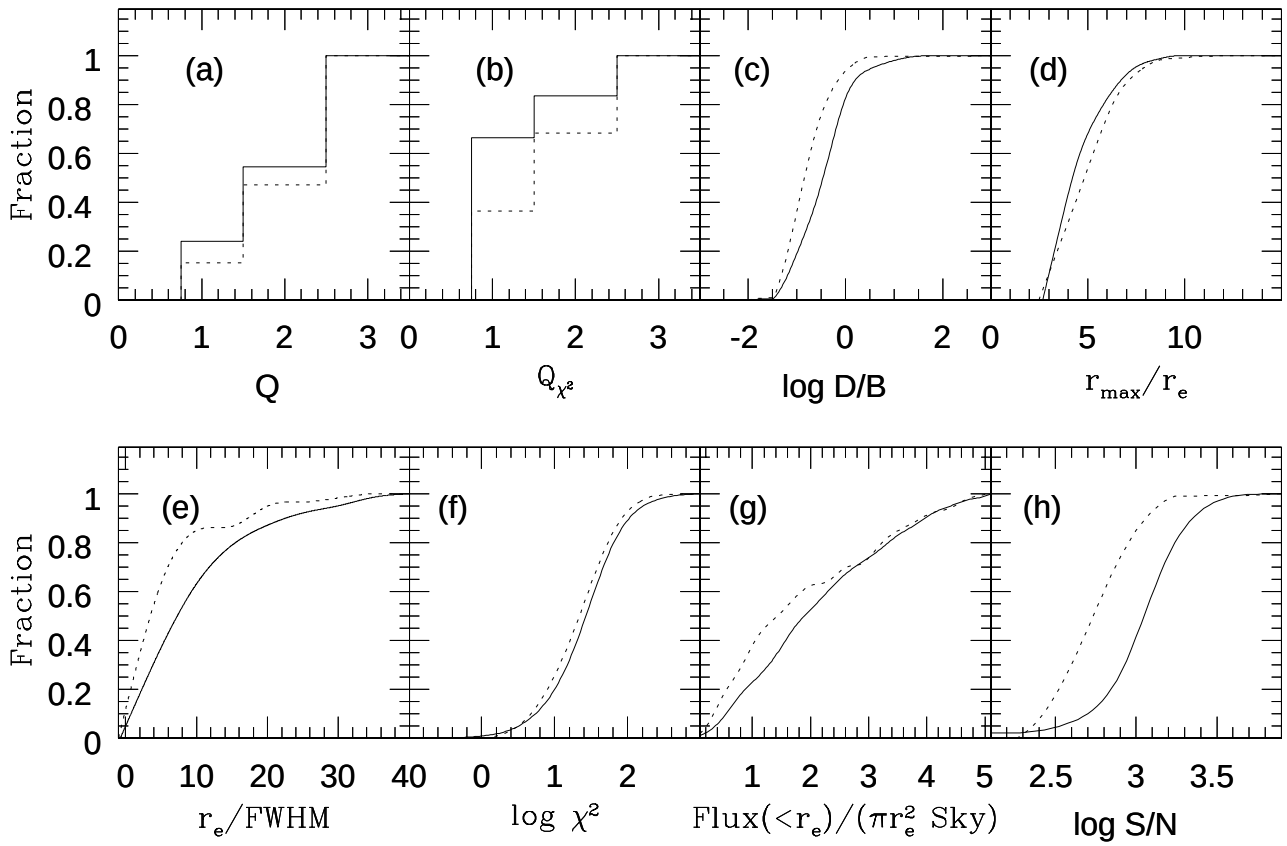

Figure 3.14 Global properties of the fits: (a) the quality parameter Q of the fit; (b) the quantities Q_{χ^2} associated to goodness of the fit as measured by the reduced χ^2; (c) the logarithm of the disk-to-bulge ratio; (d) the maximum extent of the profile (r_{max}) compared to r_e; (e) the ratio between the half-luminosity radius and the seeing FWHM; (f) the logarithm of the reduced χ^2 of the fit; (g) the ratio of the galaxy to the sky flux within the effective radius; and (h) the logarithm of the total signal-to-noise ratio of the profiles.

of galaxies with $Q_{\chi^2} = 1$ is significantly larger for the ENEARf sample than for faint cluster galaxies, while the percentage of galaxies with $Q = 1$ is almost comparable for the two sub-samples. Furthermore, the faint cluster galaxies tend to have smaller D/B (panel c), higher surface brightness (panel g), and as expected smaller S/N (panel h). From the plots one can also easily explain that for cluster galaxies the quality of the fit is on average worse than in the case of bright galaxies in ENEARf, since the smaller galaxies in general are more affected by seeing (panel e). On the other hand, the cluster galaxies form, as expected, a more uniform sample leading to slightly better fits as shown in panel (f) and require smaller extrapolations (panel d).

These plots should be compared to those presented in Saglia et al. (1997) for the EFAR sample of very distant clusters out to $\sim$ 18,000 kms^{-1} . The differences in the samples considered are underlined by panels (c) and (e) which indicate the difficulties of selecting true ellipticals at large distances and the strong effects that seeing may have in the results of fainter objects in contrast to the nearby samples.

3.4 Global parameters

Figures 3.15 and 3.16 show the global photometric parameters derived directly from the images and from the fits of the galaxy light profile for the two "homogenous" sub-samples described above. The figures show: in panel (a) the distribution of d_n in arcsec; in panel (b) the distribution of r_e also in arcsec; in panel (c) the surface brightness distribution; in panel (d) the distribution of the total R-magnitudes; in panel (e) the relation between the B magnitudes, taken from the literature, and R magnitudes measured from our data; and finally in panel (f) the $(B - R)$ color.

Comparison of the two figures clearly show the differences between the samples. As can be seen from panel (d) the ENEARf has a reasonably well-defined limiting magnitude comprising galaxies brighter than $R = 13.0$. This limit is in good agreement with the magnitude-limit adopted in the B-selected sample, the color distribution intrinsic to the early-type galaxies (panel f) and the errors associated to the B-band magnitudes, which can be as large as 0.5 mag (Alonso et al. 1993). Note that while there is a linear relation between the B and the R magnitudes the scatter is large especially at the faint end. On the other hand, the cluster galaxies are primarily fainter ($R \gtrsim 12$) and have a less defined B magnitude as can be seen from panels (e) and (f) of Figure 3.16. The angular size of the galaxies in the ENEARf (panels a and b), as measured either by d_n or r_e, is large with a median of $\sim$ 22 arcsec and $\sim$ 13 arcsec, respectively. As discussed before, this means that the results for this sample are not extremely sensitive to seeing effects, in contrast to those of the cluster sample shown in Figure 3.16 with median values of d_n and r_e of about 9 and 6 arcsec, and with an extended tail towards smaller values. The width of the distribution is because the sample is not magnitude limited, thus galaxies can cover a wide range of physical sizes. Finally, as expected the distributions of the mean effective surface brightness are similar having a peak at $\sim$ 19.5 mag arcsec^{-2}.

3.4.1 Error estimates

The errrors in the global photometric parameters such as d_n, r_e, $\bar{\mu}_e$, and m_{tot}, were estimated by Saglia et al. (1997) using numerical simulations from which they associated

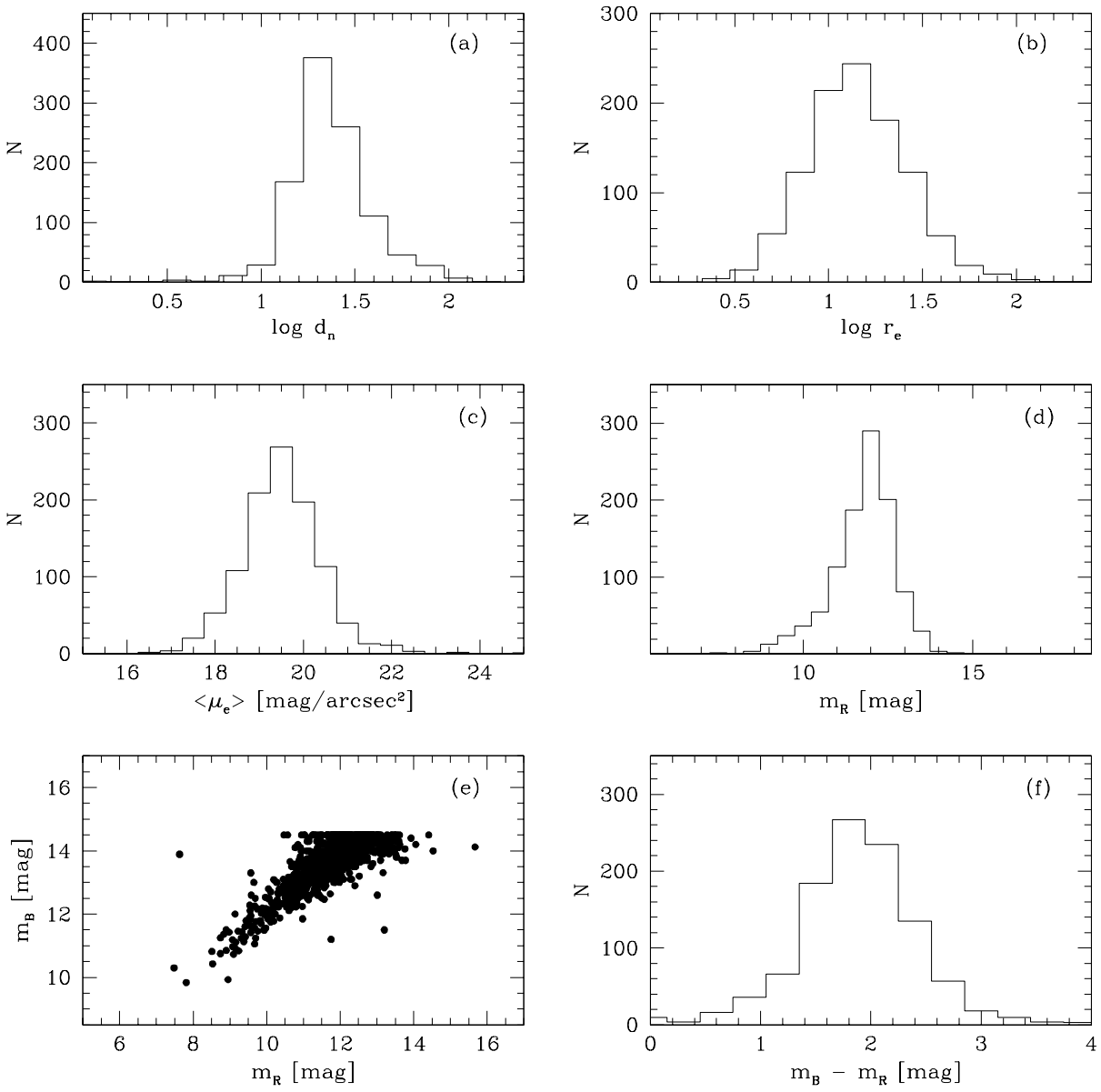

Figure 3.15 The distribution of the derived photometric parameters for the ENEARf sample. The parameter d_n is given in arcsec for a better comparisons with r_e. The lower left panel shows the B-band versus the R-band total magnitude and the right panel the distribution of the color B-R.

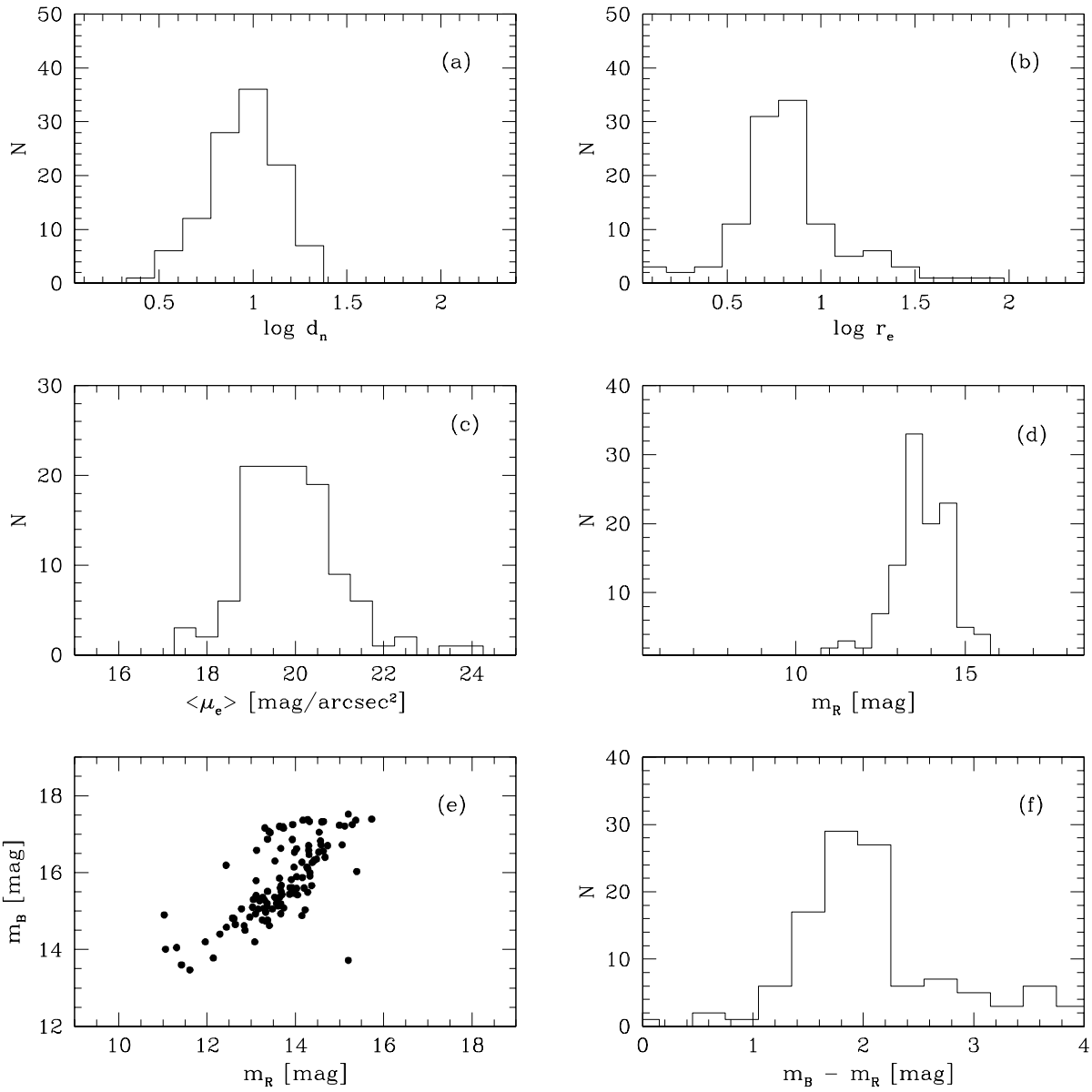

Figure 3.16 The same plots of Figure 3.15 for the faint/distance cluster galaxies.

typical errors with the quality parameter Q. However, as we have seen before the Q for our profiles tend to be higher than those obtained by these authors because of the brighter isophotal limit adopted for the fits. Therefore, we have instead compared the results of multiple observations to estimate the amplitude of our internal errors, re-scaling the original values given by Saglia et al., based on the quality parameter Q, to the scatter measured from the comparisons.

For each value of d_n an error was computed taking into account the uncertainty associated to the quality parameter Q and the rms scatter σ_{d_n} measured from multiple observations of galaxies observed using the same setup. We assume that the galaxies being compared have the same distribution of Q values of the sample as a whole with the majority having $Q = 3$. Therefore, the error for a given galaxy observed in a given setup is given by the original estimate of Saglia et al. multiplied by the factor of $\sigma_{d_n}/0.03$, where the scatter is related to that specific setup and 0.03 is the error associated to the value of $Q = 3$ (see Section 3.3.2). The same procedure was applied to derive the uncertainty associated with all other parameters of interest.

It is important to point out that the above errors do not include the contribution from errors associated to the photometric calibration. To estimate the impact on the errors we have resorted to a Monte-Carlo simulation, whereby different light profiles, covering a range of magnitudes and D/B were selected from the observed sample. For each galaxy 100 new profiles were generated by shifting the zero-point by a random offset drawn from a Gaussian distribution with a dispersion equal to the estimated zero-point error of the standard stars. For each of these simulated profiles the photometric parameters were derived and their mean and scatter were computed. This was done for a range of rms values up to 0.05 mag, the value adopted by us to be considered a photometric night. Figure 7.7 shows the value of the scatter of d_n for each type of galaxy profile used as a function of the photometric zero-point error. As can be seen the errors in d_n depend, as expected, on the type of profile being considered and that zero-point errors lead to uncertainties in d_n which are comparable to those estimated for high quality profiles. Therefore, these values should be regarded as a lower limit to the true errors. We associated the value of the errors computed from the quality of the fit and the scatter of the internal comparisons to the error of our global parameters, only if they are larger than the uncertainty of the photometric solution.

As an illustration, we show in Figure 3.18 the error distribution of our measurements for $\log d_n$, $\log r_e$, $\bar{\mu}_e$, and m_{tot} for all measured galaxies in ENEARf.

3.4.2 Homogeneization of the data

Since we are primaly interested in constructing a homogeneous data set of global paramaters to be used in the derivation of scaling relations, any residual systematic relative shifts in our calculated parameters were removed using the values obtained from multiple observations of the same galaxies. We use the measurements obtained from images taken at ESO with setups 4 and 5 (Tab.3.2) as our fiducial system. These setups were chosen because the largest number of repeated observations were observed with these setups using the same telescope, similar detectors which provide a large field of view and the best resolution.

To determine the "fiducial" system we corrected our photometric parameters using the mean difference Δy_i of the measurements of run i with all the other runs $j \neq i$

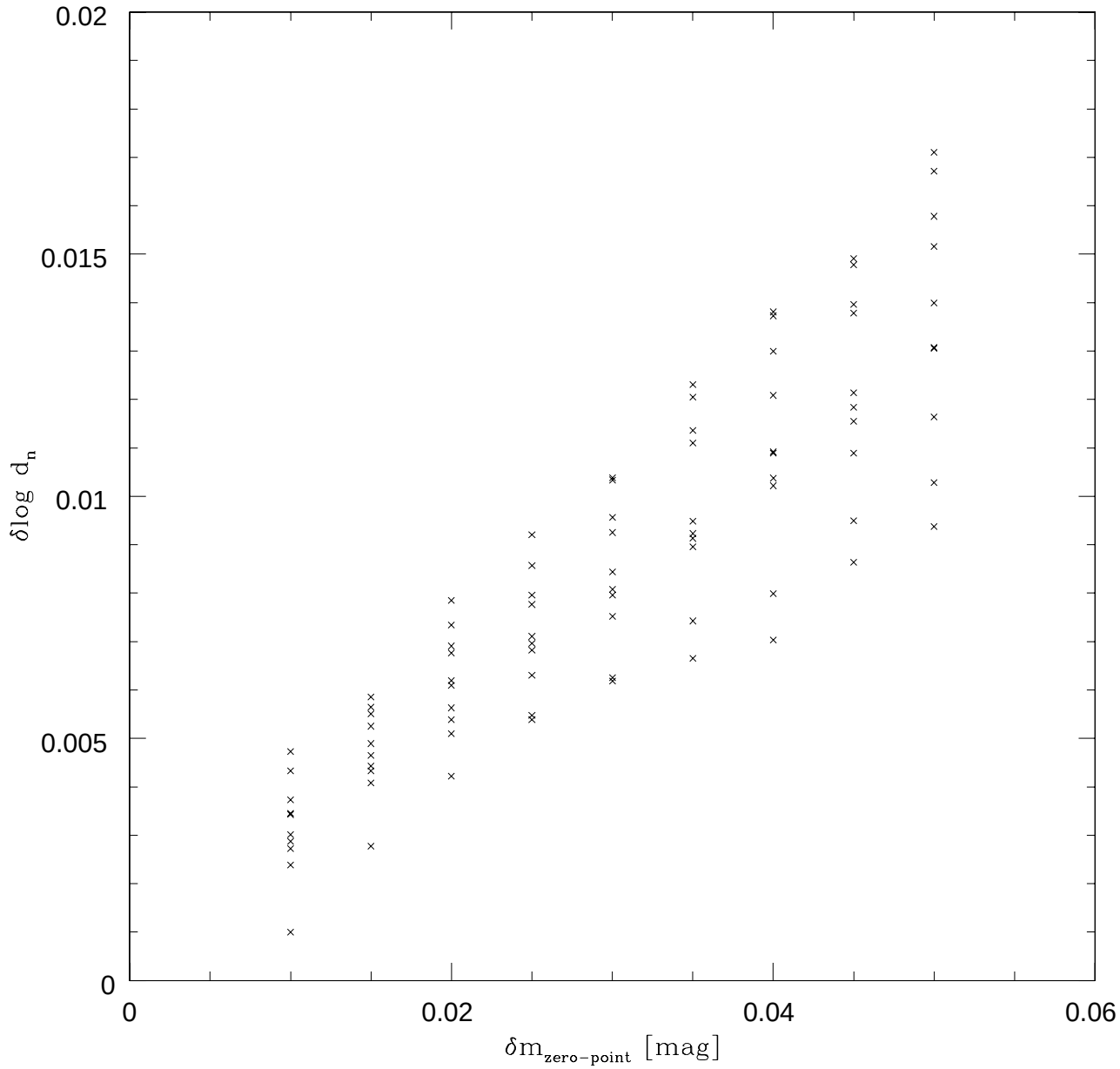

Figure 3.17 The *rms* scatter of $\log d_n$ obtained from Monte-Carlo simulations using 10 different types of galaxy profile, versus the photometric zero-point error.

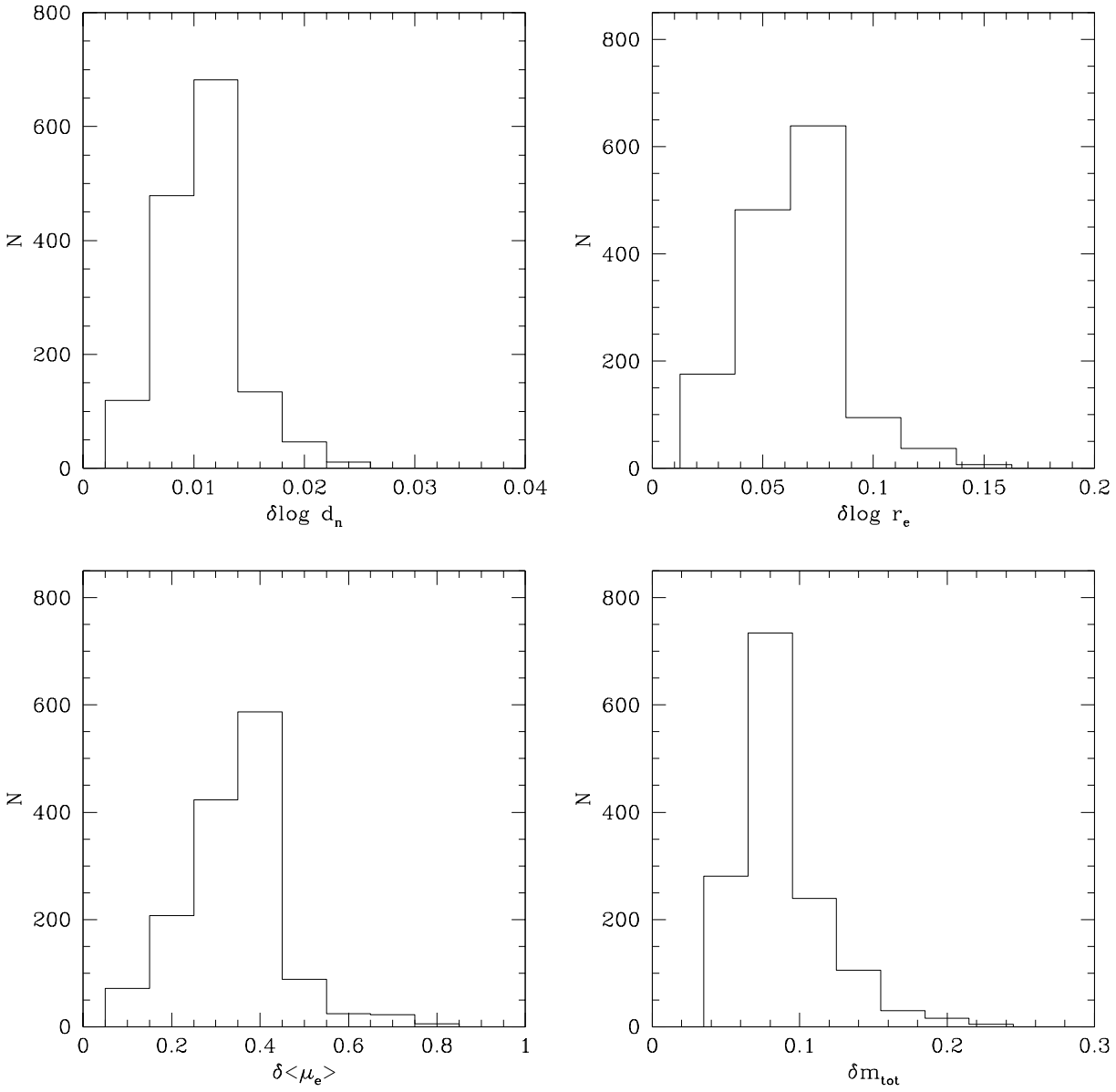

Figure 3.18 The distribution of the uncertainty of the global parameter $\log d_n$, $\log r_e$, $\bar{\mu}_e$, and m_{tot} versus the value of the parameter for all images in our sample.

for galaxies in run j in common with those in i. This offset is computed with variance weighting using the estimated errors in each measurement:

$$\Delta y_i = \epsilon_i^2 \sum_{j \neq i} \sum_{k \in i,j} \frac{y_{ik} - y_{jk}}{\Delta y_{ik}^2 + \Delta y_{jk}^2} \tag{3.8}$$

Here k runs over the galaxies in common to runs i and j, and y_{ik} corresponds to the measurement of the global photometric parameter considered for galaxy k in run i and ϵ_{ik} is the estimated error. The standard error in the mean, ϵ_i, is given by:

$$\epsilon_i = \left(\sum_{j \neq i} \sum_{k \in i,j} \frac{1}{\Delta y_{ik}^2 + \Delta y_{jk}^2} \right)^{-1/2} \tag{3.9}$$

We determined the most significant offset by finding the run with the maximum value $\Delta y_i / \epsilon_i$, and iterated towards a common zero-point by subtracting this offset from the measurements of run i. We halted the process when the most significant offset was $\Delta y_i / \epsilon_i < 2$. After three iterations the systematic offsets required to create a homogeneous fiducial data set were determined. In general, we found good agreement between the photometric parameters measured from repeated observations. The corrections required to bring them into a common system were relatively small: $\Delta log\, d_n \lesssim 0.010$, $\Delta \bar{\mu}_e \lesssim 0.1$ mag, and $\Delta log\, r_e \lesssim 0.03$. In this process we discarded galaxies which exhibited peculiarities in their profiles as indicated in the comments of Tables 3.9- 3.11. Typical cases include galaxies with other compoments besides a disk and a bulge or galaxies contaminated by the light of nearby stars or galaxies.

After defining this standard system, global parameters derived from observations obtained at MDM and FLWO were also calibrated to it. For runs with a significant number of galaxies in common with our reference system, the measured values were directly compared to it, while others runs were compared to the calibrated measurements for the same telescope. The number of internal multiple observations available for each site are shown in Table 3.7. The corrections required for all data sets were small zero-point shifts, typically: $\Delta log\, d_n \lesssim 0.003$, $\Delta \bar{\mu}_e \lesssim 0.04$ mag, and $\Delta \log\, r_e \lesssim 0.010$. These corrections are comparable to those found in determining the reference system.

In Figure 3.19 and Figure 3.20 we compare the global parameters of our repeated observations after applying the zero-point corrections. In both figures we show, from top to bottom, the differences of the calibrated measurements of $\log d_n$, $\log r_e$, $\bar{\mu}_e$, FP and the total magnitude. In Figure 3.19 each column corresponds to the comparison of galaxies observed at different sites (see figure caption). The overall comparison combining all the repeated measurements is shown in Figure 3.20. The quantitative results of these comparisons are summarized in Table 3.7 which gives: in column (1) the site; in column (2) the number of repeated measurements N_c in that site or in common with our standard system; in column (3) the mean offset and its error of $\log d_n$; in column (4) its scatter. In the remaining columns the same information is given for $\log r_e$, $\bar{\mu}_e$, FP and total magnitude m_R.

Once the photometric data are in the same system, it is possible to combine repeated measurements of each parameter to produce a final value which is given by the error-weighted mean of the measurements available. We point out that for the parameters r_e and $\bar{\mu}_e$ we combined only those measurements which differ less than 1σ. The total magnitude m_R associated to a galaxy was computed after to have determined the above

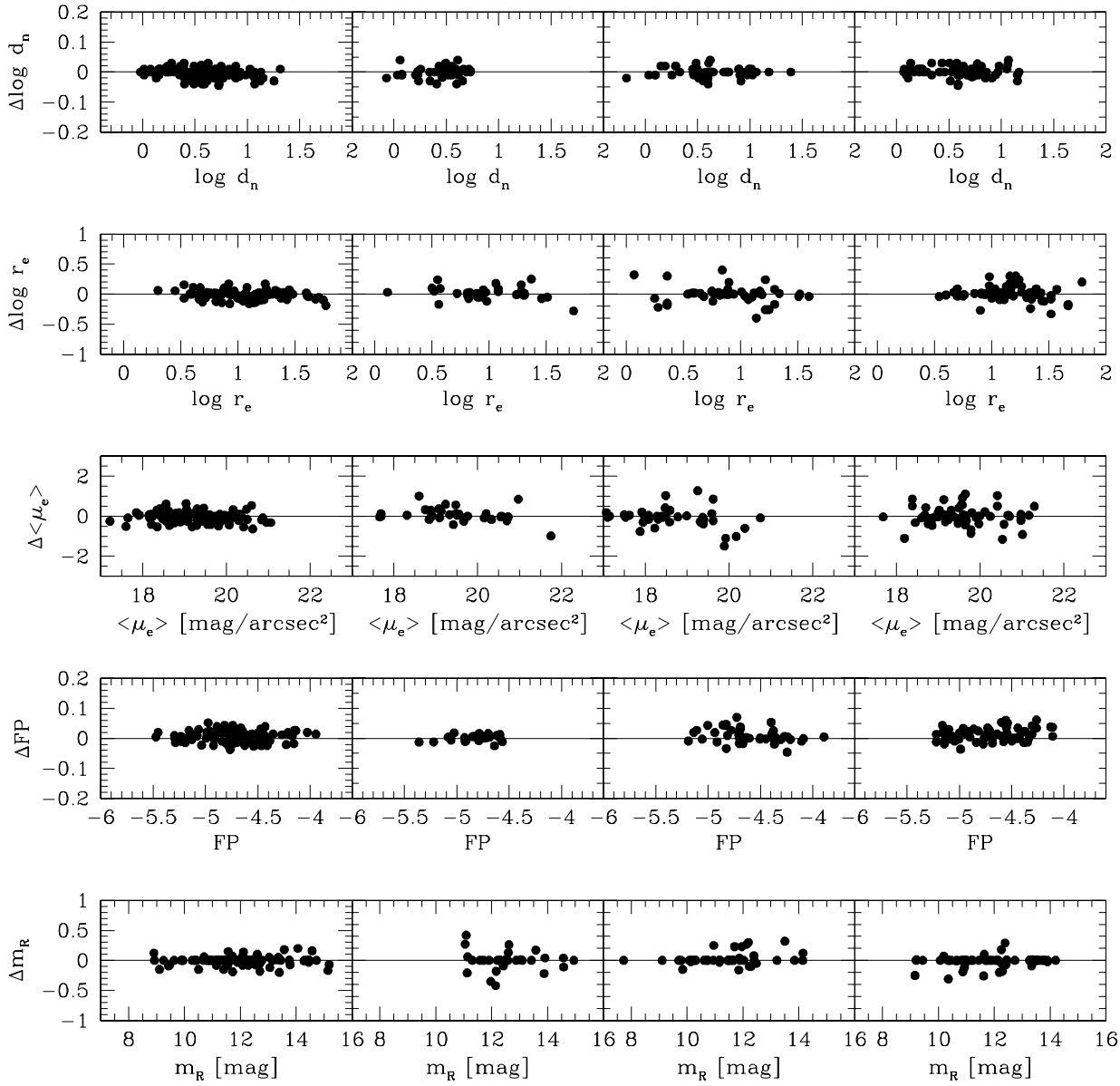

Figure 3.19 Internal comparisons of $\log d_n$, $\log r_e$, $\bar{\mu}_e$, and FP derived from data observed at ESO (left panels), at MDM (middle panles), and at FLWO (right panels).

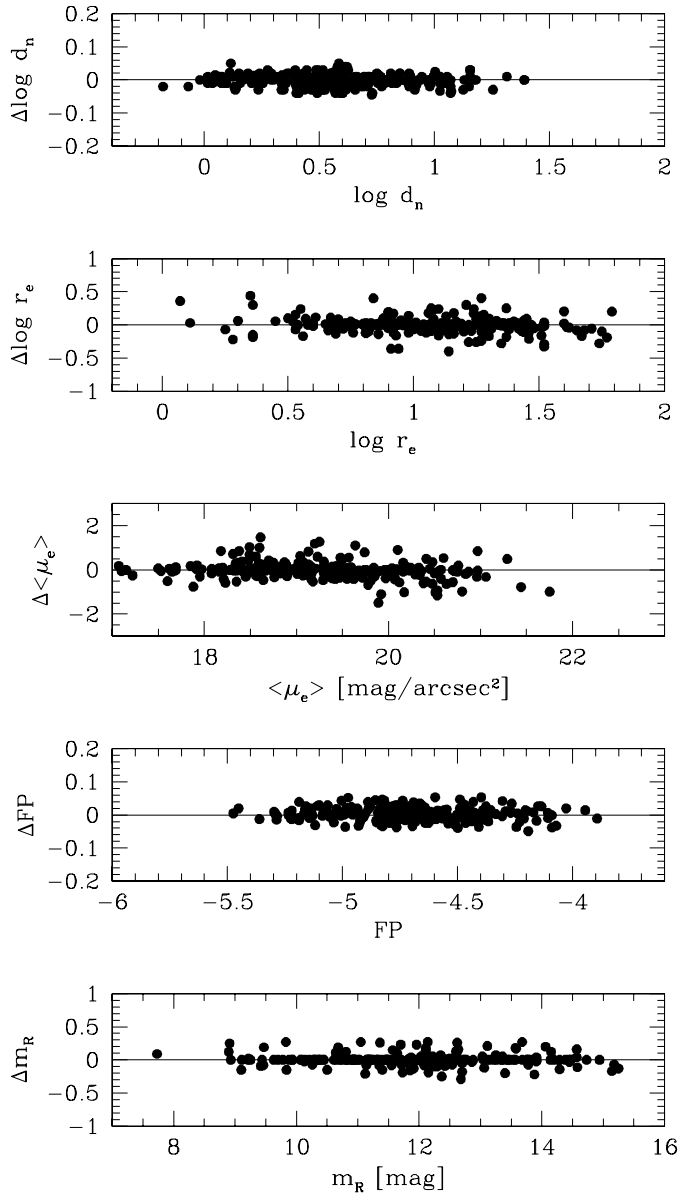

Figure 3.20 The overall internal comparison of $\log d_n$, $\log r_e$, $\bar{\mu}_e$, and FP derived from data. Δ means a difference between each result obtained from different observations and the mean value associated to the galaxy.

TABLE 3.7

INTERNAL COMPARISONS OF THE HOMOGENEIZED GLOBAL PARAMETERS

Site	N_c	$\Delta log\, d_n$	$\sigma_{log\, d_n}$	$\Delta log\, r_e$	$\sigma_{log\, r_e}$	$\Delta\bar{\mu}_e$ mag/arcsec^2	$\sigma_{\bar{\mu}_e}$ mag/arcsec^2	ΔFP	σ_{FP}	Δm_R mag	σ_{m_R} mag
(1)	(2)	(3)	(4)	(5)	(6)	(7)	(8)	(9)	(10)	(11)	(12)
ESO	145	-0.003±0.002	0.016	-0.008±0.006	0.067	-0.041±0.023	0.246	0.005±0.002	0.019	-0.011±0.007	0.070
MDM	54	-0.002±0.002	0.014	0.007±0.018	0.100	0.031±0.062	0.347	0.001±0.002	0.012	0.005±0.020	0.120
FLWO	60	-0.003±0.002	0.016	-0.014±0.022	0.146	-0.088±0.080	0.538	0.009±0.003	0.024	0.030±0.021	0.100
CTIO	71	0.001±0.002	0.017	0.010±0.018	0.109	0.020±0.068	0.405	0.004±0.002	0.014	-0.016±0.016	0.090
All	365	-0.002±0.001	0.017	-0.005±0.006	0.086	-0.020±0.021	0.305	0.002 ± 0.001	0.019	0.004±0.006	0.091

TABLE 3.8

EXTERNAL COMPARISONS OF THE GLOBAL PARAMETERS

Sources	N_c	$\Delta log\, d_n$	$\sigma_{log\, d_n}$	$\Delta log\, r_e$	$\sigma_{log\, r_e}$	$\Delta\bar{\mu}_e$ mag/arcsec^2	$\sigma_{\bar{\mu}_e}$ mag/arcsec^2	ΔFP	σ_{FP}
(1)	(2)	(3)	(4)	(5)	(6)	(7)	(8)	(9)	(10)
LC	34	0.005±0.004	0.023	–	–	–	–	–	–
7S	158	0.006±0.002	0.024	–	–	–	–	–	–
D	31	0.010±0.003	0.016	–	–	–	–	–	–
JFK	121	-0.004±0.002	0.013	-0.020±0.012	0.139	-0.037±0.046	0.509	-0.002±0.002	0.021
Lc	13	-0.007±0.004	0.016	–	–	–	–	–	–
S	12	-0.001±0.005	0.019	0.099±0.069	0.242	0.424±0.250	0.870	-0.013±0.012	0.042

NOTE.—All differences are "our measurement" - "literature measurement". The reference are: LC: Lucey & Carter (1988); 7S: Faber et al. (1989); D: Dressler et al. (1991a,b); JFK: Jørgensen, Franx, & Kjaergaard (1995a); Lc: Lucey et al. (1997); S: Smith et al. (1997).

combined parameters and not as a combination of different measurements. The final combined values for the global parameters are listed in the photometric catalog given below.

3.4.3 External comparisons

In order to evaluate our internal error estimates we use the measurements for the global photometric parameters obtained from galaxies in common with other authors. Altogether there are 337 such galaxies in our sample which are in common with six different authors. For some cases we have as many as 188 galaxies in common.

Figure 3.21 shows the comparison of our photometric parameters with those obtained by other authors. The different symbols representing the different data sets are given in the figure caption. Because the errors in the parameters r_e and $\bar{\mu}_e$ are strongly correlated (Jørgensen et al. 1996) and are sensitive to details of the procedure adopted in the fitting of the light profile, we also present the comparison of the FP which actually enters in the distance relation of the Fundamental Plane. We note that not all parameters are available from all the authors, especially in the case of those derived from profile fitting. We note that in this comparison we have also implicitly assumed that the B-band isophotal level adopted, for instance, by the 7S is consistent with that we have adopted in the R-band, as well as the other passbands used by the different authors. Despite all of these potential sources of problems, in the comparison we find a remarkably small scatter in all the parameters, with perhaps the exception of Smith et al. (1997). The results of the individual comparisons are presented in Table 3.8. For d_n in all cases the observed scatter is consistent with our internal error estimates, if we assume that the amplitude of our errors and those of the other authors are comparable. We note that for d_n the largest scatter are from the 7S and Lucey & Carter (1988). By contrast, the comparison with more recent data, such as those of JFK is excellent. The agreement is also good with respsect to the parameters that define the FP, at least in the of JFK with whom we have an extensive overlap. In the case of Smith et al. (1997) the comparison is poor but the number of galaxies in common is small, primarily of bright galaxies, for which a simple bulge model was used. These various factors may account for the very large scatter observed.

Finally, we point out that there are small zero-point offsets in all parameters, which should have a contribution from the different optical filters used in the different sets of observations. In order to allow us to use the public data these offsets are removed as described in Chapter 5. This homegenization is essential as we intend to use available data in the literature to improve the completeness of the ENEARf, to enlarge the ENEARc cluster sample (Chapter 5), and to decrease the errors in the parameters of interest by combining data from multiple observations and external data. Data sets such as those of 7S and JFK are particularly useful as they comprise the largest available data sets.

3.5 The photometric catalog

In Tables 3.9 - 3.11 we present the final tables of the global photometric parameters derived from the analysis of our data for the three sub-samples of observed galaxies: 1) ENEARf (1047 entries); 2) the set of faint and/or more distance cluster galaxies

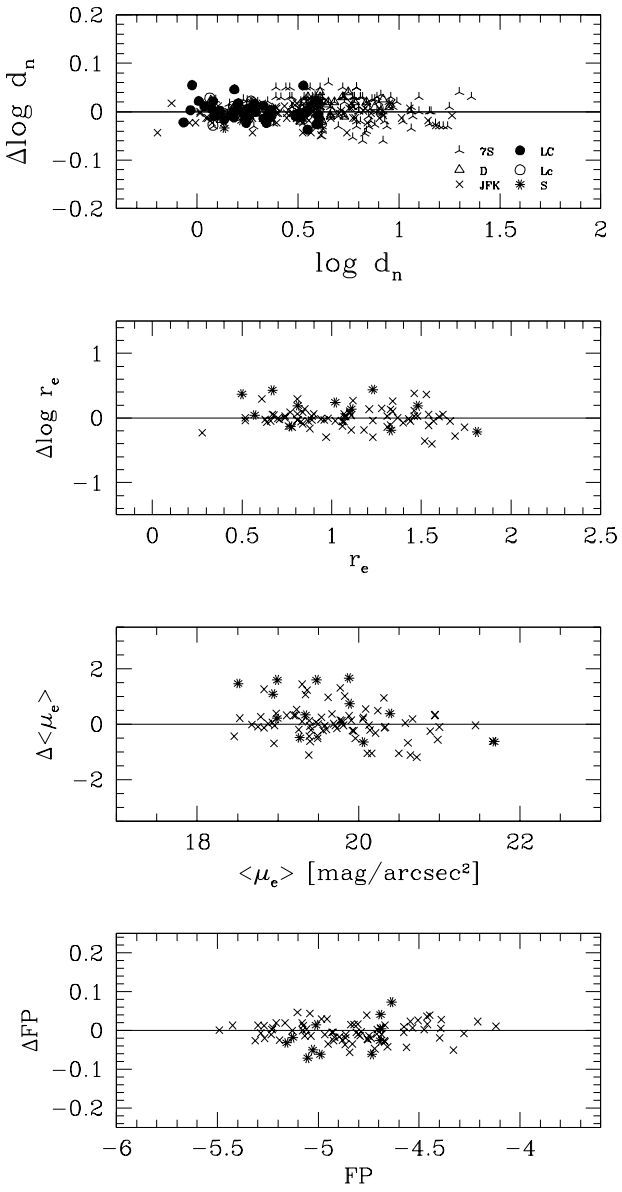

Figure 3.21 The overall external comparison of $\log d_n$, $\log r_e$, $\bar{\mu}_e$, and FP derived from our data. Δ means "our-literature" measurements. The literature sources are: LC, Lucey & Carter (1988); 7S, Faber et al. (1989); D, Dressler (1987), Dressler et al. (1991); JFK, Jørgensen et al. (1995a); Lc, Lucey et al. (1997); and S, Smith et al. (1997).

(114 entries); and 3) others (133 entries). The tables give: in column (1) the galaxy identifications from NGC, IC, MCG, Guide Star Catalog (Lasker et al. 1990) or its coordinates whenever none of the latter are available; in columns (2)-(3) the 1950.0 equatorial coordinates; in column (4) the morphological type T parameter (Lauberts & Valentjin 1989); in column (5) and (6) the total m_B magnitude and the heliocentric redshift given by the original catalogs from which our sample was drawn; in column (7) the number of our multiple observations; in coloumn (8) the total $R-$band magnitude; in coloumns (9)-(10) $\log d_n$ (d_n in arcmin/0.1) and its error; in columns (11) and (12), $\log r_e$ (r_e in arcsec) and its error; in columns (13) and (14), $\bar{\mu}_e$ (in mag/arcsec^2) and its error; in coloumn (15) the D/B ratio; in coloumn (16) the FWHM of the point-spread function (in arcsec); in colomn (17) the quality parameter Q_{χ^2}; in column (18) the row number of Table 3.12 which describes, for galaxies showing features in their light profile, the nature of the problem from the examination of their images; and in column (19) galaxies previously observed by other authors are indicated with an asterisk. Here only the first page of the table is presented. The photometric catalog can be retrieved in electronic form upon request.

Table 3.12 lists the most common causes for features observed in the light profiles which may affect the determination of the photometric measurements among which: the presence of spiral arms, dust lanes, interacting galaxies, residual contamination from nearby galaxies or stars, crowded backgrounds, or any other peculiarity. This serves to identify objects that may have to be excluded for analysis requiring reliable photometric parameters listed above, such as the derivation of galaxy distances, one of the primary goals of our imaging survey.

TABLE 3.9

THE PHOTOMETRIC CATALOG OF THE ENEARF GALAXIES

Name	α (1950)	δ (1950)	T	m_B mag	cz_{hel} km/s	N_{obs}	m_{tot} mag	$log\, d_n$	ϵ_{d_n}	$log\, r_e$	ϵ_{r_e}	$\bar{\mu}_e$ mag/arcsec^2	$\epsilon_{\bar{\mu}_e}$ mag/arcsec^2	D/B	FWHM arcsec	Q	N_{notes}	Lit
(1)	(2)	(3)	(4)	(5)	(6)	(7)	(8)	(9)	(10)	(11)	(12)	(13)	(14)	(15)	(16)	(17)	(18)	(19)
-0101033	00:04:00	+03:58:00	-3	13.50	6204	1	11.74	0.570	0.008	1.240	0.050	19.900	0.260	0.06	1.96	2		
0004+4646	00:04:54	+46:46:00	-2	14.30	5277	1	12.97	0.520	0.011	0.570	0.069	17.700	0.361	1.11	2.46	2		
N43	00:10:24	+30:39:00	-2	13.90	4785	1	13.10	0.490	0.010	0.540	0.064	17.710	0.333	1.32	2.07	2		
0011+3037	00:11:18	+30:37:00	-7	14.20	4735	2	13.62	0.410	0.020	0.520	0.090	17.940	0.250	0.92	2.53	3		
-0101058	00:12:06	+07:37:30	-3	12.50	5495	3	11.12	0.733	0.003	1.383	0.052	19.843	0.183	0.37	1.74	1		
539G4	00:12:53	-21:43:18	-2	13.00	244	4	11.50	0.200	0.010	1.585	0.023	21.467	0.081	0.33	1.08	2		
N57	00:12:54	+17:03:00	-5	13.70	5458	1	11.13	0.650	0.016	1.500	0.102	20.600	0.532	0.53	2.31	3		
N63	00:15:06	+11:10:00	-5	12.60	1179	1	11.39	0.640	0.018	1.250	0.113	19.580	0.590	3.38	0.60	3		
N68	00:15:42	+29:48:00	-3	14.05	5711	1	12.46	0.380	0.015	1.170	0.095	20.310	0.496	0.22	1.01	3	11	
N78A	00:17:53	+00:33:20	-2	14.50	5481	1	12.74	0.380	0.007	1.040	0.044	19.920	0.228	0.45	1.42	1		
N97	00:19:54	+29:28:00	-5	13.50	4730	1	11.82	0.590	0.011	1.150	0.071	19.550	0.370	0.00	1.35	2		
N108	00:23:18	+28:56:00	-2	13.30	4737	1	12.25	0.560	0.021	0.900	0.133	18.720	0.690	0.00	1.98	3		
-0102016	00:24:21	+02:46:30	-3	14.00	4346	1	12.13	0.530	0.005	1.080	0.029	19.520	0.153	0.00	1.01	1		
N125	00:26:18	+02:33:00	-2	13.83	5354	1	11.76	0.540	0.011	1.370	0.071	20.560	0.370	0.65	1.36	2		
N128	00:26:42	+02:35:00	-2	12.92	4227	1	11.05	0.800	0.005	1.200	0.032	18.960	0.165	0.28	1.27	1		
N137	00:28:30	+09:55:00	-2	14.20	5276	1	11.80	0.510	0.005	1.360	0.033	20.600	0.171	0.53	1.42	1		
0031+0659A	00:31:24	+06:59:00	-2	14.50	5449	1	14.41	0.230	0.009	0.330	0.054	17.970	0.283	2.66	1.39	2		
-0202055	00:32:06	-11:02:00	-2	14.00	6155	1	12.16	0.470	0.011	1.200	0.073	20.120	0.379	0.00	1.18	2		
242G14	00:32:08	-43:55:54	-2	14.00	5947	1	12.58	0.440	0.008	0.990	0.050	19.500	0.262	0.00	0.99	2	4, 8	
N160	00:33:24	+23:41:00	-2	13.77	5327	1	11.60	0.480	0.008	1.460	0.050	20.970	0.259	1.34	1.06	2	4	
-0202066	00:33:30	-10:23:00	-3	13.50	5981	2	11.96	0.495	0.005	1.215	0.085	20.080	0.300	0.82	1.20	1		
I1559	00:34:13	+23:42:36	-2	13.70	4555	1	13.68	0.250	0.016	0.700	0.100	19.170	0.520	0.97	1.43	3		
540G8	00:36:34	-18:53:06	-2	14.10	3931	2	12.50	0.465	0.005	1.150	0.120	20.065	0.465	1.00	1.13	1		
N193	00:36:42	+03:03:00	-3	14.30	4340	1	11.10	0.610	0.015	1.590	0.097	21.020	0.507	0.07	3.70	3		
0036+2522	00:36:48	+25:22:00	-3	14.50	4614	1	12.45	0.400	0.011	1.180	0.072	20.310	0.376	0.07	1.45	2		
N223	00:39:48	+00:34:00	-5	14.50	5355	1	12.94	0.390	0.013	0.870	0.084	19.270	0.437	4.96	2.50	3		
474G16	00:40:24	-23:48:54	-2	14.00	6692	1	12.49	0.490	0.008	0.920	0.049	19.020	0.253	0.00	0.79	1	1	
-0103001	00:41:00	+08:28:30	-2	14.50	6039	2	12.33	0.515	0.005	1.000	0.026	19.290	0.020	0.25	0.81	1		
-0103002	00:41:00	+04:23:00	-2	14.50	5748	1	12.52	0.360	0.011	1.100	0.042	19.970	0.218	6.41	2.48	2		
N233	00:41:00	+30:19:00	-5	13.80	5430	1	12.23	0.570	0.014	0.960	0.092	18.910	0.477	0.25	1.55	3		
-0203011	00:43:54	-13:42:00	-2	13.50	1758	1	12.57	0.350	0.011	1.050	0.055	19.750	0.284	17.85	4.00	2		
N252	00:45:18	+27:21:00	-2	13.40	4990	1	11.20	0.610	0.013	1.480	0.082	20.550	0.428	0.00	0.88	2		
-0103018	00:47:48	+06:07:30	-3	13.50	5820	2	12.01	0.520	0.006	1.200	0.041	19.960	0.211	0.00	1.02	1		
-0203027	00:48:06	+08:55:00	-2	13.50	3773	1	11.72	0.530	0.008	1.340	0.049	20.380	0.253	0.00	0.98	1		
-0103019	00:48:12	+07:09:00	-2	13.50	4753	1	11.92	0.510	0.008	1.270	0.049	20.220	0.253	0.00	0.80	1		
-0203028	00:48:54	+08:51:00	-3	14.00	4228	1	12.72	0.400	0.016	0.990	0.100	19.650	0.522	1.18	1.46	3		
N311	00:54:48	+30:00:00	-2	14.10	5048	1	12.15	0.350	0.009	1.360	0.055	20.930	0.288	0.06	2.44	2		
295G25	00:54:55	-41:13:42	-2	14.30	3452	2	12.39	0.545	0.005	0.860	0.026	18.660	0.010	0.09	0.80	1		
-0103049	00:55:36	+08:30:00	-3	14.50	4619	3	12.20	0.610	0.006	0.807	0.003	18.183	0.017	0.76	1.29	1		
0056+2335	00:56:18	+23:35:00	-5	14.50	5058	1	13.00	0.340	0.007	0.910	0.046	19.510	0.238	0.62	1.59	1		
295G26	00:57:28	-40:36:06	-2	14.30	6983	2	12.06	0.550	0.007	1.090	0.010	19.465	0.035	0.51	1.34	1	2	
-0103068	00:59:18	+07:05:00	-3	14.00	5769	1	11.60	0.590	0.006	1.320	0.039	20.160	0.203	0.13	0.99	1		
-0103081	01:00:48	+06:37:00	-2	12.50	2406	1	11.11	0.680	0.014	1.400	0.089	20.110	0.464	1.64	2.96	3		
N380	01:04:32	+32:13:01	-2	14.05	4414	1	11.76	0.580	0.012	1.140	0.120	19.485	0.545	0.13	0.60	2		*
243G33	01:05:29	-47:10:24	-3	13.20	6714	2	11.54	0.500	0.010	1.360	0.030	20.385	0.055	0.52	1.13	2		*
0105+3923	01:05:48	+39:23:00	-3	13.30	6149	1	11.81	0.640	0.019	1.080	0.118	19.100	0.616	0.51	3.46	3		
352G8	01:06:27	-36:36:36	-2	14.00	6623	1	13.48	0.260	0.008	0.830	0.049	19.580	0.256	0.82	0.87	1		

NOTE.—The number in column (16) identifies the row number of Table 3.12 which describes the type of cause for features observed in the light profiles of the galaxy. In column (17) galaxies previously observed by other authors are indicated with an asterisk.

TABLE 3.10

THE PHOTOMETRIC CATALOG OF THE FAINT/DISTANT CLUSTER GALAXIES

Name	α (1950)	δ (1950)	T	m_B mag	cz_{hel} km/s	N_{obs}	m_{tot} mag	$log\, d_n$	ϵ_{d_n}	$log\, r_e$	ϵ_{r_e}	$\bar{\mu}_e$ mag/arcsec^2	$\epsilon_{\bar{\mu}_e}$ mag/arcsec^2	D/B	FWHM arcsec	Q	N_{notes}	Lit
(1)	(2)	(3)	(4)	(5)	(6)	(7)	(8)	(9)	(10)	(11)	(12)	(13)	(14)	(15)	(16)	(17)	(18)	(19)
I1696	01:22:19	+01:52:37	-5	14.62	5827	1	12.84	0.380	0.009	0.915	0.075	19.645	0.115	0.16	2.77	2		*
0122-0131	01:22:21	+01:31:03	-2	17.52	5072	2	15.20	-0.195	0.015	0.685	0.055	20.495	0.175	0.00	1.66	3		
0122-0127	01:22:50	+01:27:17	-5	16.58	5242	1	14.30	0.030	0.016	0.810	0.100	20.330	0.522	0.11	3.96	3		
0122-0145	01:22:59	+01:45:44	-2	15.36	5526	3	13.26	0.360	0.006	0.690	0.028	18.743	0.120	0.00	1.02	1		*
D33	01:23:11	+01:43:01	-2	15.41	5237	1	13.11	0.350	0.011	0.810	0.050	19.325	0.045	0.31	0.60	2		*
0123-0136	01:23:14	+01:36:14	-2	15.82	5535	5	13.91	0.230	0.006	0.650	0.046	19.075	0.203	1.08	2.46	1		*
0123-0145	01:23:15	+01:45:06	-2	16.70	5178	1	14.30	-0.060	0.005	0.900	0.020	20.915	0.055	0.00	1.02	1		*
0123-0133	01:23:16	+01:33:09	-2	15.51	5318	3	13.37	0.363	0.003	0.635	0.081	18.497	0.352	0.77	2.21	1		*
0123-0131	01:23:19	+01:31:34	-5	16.72	6300	4	14.58	0.075	0.003	0.584	0.022	19.438	0.126	0.87	2.41	1		*
N548	01:23:29	+01:29:06	-3	14.62	5419	1	13.41	0.220	0.008	1.010	0.090	20.425	0.485	0.79	0.76	1		*
0123-0150	01:23:58	+01:50:02	-2	16.82	5509	2	14.57	-0.070	0.010	0.805	0.005	20.575	0.005	2.26	2.36	2		
0124-0131	01:24:43	+01:31:51	-2	15.27	4804	1	13.19	0.320	0.004	0.835	0.035	19.510	0.010	0.08	0.60	1		*
0332-3542	03:32:34	-35:42:45	-5	14.81	1233	2	12.58	-0.765	0.035	1.880	0.060	24.060	0.180	0.12	0.60	3		
0334-3532	03:34:59	-35:32:19	-2	14.77	1765	3	13.25	0.133	0.009	1.127	0.009	20.890	0.066	0.07	3.97	2		
0336-3536	03:36:12	-35:36:09	-3	14.82	855	2	12.58	-0.270	0.400	1.515	0.415	22.580	1.640	0.11	0.60	3		
0512+0612	05:12:55	+06:12:32	-2	17.16	8742	2	13.31	0.205	0.005	1.043	0.032	20.517	0.187	0.00	0.85	1		*
0513+0616	05:13:07	+06:16:02	-2	17.19	8634	2	13.72	0.235	0.005	0.767	0.082	19.557	0.397	1.42	1.79	1		*
0513+0623a	05:13:33	+06:23:34	-2	16.87	6664	2	13.37	0.335	0.005	0.707	0.007	18.963	0.113	0.00	1.46	1		*
0513+0620	05:13:49	+06:20:54	-2	17.04	7429	2	13.43	0.290	0.006	0.730	0.030	19.217	0.099	0.21	1.15	1		*
0513+0626b	05:13:52	+06:26:59	-2	17.15	8672	2	13.73	0.075	0.005	0.990	0.006	20.787	0.092	0.00	0.97	1		*
0513+0623	05:13:56	+06:23:54	-5	17.20	8675	2	13.64	0.260	0.009	0.663	0.023	19.080	0.035	0.00	1.21	2		*
0513+0622	05:13:56	+06:22:59	-5	16.72	7741	2	15.06	0.080	0.009	0.060	0.050	17.340	0.325	0.00	1.75	2		*
0513+0624	05:13:58	+06:24:37	-2	17.25	9363	3	13.94	0.173	0.003	0.712	0.010	19.532	0.059	0.00	1.26	1		*
0514+0629	05:14:14	+06:29:56	-5	16.19	9699	2	12.43	0.460	0.008	1.073	0.028	19.837	0.208	0.49	1.70	2		*
D16	05:14:37	+06:05:02	-2	16.58	9695	1	13.12	0.400	0.012	0.805	0.085	19.175	0.475	1.53	1.80	2		*
0608-3334	06:08:05	-33:34:53	-2	15.06	11557	1	12.78	0.180	0.011	1.295	0.095	21.540	0.170	0.63	1.31	2	1, 2	*
0608-3332	06:08:08	-33:32:29	-5	17.07	11335	1	13.40	-0.150	0.010	1.030	0.350	21.210	1.040	0.00	0.60	2		*
0609-3343	06:09:06	-33:43:29	-2	15.79	11692	1	13.11	0.350	0.011	0.860	0.068	19.370	0.354	0.31	0.60	2		*
0609-3317	06:09:17	-33:17:38	-2	15.44	11488	1	13.87	0.220	0.013	0.725	0.075	19.525	0.445	1.25	2.44	3		*
0609-3306	06:09:50	-33:06:39	-3	15.12	11059	1	13.36	0.250	0.011	0.970	0.100	20.215	0.515	0.36	1.05	2		*
R154	10:32:15	-28:18:33	-2	15.36	3485	1	13.53	0.330	0.006	0.610	0.020	18.675	0.245	0.21	0.97	1		*
436G45	10:32:30	-28:15:30	-5	15.35	3402	1	13.64	0.340	0.015	0.425	0.035	17.855	0.315	0.00	0.83	3		*
RMH26	10:33:43	-27:14:58	-5	15.08	2286	1	13.74	0.230	0.007	0.805	0.085	19.790	0.480	0.51	1.21	1		*
D80	10:33:52	-27:25:44	-2	15.59	4196	1	14.03	0.030	0.006	0.920	0.040	20.580	0.206	0.97	1.03	1		*
D190	10:33:59	-26:54:25	-2	16.53	3687	1	14.53	-0.090	0.011	0.850	0.054	20.790	0.279	0.00	1.38	2		*
D107	10:33:58	-27:27:42	-2	15.49	3551	1	14.28	0.030	0.007	0.730	0.042	19.890	0.218	0.84	1.24	1		*
RMH28	10:34:02	-27:05:41	-2	15.19	3006	1	13.67	0.230	0.006	0.770	0.020	19.565	0.185	0.44	0.73	1		*
D66	10:34:04	-27:19:20	-3	15.46	2816	1	13.98	0.100	0.006	0.780	0.039	19.870	0.203	0.45	0.98	1		*
D46	10:34:08	-27:13:28	-2	15.00	4776	3	13.32	0.117	0.009	1.123	0.084	20.920	0.297	0.19	0.98	2		*
D154	10:34:14	-27:12:37	-5	15.91	3193	1	14.33	-0.120	0.011	0.830	0.070	20.440	0.365	1.91	1.26	2		*
437G9	10:34:14	-27:57:24	-3	14.74	3460	1	13.32	0.330	0.008	0.750	0.049	19.080	0.255	1.39	0.83	1		*
D37	10:34:20	-27:18:04	-5	14.97	4739	1	13.33	0.300	0.015	0.815	0.015	19.540	0.080	0.00	1.15	3		*
D61	10:34:24	-27:12:35	-5	15.13	2703	1	13.61	0.360	0.015	0.340	0.095	17.270	0.494	0.00	0.99	3		*
D195	10:34:28	-27:07:44	-5	16.03	4478	1	15.39	-0.030	0.012	0.160	0.076	18.180	0.397	0.33	1.81	2		*
437G13	10:34:33	-27:39:28	-2	14.58	3499	1	12.44	0.490	0.014	0.890	0.090	19.165	0.165	0.17	0.60	3		*
D135	10:34:48	-27:23:52	-5	15.60	4115	1	13.93	0.210	0.010	0.620	0.066	19.000	0.345	0.00	0.93	2		*

NOTE.—As in Table 3.9

TABLE 3.11

THE PHOTOMETRIC CATALOG OF "OTHER" GALAXIES

Name	α (1950)	δ (1950)	T	m_B mag	cz_{hel} km/s	N_{obs}	m_{tot} mag	$log\, d_n$	ϵ_{d_n}	$log\, r_e$	ϵ_{r_e}	$\bar{\mu}_e$ mag/arcsec^2	$\epsilon_{\bar{\mu}_e}$ mag/arcsec^2	D/B	FWHM arcsec	Q	N_{notes}	Lit
(1)	(2)	(3)	(4)	(5)	(6)	(7)	(8)	(9)	(10)	(11)	(12)	(13)	(14)	(15)	(16)	(17)	(18)	(19)
-0202011	00:21:48	-14:13:00	0	14.00	7330	1	13.14	0.220	0.011	1.090	0.072	20.560	0.375	0.00	1.08	2		
-0202085	00:39:03	-10:18:00	0	13.50	3947	2	11.16	0.605	0.015	1.520	0.044	20.710	0.040	0.06	1.67	3		
N315	00:55:05	+30:04:58	0	12.50	4921	1	10.05	0.850	0.015	1.690	0.093	20.450	0.483	0.01	3.29	3		*
-0304041	01:16:24	-17:04:00	0	14.50	5807	1	12.05	0.430	0.007	1.480	0.047	21.410	0.245	0.19	0.60	1		
D15	01:22:18	+01:57:07	0	15.78	5305	1	12.88	-0.490	0.013	1.870	0.083	24.200	0.432	0.18	2.41	3		
0122-0146	01:22:44	+01:46:38	0	15.26	4854	2	13.47	0.315	0.005	0.767	0.052	19.250	0.271	0.17	0.86	1		*
0123-0134	01:23:18	+01:34:39	0	15.82	5509	4	13.58	0.223	0.005	0.784	0.028	19.598	0.120	1.40	2.80	1		*
0123-0132	01:23:25	+01:32:54	-2	0.00	5312	3	14.59	-0.183	0.009	0.903	0.034	21.197	0.117	0.00	1.77	2		
0212+3517	02:12:36	+35:17:00	-3	14.00	8168	2	13.04	0.490	0.010	0.880	0.230	18.955	0.765	0.07	2.69	2		
-0307030	02:29:51	-17:27:00	-3	14.00	8558	1	12.36	0.450	0.012	1.120	0.079	19.910	0.409	0.00	1.87	2		
+0107030	02:37:54	+05:40:00	-3	14.00	7057	1	12.24	0.430	0.008	1.240	0.048	20.360	0.252	0.00	0.77	1		
-0308003	02:41:18	-14:57:00	0	13.50	2135	1	11.21	0.490	0.007	1.800	0.047	22.190	0.245	0.19	0.60	1		
479G30	02:41:51	-26:23:54	-2	14.40	10532	1	14.45	0.130	0.009	0.520	0.057	18.960	0.296	1.63	1.78	2		
0246+4647	02:46:24	+46:47:00	-3	14.50	7730	1	11.16	0.720	0.010	1.340	0.062	19.750	0.321	0.48	1.91	2		
-0308035	02:49:24	-16:50:00	0	14.00	3297	1	11.67	0.450	0.008	1.500	0.049	21.130	0.256	0.04	0.86	1		
N1239	03:08:22	+02:44:30	-2	14.61	8643	1	12.87	0.020	0.008	1.340	0.050	21.560	0.259	0.15	0.92	2		
-0209022	03:15:12	-10:28:00	-2	14.00	8985	1	12.12	0.310	0.009	1.400	0.059	21.120	0.307	0.30	2.02	2		
301G2	03:15:28	-41:17:24	0	9.68	890	1	8.54	1.320	0.008	1.600	0.051	18.520	0.265	0.05	1.06	2		
0324-3512	03:24:46	-35:12:51	-2	15.32	15623	1	13.38	0.160	0.008	1.060	0.053	20.660	0.277	0.00	1.35	2		
358G33	03:34:51	-34:54:12	0	13.80	1597	2	11.85	0.395	0.005	1.395	0.045	20.630	0.080	1.01	1.39	1		
358G35	03:34:52	-36:09:48	0	12.26	924	2	10.78	0.855	0.005	1.255	0.005	19.005	0.025	1.70	1.65	1		
I362	04:14:21	-12:19:22	-3	14.36	8957	1	12.21	0.450	0.009	1.220	0.056	20.270	0.289	0.85	1.62	2		
-0211031	04:14:24	-12:20:30	-3	14.00	8957	2	12.38	0.490	0.010	1.095	0.045	19.715	0.145	0.86	1.39	2		
484G37	04:34:27	-22:32:48	-2	14.30	20720	1	13.27	0.170	0.008	1.100	0.053	20.690	0.276	0.69	1.33	2		
0513+0617	05:13:44	+06:17:18	-2	0.00	8708	1	13.34	0.270	0.007	0.840	0.060	19.765	0.055	0.49	1.28	1		*
0513+0626a	05:13:54	+06:26:59	-5	0.00	7101	1	13.19	0.310	0.006	0.825	0.085	19.535	0.155	0.13	0.97	1		*
0513+0626	05:13:55	+06:26:05	-2	0.00	9292	3	13.92	0.247	0.003	0.658	0.068	19.137	0.305	2.69	1.56	1		*
0513+0627	05:13:57	+06:27:28	-2	0.00	7879	1	15.02	0.030	0.011	0.285	0.015	18.535	0.065	0.00	1.28	2		*
0514+0628	05:14:03	+06:28:55	-2	0.00	9931	1	14.77	0.130	0.010	0.185	0.035	17.800	0.050	0.58	0.91	2		*
0514+0619	05:14:05	+06:19:29	-2	0.00	8410	1	14.40	-0.030	0.011	0.870	0.040	20.775	0.255	0.00	1.47	2		*
0514+0619a	05:14:10	+06:19:34	-2	0.00	8129	1	14.70	0.100	0.015	0.475	0.055	19.045	0.265	2.46	1.27	3		*
0514+0620	05:14:08	+06:20:06	-2	0.00	8677	1	14.15	0.110	0.006	0.785	0.105	20.020	0.490	0.66	1.11	1		*
0514+0626	05:14:26	+06:26:27	-2	0.00	10012	2	14.25	0.095	0.005	0.753	0.020	20.057	0.187	1.47	1.86	1		*
0532-3050	05:32:29	-30:50:00	-3	14.13	10782	1	12.41	0.400	0.008	1.180	0.054	20.260	0.279	0.31	1.38	2		
0543-2557	05:43:26	-25:57:00	-3	13.89	13341	1	13.85	0.170	0.012	0.770	0.074	19.670	0.383	0.82	1.27	2		
0543-2557a	05:43:28	-25:57:06	-3	14.11	13065	1	13.83	0.070	0.012	0.920	0.073	20.430	0.381	0.17	1.22	2		
0546-3259	05:46:37	-32:59:36	-3	14.20	11205	1	12.18	0.470	0.010	1.200	0.064	20.110	0.332	0.81	2.59	2		
0602-6345	06:02:30	-63:45:42	-3	13.64	8136	1	11.84	0.480	0.007	1.500	0.047	21.230	0.245	0.12	0.60	1		
0608-4736	06:08:20	-47:36:14	-3	14.08	8966	2	12.29	0.500	0.007	1.005	0.085	19.355	0.315	0.43	1.16	1		
0608-6543	06:08:47	-65:43:12	-3	13.57	10905	3	12.30	0.280	0.006	1.313	0.007	20.840	0.023	1.88	1.86	1		
0610-6231	06:10:08	-62:31:36	-3	13.71	8385	1	12.18	0.560	0.008	1.000	0.053	19.090	0.277	0.42	1.35	2		
0621-6458	06:21:16	-64:58:00	-3	14.08	7995	1	11.97	0.520	0.012	1.280	0.076	20.230	0.393	0.04	1.50	2		
0622-6454	06:22:10	-64:54:24	-5	14.00	8313	1	11.97	0.520	0.011	1.160	0.072	19.750	0.375	0.62	1.09	2		
0638-2550	06:38:10	-25:50:48	-2	14.08	7751	1	12.67	0.480	0.007	0.870	0.047	18.950	0.246	1.54	0.64	1		
0646+8102	06:46:00	+81:02:00	-5	14.40	7532	1	12.60	0.490	0.013	0.870	0.081	18.910	0.422	0.31	2.16	2		
0656-4544	06:56:08	-45:44:30	-3	13.56	11700	1	12.09	0.490	0.010	1.220	0.063	20.060	0.326	0.42	2.47	2		

NOTE.—Notes: As in Table 3.9

Table 3.12 Notes to the ENEAR Photometric Catalogs

N_{notes} (1)	Notes (2)
1	strong contamination by nearby galaxies
2	strong contamination by nearby bright stars
3	crowded background
4	presence of spiral arms, bars and/or rings
5	peculiar shape
6	edge-on galaxy
7	presence of dust lane
8	evidence of star formation
9	cD galaxy
10	dwarf galaxy
11	galaxy close to the edge of the detector
12	large galaxy compared to the field-of-view

Chapter 4

Spectroscopy

This Chapter describes the spectroscopic survey carried out for the ENEAR project. To date, some 2200 spectra of about 1500 galaxies have been taken. Here, we present data for 1146 ellipticals and S0s obtained from 1679 spectra. Of our 1146 galaxies, 1103 had pure absorption line spectra. For these objects, the central velocity dispersion was computed; 914 of them had no previously measured velocity dispersions. We also measured the Mg_2 line index for 94% of these objects. Analysis of 43 early-types which show strong emission lines is still ongoing. Our catalog of 1103 galaxies is one of the largest single sets of high quality and uniform spectroscopic data currently available for studying early-type galaxies in the nearby universe.

Most of the galaxies presented below are part of the all-sky ENEARf sample which was designed to study the properties and peculiar motions of nearby early-type galaxies. The sample was constructed from magnitude-limited surveys presently available; it includes galaxies out to $cz \sim 7000\mathrm{kms}^{-1}$ that are brighter than $m_{\rm B} = 14.5$, and is complimented by fainter galaxies in the field or in selected clusters. The field galaxies were observed as part of the SSRS2 redshift survey limited to $m_{\rm B} = 15.5$, whereas the cluster galaxies belong to the ENEARc sample. Some of the observed galaxies were early-type spirals which were misclassified in the original catalogs from which our sample was drawn.

406 galaxies were obwerved more than once (there are 533 repeat observations in total). The large number of repeated observations made it possible to correct statistically and accurately for data taken in different runs, using different setups, over the long duration of the project. These corrections were relatively small, typically $\lesssim 5\%$ of the velocity dispersion and 0.01 mag in the Mg_2 line-strength. Comparison of 227 of our galaxies with previously published measurements results also showed no systematic discrepancies, so our estimates of internal errors are probably reliable. Typical errors are 8% in velocity dispersion and 0.01 mag in Mg_2, in good agreement with those estimated by other authors.

4.1 The data

4.1.1 Observations

In the original phases of this project most of the data relied on the measurements of Tonry & Davis (1982) for the northern hemisphere and Reticon data, taken as part of the Southern Sky Redshift Survey, for the south; this gave a combined total of about 600 galaxies. However, comparison with modern CCD data showed that the errors in the

older measurements were large ($\sim 30\%$) and required large zero-point shifts. Therefore, we decided to re-measure all of these galaxies.

Our new spectroscopic observations have been conducted over a long period of time using a variety of sites (CASLEO[1], CTIO[2], ESO[3], and MDM[4]), detectors and gratings, with the spectral resolution ranging from 2 to 5 Å. In the course of the second phase of our program 28 observing runs were carried out and 11 different setups, corresponding to different combinations of telescope-detector-spectrograph, were used. In total, between 1992 and 1999, 154 nights were assigned to this project for spectroscopic observations, of which 137 were actually used.

Basic information about each run is summarized in Table 4.1: column (1) gives the identification number of the run, column (2) the date, column (3) the number of nights awarded, column (4) the reference number of the setup used (described in more detail in Table 4.2), and column (5) identifies the runs for which the data reduction is still ongoing. The different setups used are summarized in Table 4.2, where column (1) gives the setup reference number, column (2) the observatory and telescope used, columns (3) and (4) the number of spectra, N_m, and the number of repeated observations, N_r, using each setup, columns (5)–(9) the type, size, pixel scale, gain and readout noise of the detector, and columns (10)–(14) the slit width, grating, dispersion, resolution (as measured from the width of the calibration lines), and spectral coverage of the spectrograph. All our new spectra were obtained using long-slits.

A total of 1679 spectra of 1146 galaxies are currently available; observations and data reduction for about 500 spectra are still ongoing. The large number of spectra relative to the number of galaxies means that we have conducted many repeat observations (406 galaxies were observed more than once, and there were a total of 533 repeat observations), which are used below to estimate our errors. Some (227) of our observed galaxies had already been observed by other authors. We re-observed them to ensure that we had enough overlap with data in the public domain, since this then allows us to derive the statistical corrections necessary for bringing all of the available data into a common system. This is essential if one wishes to construct a homogeneous sample that can be used to determine a distance relation (as we do in Chapter 6) or for studying the peculiar motions of early-type galaxies in the nearby Universe (as we do in Chapter 7).

Since the primary goal of our new spectroscopic observations was to measure central velocity dispersions and line-strengths, the spectral range was chosen to cover the Mgb band (around $\lambda_0 = 5177$ Å), the E-band (5270 Å), and the FeI line (5335 Å). Most of our observations also included H_β (4861 Å) while only some covered the NaD (5895 Å) feature (at low-resolution).

We used standard observing procedures for the CCD spectra. All spectra were calibrated nightly in the usual fashion: wavelength calibration lamps were observed before and after each object (He-Ar at ESO; Hg-Ar-Xe-Ne at MDM; He-Ne-Ar at CASLEO). Continuous lamps, either inside the spectrograph (MDM) or in the dome (CASLEO, ESO) were taken nightly for flat fields, as were bias frames. Dark current was also checked for each CCD, but was always found to be negligible. Often, multiple exposures of a given galaxy were taken to facilitate cosmic-ray removal.

[1] Complejo Astronomico El Leoncito (Argentina)
[2] Cerro Tololo Interamerican Observatory (Chile)
[3] European Southern Observatory (Chile)
[4] Michigan-Dartmouth-M.I.T. Observatory (Arizona, USA)

Table 4.1 Observing runs: spectroscopy

Run (1)	Date (2)	N_p (3)	Setup (4)	Notes (5)
MDM-501	Oct 92	5	5	
ESO-651	Nov 93	6	1	
ESO-652	May 94	7	1	
MDM-502	Oct 94	6	6	
ESO-654	May 95	1	2	
ESO-653	Aug 95	4	1	
MDM-503	Dec 95	4	7	
CASLEO-801	Apr 96	3	11	
CASLEO-802	Sep 96	3	11	
ESO-655	Oct 96	5	4	
ESO-656	Nov 96	13	3	
MDM-505	Nov 96	3	8	
ESO-657	Jan 97	5	3	
MDM-506	Feb 97	2	9	
ESO-658	Mar 97	6	4	
ESO-659	Apr 97	10	4	
CASLEO-803	May 97	5	11	
MDM-507	Jun 97	5	10	
ESO-660	Oct 97	5	4	
MDM-508	Nov 97	3	9	
ESO-661	Feb 98	6	4	
ESO-662	Apr 98	7	4	
MDM-509	Apr/May 98	2	9	
ESO-663	Jun 98	3	4	
ESO-664	Aug 98	2	4	still reducing
ESO-665	Oct 98	4	4	still reducing
MDM-510	Nov 98	1	9	
ESO-666	Feb 99	11	4	still reducing

Notes: Column (3) shows the number of photometric nights for the run. Information about the setup indicated in column (4) is given in Table 4.2.

Table 4.2 Spectroscopy Observing Setups

see table.4.2.ps

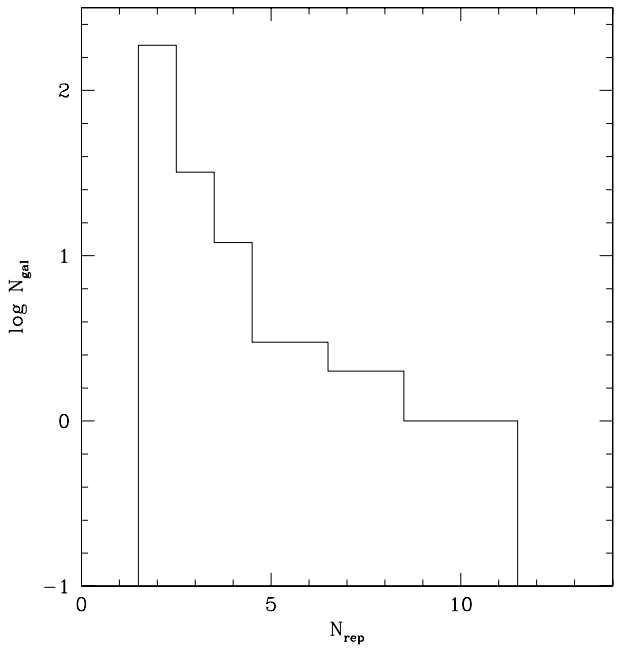

Figure 4.1 Number of galaxies in our data set that were observed more than once.

During the night, several stars with known radial velocities, in the spectral range G8 to K5 and luminosity class III, were observed. These were used as velocity templates in the measurements described below. Galaxy redshifts were measured by comparing the spectrum of the galaxy with that of a star of known (small) radial velocity observed with the same instrumental setup. Since red giant stars are the main contributors to the visible light in elliptical galaxies, the same set of stars could be used both as spectral templates for determining the galaxy velocity dispersions, and as radial velocity standards for measuring the galaxy redshifts. Normally several standard stars were observed during each observing night; these bright stars were trailed along the slit 20—40 times. This produced uniform illumination across the slit and ensured a very high signal-to-noise ratio (S/N), with typically more than 10^4 photons per pixel. This significantly reduces a source of noise in the later analysis steps.

Because relatively high S/N is required for determining velocity dispersions, we tried to obtain around 900 photons per Å, which corresponds to a S/N ratio of about 30. Typically, for each galaxy we took three consecutive exposures of 600 seconds. In this way the combined spectrum is less affect by cosmic rays. For all of our spectra, we determined the S/N ratio in two different passbands, as described in Section 4.1.3. At the continuum bands of the Mg_2 feature the median S/N is $\sim$ 45, while at the blue continuum of the NaD the mean value is $\sim$ 27.

Some relatively bright galaxies were observed systematically every night in a run and/or in different runs. The number of repeated observations of these "standards" is sometimes as high as ten. Figure 4.1 shows the distribution of repeated observations; roughly 200 galaxies were observed more than twice. These repeated observations were used to compare: 1) low to high resolution spectra; 2) spectra taken at different

telescopes or with different setups. These comparisons were then used to make our measurements internally consistent and to make our error estimates.

4.1.2 Data reduction

All spectra were reduced using the standard long-slit procedures in the IRAF[5] package (Tody 1986). The reductions are described briefly below and follow standard methods (see e.g., Wegner et al. 1999 for further details). They consist of the following steps: bias subtraction, flat field correction, rejection of cosmic-ray hits, wavelength calibration, subtraction of the sky spectrum, and extraction of the one-dimensional spectra. Though similar, the MDM and ESO/CASLEO data were reduced independently, with minor procedural differences described below.

Bias frames, taken each night, were scaled by the level of the CCD overscan strip and median filtered. These were checked for temporal variations, after which the resulting bias frame was subtracted from the other images. Because of the stability of the system at ESO, a median bias frame was calculated using images obtained throughout the run, and then subtracted from the remaining frames.

Pixel-to-pixel sensitivity variations were removed by producing a sensitivity map from a median filtering of flatfield exposures, typically 10 or more per night. These were usually produced from exposures of a tungsten lamp (either in the spectrograph or an illuminated target inside the dome), passing through the optics of the spectrograph. This map was produced by normalizing the flatfield constructed from the combined spectra to a smoothed version of itself. The rms variation in the resulting flattened response frames was typically less than 0.5%. Each galaxy or stellar spectral frame was then devided by the response function.

Cosmic-ray hits were removed using the IRAF task **lineclean**. This fits the galaxy's spectrum along the direction of the dispersion and identifies cosmic-ray hits without affecting the absorption lines.

The wavelength calibration of the pixel positions was done by using the emission lines in the calibration spectra. Typically a 5th order polynomial was fit to the data with a fitting accuracy of about ± 0.1 pixel. The wavelength calibrations generally employed more than 20 lines, and produced residuals of order ± 0.02 Å for the ESO 1200 l/mm grating spectra, which is typical for our observations. The wavelength calibration for ESO spectra used the set of He-Ar lines compiled by M. P. Diaz available from `ftp://www.lna.br/pub/instrum/cass/hearlna.dat.Z`. These gave consistently better solutions than the standard tables distributed with IRAF.

Sky subtraction was done by using the sky level determined in the IRAF task **background** from two or more regions on each side of the spectrum that are far enough from the galaxy that they are not contaminated by the object itself. The sky level at the object was interpolated using a low order polynomial fitted to the sky in a direction perpendicular to the spectrum.

The final one-dimensional galaxy spectrum was then extracted by summing across its profile on the CCD image in the region where it was greater than about 10% of its maximum. For all runs the maximum misalignment resulting from the tilt of the

[5]IRAF is distributed by the National Optical Astronomy Observatories, which is operated by the Association of Universities for Research in Astronomy, Inc., under contract with the National Science Foundation

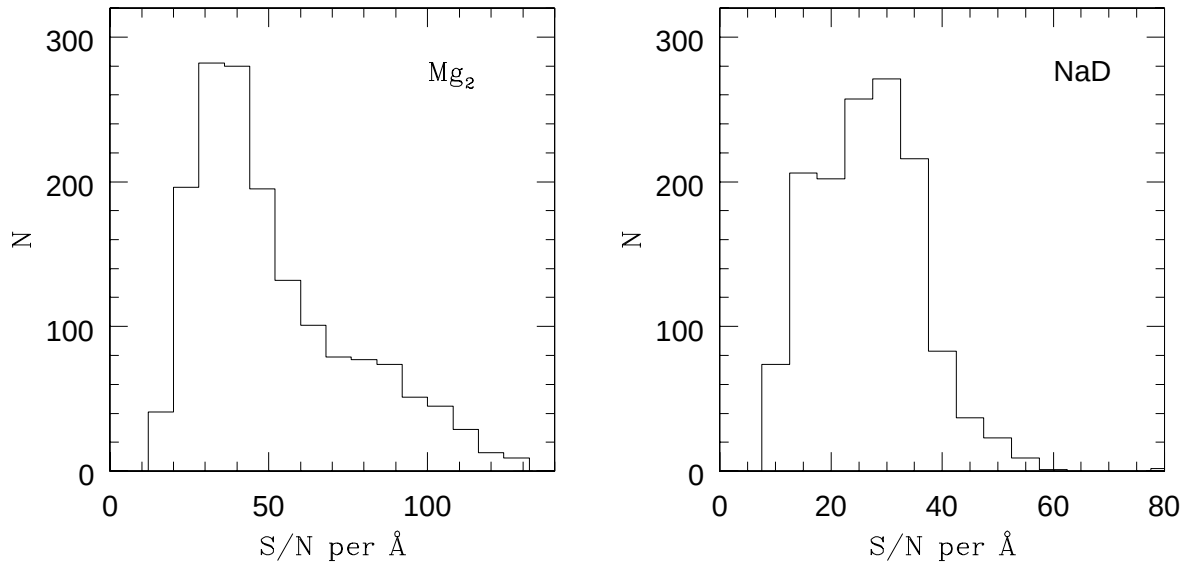

Figure 4.2 The distribution of the S/N per Å computed in the red and blue continua of the Mg_2 line index (left) and in the blue continuum of the NaD absorption line (right).

spectrum accross the CCD, in 1024 pixels, was small ($\sim$ 0.1 pixel). For the ESO spectra the objects were extracted within a region where the flux exceeds about 5% of the peak value, while the sky value was determined from the median value measured in two regions on the either side of the galaxy, and then interpolated across the galaxy spectrum.

4.1.3 Quality of the spectra

We characterized the quality of each spectrum by estimating the S/N ratio at the blue and/or red continuum regions of the absorption features. The sources of noise one must take into account are: 1) the readout noise of the instrument, which is a constant, is only important when the signal is very low, and can be reduced by increasing the exposure time t; and 2) Poisson noise, which is proportional to the square root of the collected signal (sky + galaxy) and thus also to $\sqrt{t}$. This is the dominant source of noise; it can be reduced by increasing the exposure time to strengthen the collected signal. We estimated the S/N ratio of our spectra at the continuum bands of either side of the Mg_2 feature (the rest wavelength blue continuum: 4895–4957 Å, and red continuum: 5301–5366 Å) and at the blue continuum of the NaD (the rest wavelength blue continuum: 5861-5876 Å). At each continuum band the S/N is given by $mean * gain/\sqrt{mean * gain + 100 + RON^2}$, where *mean* is the mean number of counts into that wavelength range, *gain* is the gain in e^-/ADU, *RON* is the readout noise in e^-, and 100 corresponds to the contribution of the sky to the collected signal. The final S/N is the mean of the values obtained at the two continuum bands. Determination of the S/N ratio for all the other absorption features is still ongoing. The median value of S/N for our spectra is $\sim$ 45 near the Mg_2 line and $\sim$ 27 at the NaD blue continuum region. In contrast, the S/N ratio of a typical

stellar observation is ~ 100 (stellar spectra are, essentially, noiseless).

Fig.4.2 shows the distribution of galaxy spectra as a function of S/N per Å measured near the two different line indices. The distribution of S/N in the vicinity of the Mg_2 line has an extended tail towards large S/N (left) which is not present in the case of the NaD index (right). This may be because the CCDs are more efficient at the Mg_2 index wavelengths, although some of the tail arises from the fact that, whereas both indices are observed in spectra observed at low resolution, not all high-resolution spectra include the NaD absorption line.

Early-type galaxies, being quiescent systems with no recent star formation, are expected to have spectra characterized by pure absorption lines, similar to that of G and K stars. However, about $\sim 5\%$ of the observed galaxies exhibited emission lines from HII regions of ionized gas. Most of these cases were associated with objects that either have large D/B ratios, or have arms and/or rings, or that, after inspection of the images (Chapter 3), were found to have other peculiar features. Some of these galaxies were obvious misclassifications in the original catalog, while some of the others may in fact have some residual star-formation.

The final spectra are too numerous to be presented here; instead they are split into three sub-samples and shown in Appendix D. These sub-samples are

- galaxies in the ENEARf magnitude and redshift limited sample (933 galaxies, Figure D.1a,b);
- galaxies in clusters, but fainter or more distant than the limits of the ENEARf sample (50 galaxies, Figure D.2)
- early-type galaxies which are not associated with our clusters and do not satisfy the ENEARf selection criteria as well as galaxies of morphological types $T > -2$ (120 galaxies, Figure D.3).

After inspecting the observed spectra, we found that 43 galaxies of the ENEARf data set have spectra with strong emission lines. Figure D.1b presents the one-dimensional spectra of these objects. The measurements derived from these data are not reported in this work; a more accurate analysis of these spectra is ongoing.

4.2 Spectroscopic parameters

4.2.1 Redshifts and velocity dispersions

The line-of-sight central velocity dispersion σ_0 of an elliptical galaxy is difficult to measure because a relatively high S/N is required. This parameter is determined by analysing the integrated spectrum of the whole system; that is, it is a superposition of many individual stellar spectra, each of which has been Doppler shifted because of the star's motion. A number of methods for making velocity dispersion measurements as accurately and objectively as possible have been developed (Sargent et al. 1977; Tonry & Davis 1979; Franx et al. 1989; Bender 1990). These methods are all based on a comparison between the spectrum of the galaxy whose velocity dispersion is to be determined, and a fiducial spectral template. This can either be the spectrum of an appropriate star, with spectral lines unresolved at the spectral resolution being used, or a high signal-to-noise

spectrum of a galaxy with known velocity dispersion. Although there are small, in principle significant, differences among these methods, in practice, all methods seem to give similar results, at least when applied to spectra with high S/N. Therefore, for our data at least, choosing one method or another does not make a critical difference.

The redshifts, cz, and velocity dispersions, σ_0, reported in this work were obtained using the IRAF task **fxcor** in the **rv** package. This task employs the Tonry & Davis (1979) cross-correlation technique (TD79) which generally yields more robust measures for modest S/N spectra (e.g., Rité 1998). The basic assumption behind the TD79 technique, and other similar methods, is that the spectrum of an elliptical galaxy (and also of the bulge of a disk galaxy) is well approximated by the spectrum of its luminous stars (K0-K1 giants), modified only by the effects of the stellar motion inside the galaxy. Since these motions simply introduce a Doppler shift, the galaxy spectrum is given by the convolution of the spectrum of a K giant star with the line of sight stellar velocity distribution (LOSVD). Therefore the LOSVD can be obtained with a deconvolution process from the galaxy spectrum and a suitable stellar template. In practice, given that cross-correlation and convolution are related operations, one can use the cross-corelation as a computational tool for deriving the LOSVD. The entire procedure is performed using Fourier transforms, because the Fourier transform of a convolution, or of a cross-correlation reduces to a product between individual functions' tranforms. We point out that the TD79 method uses a simple Gaussian to parametrize the observed LOSVD.

Rather than using the original TD79 algorithm, we used the modification to it that was developed by Baggley (1996) and Wegner et al. (1999). In this technique, the redshift and velocity dispersions are computed in two steps. First, an estimate of the redshift, using the whole spectrum, is made by rebinning in $\log \lambda$, removing the continuum using a low-order polynomial, and end-masking with a cosine bell function prior to the cross-correlation analysis. Next, this redshift estimate is used to make an estimate of the FWHM of the cross-correlation peak and a more accurate estimate of the redshift, but now over a more restricted wavelength range. For each galaxy-template combination the FWHM of the correlation peak was calculated using the spectral region with rest wavelength 4770–5770 Å. This FWHM was then calibrated by convolving each standard star's spectrum with a series of Gaussian broadening functions. In this way it was possible to construct a curve relating the measured FWHM to the input σ value.

4.2.1.1 Error estimates

The formal errors in the measurement of the redshift and velocity dispersions were obtained by computing the standard deviation of the values obtained from the cross-correlation against different template stars observed in the same run. These estimates include the systematic errors associated with the template-galaxy mismatches and the statistical errors due to the noise properties of the spectra. Our errors, estimated in this way, show the same dependence on S/N and on redshift and velocity dispersion as those estimated using the Tonry & Davis technique and those from using simulated spectra. The error depends on the velocity dispersion because of instrumental resolution at low σ, while at high-σ the absoprtion lines become broad and there is often only a small contrast relative to the continuum; both of these effects tend to increase the amplitude of the error.

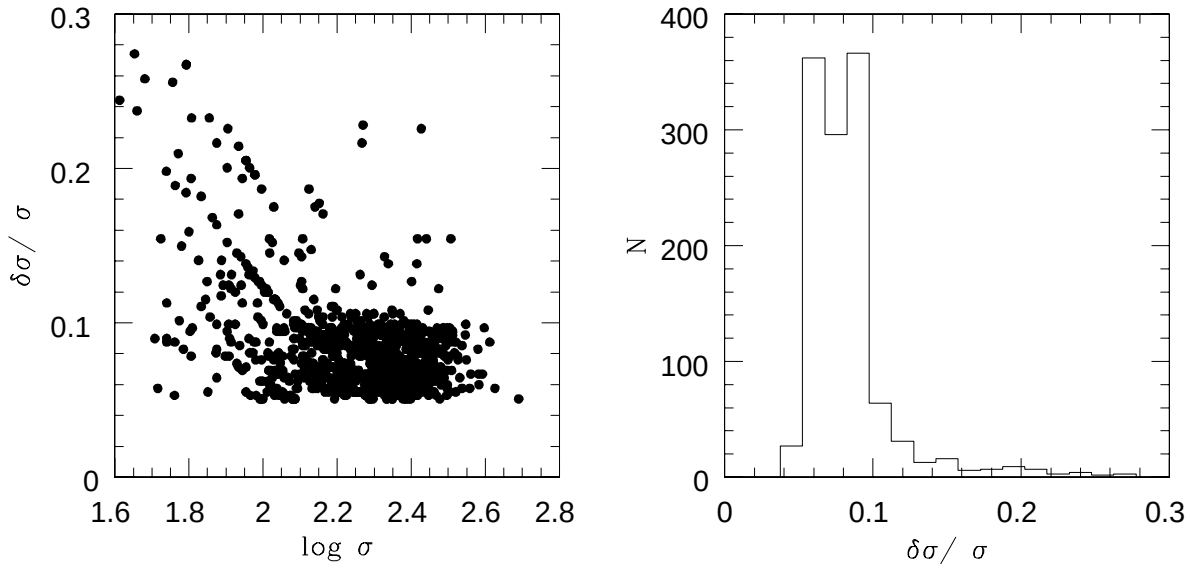

Figure 4.3 The fractional uncertainty in the velocity dispersion $\delta\sigma/\sigma$ as a function of σ (left), and the number of observed spectra as a function of $\delta\sigma/\sigma$ (right).

The normalization of the internally defined error is obtained by computing the ratio of the standard deviation of repeated exposures of the same galaxy, observed in the same run and with approximately the same S/N, to the internal error estimate. All internal errors for the run are multiplied by this factor. Typically, the errors of the measured redshifts range from 20 to 50 kms^{-1} depending mainly on the S/N of the spectrum. Figure 4.3 shows our final estimate of the fractional error $\delta\sigma/\sigma$ as a function of the velocity dispersion (left panel) as well as the number of observed galaxies that have a given $\delta\sigma/\sigma$ (right panel). The figure show that when $\sigma > 100$ kms^{-1} then the errors are essentially constant and less than about 10%, but they increase rapidly at the low-σ end. Although the median value of our errors is 0.078 ± 0.014, which is comparable to typical velocity dispersion errors quoted by other authors, the panel on the right shows that our error distribution is bimodal: it has well-defined peaks at $\delta\sigma/\sigma$ values of 0.06 and 0.09. This bi-modality arises mainly because some of our spectra were taken at low- whereas others were taken at high-resolution.

4.2.1.2 Aperture corrections

Final values of the velocity dispersion were obtained by applying an aperture correction to take into account the fact that the measured velocity dispersions depend on: 1) observational parameters such as the seeing and the size and shape of the spectrograph slit; 2) the distance of the galaxy, since a fixed slit size corresponds to different projected physical scales for galaxies at different distances; 3) the intrinsic properties of the galaxy, such as its velocity and luminosity profiles. Expressions for the aperture correction have been obtained empirically by Davies et al. (1987), using observations of nearby galaxies

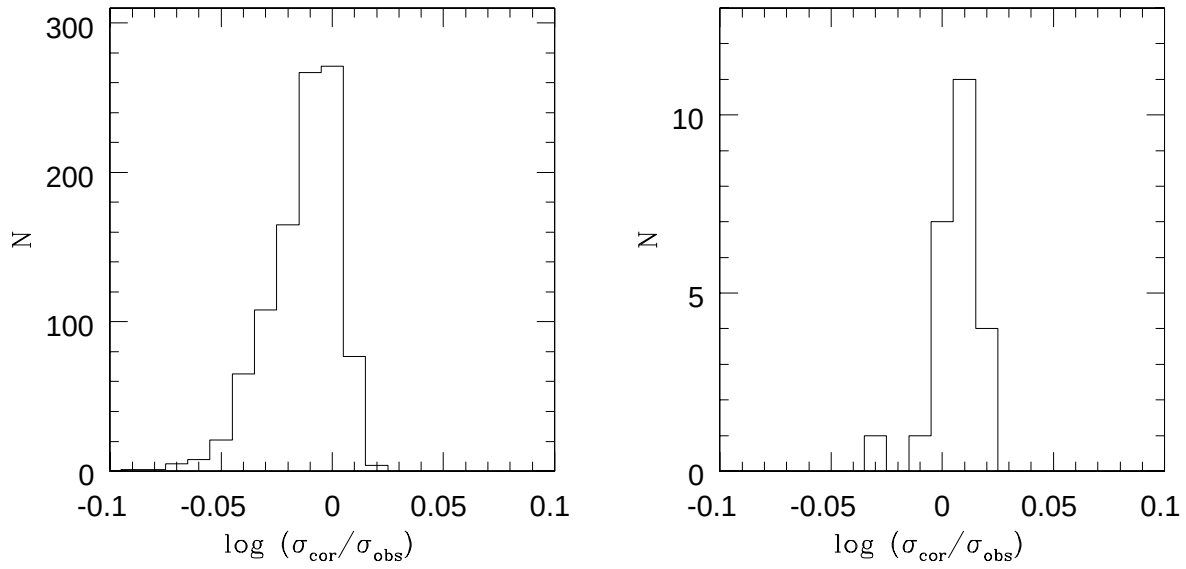

Figure 4.4 The distribution of the velocity dispersion aperture corrections applied to the ENEARf sample (left) and to the faint/distant cluster galaxies (right). In these plots, $\sigma_{\rm obs}$ is the raw observed value while $\sigma_{\rm cor}$ is the aperture-corrected value of the velocity dispersion.

with different apertures, and by Jørgensen et al. (1995b) using kinematic models. Here we adopt the standard metric aperture correction, the one most commonly used in the literature, given by:

$$\log\left(\frac{\sigma_{\rm cor}}{\sigma_{\rm obs}}\right) = 0.038 \log\left[\left(\frac{r_{\rm ap}}{r_{\rm norm}}\right)\left(\frac{cz}{cz_o}\right)\right] \qquad (4.1)$$

where $\sigma_{\rm obs}$ is the value of the velocity dispersion observed through an equivalent circular aperture of $r_{\rm ap}$, which is given by $r_{\rm ap} = 1.025\sqrt{wl/\pi}$ in arcsec, where w and l are the width and length of the slit, $\sigma_{\rm cor}$ is the corrected value normalized to a circular aperture of radius $r_{\rm norm} = 0.595\ h^{-1}$kpc ($h \equiv H_0/100$ kms^{-1} Mpc^{-1}), cz is the redshift of the galaxy, and cz_o is a reference redshift taken to be that of the Coma cluster. The standard aperture corresponds to 1.7 arcsec at the distance of Coma. Since most objects are nearby, the aperture correction for most of the sample galaxies is negative. The median difference is ~ -0.008 and the rms in $\log\sigma$ is ~ 0.010. Jørgensen et al. (1995b) found that this correction gives a similar result as when one uses the same power-law but considers the ratio of the equivalent slit aperture to the characteristic angular size of the galaxy. For the galaxies in our sample, this recipe mainly gives a zero-point shift in $\log\sigma$ while the spread of the corrections is small ($rms \sim 0.005$). An alternative relation is obtained by a combination of the two recipes (Baggley 1996). Apart from a zero-point shift in $\log\sigma$ the resulting correction is equivalent to the one we adopted (Eq. 4.1) showing a spread in the values of the correction of $rms \sim 0.011$.

Figure 4.4 shows the histogram of the applied aperture corrections of $\log\sigma_0$ for the

ENEARf sample (left) and for faint/distant cluster galaxies (right). We show these samples separately because they represent different pupulations which need different aperture corrections: most of the galaxies in the ENEARf sample have negative corrections, since they are larger or more nearby than a 20 arcsec galaxy at Coma distance; for the faint/distant cluster galaxies the correction is usually positive.

4.2.2 Line strengths

A number of studies (e.g. Gregg 1992; Jørgensen et al. 1996; Prugniel & Simien 1996; Colless et al. 1999) have shown that variations in stellar populations can affect the accuracy of the $D_n - \sigma_0$ or FP relations. Line indices are useful tools for studing the environment and the star formation history of a composite system such as a galaxy. In this thesis we will only present measurements of the Mg_2 line index (scaled to the Lick system); an accurate analysis of the other lines is still ongoing. We gave priority to the Mg_2 index in our analysis because it has been widely used as an indicator of metallicity and star-formation. Chapter 7 presents an interesting result in this regard, which was obtained from our measurements of this line.

The strength of the molecular Mg_2 feature measures the spectral intensity due to the combined effect of the broad MgH feature and the Mgb triplet. It is defined as

$$\mathrm{Mg_2} = -2.5 \log_{10} \frac{\int_{\lambda_1}^{\lambda_2} S(\lambda)/C(\lambda)\, d\lambda}{\Delta\lambda}, \tag{4.2}$$

where Mg_2 is in magnitudes, $\Delta\lambda = \lambda_2 - \lambda_1 = 42.5$ Å is the width of the Mg_2 bandpass (5154.1 – 5196.6 Å), $S(\lambda)$ is the object's spectrum and $C(\lambda)$ is a pseudo-continuum. Following Gonzáles (1993) and Worthey et al. (1994), $C(\lambda)$ was estimated by linearly interpolating between the mid-points of the side band-passes (4895.1 – 4957.6 Å and 5301.1 – 5366.1 Å) (the value assigned to the mid-point of each side-band is the average flux within the band). The wavelengths of the feature and of the continuum bands were shifted by $(1 + z)$ to account for the redshift of the galaxy. Then the Mg_2 index was calculated, in the rest frame of the galaxy, using the three wavelength regions. The flux in the line was calculated in the central region and then corrected for the continuum by linearly interpolating between the two side bands.

The measured spectral indices depend on spectral resolution as well as on the spectral response of the detector used. All these measurements must be placed on the same scale, so that the line strengths of galaxies observed with different instruments, with different telescopes, and by different observers can all be compared with each other. Since most of our spectra cannot be flux calibrated and were obtained at resolutions higher than the data leading to the definition of the Lick system the following procedure was adopted for measuring the Mg_2 line index.

First, all spectra were smoothed in velocity space with Gaussian filters of widths chosen to compensate for the relative resolution difference between the spectral resolution used in each of our observing runs and the Lick/IDS resolution of 8.6 Å. Second, we tried to account for the response of the detector on a run-by-run basis. This was done by fitting a low-order polynomial to the spectra of galaxies in common with the Faber et al. (1989) sample over a wavelength range of about 800 Å. The order of the fit was chosen so that after dividing the observed spectra by this polynomial, and then measuring the pseudo-continuum as described above, a good comparison with the values reported by

Faber et al. (1989) was obtained. This polynomial was then used, leaving the zero-point free, for all other spectra in the same run. The order of the polynomial depended on the resolution of the spectra: for our low-resolution spectra a linear fit worked well, while a high-order polynomial was required in the case of high-resolution spectra.

The following figures illustrate the effect of the variation in response between the line and continuum bands. Figure 4.5 shows the spectrum of NGC 541 observed at low- (dashed lines) and high-resolution (solid lines). Curves at the top of the figure show the observed spectra, the ones in the middle show the spectra smoothed to the Lick/IDS resolution, and the ones at the bottom show the spectra normalized by a low-order polynomial. At low resolution the continuum is determined better because a wider range in wavelength is covered. Figure 4.5 shows that for low resolution spectra the Mg_2 line appears deeper compared to the nearby continuum bands than it does in the high resolution spectrum. That is to say, measurements of the Mg_2 index show systematic offsets depending on the size of the wavelength range over which the continuum is determined.

Figure 4.6 shows this effect for a sample of galaxies which were selected because they were observed by us at both low and high resolution, as well as by Faber et al. (1989). To remove this effect we normalized the spectra by fitting a continuum, the same continuum for all the smoothed spectra of a given resolution, chosen such that the differences between our Mg_2 indices and those of the Lick system are minimized. The results of our procedure are shown in Figure 4.7 where the normalized spectra obtained in high and low resolution are compared. In contrast to the spectra in Figure 4.6, the normalized spectra here do not show any systematic differences in the Mg_2 absorption feature or in its red and blue continua.

The success of our method is further confirmed by Figure 4.8 which shows the difference between our measurements and those in common with Faber et al. (1989). We find no significant zero-point shift, and a relatively small scatter of 0.015 mag. We have also measured the Mg_2 line index directly, ignoring possible variations in the response function, following the usual prescription, for a few runs with available Lick standards. For these cases the line index is computed for the stars, the resulting value is then corrected to the Lick values, and the same correction is then applied to the galaxies. Comparison between the two methods led to consistent results: a scatter of about 0.014 mag, comparable to the scatter obtained from the comparison with galaxies measured in the Lick system by Faber et al. (1989).

4.2.2.1 Error estimates

The linestrength error estimates were obtained by using simulated spectra in the following way. For each run all high S/N stellar templates were used to generate a set of spectra of different S/N and velocity dispersions. This was done by adding Poisson noise and by convolving with a Gaussian with different *rms* to simulate galaxies with different velocity dispersions. For each template, a total of about 1000 simulated spectra were generated in 50 kms^{-1} intervals of velocity dispersion and S/N ratios in the range 10—60. For each template, σ, S/N and the rms value of the measured Mg_2 index, following the procedure described above, was computed. The error in the Mg_2 measurement for an object was assumed to be the largest value at the appropriate value of σ and S/N. Figure 4.9 shows the distribution of the estimated error δMg_2 as a function of the measured Mg_2 line index for all of our galaxies. We find that the median error is

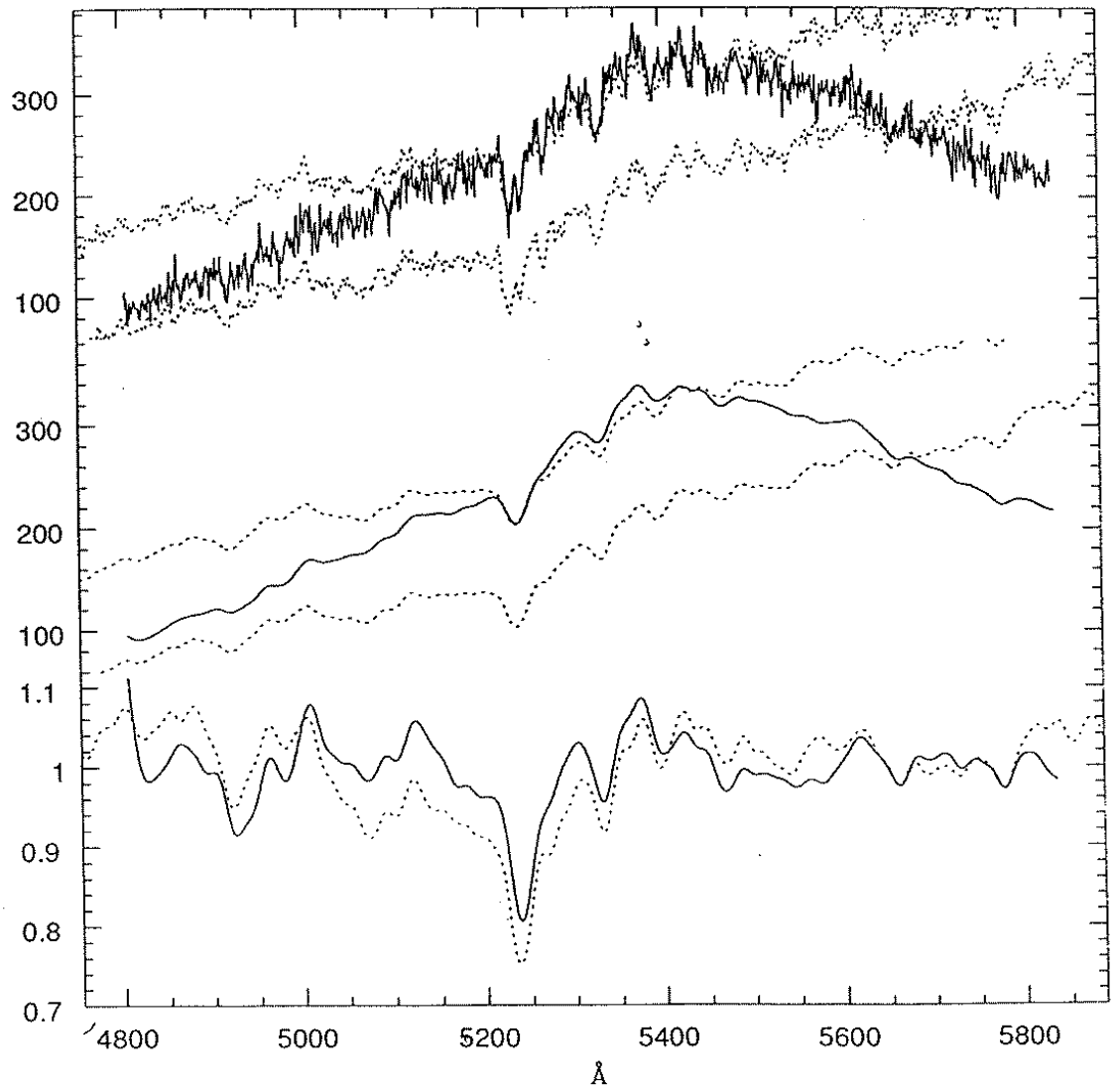

Figure 4.5 Comparison between one-dimensional spectra of NGC 541 obtained at high resolution (2 Å, solid lines) and at low resolution (4.97 Å, dashed lines). From top to bottom: the observed spectra, the spectra smoothed to the 8.6 Å Lick/IDS resolution, and the spectra normalized by a low-order polynomial. The main absorption line is the Mg_2 feature. For this galaxy, the red continuum of the Mg_2 index covers the wavelength region 4984-5048 Å, while the blue continuum ranges from 5397 to 5463 Å.

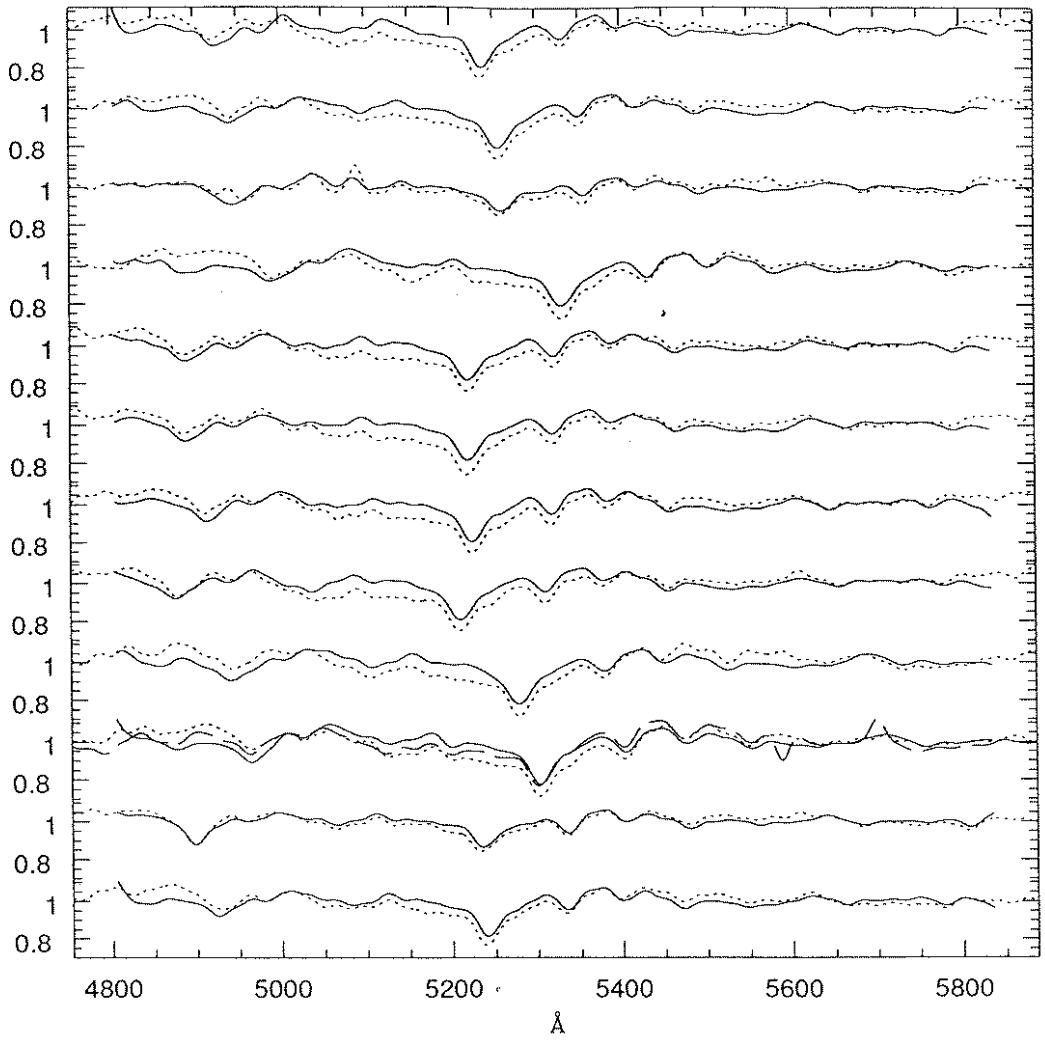

Figure 4.6 Comparison between normalized one-dimensional spectra of galaxies observed at high resolution (solid line) and at low resolution (dashed line). The spectra were normalized without taking the response of the detector into account. These galaxies were previously observed by Faber et al. (1989) and are used as calibrators of our linestrength measurements.

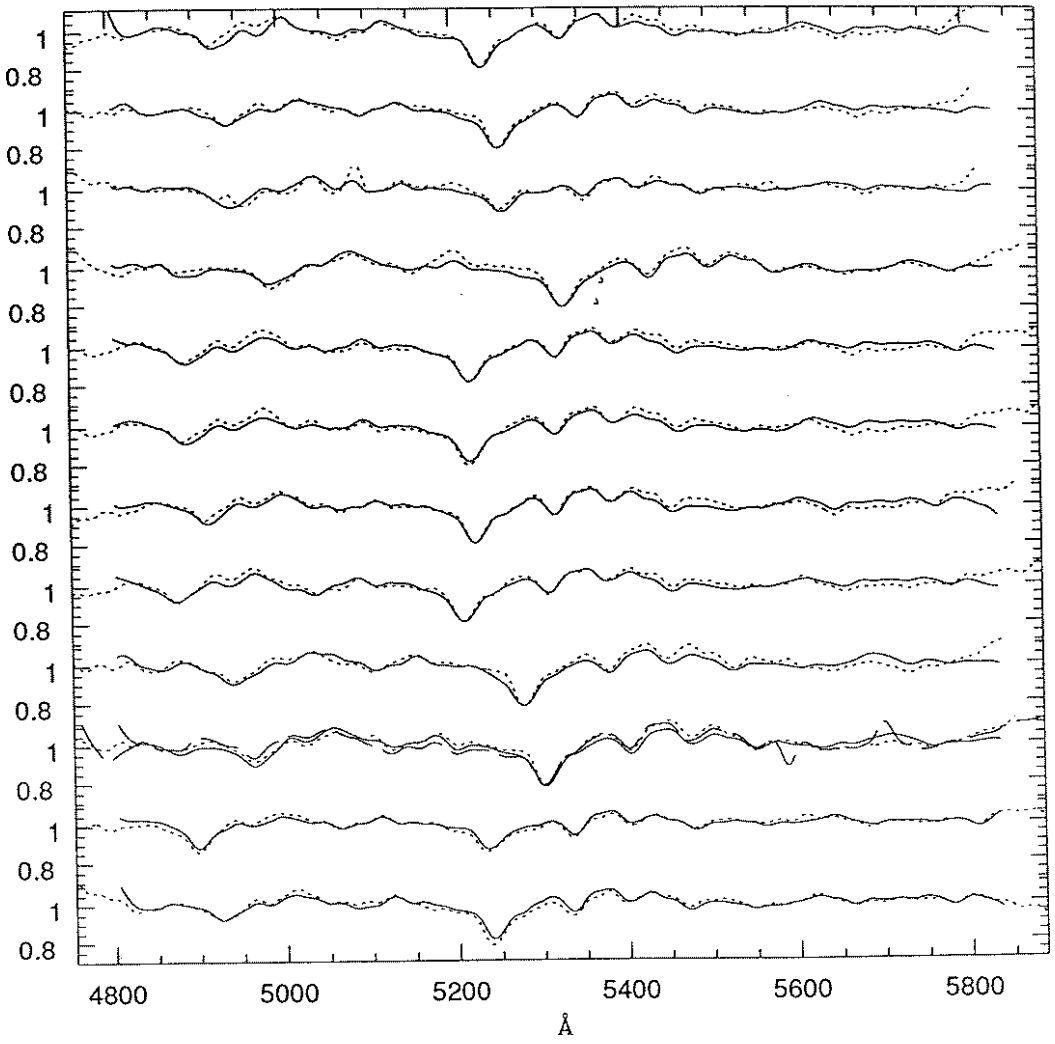

Figure 4.7 As in Figure 4.6, except that here the spectra were normalized by fitting a low-order polynomial to account for the response of the detector on a run-by-run basis.

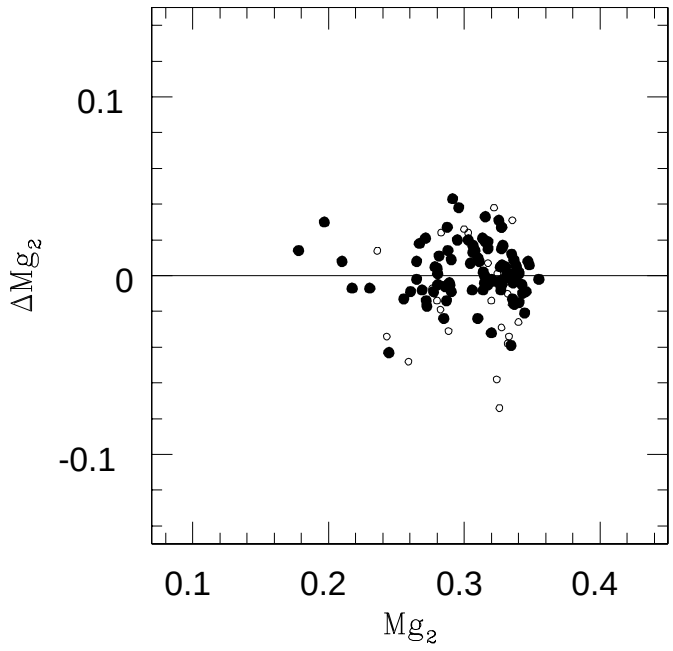

Figure 4.8 The velocity dispersion measurements derived from our spectra, observed at low resolution (open circles) and at high resolution (filled circles), versus the values obtained by Faber et al. (1989) (the Lick system).

0.008 ± 0.001 mag, which is comparable to the values obtained by other authors (e.g., JFKb found 0.013 mag).

4.2.2.2 Aperture and σ broadening corrections

Our final values for the Mg_2 line index are corrected for aperture effects and for the broadening of the line due to the velocity dispersion of the galaxies, which underestimates the value of the index for high-σ galaxies. We have adopted an aperture correction which assumes that the variation of the Mg_2 index as a function of radial distance along the galaxy is similar to the velocity profile (Franx et al. 1989). Therefore, the measured values of Mg_2 are corrected similarly to how we corrected the velocity dispersion:

$$Mg_2^{\rm cor} - Mg_2^{\rm obs} = 0.038 \log \left[\left(\frac{r_{\rm ap}}{r_{\rm norm}} \right) \left(\frac{cz}{cz_o} \right) \right] \tag{4.3}$$

We corrected for σ broadening as follows. First, the spectra of the standard stars in a run were convolved with Gaussians of different dispersions. Next, the ratio of the index measured in the original un-convolved spectra to that measured on the convolved spectra was determined as a function of the dispersion. A smooth curve was fitted to the ratios obtained for different templates. The correction for a galaxy of given σ was obtained from the value of this fit. All runs showed a correction of ~ 0.001 mag at

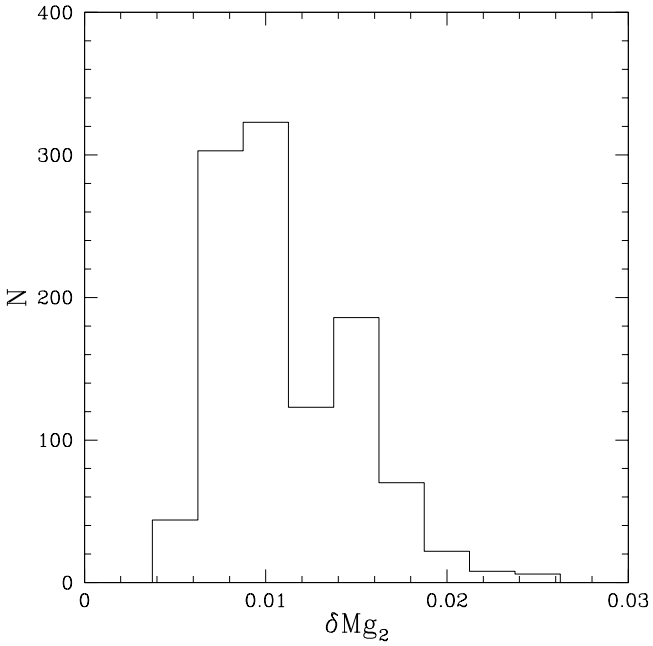

Figure 4.9 The distribution of the errors associated with our measured Mg_2 line indices.

$\sigma = 100$ kms^{-1} , and this correction increases approximately linearly to $\sim$ 0.004 mag at $\sigma = 400$ kms^{-1} .

4.2.3 Homogenizing the data

To make our spectroscopic measurements internally consistent we compared measurements from our different runs. We found that the differences show relative zero-point shifts, but no other systematic behavior. Therefore, measurements obtained in different observing runs can be brought onto a common system by simply applying zero-point corrections. The procedure we have adopted for doing this takes into account the number of overlaps available at each site and setup and tries to optimize the number of overlaps in the comparison so as to improve the statistics when determining the offset that is required to bring the different measurements to a common system. We use the high-resolution data from ESO (setup 4 in Table 4.2) as our reference system and bring all different runs at high-resolution to a common system as described below. This setup was chosen as our fiducial system because it has the best resolution, the largest number of spectra in our sample, and the largest number of repeated observations.

To determine the fiducial system we corrected our spectroscopic parameters using the mean difference Δx_i of the measurements of run i with all the other runs $j \neq i$ for galaxies in run j in common with those in i. This offset is computed with variance weighting using the estimated errors in each measurement:

$$\Delta y_i = \epsilon_i^2 \sum_{j \neq i} \sum_{k \in i,j} \frac{x_{ik} - x_{jk}}{\Delta x_{ik}^2 + \Delta x_{jk}^2} \tag{4.4}$$

Here k runs over the galaxies in common to runs i and j, $x_{i,k}$ corresponds to the measurement of either $log\sigma$ or Mg_2 for galaxy k in run i, and $\epsilon_{i,k}$ is the estimated error. The

Table 4.3 Internal comparisons of the homogeneized spectroscopic parameters

Site	N_c	$\Delta\log\sigma$ km/s	$\sigma_{\log\sigma}$ km/s	N_m	Δ Mg_2	$\sigma_{\mathbf{Mg_2}}$
(1)	(2)	(3)	(4)	(5)	(6)	(7)
ESO	290	0.003±0.003	0.057	280	0.000±0.003	0.026
MDM	109	0.005±0.004	0.043	106	-0.002±0.002	0.016
CASLEO	69	0.007±0.006	0.054	50	-0.003±0.002	0.021
All	468	0.004±0.003	0.053	436	-0.001±0.002	0.021

Notes: The differences are defined as "our - literature". The velocity dispersion and the Mg_2 linestrength measurements have been aperture corrected.

standard error in the mean, ϵ_i, is given by:

$$\epsilon_i = \left(\sum_{j \neq i} \sum_{k \in i,j} \frac{1}{\Delta x_{ik}^2 + \Delta x_{jk}^2} \right)^{-1/2} \tag{4.5}$$

We determined the most significant offset by finding the run with the maximum value of $\Delta x_i/\epsilon_i$, and iterating towards a common zero-point by subtracting this offset from the measurements of run i. We halted the process when the most significant offset was $\Delta_i/\epsilon_i < 2$. After four iterations we were able to determine the systematic offsets, for both velocity dispersion and Mg_2 index parameters, that must be applied to the measurements to create a homogeneous fiducial data set. These corrections are relatively small: they are on the order of ~ 0.015 dex and $\lesssim$0.020 mag.

Once the fiducial system was defined, we compared aperture corrected values, whenever necessary, obtained using different setups at ESO. The measurements obtained from MDM and CASLEO spectra were corrected in the following way: for runs with a significant number of galaxies in common with our reference system, the measured values were directly compared to this system, while the others were compared to calibrated measurements made with the same telescope. Table 4.3 summarizes the number of multiple measurements available from each site. Note that the numbers reported refer to comparisons of homogeneized data. The relatively large number of overlapping observations provides the information required for deriving suitable statistical corrections for all runs at the different sites.

The offsets derived from the comparison of all the runs that were not used in the definition of the fiducial system, typically $\lesssim$0.018 dex and $\lesssim$0.020 mag, are consistent with those found in defining the reference system. This suggests that the dataset is highly homogeneous. For only one run, from CASLEO, which contributes the least to the overall sample, was a large correction, $\Delta \log \sigma = 0.095$ dex required. The corrections to the Mg_2 index measured using setups with similar resolution were small, typically

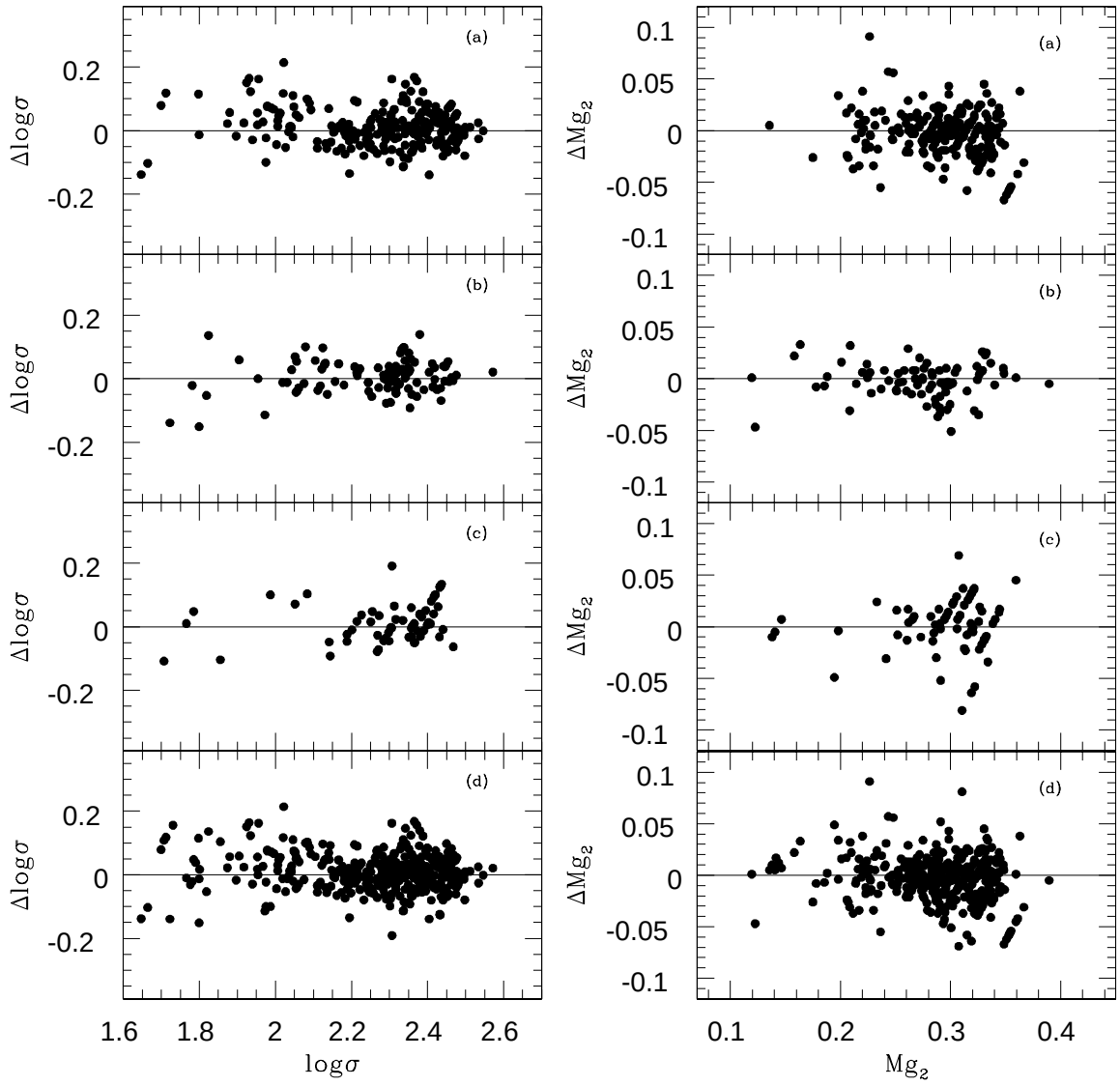

Figure 4.10 Internal consistency of the derived velocity dispersion (left) and Mg_2 line index (right). Internal comparisons between measurements obtained (a) at ESO (setups 1 to 4), (b) at MDM (setups 5 to 10), (c) at CASLEO (setup 11). The overall comparisons of our measurements are shown in panels (d). Δ means a difference between each result obtained from different observations and the mean value associated with the galaxy.

Table 4.4 External comparisons of spectroscopic parameters

Sources	N_c	$\Delta\log\sigma$ km/s	$\sigma_{\Delta\log\sigma}$ km/s	N_c	Δ Mg_2	$\sigma_{\Delta Mg_2}$
(1)	(2)	(3)	(4)	(5)	(6)	(7)
LC	33	-0.020±0.012	0.054	–	–	–
7S	159	-0.005±0.005	0.052	80	0.003±0.002	0.019
D	21	0.010±0.012	0.056	16	0.004±0.005	0.015
JFK	47	0.003±0.008	0.060	32	0.001±0.003	0.017
Lc	7	0.009±0.011	0.020	–	–	–
S	8	0.011±0.014	0.043	5	0.002±0.012	0.021

Notes: All differences are "our measurement" - "literature measurement". The references are: LC: Lucey & Carter (1988); 7S: Faber et al. (1989); D: Dressler (1987), Dressler et al. (1991); JFK: Jørgensen, Franx, & Kjaergaard (1995b); Lc: Lucey et al. (1997); S: Smith et al. (1997).

$\lesssim$0.015 mag.

The final results, obtained after the uniformization process, are presented in Figure 4.10. The figure shows the differences between $\log\sigma$ (left panels) and the Mg_2 line index (right panels) as measured in different runs, but after applying the zero-point corrections. The first three panels correspond to the different sites (see figure caption) while the bottom panels show the overall comparison. The results are summarized in Table 4.3 in which: column (1) gives the site; column (2) the number of repeated measurements, N_m, in the same or in different runs; columns (4) and (5) the mean and *rms* offset of the differences in the calibrated $\log\sigma$ and Mg_2 measurements. The results show that the corrections lead to an internally consistent system with only a small ($\lesssim$ 1%) residual offset in the velocity dispersion. We should point out that there are 21 galaxies MDM and 11 galaxies observed at CASLEO in common with ESO observations.

4.2.4 External comparisons

After all measurements are brought into a consistent system, multiple measurements of the same galaxy are combined using their individual errors as weights as described in the next section. These final values were then compared with those of previous studies. To ensure consistency, the same aperture correction to the raw measurements obtained by us were applied to the data from the literature. The left and right panels of figure 4.11 show the differences between our measurements and those of other authors, for $\log(\sigma)$ and Mg_2, respectively. The results of the individual comparisons are presented in Table 4.4. A total of 201 galaxies were used to make the comparison. We find an overall residual difference of -0.002±0.004 dex and a scatter of 0.051 in $\log(\sigma)$. For Mg_2 we find an offset of 0.003 ± 0.002 mag and a scatter of 0.018 mag in Mg_2. These observed scatters are consistent with an error per galaxy of about 8% in velocity dipersion and

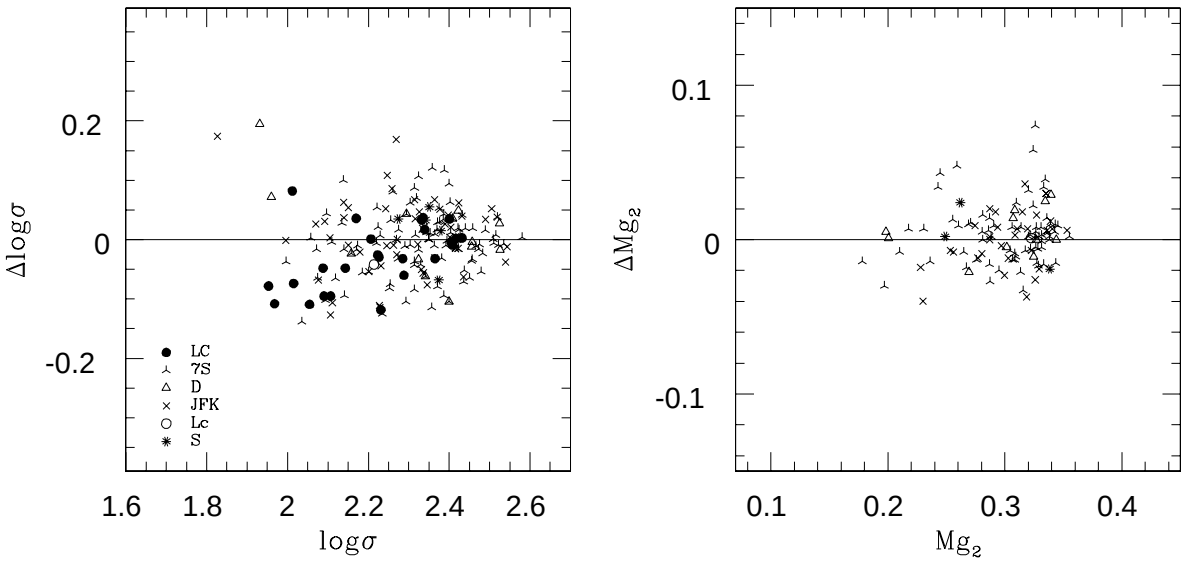

Figure 4.11 Comparison of the velocity dispersion (left) and the Mg_2 line index (right) of the observed galaxies with aperture corrected data from the literature. Δ means "our-literature" measurements. The literature sources are: 7S, Faber et al. (1989); D, Dressler (1987), Dressler et al. (1991); JFK, Jørgensen et al. (1995b); LC, Lucey & Carter (1988); Lc, Lucey et al. (1997); and S, Smith et al. (1997).

0.01 mag in Mg_2. Note, however, that most of the available data in the literature is limited to values $\gtrsim$ 100 kms^{-1} and Mg_2 $\gtrsim$0.18 mag. In fact, as we saw earlier, based on our internal estimates we expect the measurement errors to increase at low values of measured quantities (as they approach the resolution limit).

As for the photometric data, there are small zero-point offsets in the parameters, which arise from the different combinations of telescope-detector-spectrograph used in the different observations. To use the public data these offsets are removed as described in Chapter 5. This homogenization is essential if we wish to use the data in the literature to improve the completeness of the ENEARf, to enlarge the ENEARc cluster sample (Chapter 5), and to decrease the errors in the parameters of interest by combining data from multiple observations and external data. A homogeneous sample of this size is extremely useful for analysis such as the derivation of a distance indicator (Chapter 6) or the peculiar motions of early-type galaxies in the nearby Universe (Chapter 7).

4.3 The spectroscopic catalog

The final value of the spectroscopic parameters for a galaxy with multiple observations is given by the error weighted mean of the individual measurements. The final error for these galaxies is given by the standard deviation of the σ values. Whenever possible, values which differ by more than three times the *rms* from the mean were removed to

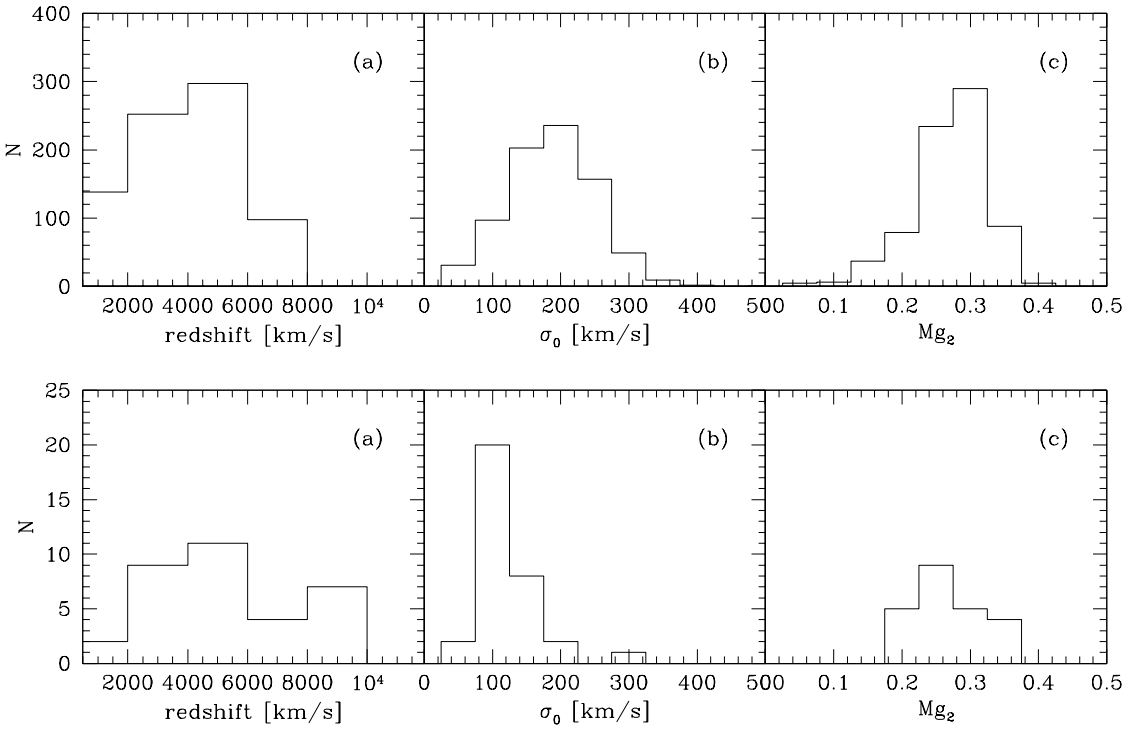

Figure 4.12 The distribution of (a) redshift, (b) velocity dispersion, and (c) Mg_2 linestrength for galaxies in the ENEARf sample (upper panels) and for faint/distant cluster galaxies (lower panels).

avoid biasing the results due to a few outliers. For small values of σ and Mg_2 only the measurements obtained at high-resolution are combined.

Tables 4.5 - 4.7 list the final, fully corrected and, if more than one observation is available, combined spectroscopic parameters derived from the analysis of our spectra for the three sub-samples of observed galaxies: 1) ENEARf (933 entries); 2) the set of faint and/or more distance cluster galaxies (50 entries); and 3) others (120 entries). Column (1) gives the standard name of the object, from NGC, IC, MCG, the Guide Star Catalog (Lasker et al. 1990) or its coordinates whenever none of the above are available; columns (2) and (3) give the 1950.0 equatorial coordinates; column (4) the morphological parameter T (Lauberts & Valentjin 1989); column (5) the total m_B magnitude given by the original catalogs from which our sample was drawn; column (6) the number of measurements used to obtain the combined redshift and velocity dispersion; columns (7) and (8) the measured heliocentric redshift and its error; columns (9) and (10) the velocity dispersion with its error; column (11) the number of measurements used to obtain the Mg_2 line index; columns (12) and (13) the Mg_2 line index and its error; column (14) galaxies showing features in their spectra; and in column (15), those galaxies which were previously observed by other authors are indicated with an asterisk. Here we present only the first few entries of the table which can be retrieved in electronic form upon

request.

Figure 4.12 shows the distribution of redshifts, velocity dispersions and Mg_2 line indices for the two final "homogenous" sub-samples, ENEARf (upper panels), and the faint/distant cluster galaxies (lower panles). These are the measurements presented in Tables 4.5 and 4.6. We show the two samples separately because they represent different pupulations with different overall properties. In the upper panel (a), the sharp break seen in the redshift distribution at $cz = 7000$ kms^{-1} reflects the redshift cutoff criteria adopted for the ENEARf sample. Galaxies beyond this redshift are seen only in the lower panel. A remarkable difference between the two samples is seen in the velocity dispersion distibutions. For the ENEARf galaxies the distribution of σ_0 has a peak at ~ 190 kms^{-1} and is well represented by a Gaussian with a dispersion of ~ 63 kms^{-1} . For the second sample, the distribution is dominated by galaxies with a velocity dispersion of ~ 100 km. This sample includes only the faint or distant galaxies; panel (a) shows that thay are primarily faint nearby galaxies ($cz < 6000$ kms^{-1}). The peak at ~ 100 kms^{-1} seen in panel (b) is due to these faint galaxies while the tail at higher values is caused by the more distant, brighter, and therefore more massive galaxies. The median value of the Mg_2 line index is only slightly smaller for the faint cluster galaxies than for the ENEARf galaxies. However, the distribution of this last sample shows a tail at lower values ($\lesssim 0.20$). These lower values of the Mg_2 linestrength are usually associated with galaxies that have large D/B ratios (e.g., 0303+4140, 235 G 51, 2258+2953), or with features in their spectra (weak emission lines e.g., 0746+7338, 0908+4651, 27 G 21, 2308+2922; depressions e.g., NGC 3598), even though some galaxies (e.g., 358 G 59, 286 G 50) do not show any peculiarities either in the spectrum or in the image. Some galaxies with large D/B ratios (e.g., NGC 3928, NGC 7743) or with peculiar features (e.g., NGC 5666) also show weak emission lines.

TABLE 4.5

THE SPECTROSCOPIC CATALOG OF THE ENEARF GALAXIES

Name	α (1950)	δ (1950)	T	m_B mag	N_{obs}	cz_{hel} km/s	$\epsilon_{cz_{hel}}$ km/s	$\log\sigma$	$\epsilon_{\log\sigma}$	N_{Mg_2}	Mg_2	ϵ_{Mg_2}	N_{notes}	Lit
(1)	(2)	(3)	(4)	(5)	(6)	(7)	(8)	(9)	(10)	(11)	(12)	(13)	(14)	(15)
-0201019	00:02:42	-11:45:00	-2	14.50	3	6745	30	2.253	0.018	3	0.259	0.006		
-0101033	00:04:00	+03:58:00	-3	13.50	2	6204	22	2.346	0.023	2	0.283	0.007		
0004+4646	00:04:54	+46:46:00	-2	14.30	2	5277	57	2.313	0.019	2	0.270	0.004		
N43	00:10:24	+30:39:00	-2	13.90	2	4785	22	2.299	0.019	2	0.290	0.004		
0011+3037	00:11:18	+30:37:00	-7	14.20	1	4735	30	2.146	0.039	1	0.274	0.064		
-0101058	00:12:06	+07:37:30	-3	12.50	1	5495	22	2.393	0.028	0	0.000	0.000		
N63	00:15:06	+11:10:00	-5	12.60	1	1179	20	1.835	0.087	1	0.088	0.126		
N68	00:15:42	+29:48:00	-3	14.05	1	5711	29	2.385	0.033	1	0.304	0.034		
N78A	00:17:53	+00:33:20	-2	14.50	1	5481	26	2.335	0.038	1	0.308	0.040		
N108	00:23:18	+28:56:00	-2	13.30	2	4737	25	2.197	0.019	2	0.234	0.003		
-0102016	00:24:21	+02:46:30	-3	14.00	1	4346	25	2.132	0.038	0	0.000	0.000		
N125	00:26:18	+02:33:00	-2	13.83	1	5354	24	2.106	0.037	1	0.213	0.054		
N128	00:26:42	+02:35:00	-2	12.92	1	4227	21	2.354	0.031	0	0.000	0.000		
194G21	00:27:19	-51:47:42	-2	14.40	1	3438	25	2.356	0.026	1	0.295	0.037		
0031+0659A	00:31:24	+06:59:00	-2	14.50	1	5449	29	2.173	0.026	1	0.255	0.043		
-0202055	00:32:06	-11:02:00	-2	14.00	1	6155	29	2.301	0.041	1	0.257	0.043		
N160	00:33:24	+23:41:00	-2	13.77	1	5327	29	2.283	0.036	1	0.298	0.037		
-0202066	00:33:30	-10:23:00	-3	13.50	1	5981	25	2.375	0.030	0	0.000	0.000		
540G7	00:35:16	-18:07:30	-5	13.90	7	6027	27	2.438	0.030	6	0.288	0.003		*
N183	00:35:48	+29:15:00	-5	13.80	1	5402	31	2.368	0.028	1	0.293	0.029		
N193	00:36:42	+03:03:00	-3	14.30	2	4340	25	2.304	0.022	2	0.295	0.001		
0036+2522	00:36:48	+25:22:00	-3	14.50	1	4614	29	2.176	0.031	1	0.262	0.032		
0037+4125	00:37:36	+41:25:00	-5	9.40	2	857	30	1.712	0.064	2	0.069	0.011		
N223	00:39:48	+00:34:00	-5	14.50	1	5355	25	2.073	0.027	1	0.190	0.039		
-0103001	00:41:00	+08:28:30	-2	14.50	1	6039	43	2.229	0.024	1	0.228	0.025		
N233	00:41:00	+30:19:00	-5	13.80	1	5430	27	2.352	0.028	1	0.239	0.046		
N252	00:45:18	+27:21:00	-2	13.40	1	4990	31	2.293	0.028	1	0.307	0.029		
-0103018	00:47:48	+06:07:30	-3	13.50	2	5820	32	2.362	0.034	2	0.309	0.007		
-0103019	00:48:12	+07:09:00	-2	13.50	1	4753	22	2.164	0.040	1	0.280	0.042		
-0103021	00:48:30	+07:20:00	-2	13.50	2	1729	18	2.036	0.035	1	0.231	0.071		*
-0203028	00:48:54	+08:51:00	-3	14.00	2	4228	31	2.310	0.015	2	0.267	0.003		
N279	00:49:36	+02:29:21	-2	14.00	1	3878	23	1.888	0.067	1	0.110	0.078		
79GA7	00:50:24	-65:29:54	-2	14.00	1	6577	27	1.997	0.246	1	0.037	0.385		
2G10	00:52:36	-84:07:42	-3	14.40	1	4721	20	2.439	0.031	1	0.322	0.036		
N304	00:53:24	+23:51:00	-2	14.00	1	4991	31	2.349	0.025	1	0.270	0.041		
-0103049	00:55:36	+08:30:00	-3	14.50	2	4619	31	2.272	0.018	2	0.251	0.008		
0056+2335	00:56:18	+23:35:00	-5	14.50	1	5058	27	2.014	0.053	1	0.196	0.055		
295G26	00:57:28	-40:36:06	-2	14.30	1	6983	26	2.322	0.026	1	0.268	0.037		
-0103079	01:00:42	+03:52:00	-5	14.50	1	2601	33	1.689	0.027	1	0.095	0.038		
-0103081	01:00:48	+06:37:00	-2	12.50	1	2406	16	2.182	0.022	0	0.000	0.000		
N384	01:04:36	+32:02:00	-5	14.45	1	4287	23	2.299	0.042	1	0.282	0.044		
0105+3923	01:05:48	+39:23:00	-3	13.30	1	6149	28	2.368	0.025	1	0.321	0.040		
13G12	01:06:21	-80:34:24	-2	13.56	1	4249	27	2.082	0.032	1	0.197	0.038		
412G7	01:06:24	-28:50:54	-3	14.40	1	5447	37	2.265	0.037	1	0.306	0.038		
I1639	01:09:12	+00:55:00	-5	14.20	2	5395	23	1.982	0.037	2	0.208	0.009		
N420	01:09:18	+31:52:00	-2	13.40	1	4951	21	2.293	0.042	1	0.251	0.043		*
N429	01:10:24	+00:36:00	-2	14.40	1	5625	23	2.256	0.037	1	0.271	0.038		
N430	01:10:30	+00:31:00	-5	13.60	2	5284	25	2.510	0.082	1	0.296	0.224		*
0111+3327	01:11:18	+33:27:00	-2	14.00	1	6297	20	2.297	0.025	1	0.293	0.041		
N442	01:12:06	+01:17:00	-3	14.50	2	5620	25	2.295	0.025	2	0.265	0.036		
352G28	01:12:40	-32:30:24	-2	13.90	2	5852	25	2.109	0.063	1	0.285	0.122		
N448	01:12:48	+01:53:00	-2	13.20	1	1917	22	2.038	0.024	1	0.262	0.037		*
N455	01:13:42	+04:55:00	-2	13.90	3	5269	22	2.311	0.014	3	0.223	0.002		
+0104023	01:14:00	+08:14:00	-3	14.50	1	5594	39	2.310	0.037	1	0.302	0.061		
113G36	01:17:38	-58:47:12	-2	13.60	1	5161	26	2.332	0.026	1	0.254	0.037		
476G4	01:18:45	-26:59:18	-2	13.70	1	5853	25	2.289	0.026	1	0.256	0.038		
+0104030	01:20:24	+04:52:00	-3	14.50	1	5299	20	2.358	0.030	1	0.321	0.031		
0120+3257	01:20:42	+32:57:00	-2	14.00	1	4288	52	2.471	0.026	1	0.311	0.043		
0120+3300	01:20:48	+33:00:00	-5	13.00	1	4915	29	2.469	0.027	1	0.328	0.043		
0120+3302	01:20:48	+33:02:00	-5	14.50	1	5519	24	2.333	0.025	1	0.329	0.041		
N516	01:21:24	+09:18:00	-2	14.30	1	2432	26	1.670	0.112	1	0.170	0.175		
0121+3311	01:21:54	+33:11:00	-2	13.60	2	4168	22	2.340	0.020	2	0.248	0.005		
N525	01:22:12	+09:26:00	-2	14.50	2	2146	31	1.926	0.061	2	0.207	0.019		
+0104040	01:22:36	+04:57:00	-2	14.50	1	5722	26	2.251	0.036	1	0.205	0.042		
0122+3325	01:22:42	+33:25:00	-2	13.70	1	4879	28	2.388	0.027	1	0.275	0.045		*
I1700	01:22:42	+14:36:00	-5	14.30	1	6356	19	2.317	0.042	1	0.246	0.043		
0122+3428	01:22:54	+34:28:00	-3	13.10	2	4862	22	2.391	0.018	2	0.275	0.001		
N533	01:22:54	+01:30:00	-5	13.44	2	5544	18	2.454	0.015	2	0.337	0.008		*

NOTE.—In column (17) galaxies previously observed by other authors are indicated with an asterisk.

TABLE 4.6

THE SPECTROSCOPIC CATALOG OF THE FAINT/DISTANT CLUSTER GALAXIES

Name	α (1950)	δ (1950)	T	m_B mag	N_{obs}	cz_{hel} km/s	$\epsilon_{cz_{hel}}$ km/s	$\log\sigma$	$\epsilon_{\log\sigma}$	N_{Mg_2}	Mg_2	ϵ_{Mg_2}	N_{notes}	Lit
(1)	(2)	(3)	(4)	(5)	(6)	(7)	(8)	(9)	(10)	(11)	(12)	(13)	(14)	(15)
ZH59	01:20:00	+02:40:00	-2	15.35	1	5234	41	2.062	0.035	1	0.203	0.037		
N1274	03:16:21	+41:22:00	-5	15.10	1	6447	96	2.288	0.045	0	0.000	0.000		*
0329-3627	03:29:13	-36:27:34	-2	14.76	1	1822	50	1.352	0.335	1	0.071	0.391		
0332-3542	03:32:34	-35:42:45	-5	14.81	1	1233	61	2.140	0.040	1	0.150	0.046		
0334-3532	03:34:59	-35:32:19	-2	14.77	1	1765	32	1.758	0.044	1	0.188	0.051		
0336-3536	03:36:12	-35:36:09	-3	14.82	1	855	32	1.791	0.059	1	0.123	0.069		
R154	10:32:15	-28:18:33	-2	15.36	1	3485	27	2.230	0.042	1	0.286	0.085		
501G27	10:33:37	-27:03:35	-5	15.25	1	3207	25	1.908	0.053	0	0.000	0.000		*
RMH28	10:34:02	-27:05:41	-2	15.19	1	3006	24	2.036	0.041	0	0.000	0.000		*
RMH29	10:34:06	-27:03:33	-2	14.93	1	3441	27	2.349	0.027	1	0.292	0.058		*
437G9	10:34:14	-27:57:24	-3	14.74	1	3460	20	2.011	0.054	1	0.255	0.090		
D195	10:34:28	-27:07:44	-5	16.03	1	4478	35	2.052	0.029	1	0.248	0.061		*
R338	10:35:19	-26:47:51	-2	15.46	1	4372	34	2.189	0.022	1	0.191	0.045		*
437G27	10:36:21	-28:30:36	-2	15.42	1	3867	51	1.535	0.109	1	0.191	0.194		
R466	10:38:11	-27:36:00	-2	14.62	1	3992	31	1.988	0.022	1	0.183	0.045		
N4467	12:26:58	+08:16:10	-5	15.07	1	1426	11	1.766	0.036	0	0.000	0.000		*
D29	12:46:52	-41:06:59	-2	14.58	1	3672	29	1.973	0.056	1	0.237	0.114		*
J357	12:47:06	-40:57:16	-5	15.18	1	2176	17	2.106	0.038	0	0.000	0.000		*
D49	12:47:25	-40:56:57	-5	15.72	1	2939	23	2.052	0.041	0	0.000	0.000		*
1995.1986	12:56:43	+28:07:27	-2	16.62	1	6709	72	2.199	0.028	1	0.329	0.045		*
1995.2006	12:57:04	+28:07:10	-2	16.53	1	6950	70	2.413	0.040	1	0.325	0.066		
1995.1803	12:57:19	+28:13:39	-2	17.32	1	7681	50	2.141	0.038	1	0.164	0.061		
1995.1849	12:57:31	+28:11:57	-2	17.33	1	7789	70	2.004	0.057	1	0.260	0.093		
1995.1051	12:59:23	+27:52:21	-2	17.36	1	8238	13	1.912	0.087	1	0.242	0.141		
1995.0429	12:59:36	+27:55:17	-2	17.33	1	7095	20	2.019	0.052	1	0.220	0.105		
1346-3034	13:46:15	-30:34:16	-5	14.71	2	4856	38	1.843	0.100	1	0.135	0.190		
1348-3015	13:48:19	-30:15:48	-5	15.89	1	4743	37	2.013	0.035	0	0.000	0.000		
445G62	13:49:16	-30:12:18	-2	15.43	1	4705	20	1.973	0.035	1	0.216	0.073		
1356-3404	13:56:55	-34:04:31	-5	15.17	1	4224	33	1.993	0.022	0	0.000	0.000		*
384G33	13:58:33	-34:00:03	-2	14.75	1	3756	30	1.899	0.041	1	0.226	0.086		
1400-3333	14:00:11	-33:33:53	-2	15.66	1	3851	30	2.259	0.059	0	0.000	0.000		
384G37	14:00:38	-33:50:02	-2	14.78	3	5723	45	1.988	0.049	2	0.264	0.010		
1400-3356	14:00:43	-33:56:35	-2	16.01	1	4502	20	1.958	0.059	1	0.261	0.119		
1401-3340	14:01:12	-33:40:24	-5	16.56	1	4961	57	2.147	0.026	0	0.000	0.000		
1403-3404	14:03:07	-34:04:20	-2	14.76	1	4526	36	1.975	0.038	0	0.000	0.000		
1403-3257	14:03:10	-32:57:58	-2	15.30	2	4129	33	1.959	0.049	1	0.246	0.165		
1404-3403	14:04:57	-34:03:56	-2	15.73	1	4437	20	1.995	0.054	1	0.185	0.110		
1842-6324a	18:42:09	-63:24:53	-2	15.03	1	4206	33	2.062	0.046	1	0.274	0.094		*
2343-2817	23:43:46	-28:17:02	-2	15.50	1	7551	75	2.230	0.030	1	0.277	0.031		*
2343-2816	23:43:47	-28:16:50	-5	15.03	1	8673	44	2.209	0.039	1	0.273	0.041		*
2344-2812	23:44:36	-28:12:28	-2	16.14	1	8784	70	2.010	0.043	1	0.279	0.072		*
2344-2824	23:44:40	-28:24:07	-5	16.35	2	8301	75	2.177	0.021	1	0.277	0.032		*
2344-2823	23:44:47	-28:23:49	-2	14.88	1	8299	35	2.219	0.038	1	0.338	0.040		*
2344-2824a	23:44:52	-28:24:50	-5	14.76	1	8302	66	2.450	0.032	0	0.000	0.000		*
2344-2823b	23:44:52	-28:23:13	-5	14.20	1	8231	65	2.442	0.032	1	0.347	0.033		*
2344-2823a	23:44:55	-28:23:06	-5	14.05	1	8423	20	2.222	0.042	1	0.357	0.043		*
2345-2817	23:45:03	-28:17:25	-2	17.25	1	7912	63	1.922	0.038	1	0.255	0.040		*
2345-2830a	23:45:44	-28:30:36	-5	15.05	1	7888	55	2.557	0.037	1	0.329	0.057		*
2345-2833	23:45:50	-28:33:24	-2	15.85	1	8117	75	2.216	0.030	1	0.298	0.031		*
471G27	23:49:15	-28:14:36	-2	14.50	1	8813	36	2.141	0.028	1	0.186	0.041		

NOTE.—As in Table 4.5

TABLE 4.7

THE SPECTROSCOPIC CATALOG OF "OTHER" GALAXIES

Name	α (1950)	δ (1950)	T	m_B mag	N_{obs}	cz_{hel} km/s	$\epsilon_{cz_{hel}}$ km/s	$\log\sigma$	$\epsilon_{\log\sigma}$	N_{Mg_2}	Mg_2	ϵ_{Mg_2}	N_{notes}	Lit
(1)	(2)	(3)	(4)	(5)	(6)	(7)	(8)	(9)	(10)	(11)	(12)	(13)	(14)	(15)
409G12	00:02:09	-30:45:42	-5	14.23	1	7985	63	2.387	0.033	1	0.243	0.051		*
-0102001	00:17:27	+06:37:00	0	14.50	1	3725	39	1.619	0.312	1	0.171	0.486		
-0202011	00:21:48	-14:13:00	0	14.00	2	7330	22	2.182	0.028	2	0.288	0.002		
112GA8	00:33:34	-59:58:12	-2	14.26	1	10133	20	2.455	0.036	1	0.306	0.042		
-0202085	00:39:03	-10:18:00	0	13.50	1	3947	26	2.232	0.032	1	0.276	0.033		
N386	01:04:46	+32:05:43	0	15.34	1	5024	24	2.323	0.035	1	0.306	0.036		*
244G22	01:20:40	-42:49:30	-2	14.40	1	7031	20	2.256	0.029	1	0.291	0.034		
D15	01:22:18	+01:57:07	0	15.78	1	5305	42	2.055	0.036	1	0.162	0.038		
N538	01:22:53	+01:48:37	1	14.73	2	5364	42	2.323	0.024	2	0.303	0.002		*
0123-0132	01:23:25	+01:32:54	-2	0.00	1	5312	20	2.389	0.033	1	0.324	0.034		
+0106025	01:58:45	+07:04:00	0	13.50	1	4078	28	2.162	0.028	1	0.282	0.029		
478G12	02:09:05	-25:15:12	-2	14.40	1	9522	55	2.394	0.038	1	0.333	0.044		
0212+3517	02:12:36	+35:17:00	-3	14.00	1	8168	29	2.329	0.025	1	0.277	0.041		
545G17	02:24:43	-19:28:36	-2	14.40	1	9904	28	2.413	0.032	1	0.326	0.037		
-0207040	02:33:18	-13:53:30	0	15.00	1	4592	20	2.075	0.034	1	0.196	0.036		
+0107030	02:37:54	+05:40:00	-3	14.00	1	7057	27	2.288	0.027	1	0.287	0.043		
154G9	02:41:23	-54:47:18	-2	14.06	2	9760	20	2.431	0.018	2	0.324	0.002		
479G30	02:41:51	-26:23:54	-2	14.40	1	10532	35	2.280	0.028	1	0.268	0.033		
0246+4647	02:46:24	+46:47:00	-3	14.50	1	7730	70	2.561	0.026	1	0.357	0.042		
-0208047	03:03:48	+09:44:30	0	14.50	1	4504	38	2.287	0.043	1	0.289	0.045		
N1239	03:08:22	+02:44:30	-2	14.61	1	8643	20	2.424	0.030	1	0.319	0.050		
0310-0030	03:10:12	+00:30:00	0	14.50	1	6826	21	2.242	0.037	1	0.286	0.039		
-0209022	03:15:12	-10:28:00	-2	14.00	2	8985	39	2.435	0.022	2	0.323	0.003		
301G2	03:15:28	-41:17:24	0	9.68	2	890	23	2.269	0.057	1	0.332	0.145		
0324-3512	03:24:46	-35:12:51	-2	15.32	2	15623	60	2.379	0.020	2	0.302	0.018		
155G46	03:30:37	-55:03:24	-7	14.50	1	13700	50	2.400	0.033	1	0.317	0.051		
358G33	03:34:51	-34:54:12	0	13.80	2	1597	20	1.572	0.097	2	0.186	0.015		
I362	04:14:21	-12:19:22	-3	14.36	1	8957	71	2.410	0.034	1	0.316	0.056		
-0211031	04:14:24	-12:20:30	-3	14.00	2	8957	22	2.466	0.060	2	0.296	0.050		
484G37	04:34:27	-22:32:48	-2	14.30	2	20720	20	2.434	0.069	2	0.319	0.005		
553G14	05:07:05	-18:46:42	-2	14.30	2	7462	20	2.068	0.025	2	0.275	0.001		
486G57	05:18:34	-26:50:00	-2	14.40	2	13720	20	2.435	0.027	2	0.322	0.006		
0532-3050	05:32:29	-30:50:00	-3	14.13	2	10782	16	2.489	0.030	2	0.350	0.020		
0543-2557	05:43:26	-25:57:00	-3	13.89	2	13341	50	2.364	0.044	2	0.359	0.008		
0543-2557a	05:43:28	-25:57:06	-3	14.11	1	13065	24	2.167	0.028	1	0.299	0.032		
0545-1953	05:45:38	-19:53:00	-2	14.10	2	8527	20	2.358	0.072	2	0.286	0.011		
0546-2529	05:46:36	-25:29:36	-3	14.02	2	11942	57	2.373	0.031	2	0.289	0.038		
0546-3259	05:46:37	-32:59:36	-3	14.20	2	11205	36	2.526	0.026	2	0.331	0.009		
0602-6345	06:02:30	-63:45:42	-3	13.64	1	8136	50	2.471	0.035	1	0.355	0.041		
0608-4736	06:08:20	-47:36:14	-3	14.08	2	8966	20	2.487	0.020	2	0.334	0.009		
0608-6543	06:08:47	-65:43:12	-3	13.57	1	10905	45	2.526	0.042	1	0.313	0.049		
0610-6231	06:10:08	-62:31:36	-3	13.71	1	8385	33	2.393	0.038	1	0.301	0.044		
0621-6458	06:21:16	-64:58:00	-3	14.08	1	7995	25	2.443	0.031	1	0.354	0.036		
0622-6454	06:22:10	-64:54:24	-5	14.00	1	8313	47	2.406	0.027	1	0.362	0.031		
0624-2435	06:24:49	-24:35:12	-2	14.18	2	7004	20	2.475	0.023	2	0.348	0.006		
0646+8102	06:46:00	+81:02:00	-5	14.40	1	7532	28	2.502	0.034	1	0.293	0.056		
0656-4544	06:56:08	-45:44:30	-3	13.56	1	11700	20	2.541	0.033	1	0.347	0.039		
0722+1916	07:22:24	+19:16:00	-5	14.40	1	8468	26	2.504	0.037	1	0.249	0.060		
0736+5532	07:36:54	+55:32:00	-5	14.20	1	10193	27	2.605	0.029	1	0.295	0.047		
0750+5537	07:50:06	+55:37:00	-5	14.30	1	7572	27	2.332	0.029	1	0.350	0.047		
N2474	07:54:08	+52:59:31	-5	0.00	1	5341	42	2.380	0.028	1	0.299	0.045		
0757+5642	07:57:48	+56:42:00	-3	14.20	1	8598	53	2.498	0.041	1	0.284	0.068		
I2377	08:24:05	-13:08:29	0	14.50	2	6044	36	2.143	0.022	2	0.231	0.003		
0848+5348	08:48:18	+53:48:00	-5	14.40	1	9231	29	2.469	0.024	1	0.210	0.039		
0849+1708	08:49:06	+17:08:00	-2	14.50	2	8634	29	2.383	0.018	2	0.271	0.009		
0856+1122	08:56:24	+11:22:00	-3	14.20	1	8988	32	2.505	0.041	1	0.281	0.083		
0913+1750	09:13:18	+17:50:00	-5	14.10	2	8604	53	2.351	0.029	2	0.362	0.008		
0915+1625	09:15:24	+16:25:00	-5	14.30	1	8977	32	2.507	0.026	1	0.358	0.027		
565G30	09:35:42	-20:07:06	-3	13.75	1	9863	75	2.412	0.043	1	0.276	0.087		
0939+0430	09:39:48	+04:30:00	-2	14.10	1	8679	32	2.423	0.042	1	0.286	0.086		
N2970	09:40:33	+32:12:30	-3	14.78	1	1602	29	1.635	0.037	1	0.112	0.061		
0944-2120	09:44:11	-21:20:24	-2	13.56	1	8775	39	2.309	0.035	1	0.288	0.071		
566G15	09:47:09	-21:30:30	-2	14.14	1	8499	31	2.373	0.040	1	0.296	0.082		
435G49	10:08:31	-28:39:18	-5	14.52	1	4211	33	2.111	0.047	1	0.227	0.078		
-0326030	10:08:54	-16:57:00	-2	14.00	2	9059	40	2.461	0.022	2	0.285	0.005		
R461	10:38:03	-27:37:12	-2	0.00	1	4503	36	1.856	0.024	1	0.114	0.049		
319G14	11:18:02	-41:14:42	-2	14.20	1	9434	40	2.293	0.034	0	0.000	0.000		
1150-3217	11:50:36	-32:17:18	-5	14.09	1	8193	28	2.359	0.046	1	0.350	0.077		

NOTE.—As in Table 4.5

Chapter 5

The cluster sample

The Tully-Fisher relation for spirals and the $D_n - \sigma$ or Fundamental Plane (FP) relations for early-type galaxies place important constraints on models of galaxy formation, and likely convey information about the importance of environmental effects in the evolution of galaxies, even though the physical origins of these relations are still unexplained. Since these scaling relations can also be used as distance indicators, they allow one to map the peculiar velocity field of galaxies in the nearby universe. To measure these relations accurately requires large homogeneous spectroscopic and photometric datasets. This Chapter describes how our new observations of cluster galaxies (the ENEARc sample) were combined with data from the literature to construct just such a dataset.

Most of the new data reported here are a subset of the ENEARf sample. Clusters in our sample were selected based on complete redshift surveys of magnitude-limited samples. Our approach differs from earlier work in a way that, for early type galaxies, is critical: groups, identified in the parent redshift catalogs by an objective algorithm, were used to assign our early-type galaxies to clusters. Although distances are available for 581 cluster galaxies at present, in this Chapter we present results for a subsample of 446 of them which are in 28 clusters and groups.

5.1 Defining the cluster sample

5.1.1 Selection

Clusters out to 8000-10000 kms^{-1} were selected; they were based on groups that were identified by applying objective group-finding algorithms (e.g., Huchra & Geller 1982) to complete redshift surveys of magnitude-limited samples. Here, we summarize the main features. The grouping algorithm identifies isodensity contours of the galaxy distribution in a magnitude-limited sample. It starts with a galaxy which has not yet been assigned to a group. It then searches around this galaxy for companions with projected separation

$$d_{12} \leq d_L(cz_1, cz_2, m_1, m_2) \tag{5.1}$$

and with line-of-sight velocity difference

$$cz_{12} \leq cz_L(cz_1, cz_2, m_1, m_2), \tag{5.2}$$

where cz_1 and cz_2 are the redshifts of the galaxy and its companion, and m_1 and m_2 are their magnitudes. In this way new companions are added to the list of group members.

Then the algorithm searches the surroundings of each companion. The loop is repeated until no new members are found.

For most of the sky ($\sim$ 6.5 steradians) large groups (more than $\sim$ 15 members) were drawn from the CfA1 (Geller & Huchra 1983) and SSRS (Maia et al. 1989) group catalogs. These groups were complemented, at low galactic latitudes, by groups identified in the ORS catalog (Santiago et al. 1995). Over the fraction of the sky sampled by the CfA2 and SSRS2 ($\sim$ 4.2 steradians, including more than a third of both galactic caps), we have used those groups identified by Ramella et al. (1997) in the CfA2 and Ramella et al. (1999) in the SSRS2, rather than those identified from the shallower surveys. We should point out that the selection criteria is not uniform over the sky because of the different magnitude-limits and the different density contrast thresholds adopted in identifying groups. However, since we are primarily interested in richer systems these differences are of little importance to us.

The resulting group catalog consists of 978 groups of which 32 are rich ($>$ 15 members), 318 are medium-size (5-15 members), and 628 have fewer than five members. All but three of our richest groups were identified with known clusters in the literature. These three had a relatively small number of bright early-types. For each group, the combined group catalog provides the number of group members (which includes all morphological-types), a well-defined central position, heliocentric radial velocity and velocity dispersion, based on the brightest cluster galaxies of all morphological types. The group catalog also provides an estimate of the physical size of the group, as expressed by its pair radius R_p (Ramella et al. 1989), which gives the mean projected separation

$$R_p = \frac{8\ cz_{\rm gr}}{\pi H_0}\ \sin\left[\frac{1}{N_{\rm mem}(N_{\rm mem}-1)}\sum_i\sum_{j>i}\theta_{ij}\right] \qquad (5.3)$$

where $cz_{\rm gr}$ is the mean radial velocity of the group, $N_{\rm mem}$ is the number of group members, and θ_{ij} is the angular separation of group members i and j. This parameter can be used to establish cluster membership more reliably for galaxies fainter than the limiting magnitudes of the redshift surveys used above.

Groups with at least 15 members were cross-identified with the Abell and the ACO cluster catalogs (Abell 1958; Abell et al. 1989). Some of these clusters contain early type galaxies which are fainter than the limiting magnitudes of the parent redshift survey, but for which photometric and spectroscopic data is, nevertheless, available in the literature. We added these fainter objects to our compilation of early-type cluster galaxies. In addition, there were some clusters in which all early-type galaxies were fainter than the magnitude limit. We included such clusters provided they contained at least four early-type galaxies for which the data required to estimate distances was available.

A special procedure was adopted to handle the Centaurus cluster, which is known to have two distinct components (Lucey & Carter 1988) but is identified as a single large group in the group catalog. In this case, we assigned membership based on the observed redshift distribution along the line-of-sight. The resulting list of members is in good agreement with that of Lucey & Carter (1988). On the other hand, physical characteristics were computed after splitting the system into two groups, hereafter Cen30 and Cen45.

Five additional clusters, three previously studied by Jørgensen et al. (1995a,b) (A539, S639, and A3381) and two observed by Smith et al. (1997) (7S21 and A347), were included in our sample. These clusters are not present in the group catalog either because

they are located at very low galactic latitudes, or because all the member galaxies are fainter than the limiting magnitude which was used when identifying groups.

5.1.2 Membership assignment

We selected early-type galaxies from the entire set of galaxies identified by the grouping algorithm. In addition, we added the fainter objects described above.

A galaxy was assigned to a cluster if it satisfied both of the following conditions:

- $d \leq 1.5R_p$, where d is the projected distance of the galaxy relative to the center of the group, as determined by the group finding algorithm, and R_p is the group pair radius. For the five additional clusters taken from the literature, which were not identified with the finding algorithm, we fixed R_p to 1 Mpc;
- $\mid cz - cz_{\rm cl} \mid \leq 1.5\sigma_{\rm cl}$ where cz is the radial velocity of the galaxy, $cz_{\rm cl}$ and $\sigma_{\rm cl}$ are the systemic and velocity dispersion of the group, respectively.

Although this second requirement is rather restrictive, and does not faithfully represent the region within the caustic which demarks the boundary of a cluster in redshift space (e.g., Kaiser 1987; Regos & Geller 1989), the relatively small number of galaxies per cluster and the dependence of the caustic on Ω make an approach based on caustics untenable. So, we also define "peripheral" objects using different criteria depending on the richness of the cluster. For rich clusters (with more than $\sim$ 15 members), "peripheral" galaxies are those which satisfy one of two conditions: $1.5R_p < d < 3R_p$ and $\mid cz - cz_{\rm cl} \mid < \sigma_{\rm cl}$ or $1.5\sigma_{\rm cl} < \mid cz - cz_{\rm cl} \mid < 3\sigma_{\rm cl}$ and $d < R_p$, while for clusters with fewer members the first condition is limited to $1.5R_p < d < 2R_p$. These conditions are intended to approximately represent the region in redshift-space occupied by cluster members. Applying the above criteria we find that the sample of galaxies in clusters increases by about 14%. The impact of these objects in the derivation of the distance relation is discussed in more detail in Chapter 6, where we also examine the implications of using estimated distances in the assignment criteria.

To evaluate the resulting assignments, Figure 5.1 shows the projected distribution of objects in and around each cluster (upper panel). The dashed circle corresponds to the angular size of $1.5R_p$ at the cluster redshift. The lower panel shows the radial velocity versus angular distance from the cluster center; the solid horizontal line shows the radial velocity of the cluster computed from the finding algorithm, the vertical dashed line corresponds to the angular size of R_p and the small horizontal lines correspond to $\pm 1.5\sigma_{cl}$. Note that, in some cases, early-type galaxies are not uniformly distributed around the cluster center and/or its mean redshift. This happens because these cluster parameters were computed taking into account all galaxies, whatever their morphological type. In these plots, dots represent galaxies in the field, or late morphological types, taken from the available redshift surveys; small filled circles are galaxies satisfying our assignment criteria and with measured distances; small open circles are early-type galaxies in the cluster but without distance measurements; small filled and open triangles refer to the "peripheral" galaxies and crosses represent early-type galaxies in our ENEAR catalog that are in the field of view of the cluster but were not assigned to it either because of the redshift or the angular distance from the group center.

There are 678 galaxies in the ENEARc catalog. The cluster galaxies considered in this work consist of 446 galaxies with both velocity dispersion and d_n measurements. Of

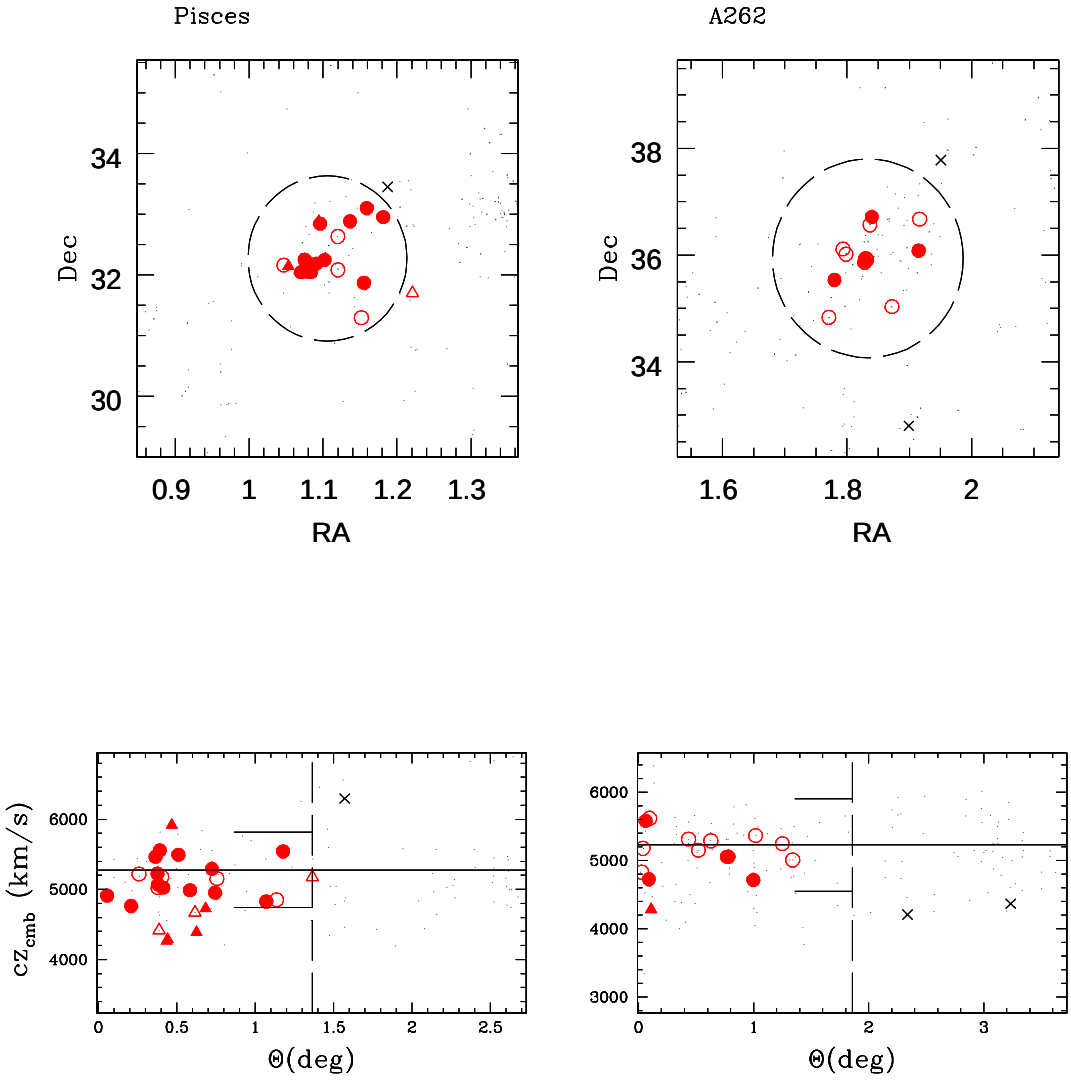

Figure 5.1 The distribution of galaxies, in the equatorial coordinate system (upper panel), and the radial velocity versus angular distance from the cluster center (lower panel). A detailed description of this figure and those following is given in the text.

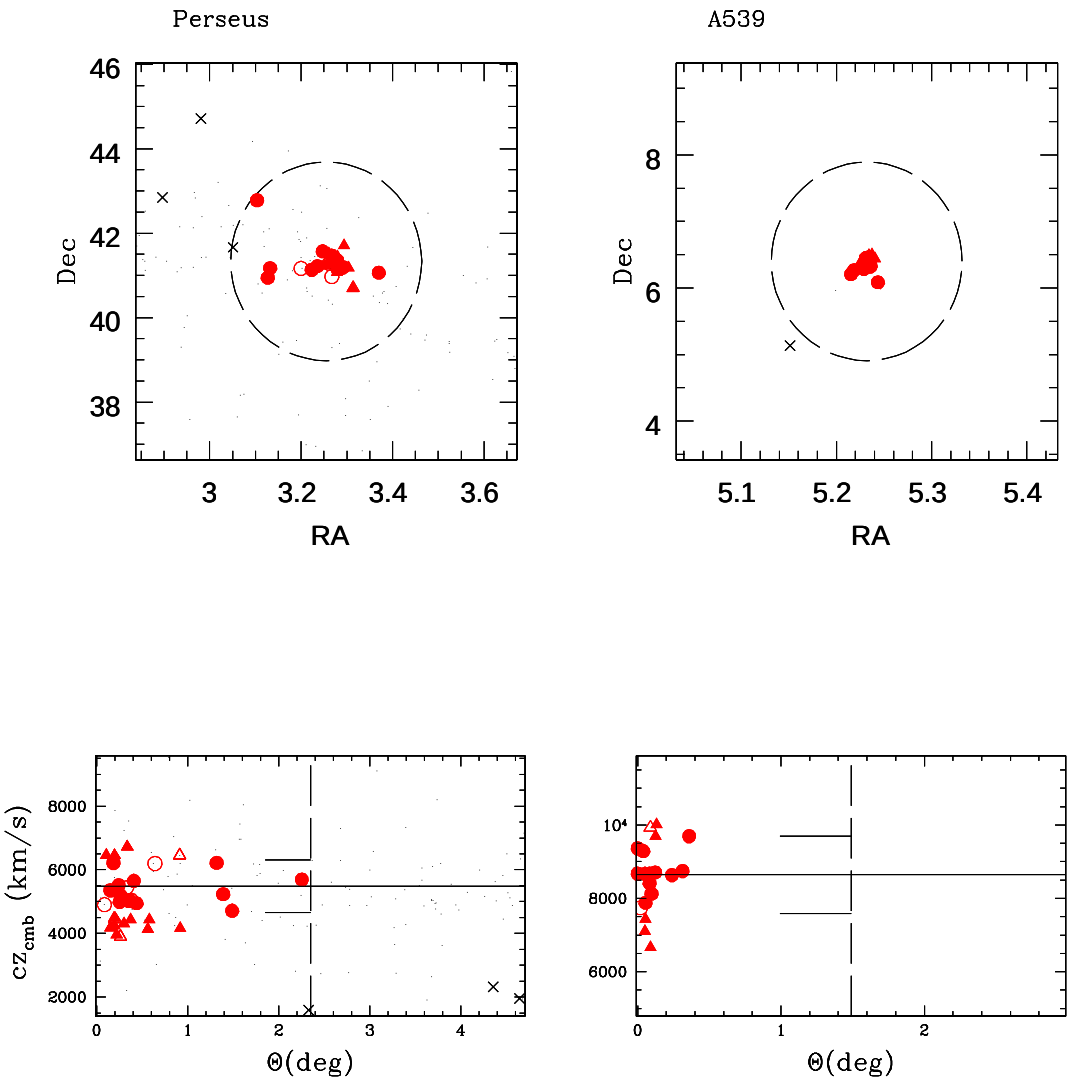

Figure 5.1 Continued

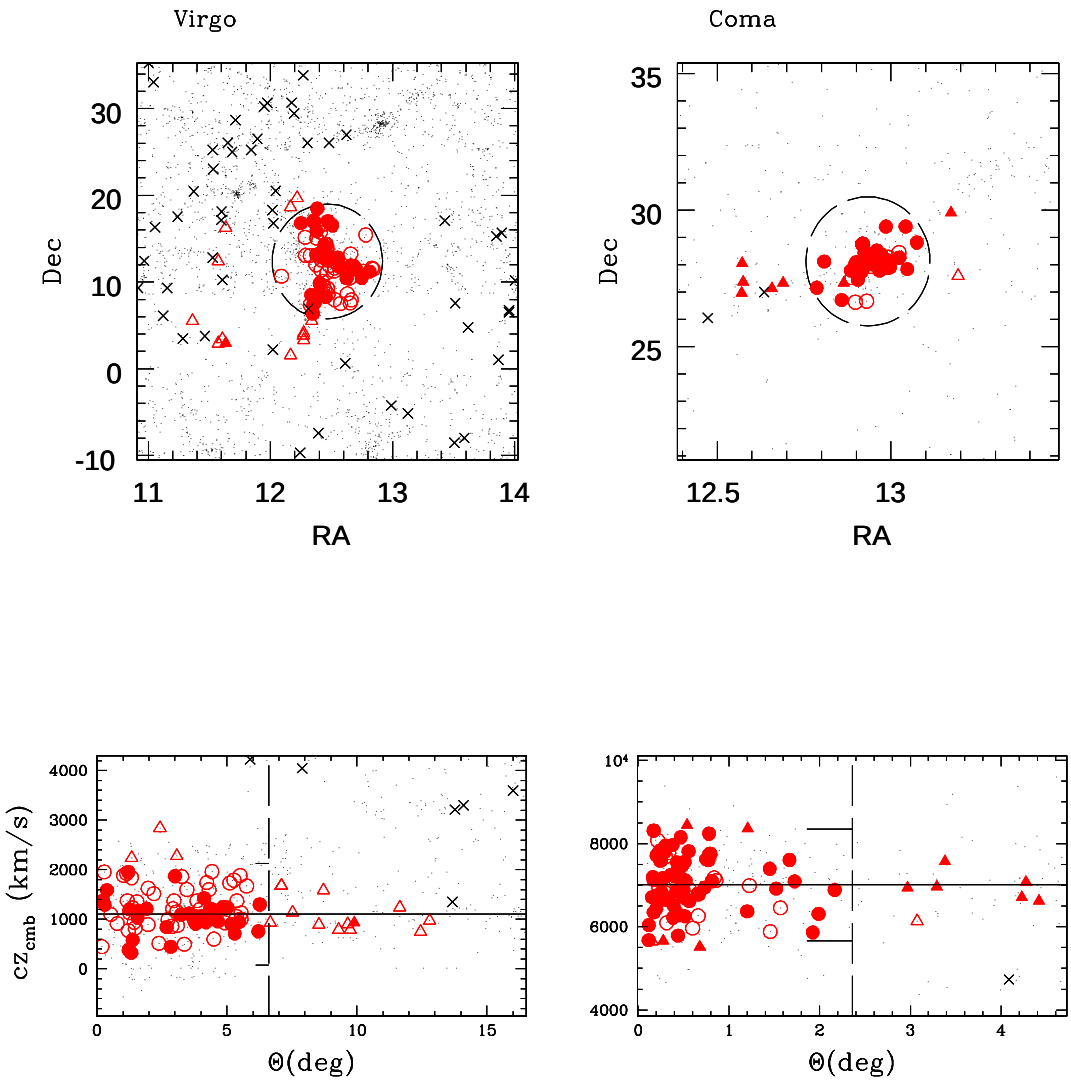

Figure 5.1 Continued

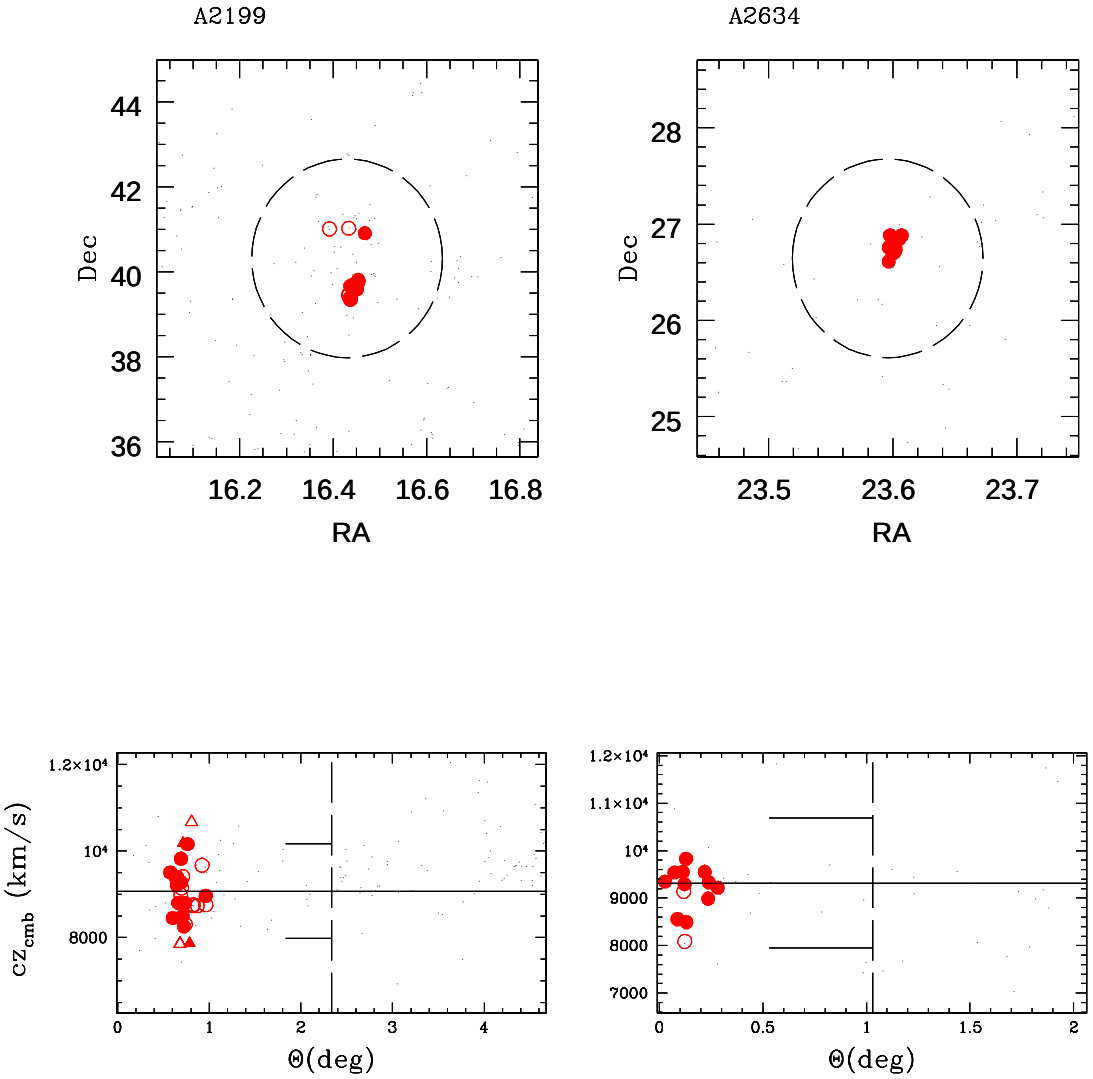

Figure 5.1 Continued

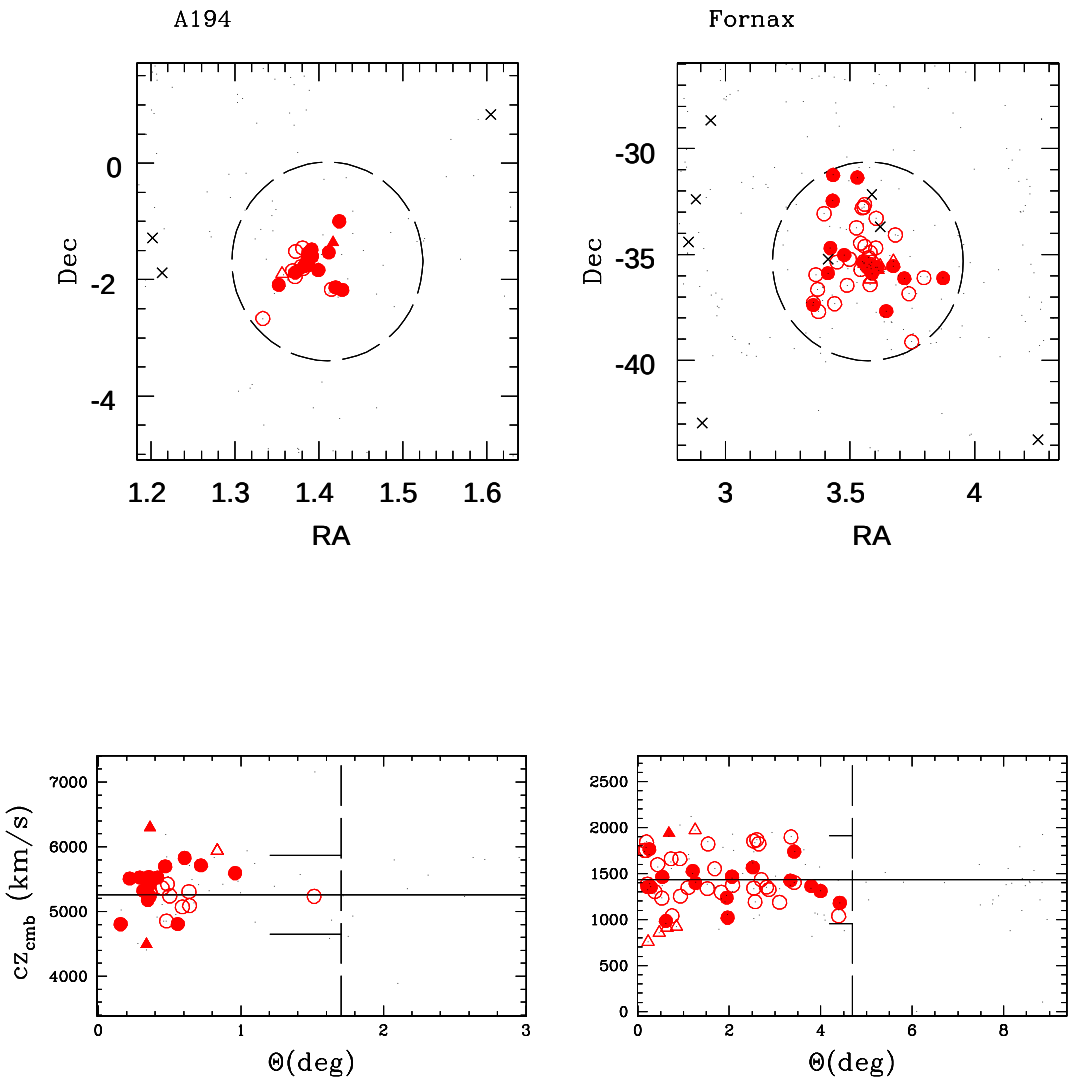

Figure 5.1 Continued

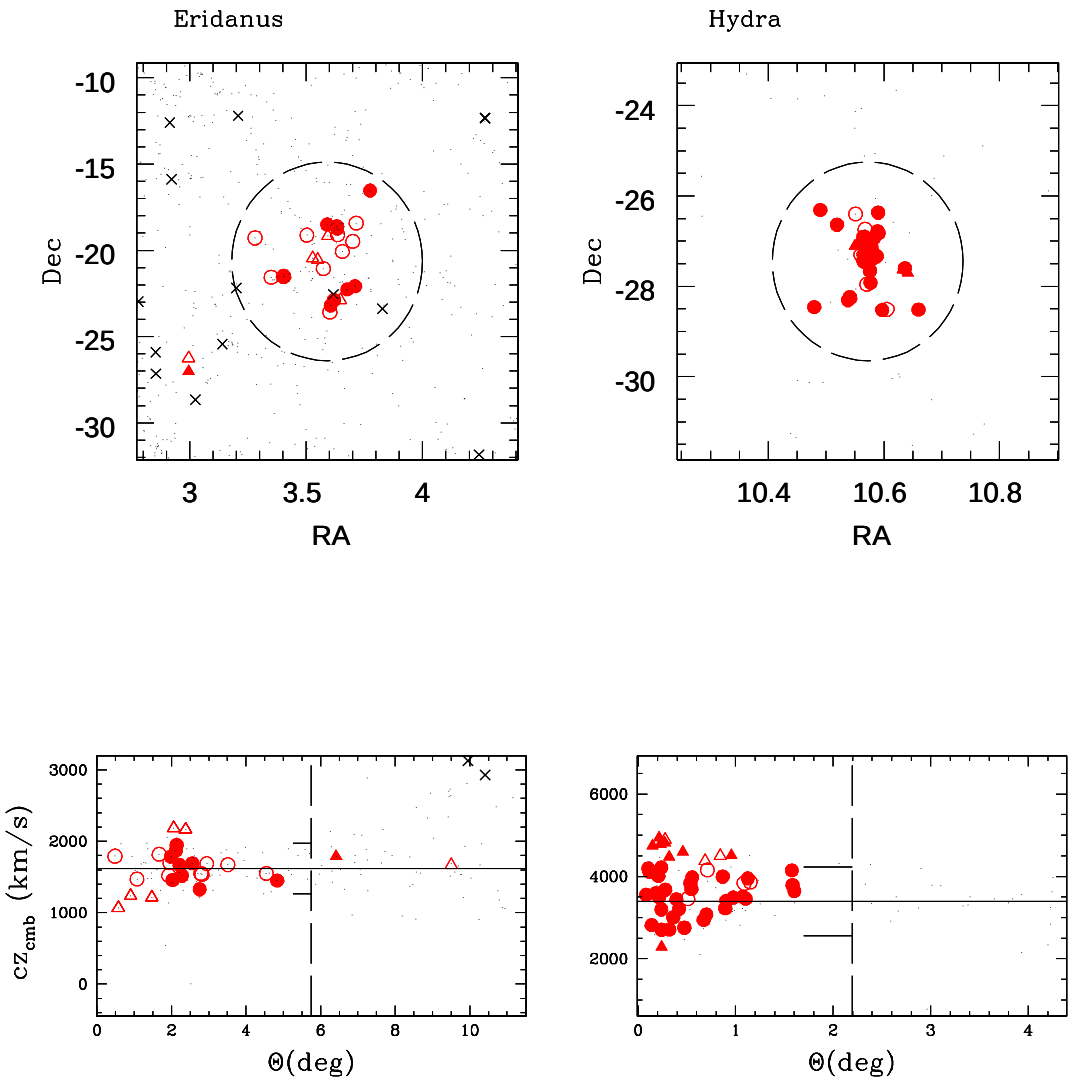

Figure 5.1 Continued

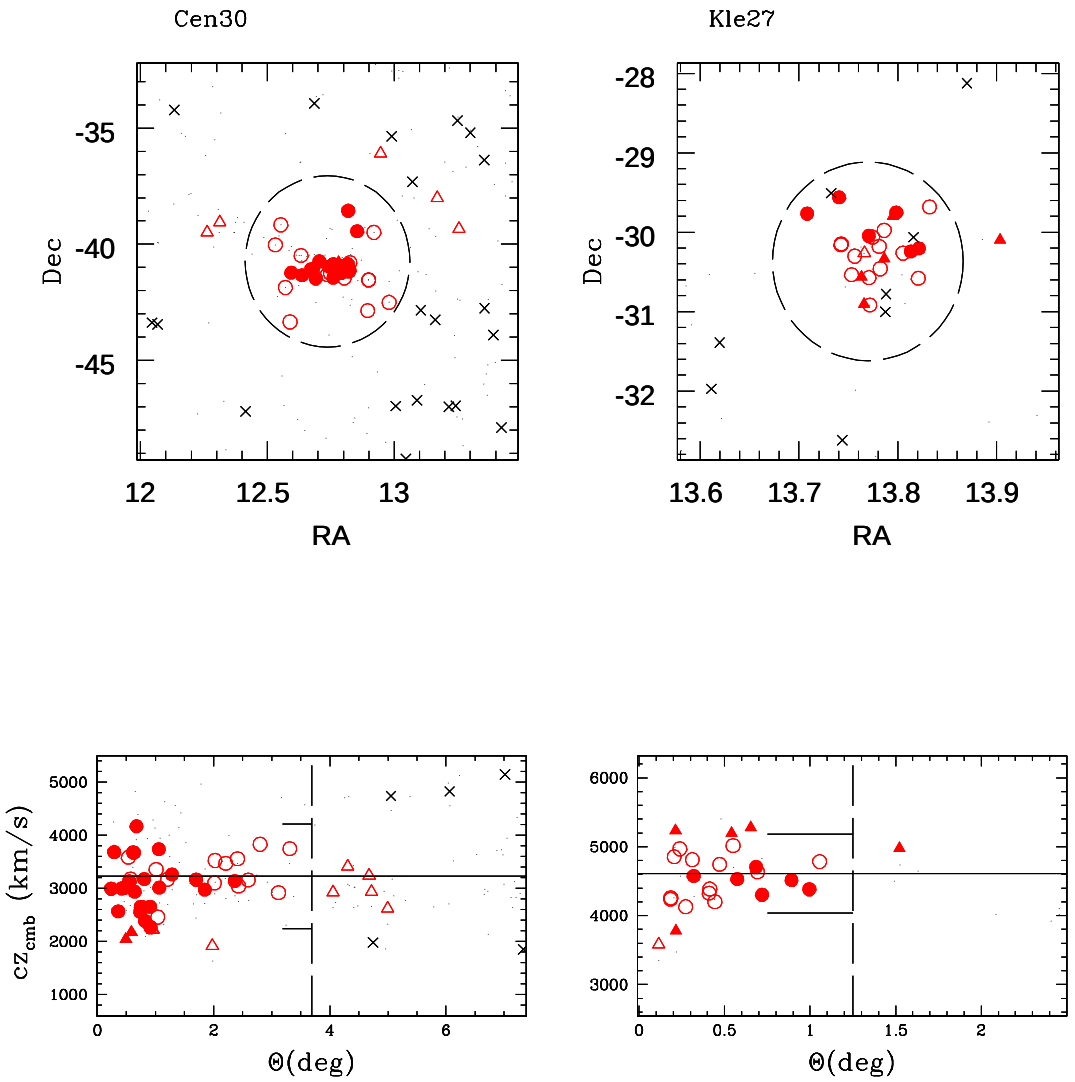

Figure 5.1 Continued

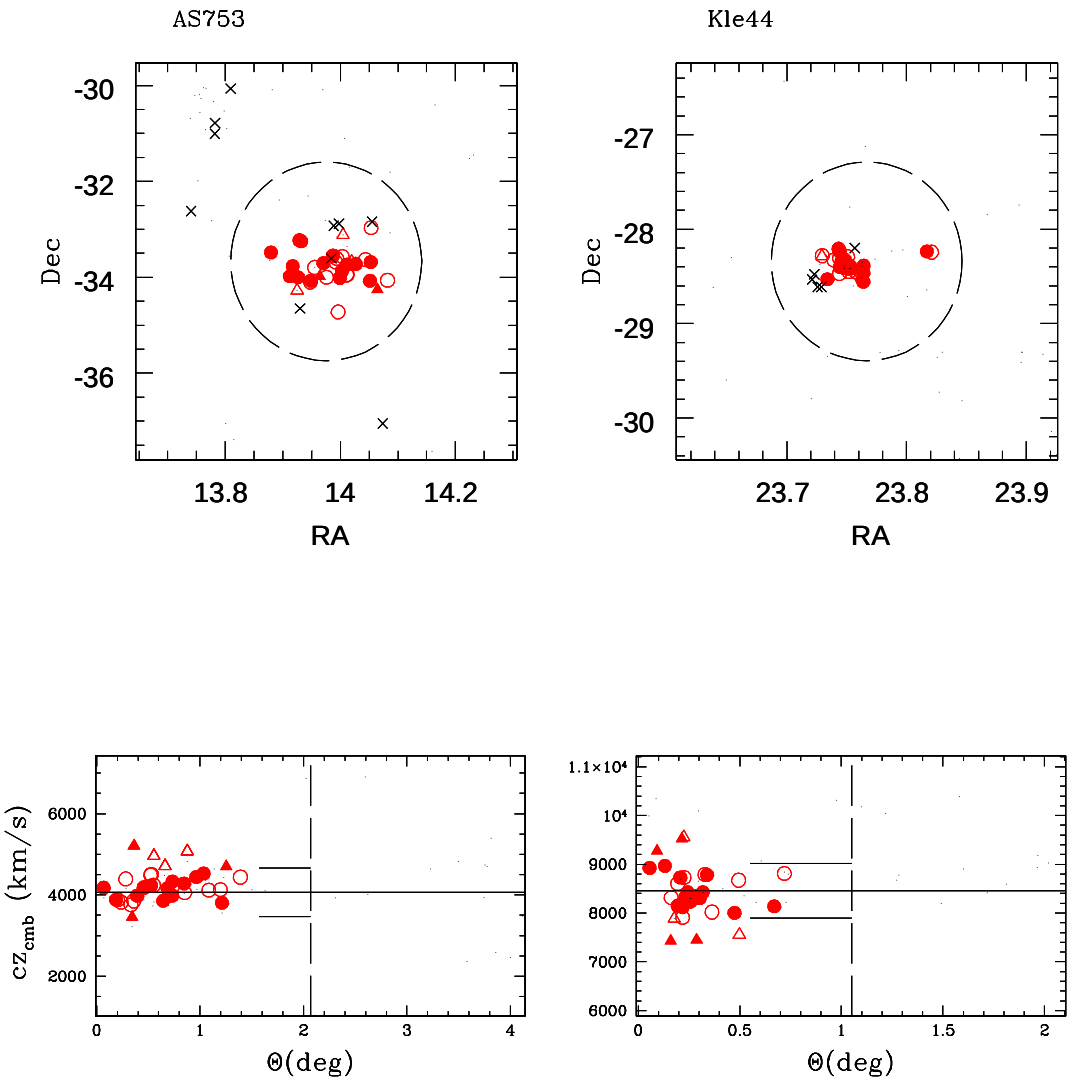

Figure 5.1 Continued

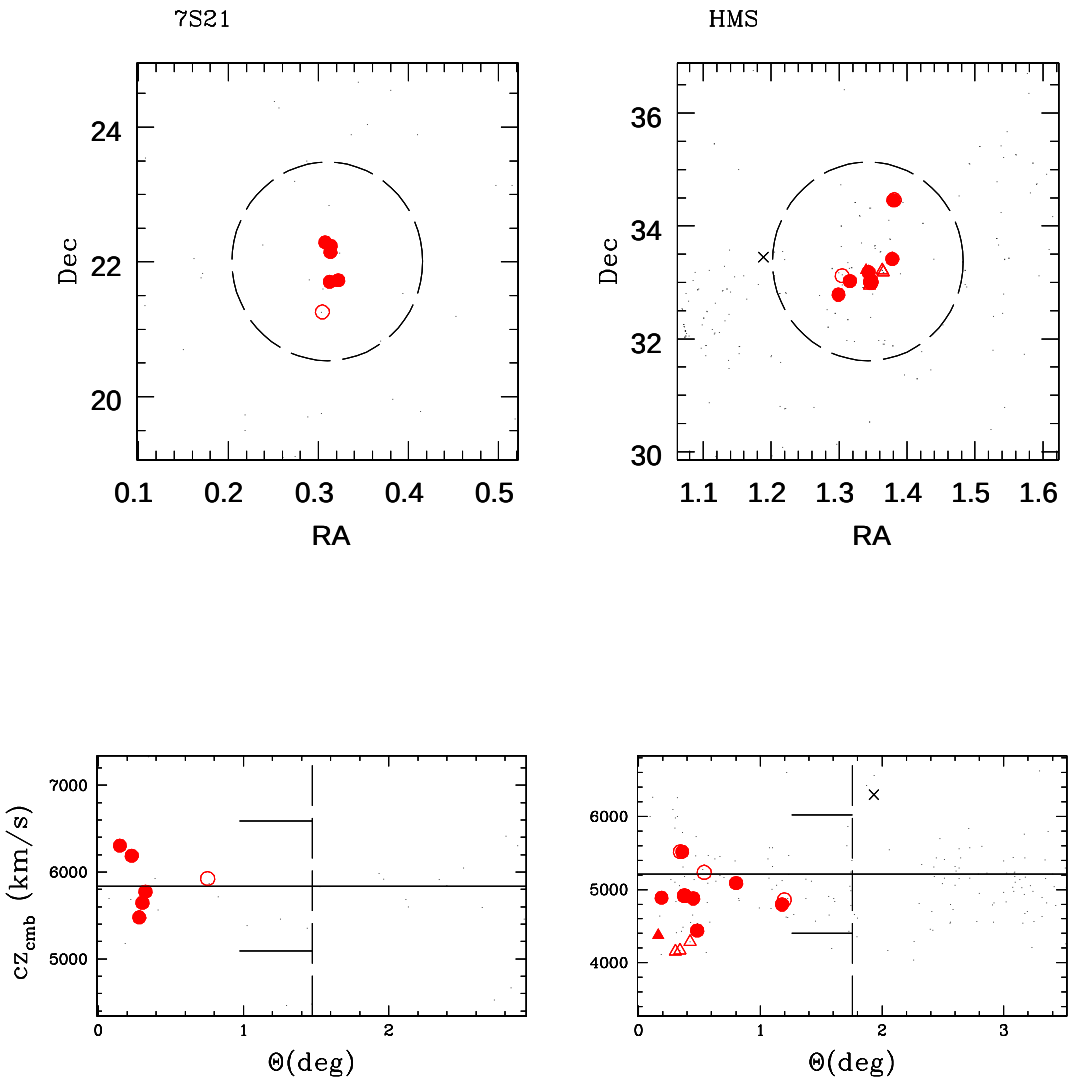

Figure 5.1 Continued

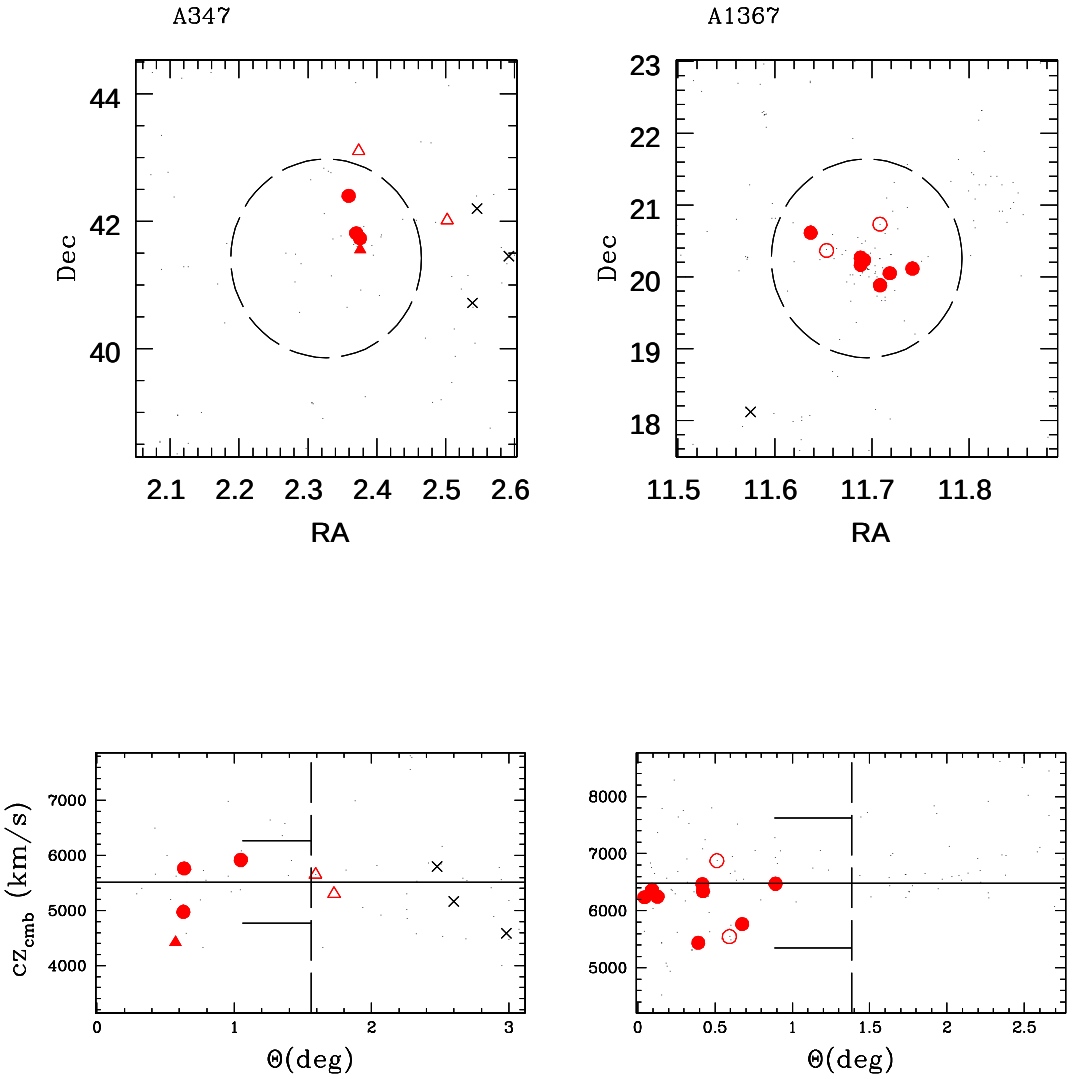

Figure 5.1 Continued

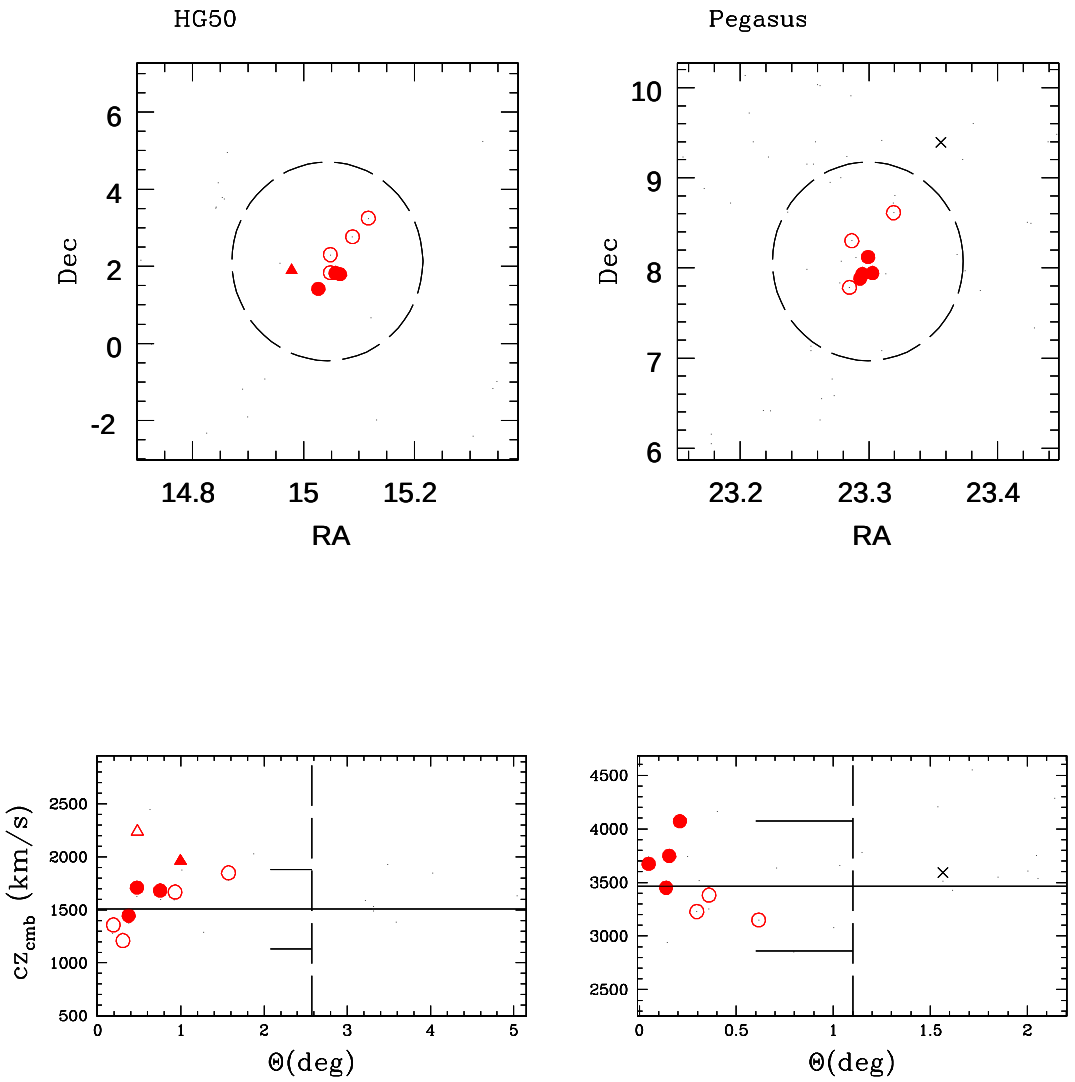

Figure 5.1 Continued

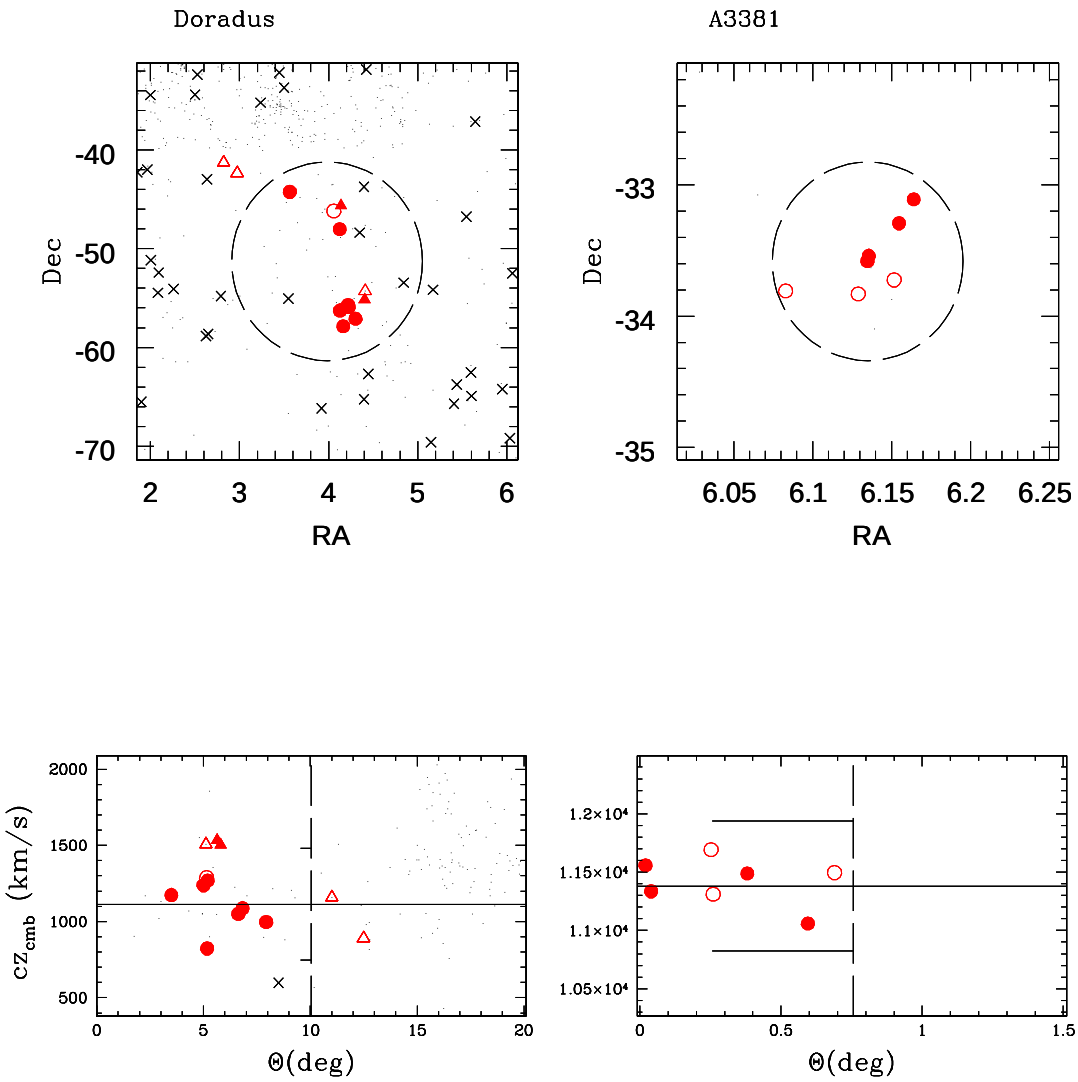

Figure 5.1 Continued

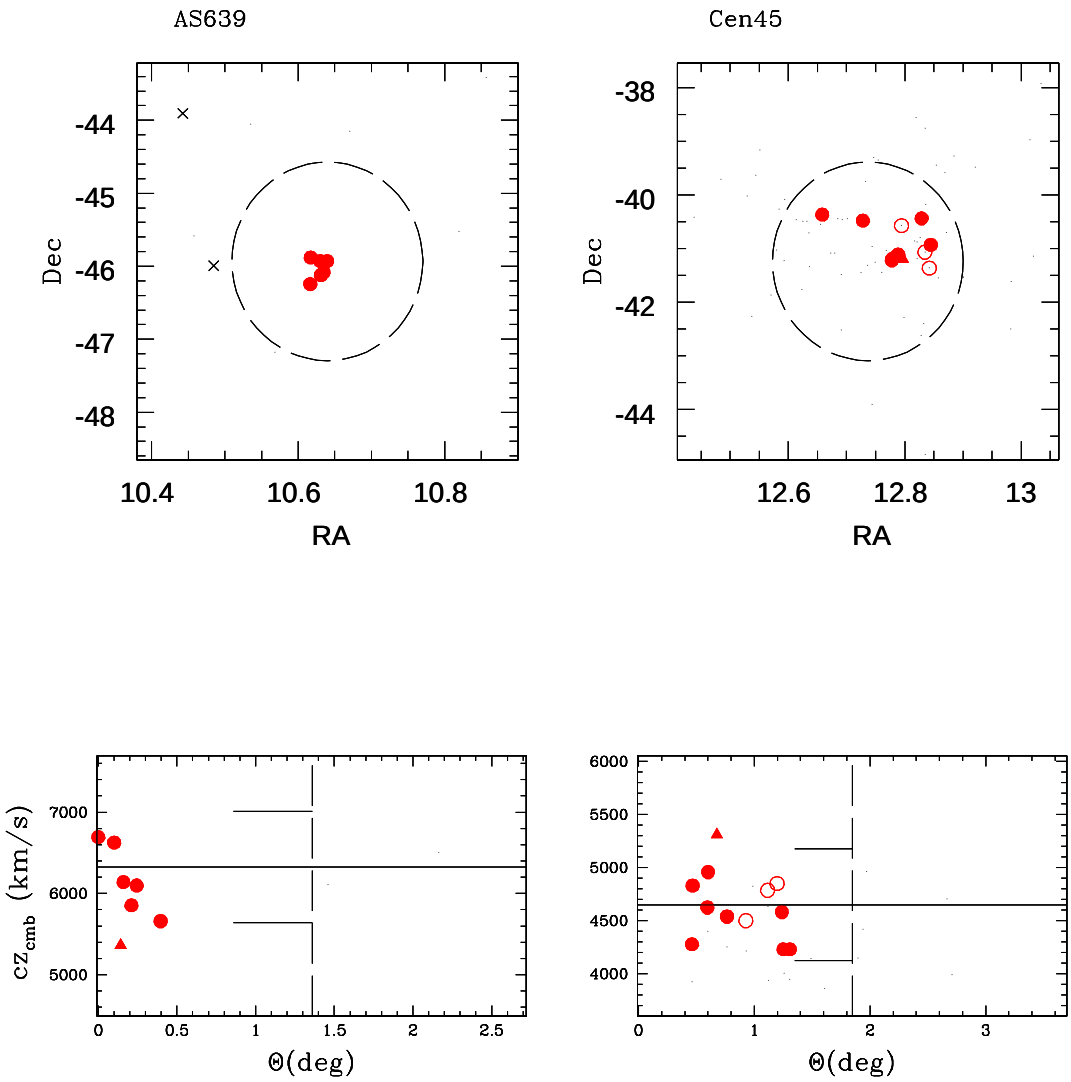

Figure 5.1 Continued

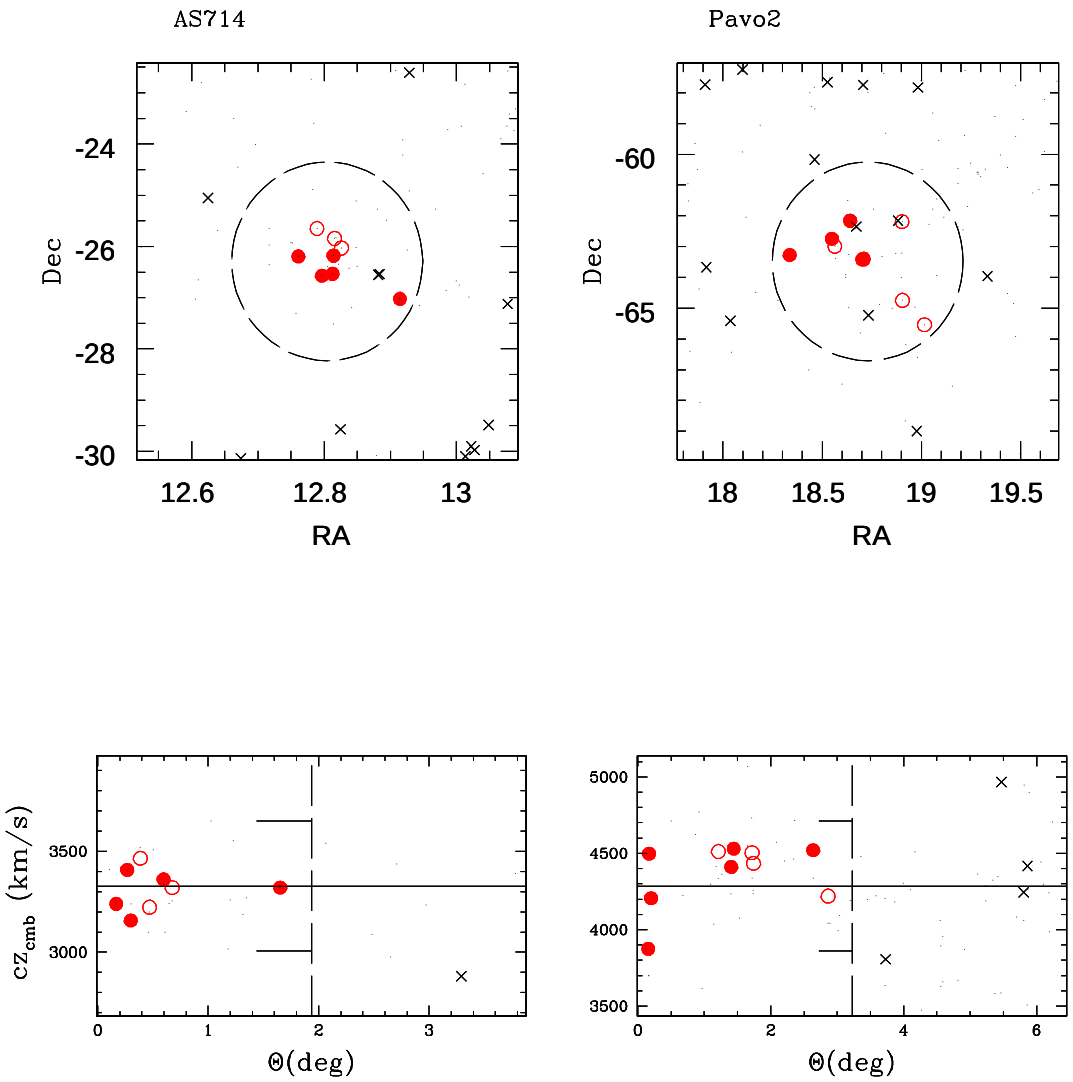

Figure 5.1 Continued

Table 5.1 Galaxies excluded by our cluster membership assignment

Galaxy	α (1950)	δ (1950)	$cz_{\rm hel}$ km/s	$m_{\rm B}$ mag	Cluster	R_p Mpc	$\sigma_{\rm cl}$ km/s	$R_{\rm proj}$ Mpc	Δ_{cz} km/s	References
(1)	(2)	(3)	(4)	(5)	(6)	(7)	(8)	(9)	(10)	(11)
N380	01:04:32	32:13:01	4414	14.05	Pisces	0.837	358	0.360	982	F, S
N392	01:05:36	32:52:00	4672	13.90	Pisces	0.837	358	0.581	724	F, S
D75	01:20:39	00:54:11	8269	–	A194	1.042	408	1.077	2929	JFKa
N533	01:22:54	01:30:00	5544	13.44	A194	1.042	408	1.736	204	JFKa
U1269	01:46:11	34:44:05	3848	15.43	A262	1.130	450	1.208	979	S
U1837	02:19:49	42:47:06	6582	14.63	A347	1.000	500	1.319	1063	S
U1841	02:20:02	42:45:54	6373	14.29	A347	1.000	500	1.319	1063	S
PER195	03:15:59	40:57:52	8342	14.20	Perseus	1.500	550	0.373	2856	D, S
N1705	04:53:06	-53:26:30	597	13.06	Doradus	1.300	245	1.713	530	MDL
D108	12:56:40	28:20:05	5071	–	Coma	1.925	895	0.308	1871	Da, Lc
N4867	12:56:50	28:14:24	4818	15.50	Coma	1.925	895	0.258	2124	F, JFK, Lc
D106	12:56:58	28:10:05	5092	15.00	Coma	1.925	895	0.254	1850	Da, Lc
I3998	12:57:23	28:14:46	9371	15.60	Coma	1.925	895	0.389	2429	Da, Lc, S
N4894	12:57:52	28:14:20	4587	16.98	Coma	1.925	895	0.507	2355	Da, S
I4045	12:58:24	28:11:30	8655	16.40	Coma	1.925	895	0.637	1713	F, Lc, JFK
I4051	12:58:28	28:16:30	4964	14.80	Coma	1.925	895	0.673	1978	F, Lc, JFK
1351-2934	13:51:06	-29:34:59	6923	14.75	Kle27	0.670	382	0.875	2258	W
W39	13:59:18	-32:55:44	10630	15.47	AS753	0.979	401	1.175	6433	JFKa, W
W53	14:00:12	-33:45:26	2718	18.04	AS753	0.979	401	1.075	1479	W
W56	14:00:18	-33:46:56	2718	14.37	AS753	0.979	401	1.097	1479	JFKa
384G37	14:00:38	-33:50:02	5723	14.78	AS753	0.979	401	1.149	1526	JFKa
1627+3932	16:27:02	39:32:45	10666	–	A2199	2.466	731	1.285	1603	L
D21	18:41:40	-63:22:42	3628	–	Pavo2	1.607	284	0.697	842	LC
1842-6327	18:42:57	-63:27:37	3495	14.85	Pavo2	1.607	284	0.737	975	LC
2335+2642b	23:35:16	26:42:14	11106	17.31	A2634	1.117	914	0.197	1752	L
2335+2642	23:35:56	26:42:30	10873	–	A2634	1.117	914	0.125	1519	L, S
2335+2648	23:35:57	26:48:49	7532	17.59	A2634	1.117	914	0.287	1822	L
D69	23:44:37	-28:17:42	10071	16.88	Kle44	1.034	375	1.077	1296	JFKa, LC
2345-2813	23:45:20	-28:13:54	10688	17.12	Kle44	1.034	375	0.904	1913	LC
D39	23:45:43	-28:27:24	10554	16.30	Kle44	1.034	375	1.226	1779	JFKa, LC
D65	23:45:47	-28:21:10	9996	15.00	Kle44	1.034	375	1.066	1221	JFKa, LC

Note: The references are: D: Dressler et al. (1987); Da: Dressler (1987); F: Faber et al. (1989); HG: groups form Huchra & Geller. (1982); JFK: Jørgensen, Franx, & Kjaergaard (1992); JFKa: Jørgensen, Franx, & Kjaergaard (1995a); L: Lucey et al. (1991); Lc: Lucey et al. (1997); LC: Lucey & Carter (1988); MDL: groups from Maia et al. (1989); S: Smith et al. (1997); W: Willmer et al. (1991).

these, 385 satisfy the most stringent membership criteria, whereas 61 are "peripheral" cluster objects. We should point out that 31 galaxies previously assigned to the selected cluster sample by previous authors were found not to be members, according to the criteria adopted in this work. Therefore, they are not included in the ENEARc sample. These galaxies are listed in Table 5.1, where column (1) gives the name of the galaxy; columns (2) and (3) the equatorial coordinates; column (4) the heliocentic redshift; column (5) the total magnitude $m_{\rm B}$; column (6) the name of the cluster to which the galaxy is assigned; column (7) the pair radius R_p of the cluster; column (8) the cluster velocity dispersion; column (9) the projected distance of the galaxy from the cluster center, computed using the angular separation and the redshift of the cluster; column (10) the difference between the galaxy and cluster redshifts; and column (11) gives the reference of the previous works. Note that Willner et al. (1991) had already identified W56 and 384 G 37 as contaminating objects in AS753, and Jørgensen (1997) also noted that W39 had been wrongly assigned to AS753.

Finally, we emphasize that the group catalog discussed above plays a critical role in the analysis of the peculiar velocity field of the ENEARf sample.

5.2 Properties of the cluster sample

The resulting cluster sample consists of 28 clusters listed in Table 5.2. In the Table column (1) gives the name of the cluster; columns (2) and (3) the right ascension and declination, as determined from the group finding algorithm; column (4) the heliocentric radial velocity; column (5) the cluster velocity dispersion; column (6) the value of the radius R_p; column in column (7) the number of galaxies with measured distances; column (7) we identify clusters observed only by the other authors; and column (9) gives the sources in the literature in which these clusters were studied previously. The global parameters characterizing the clusters are those computed for the groups. Section 5.4 lists the individual member galaxies.

Fig. 5.1 shows the projected distribution of the 28 clusters in galactic coordinates; the symbols are inversely proportional to the cluster redshifts, and Figure 5.2 shows the distribution of cluster redshifts. It is also useful to refer back to Figure 2.6, which compares the distribution of clusters with that of the underlying galaxy distribution, in Cartesian supergalactic coordinates. (Note that the galaxy samples reach different limiting magnitudes in different directions of the sky.) Four clusters lie inside the Perseus-Pisces region ($0^h < \alpha < 4^h$ and $+20^o < \delta < +45^o$, Smith et al. 1997). The two dominant concentrations of galaxies, the GA and PP superclusters, are indicated on the three panels. As can be seen from these Figures the cluster sample is distributed uniformly across the sky. Furthermore, the clusters span a wide range of richness and probe the most prominent structures in the nearby universe.

Figure 5.3 shows the distribution of the spectroscopic parameters, redshift, σ, and Mg_2 index (upper panels), and the photometric parameters d_n, r_e and $\bar{\mu}_e$ (lower panels), of the early-type population that make up the cluster sample. The number of observations available for determining the FP relation is $\sim 70\%$ of the d_n measurements. The data in this Figure come from a variety of sources; to combine them to build a distance relation, it is essential to scale all the observed quantities to a common system. This is discussed in the next section.

Table 5.2 The cluster sample

Name	α (1950)	δ (1950)	$cz_{\rm hel}$ km/s	$\sigma_{\rm cl}$ km/s	R_p Mpc	$N_{\rm gal}$		Reference
(1)	(2)	(3)	(4)	(5)	(6)	(7)	(8)	(9)
Northern hem.								
Pisces	01:06:21	32:16:19	5396	358	0.837	22		F, S
A262	01:50:00	35:56:19	4827	450	1.130	7		F, S
Perseus	03:15:18	41:19:58	5486	550	1.110	26		D, F, S
A539	05:13:55	06:24:00	8741	701	-	17	*	JFKb
Virgo	12:28:02	12:22:55	1199	685	0.846	33		F, HG
Coma	12:56:01	28:07:18	6942	895	1.925	75		D, Da, F, JFKa,Lc, S
A2199	16:25:48	40:19:18	9063	731	2.466	15	*	F, L, Lc, S
A2634	23:35:45	26:38:39	9354	914	1.117	12	*	F, L, Lc, S
Southern hem.								
A194	01:24:37	-01:41:10	5340	408	1.042	17		F, LC, L, JFKb
Fornax	03:34:19	-35:19:27	1379	320	0.781	17		D, F, HG, MDL
Eridanus	03:35:25	-20:38:24	1665	236	1.082	10		HG, Wa
Hydra	10:34:19	-27:26:53	3718	555	0.867	41		F, JFKb, LC
Cen30	12:44:12	-40:44:19	3041	658	1.385	25		Db, F, HG, LC
Klem27	13:46:11	-30:22:03	4665	382	0.670	11		Db, JFKb, Wb
AS753	13:58:31	-33:40:08	4197	401	0.979	18		Db, JFKb, Wb
Klem44	23:46:00	-28:20:28	8775	375	1.034	22		F, JFKb, LC
Poor clusters								
7S21	00:18:36	22:00:29	5840	-	-	6	*	S
HMS	01:20:33	33:22:22	4884	540	1.065	9		S
A347	02:19:36	41:25:00	5519	-	-	6	*	S
A1367	11:41:41	20:15:25	6464	760	1.043	8		F, HG
HG50	15:02:35	02:07:39	1738	249	0.451	4		F, HG
Pegasus	23:17:57	08:04:21	4197	405	0.444	4		F
Doradus	03:59:05	-51:16:59	1127	245	1.300	9		HG, JKFb, MDL
A3381	06:08:06	-33:34:59	11381	372	-	4	*	HG, JFKb, MDL
AS639	10:38:24	-45:55:59	6269	456	-	7	*	JFKb
Cen45	12:28:36	-40:26:19	4650	350	0.990	10	*	F, HG, LC
AS714	12:48:17	-26:17:27	3328	215	0.750	5		A
Pavo2	18:43:49	-63:28:48	4470	284	1.607	6		F, HG, LC, MDL

Notes: Asterisks denote clusters that were not observed by us; that data for these clusters comes entirely from other authors. The references are: A: Abell et al. (1989); D: Dressler et al. (1987); Da: Dressler (1987); Db: Dressler et al. (1991); F: Faber et al. (1989); HG: groups form Huchra & Geller. (1982); JFK: Jørgensen, Franx, & Kjaergaard (1992); JFKa: Jørgensen, Franx, & Kjaergaard (1995a); L: Lucey et al. (1991); Lc: Lucey et al. (1997); LC: Lucey & Carter (1988); MDL: groups from Maia et al. (1989); S: Smith et al. (1997); Wa: Willmer et al. (1989); Wb: Willmer et al. (1991).

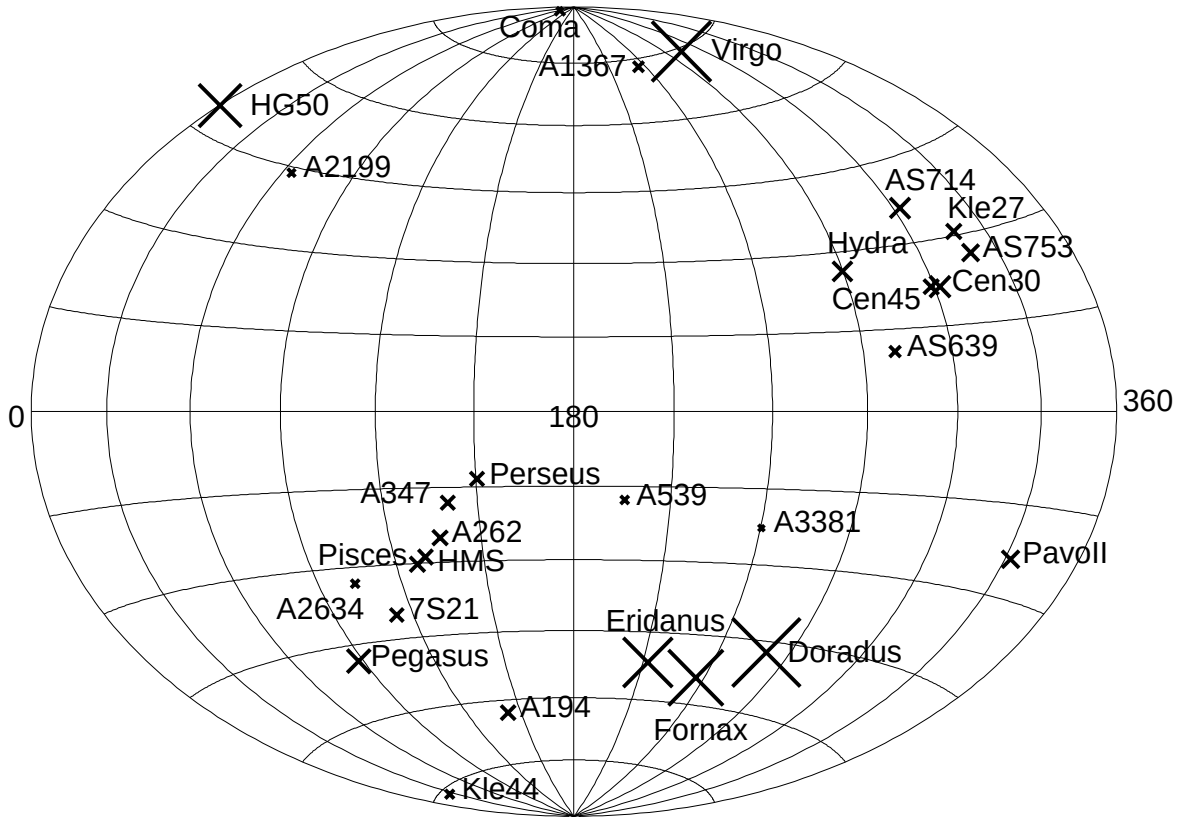

Figure 5.1 The spatial distribution of the 28 clusters in galactic coordinates. The size of the symbols is inversely proportional to the cluster redshift.

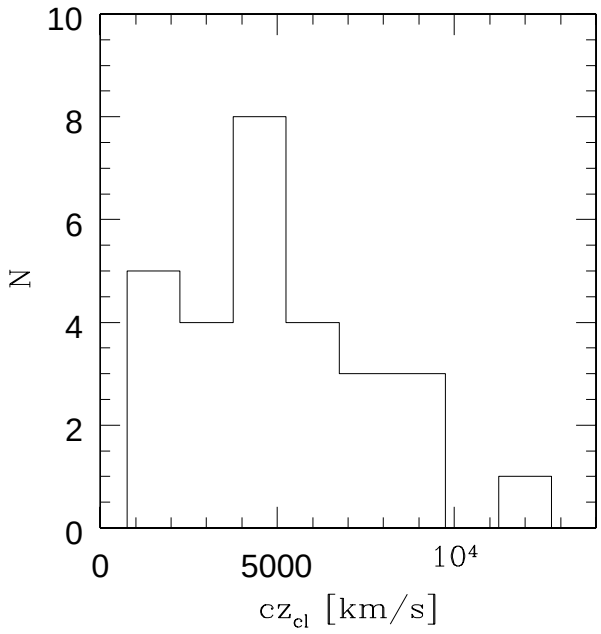

Figure 5.2 The redshift distribution of the 28 clusters.

5.3 Calibrating the data

As described in Chapter 2, we have gathered a substantial amount of both spectroscopic (1679) and photometric (1636) data of early-type galaxies with the following goals in mind:

- to measure distances for an all-sky sample (ENEARf) of early-type galaxies brighter than $m_B = 14.5$ and $cz < 7000$ kms^{-1} for peculiar velocity studies;
- to increase the number of galaxies in clusters for which measured distances are available, so as to improve the statistical accuracy of distance relations;
- to measure a significant number of galaxies previously observed by others so as to scale as much data as possible to a common system;
- to increase the number of repeated observations so as to better estimate measurement errors.

These measurements include: 1) repeated observations by us of the same galaxy, which are used to estimate the amplitude of our error on a run-by-run basis; 2) measurements of galaxies already observed by others, so as to scale the structural parameters (d_n, half-luminosity radii, magnitudes, velocity dispersion and line indexes) to a homogeneous system. By bringing these various systems together one can safely combine our new

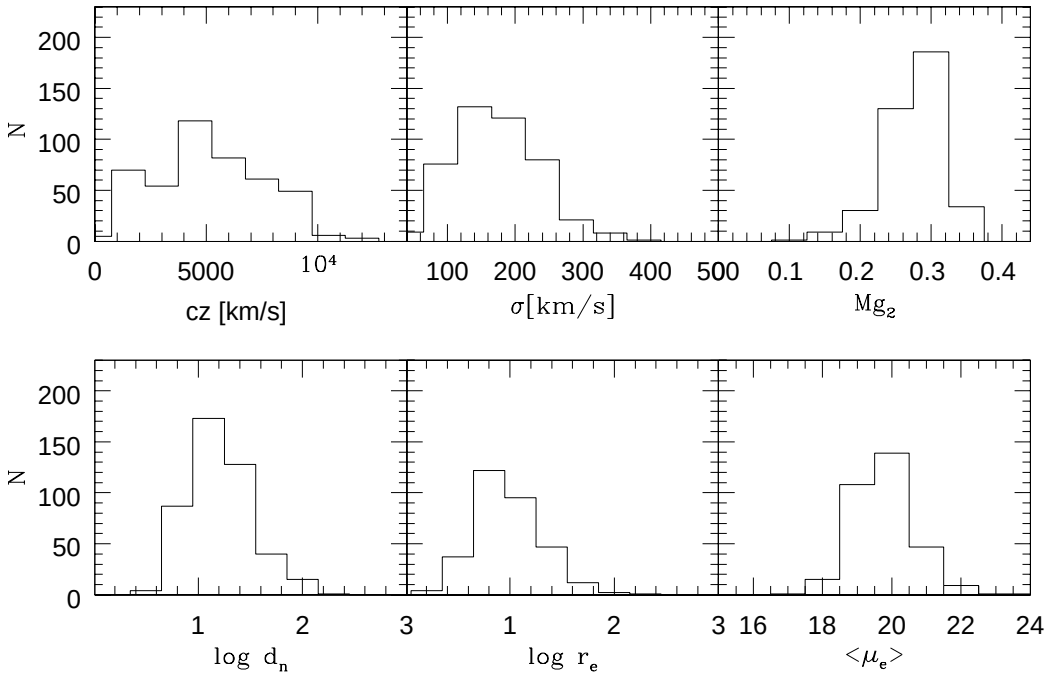

Figure 5.3 (Upper panels) The distribution of spectroscopic parameters for the ENEARc galaxies: redshift, velocity dispersion, and Mg_2 line index. (Lower panels) The distribution of photometric parameters for the cluster galaxies: $\log d_n$, $\log r_e$ (d_n and r_e in arcsec), and $\bar{\mu}_e$.

measurements to those of other authors. This results in a sample of 1694 early-type galaxies with measured distances.

The raw data, details of the observations (carried out primarily at CTIO, ESO and MDM), data reduction and error estimates are presented in Chapters 3 and 4. Here, our main focus is to describe in detail the procedure adopted in the homogenizing the data from various sources and combining it in a sensible way.

5.3.1 The spectroscopic data

The current status of the spectroscopic data assembled for the ENEARc sample is summarized in Table 5.3. Column (1) lists the source of measurements; column (2) the number of measurements from each source which may, at least in our case, include repeated observations; column (3) the number of galaxies for which there is only one source; column (4) the number of galaxies from each source that are in common with our observations, and columns (5)–(7) give the same information but for measurements of the Mg_2 index.

Column (3) of the table shows that about 46% of the cluster sample still relies on a single source for the velocity dispersion measurement. In total there are 208 galaxies with only one source of spectroscopic measurements, thus reinforcing the necessity of somehow

Table 5.3 Spectroscopy: sources of the cluster sample

Source (1)	N_σ (2)	N_σ(sing) (3)	N_σ(com) (4)	N_{Mg_2} (5)	N_{Mg_2}(sing) (6)	N_{Mg_2}(com) (7)
Our	166	32	–	136	50	–
LC	86	21	24	—	–	–
7S	201	20	62	149	49	43
D	45	4	5	45	18	5
JFKb	118	55	32	107	70	29
Lc	72	1	1	70	22	1
S	86	54	6	79	55	3

Notes: The references are indicated as in Tab.5.2.

scaling all measurements to a common system. On the other hand, the number of objects in common with our observations is also relatively large and, with exception of the 7S, they represent most of the observations obtained by other authors, who have usually only studied galaxies that are in clusters. Comparison of columns (2) and (3) shows that there is also considerable overlap among different authors; this gives additional leverage to the effort of building a common system and verifying that it is self-consistent. Furthermore, once simple offsets have been removed, multiple measurements of the same galaxy provide a way to eliminate disparate measurements and to improve the statistical error in the measurement per galaxy.

Figure 5.4 shows the number of galaxies as a function of the total number of spectroscopic observations, regardless of the source, assembled for the whole ENEAR sample. There are about 800 galaxies with at least two measurements which corresponds to $\sim 40\%$ of the total spectroscopic database. Data from the literature amounts to $\sim 50\%$ of the repeated observations. Most of these data ($\sim 80\%$) are for cluster galaxies. Note that our 166 observations are for 124 galaxies, of which 32 had no previously measured velocity dispersion.

The first step in the construction of a homogeneous data set is to define a "fiducial" system to which all other measurements can then be compared and converted. The ENEAR data set was chosen as the standard system because: 1) it is the largest sample available, with 1679 high signal-to-noise long-slit spectra, a substantial fraction of which were taken at high-resolution (see Chapter 4); 2) it was designed to have a significant overlap with other samples, 3) it represents a homogeneous set of measurements, all obtained with the same procedures. In addition, the spectra are all readily available for inspection. Even so, as discussed in Chapter 4, these spectra were obtained from a variety of telescope-instrument setups. Therefore, they have also to be homogenized. To create the reference system, we used the repeated observations and derived the offsets that must be applied to the spectroscopic measurements of each run, adopting an iterative aproach. A detailed description of this is given in Chapter 4. The internal comparisons of

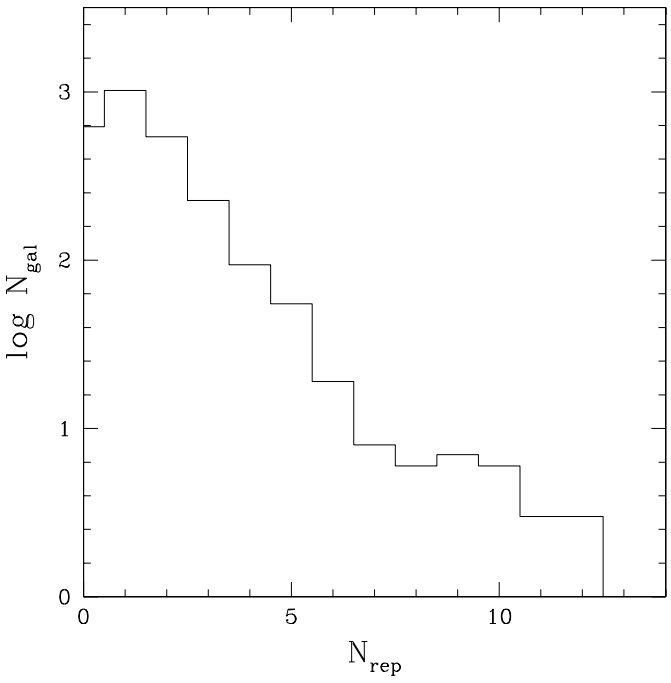

Figure 5.4 The distribution of repeated spectroscopic observations; this includes our measurements as well as those from the literature.

the redshift, velocity dispersion, and the Mg_2 index were found to be in good agreement over the entire range of measurements (see Table 4.3 and Figure 4.10).

Once our measurements were corrected to an internally consistent system, we were in a good position to use the relatively large number of galaxies in common with other authors to convert them to our reference system. The external comparisons shown in Figure 4.11 of Chapter 4 demonstrate that there is no evidence for strong variations of the differences over the range of measured values, except for small offsets at the $\lesssim 2\sigma$ level. Thus, we have converted the external datasets to our "fiducial" system by adding the offsets listed in Table 4.4. Figure 5.5 shows the observed differences between our measurements and the calibrated data of each external source, for velocity dispersion (left panels) and Mg_2 index (right panels). Each panel shows the comparison with a different literature source; these are those with whom we have enough (≥ 10) overlaps: Faber et al. (1989) (7S), Dressler (1987) and Dressler et al. (1991) (D), Jørgensen (1995b) (JFKb), and Lucey & Carter (1988) LC. In all cases, the offsets were completely removed. We have compared the data from the literature sources for which there are fewer overlaps with our data (i.e., Lucey et al. 1997 and Smith et al. 1997), with the data of the other four authors, that we were able to calibrate to the "fiducial" system (Figures 5.6). From this comparison, we have excluded data which were obtained by these authors as a combination of their measurements with those of the other works.

Once all the spectroscopic measurements were in a common system we combined all the available data. For a galaxy with multiple observations, the final combined value of the spectroscopic parameters was given by the error-weighted mean of the individual measurements, eliminating, whenever possible, measurements which differed by more

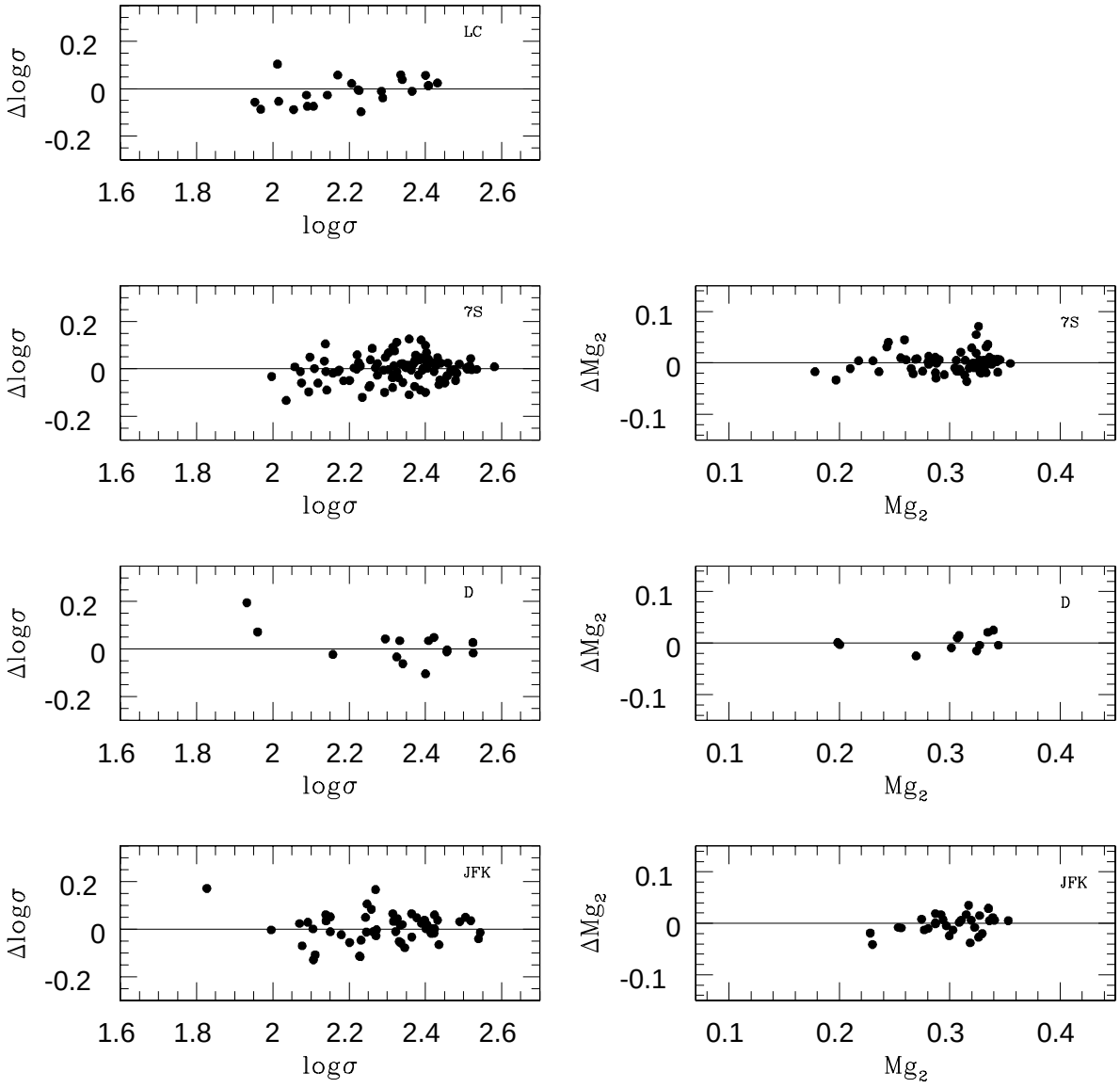

Figure 5.5 Comparison of our measurements with those of other authors. All these comparisons have more than 10 overlaps. Different panels show the comparison for each individual source: Faber et al. (1989) (7S), Dressler (1987) and Dressler et al. (1991) (D), Jørgensen et al. (1995b) (JFKb), and Lucey & Carter (1988) LC.

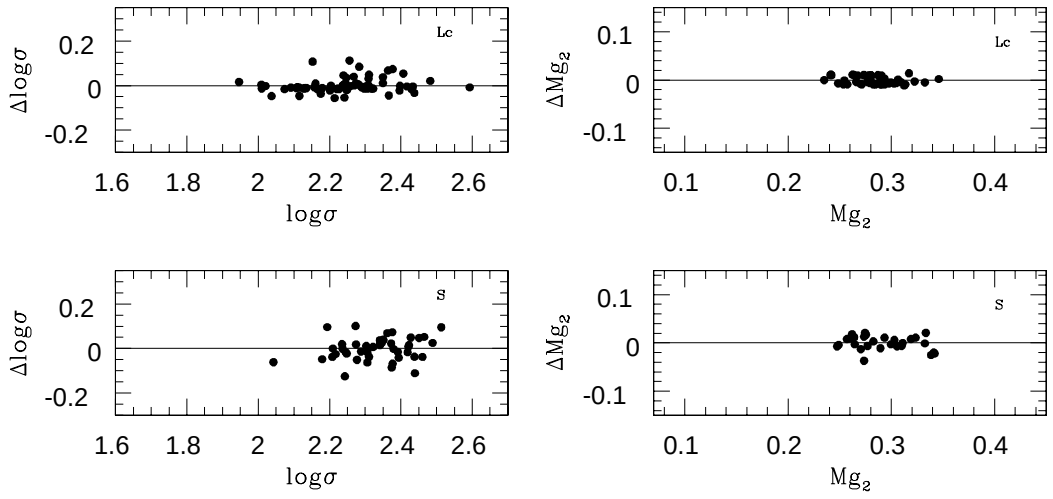

Figure 5.6 Comparison of data from the literature, with fewer than 10 overlaps with our measurements, with those of the previous four sources shown in Figure 5.5 already calibrated to the "fiducial" system. Different panels show the comparison for each individual source: Lucey et al. (1997) (Lc) and Smith et al. (1997) (S).

than $3\sigma_{rms}$ from the mean.

5.3.2 The photometric data

The photometric data assembled for the ENEARc sample is summarized in Table 5.4: column (1) gives the source of measurements; column (2) the passband in which the data were measured; column (3) the number of measurements from each source which may, at least in our case, include repeated observations; column (4) the number of galaxies for which there is only one source; column (5) the number of galaxies from each source that were also observed by us; and columns (6)–(8) give the same information but for measurements of the FP parameters, namely the half-light radius and the mean surface brightness within that radius.

The Table shows that about 70% of the cluster sample relies on data from a single source, making the cross-comparison between different sources extremely important. Column (4) shows that the number of galaxies we observed that are also in other samples is large. This was done to insure that such a comparison would be possible.

At present the cluster sample contains 446 galaxies with measured d_n and 310 galaxies with R-band r_e and μ_e measurements; we provided measurements for 133 of them. In particular, our new data contributes more than one-third of the available FP parameters.

We have eliminated galaxies in clusters for which a simple combination of a $r^{1/4}$ bulge and an exponential disk was a poor fit to the light profile, either because of their intrinsic shape or because of the presence of close companions, from our own measurements. Galaxies observed in images with a FHWM of the point spread function larger than 2.5 arcsec were also eliminated. We also did not consider galaxies with disk-to-bulge ratios $D/B > 2$, which tend to be later types than S0s (recall that at the time our sample

Table 5.4 The cluster sample: Photometry

Source (1)	Filter (2)	N_{d_n} (3)	N_{d_n}(sing) (4)	N_{d_n}(com) (5)	$N_{\rm FP}$ (6)	$N_{\rm FP}$(sing) (7)	$N_{\rm FP}$(com) (8)
O	R	196	37	–	196	37	–
LC	V	64	9	22	—	–	–
7S	B	204	38	76	154	50	64
D	B	45	3	10	—	–	–
JFKa	Gunn-r	159	62	73	153	63	67
Lc	V	72	0	16	—	–	–
S	R	96	54	13	96	62	14

Notes: The references are indicated as in Tab.5.2.

was built the morphological classifications were not optimal). This pruning was done because spurious data could affect the determination of the $D_n - \sigma$ distance indicator. The removed galaxies are part of the photometric catalog (Tables 3.9 - Tables 3.11) presented in Chapter 3, where all our photometric measurements and where notes to individual galaxies are reported.

The main focus now is to combine the measurements of different authors in a uniform way so as to build a homogeneous data set. This is particularly important for the photometric data because most of the available data come from different authors, many of whom used different passbands; in principle, this could affect the uniformity of the measurements.

As described in Chapter 3, we have obtained 1636 R-band images of 1294 galaxies which include repeated observations of the same galaxies in a single run and in different runs, as well as observations of galaxies in common with other authors, to provide the data that is required for building a homogeneous data set.

Figure 5.7 shows the number of galaxies as a function of the number of repeated photometric observations, regardless of the source, assembled for the ENEAR sample of early-types as a whole. There are about 900 galaxies with at least two measurements; this corresponds to $\sim 48\%$ of the total sample of photometric data included in the ENEAR database. Data from the literature comprises $\sim 50\%$ of the repeated observations; most of these ($\sim 80\%$) are for cluster galaxies.

The same procedure described above was used to calibrate the photometric parameters such as d_n, the effective radius r_e, and the mean surface brightness within that radius, $\bar{\mu}_e$, to a fiducial system. First, we checked the consistency of our data by comparing the light profiles of galaxies observed more than once. For these objects, the dispersion among different measured surface brightness profiles was found to be small (~ 0.05 mag/arcsec^2 over an interval typically of 3 magnitudes). This shows that our overall reduction and calibration procedures lead to reliable results. As before, we chose our own observations as the reference system, which we constructed following the same

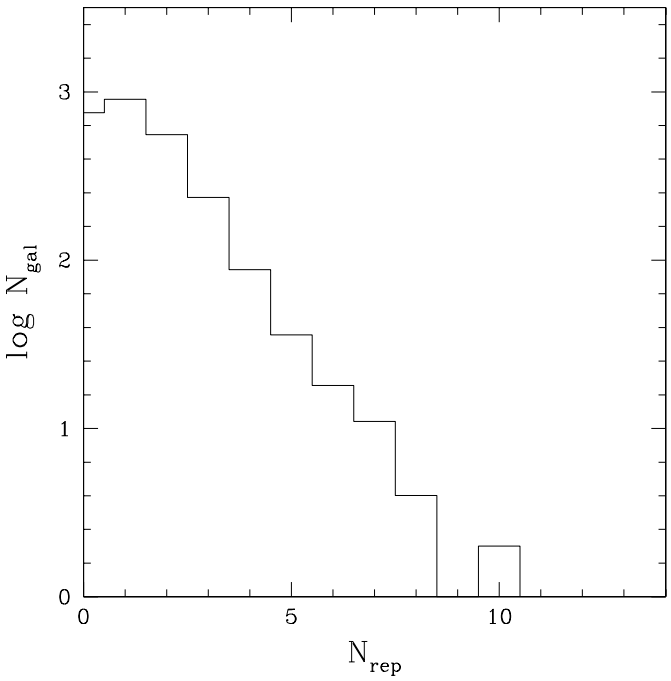

Figure 5.7 The distribution of the repeated photometric observations which include our measurements and those from the literature.

iterative procedure described in Chapter 3: the mean differences between the values of d_n derived from galaxies observed in different runs was minimized. Figures 3.19 and 3.20 show the high degree of internal consistency of our sample.

The measurements available in the literature were calibrated to our internal reference system by applying the offsets listed in Table 3.8, since no systematic trends were found. Figure 5.8 compares our measurements of d_n with those obtained by other authors after each individual data set was calibrated to the fiducial system. For the other parameters, r_e, $\bar{\mu}_e$, and FP=logr_e-0.30$\bar{\mu}_e$ this comparison was only possible with the data from Jørgensen et al. (1995b) and Smith et al. (1997), since only they observed in similar bands. As seen in Chapter 3, the comparison of our data with Smith et al. is poor, because the small number of galaxies in common are usually bright, and only a simple bulge model was used. Therefore, here we only show how our data compare with that of Jørgensen et al., with whom we have an extensive overlap (Figure 5.9). As can be seen, the agreement between our measurements is good; there is no evidence of systematic trends. This justifies using a single offset to calibrate their data to ours.

As before, once this calibration is done, the database can be extended by adding to the sample galaxies from other sources; for the objects in common, this is done by using the error-weighted mean of the individual measurements, eliminating, whenever possible, discordant measurements which differ by more than $3\sigma_{rms}$ from the mean.

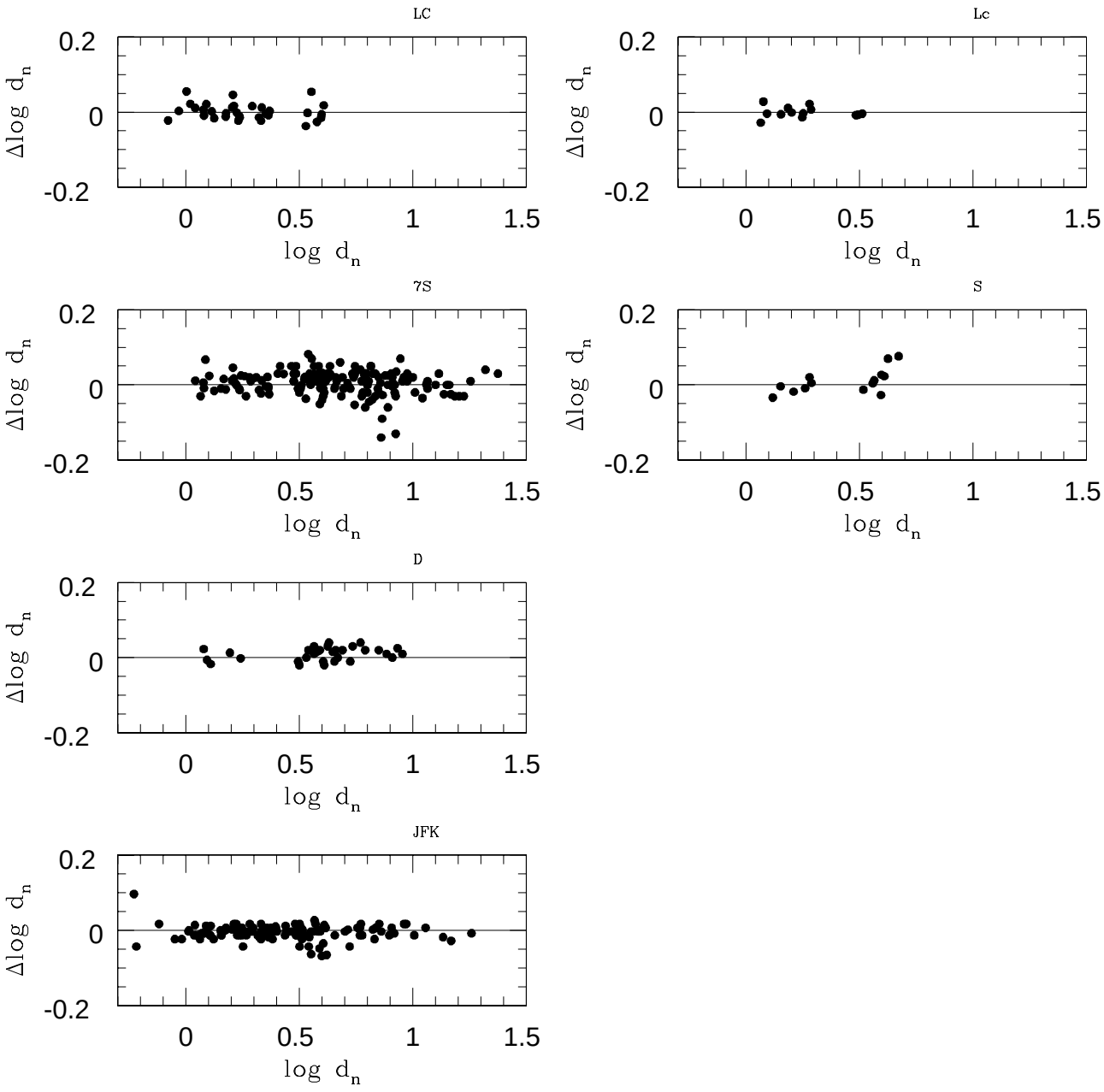

Figure 5.8 Comparison of our measurements of $\log d_n$ with those of other authors. Different panels show this comparison for individual sources: 7S is Faber et al. (1989) (7S); D is Dressler (1987) and Dressler et al. (1991); JFK is Jørgensen et al. (1995b), and LC is Lucey & Carter (1988).

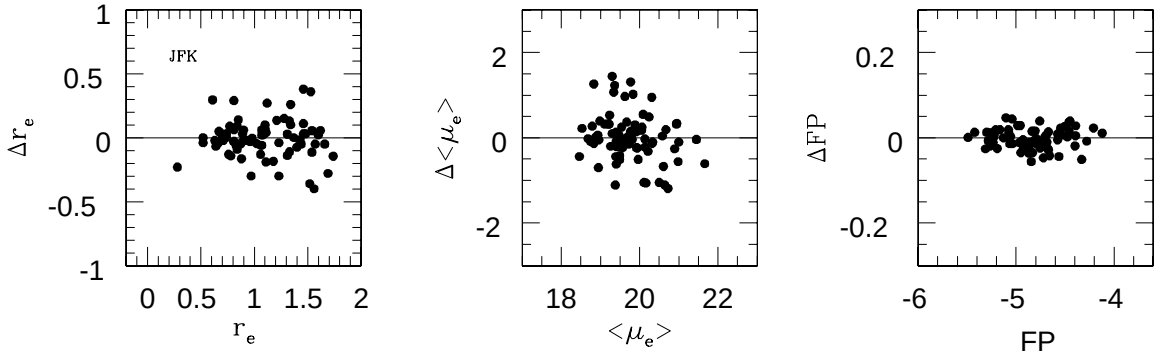

Figure 5.9 Comparison of our measurements of r_e, $\bar{\mu}_e$, and FP with those of Jørgensen et al. (1995b).

5.4 The combined cluster sample

Combining all the spectroscopic and photometric data available, and following the assignment criteria described earlier, we have assembled the cluster sample given in Table 5.5. This sample will be used in Chapter 7 to build a composite $D_n - \sigma$ relation. Column (1) gives the standard name of the galaxy; columns (2) and (3) its equatorial coordinates; column (4) the morphological parameter T of Lauberts & Valentijn (1989); column (5) the total magnitude $m_{\rm B}$; column (6) the number of redshift and σ measurements made by us; column (7) the number of redshift and σ measurements from the literature; columns (8) and (9) the heliocentric redshift and its error; and columns (10) and (11) give the combined velocity dispersion measurement and its error. The corresponding values for the Mg_2 line index are reported in coloumns (12), (13), (14), and (15). Coloumns (16), (17), (18), and (19) are for the photometric parameter $\log d_n$ (d_n in arcmin/0.1). Columns (20) and (21) give the number of contributions to the FP made by us and from the literature, respectively. The values of the FP parameters $\log r_e$ (r_e in arcsec) and $\bar{\mu}_e$ are given in columns (22) and (24), while their errors are in columns (23) and (25), respectively.

In all, the sample consists of 446 galaxies with velocity dispersion and d_n measurements. Of these galaxies, 385 are within $1.5R_p$ and $1.5\sigma_{\rm cl}$, and 61 are "peripheral" objects. There are an additional 232 galaxies that can be added to the sample as they have been found to satisfy our membership assignment criteria. Currently, spectroscopic and photometric data for 135 of these is already available. It is our intention to include them in the sample in the near future.

TABLE 5.5

COMBINED DATA OF THE CLUSTER SAMPLE

Name	α (1950)	δ (1950)	T	m_B mag	N_s^o	N_s^l	cz_{hel} km/s	$\epsilon_{cz_{hel}}$ km/s	$\log\sigma$	$\epsilon_{\log\sigma}$	N_M^o	N_M^l	Mg_2	ϵ_{Mg_2}	N_d^o	N_d^l	$logd_n$	ϵ_{logd_n}	N_F^o	N_F^l	$\log r_e$	ϵ_{r_e}	$\bar{\mu}_e$ mag/$''^2$	ϵ_{μ_e} mag/$''^2$
(1)	(2)	(3)	(4)	(5)	(6)	(7)	(8)	(9)	(10)	(11)	(12)	(13)	(14)	(15)	(16)	(17)	(18)	(19)	(20)	(21)	(22)	(23)	(24)	(25)
Pisces																								
Z17005	00:56:43	+32:52:04	-5	15.58	0	1	4651	50	2.010	0.030	0	1	0.208	0.009	0	1	0.191	0.025	0	1	0.636	0.028	19.140	0.325
CGCG501-070	00:59:25	+32:11:00	-5	14.89	0	1	4263	47	2.294	0.024	0	1	0.327	0.007	0	1	0.365	0.025	0	1	0.627	0.028	18.400	0.325
CGCG501-077	01:02:49	+32:09:44	-5	15.30	0	1	5156	54	2.079	0.024	0	1	0.270	0.007	0	1	0.248	0.025	0	1	0.891	0.028	19.790	0.325
I1618	01:03:11	+32:08:41	-2	15.44	0	1	4730	50	1.948	0.040	0	1	0.226	0.012	0	1	0.187	0.025	0	1	0.946	0.028	20.190	0.325
Z01047	01:04:12	+32:02:30	-5	15.55	0	1	5493	56	2.110	0.030	0	1	0.288	0.009	0	1	0.213	0.025	0	1	0.538	0.028	18.660	0.325
N375	01:04:20	+32:04:52	-2	15.38	0	1	5920	60	2.249	0.040	0	1	0.277	0.012	0	1	0.257	0.025	0	1	0.539	0.028	18.500	0.325
N379	01:04:30	+32:15:16	-3	14.16	0	3	5556	50	2.356	0.011	0	2	0.300	0.006	0	3	0.569	0.031	0	1	1.240	0.112	19.890	0.365
N383	01:04:39	+32:08:46	-3	13.59	0	3	5071	46	2.449	0.011	0	2	0.311	0.006	0	3	0.705	0.023	0	1	1.490	0.063	20.270	0.365
N384	01:04:39	+32:01:32	-5	14.35	0	1	4266	47	2.410	0.021	0	1	0.314	0.006	0	1	0.504	0.025	0	1	0.889	0.028	18.880	0.325
N382	01:04:42	+32:08:00	-5	14.20	0	3	5228	47	2.299	0.011	0	2	0.276	0.006	0	3	0.408	0.046	0	1	0.790	0.317	18.900	0.365
N385	01:04:42	+32:03:10	-3	14.38	0	3	5024	46	2.294	0.011	0	2	0.293	0.006	0	3	0.477	0.039	0	1	1.100	0.155	19.680	0.365
N388	01:05:01	+32:02:36	-5	15.33	0	1	5464	56	2.130	0.024	0	1	0.257	0.007	0	1	0.261	0.025	0	1	0.580	0.028	18.670	0.325
Z01032	01:05:27	+32:11:13	-2	15.89	0	1	4763	51	2.011	0.040	0	1	0.274	0.012	0	1	0.074	0.025	0	1	0.799	0.028	20.080	0.325
N394	01:05:40	+32:52:53	-2	14.74	0	1	4388	48	2.257	0.021	0	1	0.270	0.006	0	1	0.406	0.025	0	1	0.751	0.028	18.760	0.325
N397	01:05:45	+32:50:34	-5	15.46	0	1	4988	52	2.083	0.030	0	1	0.261	0.009	0	1	0.222	0.025	0	1	0.715	0.028	19.280	0.325
N398	01:06:08	+32:14:53	-2	15.21	0	1	4912	52	2.006	0.030	0	1	0.264	0.009	0	1	0.268	0.025	0	1	0.854	0.028	19.630	0.325
CGCG501-102	01:07:12	+32:38:00	-5	15.19	0	1	5176	54	2.187	0.024	0	1	0.280	0.007	0	1	0.284	0.025	0	1	0.760	0.028	19.170	0.325
0108+3253	01:08:12	+32:53:00	-5	12.60	0	3	5294	42	2.470	0.011	0	2	0.352	0.006	0	3	0.744	0.021	0	1	1.440	0.071	19.930	0.365
CGCG501-126	01:09:05	+31:17:38	-2	15.73	0	1	4852	51	1.919	0.030	0	1	0.230	0.009	0	1	0.101	0.025	0	1	0.833	0.028	20.080	0.325
N420	01:09:18	+31:52:00	-2	13.40	1	1	4951	45	2.276	0.018	1	1	0.250	0.001	1	1	0.565	0.009	1	1	1.450	0.220	20.715	0.835
I1638	01:09:35	+33:05:58	-2	14.91	0	1	4828	51	2.153	0.016	0	1	0.278	0.005	0	1	0.341	0.025	0	1	0.943	0.028	19.630	0.325
I1648	01:10:55	+32:57:13	-2	15.18	0	1	5541	57	2.083	0.030	0	1	0.269	0.009	0	1	0.272	0.025	0	1	0.815	0.028	19.470	0.325
Abell 262																								
0146+3532	01:46:48	+35:32:00	-3	13.10	0	2	5054	40	2.371	0.011	0	1	0.300	0.006	0	2	0.644	0.026	0	0	0.000	0.000	0.000	0.000
A01076	01:49:36	+35:52:08	-5	15.66	0	1	4284	47	2.094	0.024	0	1	0.272	0.007	0	1	0.153	0.025	0	1	0.853	0.028	20.020	0.325
N704	01:49:41	+35:52:50	-2	14.87	0	1	4724	50	2.194	0.024	0	1	0.288	0.007	0	1	0.377	0.025	0	1	0.852	0.028	19.220	0.325
N703	01:49:43	+35:55:30	-5	14.58	0	1	5580	57	2.341	0.030	0	1	0.313	0.009	0	1	0.455	0.025	0	1	1.060	0.028	19.690	0.325
0150+3643	01:50:24	+36:43:00	-3	14.40	1	0	5055	40	2.309	0.018	1	0	0.285	0.018	1	0	0.494	0.037	1	0	0.760	0.339	18.520	0.365
0154+3605	01:54:54	+36:05:00	-5	13.70	0	2	4714	37	2.407	0.011	0	2	0.255	0.006	2	1	0.583	0.030	2	1	1.240	0.112	19.850	0.365
CGCG522-089	01:55:02	+36:40:29	-5	15.70	0	1	5245	54	1.953	0.030	0	1	0.222	0.009	0	1	0.119	0.025	0	1	0.989	0.028	20.550	0.325
Perseus																								
0306+4247	03:06:00	+42:47:00	-2	14.50	2	0	5690	45	2.336	0.015	2	0	0.247	0.001	1	0	0.644	0.026	1	0	0.840	0.282	18.290	0.365
I293	03:07:40	+40:56:54	-5	15.04	0	1	4714	50	2.171	0.040	0	1	0.274	0.012	0	1	0.336	0.025	0	1	1.296	0.028	20.760	0.325
N1224	03:07:57	+41:10:31	-2	14.45	0	1	5235	54	2.384	0.030	0	1	0.274	0.009	0	1	0.544	0.025	0	1	1.154	0.028	19.710	0.325
I310	03:13:24	+41:08:00	-2	13.12	2	3	5651	45	2.350	0.021	2	2	0.269	0.009	1	3	0.597	0.030	1	1	1.330	0.091	20.060	0.365
N1260	03:14:09	+41:13:20	-2	14.20	3	2	5519	44	2.273	0.027	1	1	0.245	0.017	1	2	0.564	0.010	1	0	1.750	0.035	21.850	0.365
I312	03:14:50	+41:34:19	-2	14.60	0	1	4988	52	2.342	0.040	0	1	0.310	0.012	0	1	0.532	0.025	0	1	1.098	0.028	19.580	0.325
CR19	03:15:00	+41:17:00	-5	15.80	0	1	3544	41	2.081	0.030	0	1	0.243	0.009	0	1	0.134	0.025	0	1	1.035	0.028	20.610	0.325
CR20	03:15:06	+41:14:00	-5	14.81	0	1	6461	64	2.294	0.021	0	1	0.269	0.006	0	1	0.456	0.025	0	1	1.181	0.028	20.140	0.325
BGP044	03:15:39	+41:31:18	-5	15.36	0	1	4247	46	2.192	0.030	0	1	0.279	0.009	0	1	0.294	0.025	0	1	0.975	0.028	19.940	0.325
CR28	03:16:00	+41:28:00	-5	15.23	0	1	6213	62	2.317	0.003	0	1	0.292	0.009	0	1	0.362	0.025	0	1	0.796	0.028	19.040	0.325
N1272	03:16:06	+41:18:00	-3	14.50	2	3	4172	33	2.418	0.003	1	2	0.336	0.010	1	3	0.634	0.027	1	1	1.480	0.065	20.390	0.365
N1273	03:16:06	+41:20:00	-2	13.78	0	3	5354	53	2.312	0.011	0	2	0.263	0.006	0	3	0.582	0.031	0	1	0.960	0.214	18.830	0.365
I1907	03:16:16	+41:23:58	-2	14.77	0	1	4489	48	2.285	0.040	0	1	0.292	0.012	0	1	0.468	0.025	0	1	1.159	0.028	20.010	0.325
N1274	03:16:21	+41:22:00	-5	15.10	1	2	6447	51	2.279	0.008	0	1	0.296	0.006	0	2	0.494	0.037	0	0	0.000	0.000	0.000	0.000
BGP111	03:16:26	+41:16:00	-5	16.52	0	1	3963	44	1.925	0.030	0	1	0.283	0.009	0	1	0.023	0.025	0	1	0.531	0.028	19.330	0.325
N1278	03:16:42	+41:22:00	-5	14.40	1	4	5186	41	2.377	0.034	0	2	0.309	0.026	0	3	0.655	0.026	0	1	1.360	0.085	20.020	0.365
UGC2673	03:16:43	+41:04:15	-5	14.79	0	1	4434	48	2.290	0.040	0	1	0.302	0.012	0	1	0.457	0.025	0	1	1.258	0.028	20.270	0.325
N1281	03:16:47	+41:26:58	-5	14.66	0	1	4300	47	2.432	0.030	0	1	0.328	0.009	0	1	0.503	0.025	0	1	0.868	0.028	18.820	0.325
N1282	03:17:00	+41:11:00	-5	14.30	1	3	5025	40	2.353	0.027	0	2	0.290	0.024	0	3	0.590	0.030	1	1	1.180	0.070	19.510	0.170
N1283	03:17:00	+41:13:00	-5	14.01	0	3	6727	64	2.320	0.011	0	2	0.291	0.006	0	3	0.470	0.040	0	1	0.920	0.235	19.110	0.365
BGP33	03:17:31	+41:11:30	-2	15.14	0	1	4950	52	2.216	0.030	0	1	0.293	0.009	0	1	0.394	0.025	0	1	0.853	0.028	19.130	0.325
I313	03:17:39	+41:42:50	-2	15.05	0	1	4432	48	2.375	0.030	0	1	0.335	0.009	0	1	0.507	0.025	0	1	1.092	0.028	19.580	0.325
N1293	03:18:12	+41:11:00	-5	13.67	0	3	4132	44	2.320	0.011	0	2	0.318	0.006	0	3	0.550	0.033	0	1	0.980	0.205	19.030	0.365
U2698	03:18:45	+40:41:08	-5	14.31	0	1	4167	46	2.557	0.024	0	1	0.340	0.007	0	1	0.620	0.025	0	1	1.005	0.028	18.880	0.325
U2717	03:21:18	+40:30:53	-5	15.06	0	1	3793	43	2.189	0.024	0	1	0.239	0.007	0	1	0.528	0.025	0	1	1.135	0.028	19.680	0.325
U2725	03:22:10	+41:03:56	-2	14.88	0	1	6215	62	2.333	0.030	0	1	0.297	0.009	0	1	0.482	0.025	0	1	0.898	0.028	18.980	0.325

TABLE 5.5—*Continued*

Name	α (1950)	δ (1950)	T	m_B	N_s^o	N_s^l	cz_{hel}	$\epsilon_{cz_{hel}}$	$\log\sigma$	$\epsilon_{\log\sigma}$	N_M^o	N_M^l	Mg_2	ϵ_{Mg_2}	N_d^o	N_d^l	$logd_n$	ϵ_{logd_n}	N_F^o	N_F^l	$log\,r_e$	ϵ_{r_e}	$\bar{\mu}_e$	$\epsilon_{\bar{\mu}_e}$
				mag			km/s	km/s															mag/″^{2}	mag/″^{2}
(1)	(2)	(3)	(4)	(5)	(6)	(7)	(8)	(9)	(10)	(11)	(12)	(13)	(14)	(15)	(16)	(17)	(18)	(19)	(20)	(21)	(22)	(23)	(24)	(25)
Abell 539																								
0512+0612	05:12:55	+06:12:32	-2	17.16	0	1	8742	79	2.189	0.011	0	1	0.242	0.005	0	1	0.209	0.072	0	1	1.080	0.162	20.810	0.365
0513+0616	05:13:07	+06:16:02	-2	17.19	0	1	8634	79	2.214	0.011	0	1	0.263	0.005	0	1	0.239	0.067	0	1	0.930	0.229	20.350	0.365
0513+0623a	05:13:33	+06:23:34	-2	16.87	0	1	6664	63	2.367	0.011	0	1	0.257	0.005	0	1	0.349	0.052	0	1	0.720	0.372	19.190	0.365
0513+0617	05:13:44	+06:17:18	-2	0.00	0	1	8708	79	2.340	0.011	0	1	0.316	0.005	0	1	0.279	0.061	0	1	0.780	0.324	19.710	0.365
0513+0620	05:13:49	+06:20:54	-2	17.04	0	1	7429	69	2.282	0.011	0	1	0.273	0.005	0	1	0.299	0.059	0	1	0.700	0.390	19.300	0.365
0513+0626b	05:13:52	+06:26:59	-2	17.15	0	1	8672	79	2.156	0.011	0	1	0.230	0.005	0	1	0.089	0.095	0	1	0.980	0.205	20.970	0.365
0513+0626a	05:13:54	+06:26:59	-5	0.00	0	1	7101	66	2.245	0.011	0	1	0.236	0.005	0	1	0.329	0.055	0	1	0.740	0.355	19.380	0.365
0513+0626	05:13:55	+06:26:05	-2	0.00	0	1	9292	84	2.264	0.011	0	1	0.280	0.005	0	1	0.249	0.066	0	1	0.860	0.270	20.050	0.365
0513+0623	05:13:56	+06:23:54	-5	17.20	0	1	8675	79	2.342	0.011	0	1	0.293	0.005	0	1	0.279	0.061	0	1	0.620	0.468	19.120	0.365
0513+0627	05:13:57	+06:27:28	-2	0.00	0	1	7879	73	2.142	0.011	0	1	0.269	0.005	0	1	0.049	0.104	0	1	0.270	1.049	18.600	0.365
0513+0624	05:13:58	+06:24:37	-2	17.25	0	1	9363	84	2.210	0.011	0	1	0.263	0.005	0	1	0.179	0.077	0	1	0.700	0.390	19.670	0.365
0514+0619	05:14:05	+06:19:29	-2	0.00	0	1	8410	77	2.078	0.011	0	1	0.199	0.005	0	1	-0.001	0.117	0	1	0.910	0.240	21.030	0.365
0514+0619a	05:14:10	+06:19:34	-2	0.00	0	1	8129	75	2.188	0.011	0	1	0.262	0.005	0	1	0.119	0.089	0	1	0.530	0.576	19.310	0.365
0514+0620	05:14:08	+06:20:06	-2	0.00	0	1	8677	79	2.162	0.011	0	1	0.265	0.005	0	1	0.139	0.085	0	1	0.890	0.252	20.510	0.365
0514+0629	05:14:14	+06:29:56	-5	16.19	0	1	9699	87	2.502	0.011	0	1	0.338	0.005	0	1	0.469	0.040	0	1	1.130	0.145	20.250	0.365
0514+0626	05:14:26	+06:26:27	-2	0.00	0	1	10012	90	2.238	0.011	0	1	0.301	0.005	0	1	0.089	0.095	0	1	0.790	0.317	20.430	0.365
D16	05:14:37	+06:05:02	-2	16.58	0	1	9695	87	2.306	0.011	0	1	0.289	0.006	0	1	0.396	0.047	0	1	0.890	0.252	19.650	0.365
Virgo																								
N4239	12:14:42	+16:48:00	-5	13.50	1	1	946	13	1.854	0.120	1	1	0.170	0.015	0	1	0.504	0.037	0	0	0.000	0.000	0.000	0.000
N4318	12:20:12	+08:29:00	-5	14.40	1	1	1215	15	1.977	0.011	0	1	0.000	0.000	0	1	0.504	0.037	0	0	0.000	0.000	0.000	0.000
N4339	12:21:00	+06:22:00	-5	12.83	1	1	1298	16	1.997	0.011	0	1	0.257	0.005	1	1	0.744	0.021	0	0	0.000	0.000	0.000	0.000
N4342	12:21:06	+07:22:00	-3	13.91	0	1	714	20	2.375	0.011	0	1	0.300	0.005	0	1	0.744	0.021	0	0	0.000	0.000	0.000	0.000
N4350	12:21:24	+16:58:00	-2	12.30	0	1	1247	15	2.254	0.011	0	1	0.000	0.000	1	0	0.994	0.012	1	0	1.210	0.120	18.330	0.365
N4365	12:21:54	+07:36:00	-5	11.18	0	3	1240	15	2.394	0.008	0	1	0.317	0.006	0	2	1.114	0.009	0	0	0.000	0.000	0.000	0.000
N4374	12:22:30	+13:10:00	-5	10.82	1	3	1033	14	2.449	0.007	1	1	0.304	0.001	1	2	1.264	0.006	0	0	0.000	0.000	0.000	0.000
N4379	12:22:42	+15:53:00	-3	12.77	2	0	1071	14	2.122	0.046	1	0	0.234	0.061	1	0	0.804	0.018	1	0	1.580	0.051	20.340	0.365
N4382	12:22:54	+18:28:00	-2	10.43	0	1	758	12	2.253	0.011	0	1	0.000	0.000	1	0	1.264	0.006	1	0	1.790	0.032	19.450	0.365
N4387	12:23:12	+13:05:00	-5	13.42	1	1	583	10	1.966	0.049	0	1	0.237	0.005	0	1	0.714	0.023	0	0	0.000	0.000	0.000	0.000
N4415	12:24:08	+08:42:42	-5	14.20	3	0	910	13	1.662	0.023	1	0	0.146	0.032	1	0	0.184	0.076	1	0	1.300	0.098	20.660	0.365
N4417	12:24:18	+09:51:42	-2	12.43	2	0	843	12	2.134	0.018	1	0	0.252	0.023	1	0	0.914	0.014	1	0	1.220	0.118	18.680	0.365
N4434	12:25:00	+08:26:00	-5	13.20	0	2	1068	14	2.066	0.011	0	1	0.260	0.006	0	2	0.694	0.024	0	0	0.000	0.000	0.000	0.000
N4458	12:26:25	+13:31:06	-5	13.32	0	2	1951	21	2.029	0.011	0	1	0.215	0.006	1	2	0.629	0.005	1	0	1.170	0.132	19.480	0.365
N4459	12:26:30	+14:15:00	-2	11.95	0	1	1215	15	2.228	0.011	0	1	0.000	0.000	1	0	1.064	0.010	1	0	1.580	0.051	19.450	0.365
N4467	12:26:58	+08:16:10	-5	15.07	1	2	1426	22	1.867	0.046	0	1	0.262	0.005	0	1	0.244	0.067	0	0	0.000	0.000	0.000	0.000
N4472	12:27:12	+08:17:00	-5	9.84	2	2	997	13	2.461	0.007	2	1	0.313	0.005	1	2	1.374	0.005	0	0	0.000	0.000	0.000	0.000
N4478	12:27:46	+12:36:18	-5	12.57	0	3	1370	16	2.153	0.008	0	1	0.250	0.006	0	2	0.934	0.014	0	0	0.000	0.000	0.000	0.000
N4486B	12:28:00	+12:46:00	-7	14.50	0	1	1586	18	2.209	0.011	0	0	0.000	0.000	0	1	0.554	0.033	0	0	0.000	0.000	0.000	0.000
N4486	12:28:17	+12:40:06	-3	10.30	1	3	1292	16	2.541	0.019	1	1	0.293	0.004	1	2	1.314	0.006	0	0	0.000	0.000	0.000	0.000
N4489	12:28:18	+17:02:00	-5	13.20	1	1	960	13	1.688	0.011	0	1	0.194	0.005	1	1	0.589	0.005	1	0	1.290	0.100	20.010	0.365
N4515	12:30:30	+16:32:00	-3	13.30	1	0	940	20	1.903	0.067	1	0	0.204	0.085	1	0	0.584	0.030	1	0	1.090	0.159	19.220	0.365
N4550	12:33:00	+12:30:00	-2	12.73	1	0	381	20	2.011	0.056	1	0	0.172	0.075	1	0	0.864	0.016	1	0	1.470	0.066	19.810	0.365
N4551	12:33:06	+12:32:00	-5	13.27	1	1	1198	15	1.998	0.011	1	1	0.263	0.003	1	1	0.749	0.015	1	0	1.390	0.080	19.820	0.365
N4552	12:33:06	+12:50:00	-5	11.30	0	2	322	20	2.398	0.011	0	1	0.321	0.006	0	2	1.164	0.008	0	0	0.000	0.000	0.000	0.000
N4564	12:33:55	+11:42:54	-5	12.24	0	2	1165	15	2.184	0.011	0	1	0.314	0.006	0	2	0.914	0.014	0	0	0.000	0.000	0.000	0.000
N4596	12:37:24	+10:27:00	-2	11.88	0	1	1870	20	2.149	0.011	0	0	0.000	0.000	1	0	0.984	0.012	1	0	1.780	0.032	20.370	0.365
N4621	12:39:30	+11:55:00	-5	11.28	0	3	444	20	2.345	0.022	0	1	0.322	0.017	0	2	1.144	0.008	0	0	0.000	0.000	0.000	0.000
N4636	12:40:18	+02:58:00	-5	11.01	0	2	937	13	2.278	0.011	0	1	0.308	0.006	0	2	1.094	0.009	0	0	0.000	0.000	0.000	0.000
N4649	12:41:06	+11:49:00	-5	10.30	0	2	1095	14	2.531	0.011	0	1	0.336	0.006	0	2	1.314	0.006	0	0	0.000	0.000	0.000	0.000
N4660	12:42:00	+11:28:00	-5	12.30	0	2	1115	14	2.295	0.011	0	1	0.293	0.006	0	2	0.924	0.014	0	0	0.000	0.000	0.000	0.000
I3773	12:44:44	+10:28:36	-5	14.30	2	0	1095	14	1.725	0.217	1	0	0.095	0.780	1	0	0.224	0.070	1	0	1.490	0.063	21.600	0.365
N4733	12:48:36	+11:11:00	-3	13.20	1	1	905	13	1.733	0.163	1	1	0.190	0.003	0	1	0.594	0.030	0	0	0.000	0.000	0.000	0.000
Coma																								
1236+2657	12:36:48	+26:57:19	-5	0.00	0	1	6623	62	2.296	0.011	0	1	0.000	0.000	0	1	0.249	0.066	0	1	0.630	0.458	19.530	0.365
1236+2802	12:36:51	+28:02:51	-5	0.00	0	1	6710	63	2.420	0.011	0	1	0.000	0.000	0	1	0.342	0.053	0	1	0.710	0.381	19.490	0.365
1237+2722	12:37:00	+27:22:28	-5	0.00	0	1	7068	66	2.235	0.011	0	0	0.000	0.000	0	1	0.310	0.057	0	1	0.840	0.282	20.060	0.365
1241+2708	12:41:25	+27:08:11	-5	0.00	0	1	7566	70	2.189	0.011	0	1	0.000	0.000	0	1	0.175	0.078	0	1	0.900	0.246	20.770	0.365
N4673	12:43:06	+27:20:00	-5	13.70	0	1	6939	61	2.364	0.011	0	1	0.000	0.000	0	1	0.580	0.031	0	1	0.820	0.296	19.020	0.365
N4692	12:45:28	+27:29:39	-5	13.95	0	3	7996	73	2.409	0.029	0	1	0.311	0.022	0	3	0.490	0.026	0	1	1.210	0.120	20.660	0.365
1247+2709	12:47:16	+27:09:37	-5	16.06	0	1	6887	65	2.325	0.011	0	1	0.000	0.000	0	1	0.376	0.049	0	1	0.990	0.200	20.410	0.365

TABLE 5.5—*Continued*

Name	α (1950)	δ (1950)	T	m_B	N_s^o	N_s^t	cz_{hel}	$\epsilon_{cz_{hel}}$	$\log\sigma$	$\epsilon_{\log\sigma}$	N_M^o	N_M^t	Mg_2	ϵ_{Mg_2}	N_d^o	N_d^t	$logd_n$	ϵ_{logd_n}	N_F^o	N_F^t	$log\,r_e$	ϵ_{r_e}	$\bar{\mu}_e$	$\epsilon_{\bar{\mu}_e}$
				mag			km/s	km/s															mag/$''^2$	mag/$''^2$
(1)	(2)	(3)	(4)	(5)	(6)	(7)	(8)	(9)	(10)	(11)	(12)	(13)	(14)	(15)	(16)	(17)	(18)	(19)	(20)	(21)	(22)	(23)	(24)	(25)
1248+2806	12:48:28	+28:06:54	-5	0.00	0	1	7606	70	2.247	0.011	0	1	0.000	0.000	0	1	0.299	0.059	0	1	0.970	0.209	20.600	0.365
I832	12:51:33	+26:42:46	-5	16.17	0	1	7094	66	2.339	0.011	0	1	0.000	0.000	0	1	0.305	0.058	0	1	0.980	0.205	20.590	0.365
N4789	12:51:53	+27:20:19	-5	13.42	0	3	8367	76	2.433	0.008	0	1	0.291	0.006	0	3	0.561	0.028	0	1	1.190	0.126	20.330	0.365
N4807	12:53:06	+27:47:00	-3	14.40	0	3	6941	61	2.325	0.008	0	1	0.279	0.006	0	3	0.418	0.015	0	1	0.830	0.289	19.610	0.365
N4816	12:53:48	+28:01:00	-3	14.10	0	4	6878	55	2.330	0.011	0	2	0.310	0.006	0	4	0.390	0.048	0	1	1.230	0.115	21.070	0.365
1253+2801	12:53:54	+28:01:16	-5	16.47	0	1	6903	65	2.268	0.011	0	0	0.000	0.000	0	1	0.235	0.068	0	1	0.600	0.491	19.510	0.365
1254+2806	12:54:01	+28:06:03	-5	16.53	0	2	6275	60	2.236	0.011	0	1	0.282	0.006	0	2	0.193	0.075	0	1	0.760	0.339	20.220	0.365
N4824	12:54:09	+27:48:33	-5	16.77	0	2	7117	66	2.204	0.011	0	1	0.278	0.006	0	2	0.149	0.083	0	1	0.680	0.408	20.060	0.365
N4827	12:54:18	+27:26:55	-5	15.51	0	1	7599	70	2.447	0.011	0	1	0.000	0.000	0	1	0.460	0.040	0	1	1.010	0.191	20.140	0.365
N4839	12:54:59	+27:46:00	-3	13.60	0	5	7335	58	2.438	0.011	0	2	0.313	0.006	1	5	0.501	0.003	1	2	1.480	0.046	21.287	0.037
N4841B	12:55:09	+28:45:06	-5	13.77	0	2	6793	65	2.363	0.011	0	1	0.301	0.006	0	3	0.442	0.072	0	1	0.990	0.200	20.200	0.365
1255+2827	12:55:24	+28:27:01	-2	16.69	0	2	7245	67	2.238	0.011	0	1	0.270	0.006	0	2	0.181	0.077	0	1	0.540	0.563	19.430	0.365
N4850	12:55:57	+28:14:16	-2	16.19	0	2	6039	58	2.238	0.011	0	1	0.268	0.006	0	2	0.280	0.061	0	1	0.740	0.355	19.810	0.365
1256+2817	12:56:05	+28:17:04	-5	16.23	0	2	7191	67	2.260	0.011	0	1	0.301	0.006	0	2	0.286	0.060	0	1	0.880	0.257	20.270	0.365
I3947	12:56:27	+28:03:16	-5	16.68	0	2	5677	55	2.152	0.011	0	1	0.277	0.006	0	2	0.184	0.076	0	1	0.580	0.514	19.550	0.365
1256+2814a	12:56:36	+28:14:23	-2	16.70	0	1	8311	66	1.929	0.011	0	1	0.000	0.000	0	1	-0.151	0.002	0	1	0.720	0.372	20.960	0.365
N4860	12:56:39	+28:23:36	-5	14.69	0	6	7948	73	2.453	0.043	0	3	0.333	0.009	0	4	0.420	0.044	0	1	0.880	0.257	19.840	0.365
1256+2816	12:56:41	+28:16:06	-2	16.51	0	2	7715	61	2.255	0.011	0	2	0.292	0.006	0	2	0.199	0.074	0	0	0.000	0.000	0.000	0.000
I3957	12:56:43	+28:02:21	-5	15.60	0	3	6350	50	2.182	0.011	0	2	0.292	0.006	1	5	0.155	0.001	1	2	0.610	0.040	19.170	0.180
1995.1986	12:56:43	+28:07:27	-2	16.62	1	1	6709	53	2.220	0.021	1	1	0.328	0.000	1	1	0.186	0.008	1	0	0.760	0.339	19.630	0.365
I3959	12:56:44	+28:03:12	-5	15.20	0	5	7121	56	2.292	0.011	0	2	0.306	0.006	1	6	0.287	0.003	1	3	0.765	0.005	19.275	0.005
N4864	12:56:48	+28:14:54	-5	14.80	0	3	6760	54	2.290	0.011	0	2	0.286	0.006	0	4	0.346	0.053	0	1	0.930	0.229	20.050	0.365
1256+2802	12:56:49	+28:02:43	-2	16.83	0	2	6675	53	2.111	0.011	0	2	0.261	0.006	0	3	0.111	0.004	0	1	0.970	0.209	20.500	0.365
1256+2809	12:56:56	+28:09:25	-5	15.90	0	1	6439	51	1.849	0.011	0	1	0.229	0.005	0	2	-0.054	0.028	0	1	0.830	0.289	20.980	0.365
N4869	12:56:58	+28:10:54	-5	14.90	0	3	6703	53	2.303	0.011	0	2	0.315	0.006	1	5	0.363	0.003	1	2	1.045	0.125	20.000	0.520
1257+2800	12:57:00	+28:00:46	-2	17.05	0	2	7834	62	2.161	0.011	0	2	0.269	0.006	1	2	0.083	0.021	1	0	0.510	0.604	19.070	0.365
1257+2814d	12:57:01	+28:14:42	-2	17.09	0	2	7601	60	2.097	0.011	0	2	0.243	0.006	0	3	0.026	0.004	0	1	0.560	0.538	19.440	0.365
1257+2816	12:57:02	+28:16:04	-2	0.00	0	2	6731	63	2.021	0.011	0	1	0.231	0.006	0	2	-0.098	0.146	0	1	0.510	0.604	20.310	0.365
1257+2803	12:57:06	+28:03:45	-5	16.84	0	1	7833	73	1.904	0.011	0	1	0.236	0.006	0	1	-0.056	0.133	0	0	0.000	0.000	0.000	0.000
1257+2813	12:57:06	+28:13:42	-2	15.10	0	1	6837	54	2.228	0.011	0	1	0.287	0.006	0	3	0.232	0.068	0	2	0.840	0.282	19.660	0.365
1257+2815b	12:57:08	+28:15:19	-2	16.34	0	1	5662	45	2.181	0.011	0	1	0.289	0.006	0	2	0.218	0.071	0	1	0.810	0.302	19.640	0.365
N4874	12:57:10	+28:13:48	-3	14.01	0	4	7176	57	2.398	0.011	0	2	0.323	0.006	1	6	0.519	0.005	1	3	1.810	0.030	21.680	0.365
N4872	12:57:10	+28:13:09	-5	14.65	0	3	7145	57	2.328	0.011	0	2	0.300	0.006	1	5	0.269	0.001	1	2	0.510	0.604	18.330	0.365
1257+2810	12:57:13	+28:10:43	-2	16.63	0	3	7834	62	2.241	0.008	0	3	0.277	0.005	1	3	0.211	0.005	1	1	0.685	0.185	19.245	0.735
1257+2813a	12:57:15	+28:13:32	-2	16.40	0	2	7796	62	2.017	0.011	0	2	0.242	0.006	0	4	-0.027	0.001	0	2	0.380	0.814	18.960	0.365
N4876	12:57:19	+28:10:54	-5	15.10	0	4	6654	53	2.274	0.006	0	1	0.244	0.006	1	5	0.264	0.045	1	3	0.855	0.185	19.695	0.705
1257+2815a	12:57:19	+28:15:57	-5	16.00	0	3	6652	53	2.134	0.011	0	2	0.280	0.006	1	4	0.071	0.007	1	1	0.690	0.030	20.005	0.085
1257+2824	12:57:31	+28:24:00	-5	16.31	0	3	7544	71	2.083	0.011	0	2	0.264	0.006	0	3	0.040	0.106	0	0	0.000	0.000	0.000	0.000
1257+2818	12:57:31	+28:18:24	-2	16.30	0	2	7961	63	2.233	0.011	0	2	0.289	0.006	1	2	0.259	0.005	1	0	1.290	0.100	21.190	0.365
N4881	12:57:33	+28:30:60	-3	14.85	0	6	6691	53	2.258	0.036	0	3	0.282	0.012	0	5	0.351	0.052	0	2	1.030	0.040	20.460	0.020
N4886	12:57:40	+28:15:32	-5	15.05	0	5	6218	49	2.216	0.008	0	3	0.253	0.001	0	6	0.247	0.003	0	3	0.910	0.240	19.870	0.365
N4889	12:57:42	+28:15:00	-3	13.17	0	4	6512	52	2.595	0.011	0	2	0.348	0.006	0	6	0.705	0.005	0	3	1.510	0.060	20.300	0.365
I4011	12:57:42	+28:16:18	-5	15.60	0	4	7216	57	2.066	0.008	0	3	0.270	0.010	0	5	0.089	0.003	0	2	0.680	0.408	19.650	0.365
I4012	12:57:43	+28:20:48	-5	15.70	0	3	7228	57	2.258	0.011	0	2	0.292	0.006	0	4	0.220	0.070	0	1	0.480	0.647	18.980	0.365
1257+2826	12:57:44	+28:26:31	-5	16.03	0	3	6764	65	2.173	0.011	0	2	0.266	0.006	0	3	0.117	0.089	0	0	0.000	0.000	0.000	0.000
1257+2820	12:57:48	+28:20:48	-2	16.10	0	2	7381	59	2.137	0.011	0	2	0.279	0.006	0	3	0.093	0.094	0	1	0.620	0.468	20.030	0.365
I4021	12:57:50	+28:18:30	-2	15.88	0	3	5789	57	2.204	0.011	0	2	0.299	0.006	0	3	0.163	0.080	0	0	0.000	0.000	0.000	0.000
N4898W	12:57:53	+28:13:35	-5	14.60	0	1	6848	65	2.306	0.011	0	1	0.266	0.005	0	1	0.514	0.036	0	0	0.000	0.000	0.000	0.000
1257+2828	12:57:53	+28:28:27	-2	15.32	0	2	8446	67	2.326	0.011	0	2	0.284	0.006	0	2	0.469	0.040	0	0	0.000	0.000	0.000	0.000
N4898E	12:57:54	+28:13:41	-5	15.92	0	1	6349	61	2.150	0.011	0	1	0.254	0.005	0	1	0.124	0.088	0	0	0.000	0.000	0.000	0.000
1257+2819	12:57:58	+28:19:04	-2	16.74	0	2	8153	65	2.143	0.011	0	2	0.281	0.006	0	2	0.136	0.085	0	0	0.000	0.000	0.000	0.000
1258+2747	12:58:02	+27:47:04	-5	17.18	0	2	7815	72	2.009	0.011	0	1	0.260	0.006	0	2	0.010	0.114	0	1	0.670	0.418	20.530	0.365
1258+2813	12:58:03	+28:13:38	-2	0.00	0	2	6927	55	2.185	0.011	0	2	0.272	0.006	0	2	0.063	0.101	0	0	0.000	0.000	0.000	0.000
N4906	12:58:15	+28:11:30	-5	15.20	0	3	7505	60	2.228	0.011	0	2	0.288	0.006	1	4	0.259	0.006	1	1	0.925	0.005	20.180	0.260
1258+2816	12:58:16	+28:16:06	-2	16.86	0	2	7560	60	2.121	0.011	0	2	0.275	0.006	1	2	0.099	0.005	1	0	0.880	0.257	20.290	0.365
1258+2814	12:58:18	+28:14:04	-2	16.99	0	2	6255	50	2.111	0.011	0	2	0.239	0.006	0	2	0.074	0.098	0	0	0.000	0.000	0.000	0.000
1258+2822	12:58:20	+28:22:08	-2	17.31	0	1	6611	52	1.948	0.011	0	1	0.253	0.006	0	1	-0.035	0.126	0	0	0.000	0.000	0.000	0.000
N4923	12:59:07	+28:06:57	-5	14.85	0	4	5516	54	2.299	0.011	0	2	0.306	0.006	0	4	0.356	0.051	0	1	0.850	0.276	19.900	0.365
I843	12:59:10	+29:23:58	-5	15.67	0	1	7397	69	2.408	0.011	0	0	0.000	0.000	0	1	0.394	0.047	0	1	0.980	0.205	20.300	0.365
1259+2809	12:59:26	+28:09:43	-5	0.00	0	2	7621	70	2.270	0.011	0	1	0.285	0.006	0	2	0.179	0.077	0	1	0.620	0.468	19.750	0.365
1995.1051	12:59:23	+27:52:21	-2	17.36	1	0	8238	66	1.912	0.018	1	0	0.242	0.018	1	0	-0.106	0.149	1	0	1.110	0.152	21.690	0.365
N4926	12:59:29	+27:53:36	-3	14.40	0	5	7751	62	2.420	0.011	0	2	0.324	0.006	1	5	0.491	0.003	1	2	1.043	0.033	19.880	0.086
1995.0429	12:59:36	+27:55:17	-2	17.33	1	0	7095	56	2.019	0.067	1	0	0.220	0.085	1	0	-0.126	0.156	1	0	1.010	0.191	21.370	0.365
I4133	13:01:27	+28:15:23	-5	16.53	0	2	6369	60	2.233	0.011	0	1	0.289	0.006	0	2	0.236	0.068	0	1	0.700	0.390	19.800	0.365
N4952	13:02:36	+29:24:00	-5	13.60	0	1	5865	46	2.444	0.011	0	0	0.000	0.000	0	1	0.531	0.034	0	1	1.010	0.191	19.890	0.365

TABLE 5.5—*Continued*

Name	α (1950)	δ (1950)	T	m_B mag	N_s^o	N_s^l	cz_{hel} km/s	$\epsilon_{cz_{hel}}$ km/s	log σ	$\epsilon_{\log\sigma}$	N_M^o	N_M^l	Mg_2	ϵ_{Mg_2}	N_d^o	N_d^l	$logd_n$	ϵ_{logd_n}	N_F^o	N_F^l	$log\, r_e$	ϵ_{r_e}	$\bar{\mu}_e$ mag/$''^2$	$\epsilon_{\bar{\mu}_e}$ mag/$''^2$
(1)	(2)	(3)	(4)	(5)	(6)	(7)	(8)	(9)	(10)	(11)	(12)	(13)	(14)	(15)	(16)	(17)	(18)	(19)	(20)	(21)	(22)	(23)	(24)	(25)
N4957	13:02:48	+27:50:14	-5	14.27	0	**3**	6921	65	**2.358**	0.018	0	1	0.301	0.015	0	**3**	0.425	0.011	0	1	1.150	0.138	20.710	0.365
N4971	13:04:31	+28:48:45	-5	16.26	0	1	6307	60	2.269	0.011	0	0	0.000	0.000	0	1	0.296	0.059	0	1	0.860	0.270	20.200	0.365
N5004	13:08:42	+29:54:00	-2	14.30	0	1	6960	63	2.390	0.011	0	0	0.000	0.000	0	1	0.499	0.037	0	1	1.020	0.187	20.040	0.365
Abell 2199																								
1626+3940	16:26:13	+39:40:40	-5	16.63	0	1	9398	85	2.196	0.011	0	1	0.000	0.000	0	1	0.134	0.086	0	0	0.000	0.000	0.000	0.000
A2199Z34Ac	16:26:14	+39:21:46	-2	15.70	0	1	8964	84	**2.337**	0.021	0	1	0.324	0.006	0	1	0.175	0.025	0	1	0.474	0.028	18.550	0.325
A2199-S26	16:26:40	+39:40:50	-5	15.45	0	4	8806	81	2.239	0.008	0	**3**	0.287	0.004	0	4	0.144	0.001	0	1	0.970	0.209	20.380	0.365
1626+3942	16:26:41	+39:42:53	-3	0.00	0	1	9407	85	2.365	0.011	0	0	0.000	0.000	0	1	0.112	0.090	0	0	0.000	0.000	0.000	0.000
1626+3937a	16:26:48	+39:37:48	-2	16.14	0	2	10177	91	2.459	0.011	0	1	0.325	0.006	0	2	0.263	0.064	0	0	0.000	0.000	0.000	0.000
1626+3939	16:26:51	+39:39:29	-5	16.89	0	4	9824	88	2.143	0.011	0	2	0.265	0.006	0	4	-0.061	0.134	0	0	0.000	0.000	0.000	0.000
1626+3938	16:26:53	+39:38:34	-5	16.23	0	5	8497	77	2.401	0.008	0	**3**	0.265	0.002	0	5	0.153	0.002	0	1	0.300	0.979	17.950	0.365
N6166	16:26:55	+39:39:37	-5	13.01	0	4	9284	85	2.459	0.017	0	**3**	0.321	0.002	0	4	0.418	0.003	0	1	1.890	0.025	22.170	0.365
1627+3935	16:27:01	+39:35:36	-2	0.00	0	1	10162	91	2.074	0.011	0	1	0.000	0.000	0	1	-0.088	0.143	0	0	0.000	0.000	0.000	0.000
1627+3938	16:27:03	+39:38:11	-5	16.82	0	5	8259	76	2.200	0.008	0	**3**	0.274	0.001	0	5	-0.002	0.083	0	1	0.400	0.778	18.960	0.365
1627+3934	16:27:03	+39:34:19	-5	16.73	0	2	7872	72	2.100	0.011	0	1	0.274	0.006	0	2	0.039	0.107	0	0	0.000	0.000	0.000	0.000
1627+3943	16:27:07	+39:43:28	-5	17.16	0	**3**	9215	83	2.289	0.008	0	2	0.302	0.001	0	**3**	0.070	0.001	0	1	0.270	1.049	18.150	0.365
A2199-S44	16:27:13	+39:48:41	-5	16.43	0	**3**	9504	87	2.253	0.011	0	2	0.300	0.006	0	**3**	0.100	0.093	0	0	0.000	0.000	0.000	0.000
A2199-S43	16:27:15	+39:47:11	-5	16.33	0	**3**	8456	78	2.243	0.011	0	2	0.300	0.006	0	**3**	0.075	0.098	0	0	0.000	0.000	0.000	0.000
N6173	16:28:06	+40:55:00	-5	13.19	0	2	8800	81	2.415	0.011	0	1	0.332	0.006	0	2	0.564	0.032	0	0	0.000	0.000	0.000	0.000
Abell 2634																								
2335+2636	23:35:48	+26:36:35	-5	0.00	0	2	9348	84	2.384	0.011	0	1	0.276	0.006	0	2	0.186	0.076	0	0	0.000	0.000	0.000	0.000
2335+2645	23:35:48	+26:45:30	-5	0.00	0	**3**	9552	86	2.262	0.008	0	2	0.285	0.001	0	**3**	0.033	0.076	0	1	0.370	0.833	18.680	0.365
2335+2652	23:35:52	+26:52:53	-5	16.82	0	2	9332	84	2.290	0.011	0	1	0.265	0.006	0	2	0.217	0.071	0	0	0.000	0.000	0.000	0.000
2335+2642a	23:35:59	+26:42:07	-5	0.00	0	**3**	9538	86	2.332	0.008	0	2	0.326	0.001	0	**3**	0.255	0.015	0	1	0.920	0.235	19.810	0.365
2336+2645	23:36:03	+26:45:29	-5	17.43	0	2	9828	88	2.274	0.011	0	1	0.297	0.006	0	2	0.040	0.106	0	0	0.000	0.000	0.000	0.000
2336+2642	23:36:04	+26:42:09	-2	17.14	0	2	8556	78	2.346	0.011	0	1	0.314	0.006	0	2	0.158	0.081	0	0	0.000	0.000	0.000	0.000
2336+2645a	23:36:06	+26:45:10	-2	16.94	0	**3**	8491	77	2.316	0.008	0	2	0.302	0.000	0	**3**	0.157	0.008	0	1	0.740	0.355	19.550	0.365
2336+2644	23:36:08	+26:44:04	-5	16.76	0	**3**	9293	84	2.343	0.008	0	1	0.300	0.006	0	**3**	0.246	0.008	0	1	0.800	0.310	19.470	0.365
2336+2650	23:36:12	+26:50:30	-2	0.00	0	2	9554	86	2.220	0.011	0	1	0.279	0.006	0	2	0.040	0.106	0	0	0.000	0.000	0.000	0.000
2336+2650a	23:36:19	+26:50:46	-2	0.00	0	2	8990	81	2.233	0.011	0	1	0.263	0.006	0	2	0.020	0.111	0	0	0.000	0.000	0.000	0.000
2336+2646	23:36:23	+26:46:08	-2	0.00	0	1	9643	87	2.143	0.011	0	1	0.258	0.006	0	2	-0.003	0.117	0	0	0.000	0.000	0.000	0.000
2336+2653	23:36:26	+26:53:06	-2	17.28	0	2	9217	83	2.204	0.011	0	1	0.285	0.006	0	2	0.103	0.092	0	0	0.000	0.000	0.000	0.000
Abell 194																								
D12	01:21:08	-02:05:28	-2	15.94	0	1	5592	54	2.016	0.011	0	1	0.297	0.006	0	1	0.199	0.074	0	1	0.060	1.701	19.410	0.365
I1696	01:22:19	-01:52:37	-5	14.62	0	2	5827	56	2.211	0.022	0	2	0.298	0.001	1	2	0.362	0.017	1	1	0.840	0.282	19.530	0.365
0122-0145	01:22:59	-01:45:44	-2	15.36	0	4	5526	44	2.143	0.024	0	1	0.254	0.025	1	**3**	0.371	0.004	1	1	0.655	0.045	18.695	0.285
D33	01:23:11	-01:43:01	-2	15.41	0	4	5237	51	2.185	0.020	0	1	0.259	0.022	1	**3**	0.364	0.003	1	1	0.810	0.050	19.325	0.045
N541	01:23:12	-01:38:00	-3	14.00	4	5	5417	49	2.330	0.014	4	2	0.330	0.009	2	4	0.543	0.006	2	1	1.395	0.065	20.685	0.075
0123-0136	01:23:14	-01:36:14	-2	15.82	0	**3**	5535	54	2.089	0.006	0	1	0.244	0.006	**3**	**3**	0.243	0.005	**3**	1	0.747	0.032	19.497	0.160
0123-0145	01:23:15	-01:45:06	-2	16.70	0	2	5178	41	1.890	0.008	0	2	0.000	0.000	1	1	-0.038	0.007	1	1	0.900	0.020	20.915	0.055
0123-0131	01:23:19	-01:31:34	-5	16.72	0	4	6300	50	2.000	0.035	0	1	0.206	0.054	**3**	**3**	0.088	0.003	**3**	1	0.607	0.012	19.563	0.150
N545	01:23:24	-01:36:00	-3	13.70	2	7	5321	48	2.387	0.007	2	2	0.323	0.005	2	4	0.603	0.003	2	1	1.420	0.074	20.630	0.365
N548	01:23:29	-01:29:06	-3	14.62	0	5	5419	43	2.180	0.042	0	2	0.252	0.006	1	4	0.237	0.003	1	1	1.010	0.090	20.425	0.485
N547	01:23:30	-01:36:00	-5	13.40	1	6	5524	50	2.383	0.019	1	2	0.327	0.006	2	4	0.604	0.003	2	1	1.100	0.155	19.690	0.365
0123-0150	01:23:58	-01:50:02	-2	16.82	0	1	5509	44	1.904	0.011	0	1	0.000	0.000	2	0	-0.056	0.133	2	0	1.010	0.191	21.230	0.365
0124-0131	01:24:43	-01:31:51	-2	15.27	0	**3**	4804	38	2.206	0.040	0	1	0.270	0.034	1	**3**	0.346	0.005	1	1	0.835	0.035	19.510	0.010
D60	01:25:02	-01:21:49	-2	15.10	0	1	4489	45	2.052	0.011	0	1	0.233	0.006	0	1	0.339	0.053	0	1	0.920	0.235	19.810	0.365
N564	01:25:12	-02:08:00	-5	14.02	0	**3**	5699	45	2.368	0.008	0	2	0.301	0.007	0	**3**	0.552	0.007	0	1	1.130	0.145	19.930	0.365
D71	01:25:28	-00:59:50	-2	0.00	0	1	5712	55	1.938	0.011	0	1	0.201	0.006	0	1	0.159	0.081	0	1	0.950	0.219	20.650	0.365
I120	01:25:40	-02:10:40	-2	15.36	0	1	4806	48	2.038	0.011	0	1	0.247	0.006	0	1	0.229	0.069	0	1	0.900	0.246	20.210	0.365
Fornax																								
357G22	03:20:47	-37:23:12	-2	9.93	**3**	1	1739	14	2.342	0.020	**3**	0	0.252	0.004	1	1	1.364	0.040	1	0	1.350	0.087	17.650	0.365
358G2	03:24:35	-35:53:18	-2	13.80	1	0	1466	12	1.961	0.039	1	0	0.209	0.035	1	0	0.434	0.043	1	0	1.210	0.120	20.110	0.365
358G6	03:25:20	-34:42:00	-5	14.30	2	0	1237	10	1.705	0.037	2	0	0.153	0.013	2	1	0.231	0.090	2	0	1.220	0.120	20.555	0.455
418G4	03:26:06	-32:27:30	-5	12.63	1	**3**	1425	12	2.191	0.017	1	2	0.300	0.002	2	**3**	0.790	0.006	2	1	1.053	0.060	18.583	0.335
418G5	03:26:17	-31:14:24	-5	11.51	1	2	1180	10	2.203	0.011	1	1	0.258	0.003	0	2	1.044	0.011	0	0	0.000	0.000	0.000	0.000
358G12	03:28:38	-35:01:24	-2	12.91	1	2	1527	13	2.152	0.008	1	1	0.269	0.013	0	2	0.794	0.019	0	0	0.000	0.000	0.000	0.000

TABLE 5.5—*Continued*

Name	α (1950)	δ (1950)	T	m_B	N_s^o	N_s^l	cz_{hel}	$\epsilon_{cz_{hel}}$	$\log\sigma$	$\epsilon_{\log\sigma}$	N_M^o	N_M^l	Mg_2	ϵ_{Mg_2}	N_d^o	N_d^l	$logd_n$	ϵ_{logd_n}	N_F^o	N_F^l	$log\, r_e$	ϵ_{r_e}	$\bar{\mu}_e$	$\epsilon_{\bar{\mu}_e}$
(1)	(2)	(3)	(4)	(5)	(6)	(7)	(8)	(9)	(10)	(11)	(12)	(13)	(14)	(15)	(16)	(17)	(18)	(19)	(20)	(21)	(22)	(23)	(24)	(25)
				mag			km/s	km/s															mag/″2	mag/″2
418G10	03:31:52	-31:21:36	-2	13.13	1	0	1310	10	2.058	0.066	1	0	0.268	0.064	1	0	0.774	0.020	1	0	0.930	0.229	18.120	0.365
358G23	03:33:21	-35:23:30	-2	12.56	1	2	1352	11	2.233	0.041	1	1	0.295	0.016	1	2	0.864	0.010	1	0	1.220	0.118	18.720	0.365
358G27	03:34:08	-35:36:18	-5	12.33	2	2	1352	11	2.061	0.034	2	1	0.253	0.006	1	3	0.849	0.009	1	1	1.545	0.135	20.125	0.675
0334-3532	03:34:59	-35:32:19	-2	14.77	1	0	1765	15	1.758	0.085	1	0	0.188	0.062	2	0	0.114	0.010	2	0	2.245	0.215	24.230	0.410
358G38	03:35:17	-35:54:30	-2	12.65	1	2	986	20	2.113	0.008	1	1	0.235	0.005	1	2	0.834	0.020	1	0	1.100	0.155	18.410	0.365
358G45	03:36:34	-35:36:42	-5	11.11	1	3	1464	12	2.511	0.014	1	2	0.334	0.002	2	3	1.191	0.002	2	1	1.650	0.044	19.560	0.365
358G46	03:36:57	-35:45:18	-5	11.46	1	2	1942	16	2.389	0.031	1	1	0.313	0.003	2	2	1.171	0.009	2	0	1.480	0.040	18.565	0.195
301G23	03:38:51	-37:40:18	-5	14.30	1	2	1566	14	2.101	0.032	1	0	0.228	0.048	1	2	0.614	0.020	1	0	0.950	0.219	18.660	0.365
358G52	03:40:25	-35:33:06	-2	12.20	1	2	1395	12	2.204	0.008	1	1	0.247	0.009	2	2	0.874	0.012	2	0	1.285	0.025	19.030	0.140
358G59	03:43:10	-36:07:42	-5	14.10	1	0	1020	20	1.715	0.067	1	1	0.153	0.007	1	1	0.424	0.044	0	0	0.000	0.000	0.000	0.000
359G7	03:52:36	-36:06:48	-3	12.53	1	4	1364	11	2.078	0.005	1	2	0.276	0.007	0	3	0.796	0.008	0	1	1.460	0.068	20.310	0.365
Eridanus																								
548G19	03:24:15	-21:31:48	-3	14.46	1	0	1326	10	1.742	0.039	1	0	0.180	0.035	0	1	0.414	0.045	0	0	0.000	0.000	0.000	0.000
548G53	03:35:23	-18:30:06	-2	14.00	1	0	1948	16	2.208	0.034	1	0	0.226	0.022	1	0	0.654	0.026	1	0	1.150	0.138	19.400	0.365
482G19	03:36:19	-23:11:24	-5	11.44	1	4	1692	14	2.391	0.010	1	2	0.319	0.002	2	2	1.074	0.010	0	0	0.000	0.000	0.000	0.000
482G26	03:37:11	-22:53:06	-2	13.40	1	0	1518	13	1.890	0.034	1	0	0.209	0.022	1	0	0.634	0.027	1	0	1.130	0.145	19.380	0.365
548G66	03:37:52	-18:36:18	-2	14.10	1	0	1869	15	1.882	0.034	1	0	0.165	0.022	2	0	0.289	0.005	2	0	1.550	0.039	21.630	0.040
548G67	03:37:57	-18:44:30	-3	11.06	1	3	1784	15	2.434	0.012	1	1	0.327	0.005	3	2	1.074	0.010	0	0	0.000	0.000	0.000	0.000
482G29	03:38:23	-27:01:18	-2	13.90	1	0	1790	15	1.887	0.066	1	0	0.227	0.064	1	0	0.614	0.028	1	0	0.970	0.209	18.830	0.365
549G1	03:40:38	-22:16:06	-5	12.57	3	4	1457	12	2.166	0.006	3	2	0.258	0.007	2	3	0.785	0.007	2	1	1.383	0.069	19.793	0.171
549G9	03:42:39	-22:04:42	-5	12.84	1	3	1666	14	2.148	0.027	1	2	0.276	0.004	1	3	0.726	0.004	1	1	1.325	0.065	19.855	0.365
-0310047	03:46:12	-16:32:00	-2	13.50	1	0	1450	11	2.284	0.034	1	0	0.262	0.022	1	0	0.814	0.018	1	0	1.250	0.110	19.150	0.365
Hydra																								
436G30	10:28:43	-28:27:42	-5	13.94	1	0	3645	35	2.491	0.031	1	0	0.319	0.035	2	0	0.624	0.010	2	0	0.975	0.005	18.735	0.075
501G3	10:29:27	-26:18:30	-3	14.03	2	1	4142	34	2.324	0.009	2	1	0.285	0.002	3	1	0.503	0.011	3	0	1.130	0.035	19.790	0.141
501G13	10:31:09	-26:38:24	-2	14.20	1	1	3504	28	2.327	0.025	1	1	0.295	0.012	1	1	0.551	0.018	1	1	0.940	0.010	19.110	0.120
R154	10:32:15	-28:18:33	-2	15.36	1	0	3485	37	2.230	0.011	1	0	0.286	0.014	0	1	0.339	0.053	0	1	0.630	0.458	18.920	0.365
436G44	10:32:27	-28:14:24	-2	14.16	0	1	3221	25	2.211	0.011	0	1	0.258	0.006	0	1	0.569	0.031	0	1	0.980	0.205	19.370	0.365
436G45	10:32:30	-28:15:30	-5	15.35	0	1	3402	37	2.278	0.011	0	1	0.268	0.006	0	1	0.359	0.051	0	1	0.460	0.677	18.170	0.365
501G21	10:32:59	-27:06:10	-2	14.41	0	1	4592	46	2.162	0.011	0	0	0.000	0.000	0	1	0.404	0.046	0	0	0.000	0.000	0.000	0.000
501G27	10:33:37	-27:03:35	-5	15.25	1	2	3207	35	1.885	0.068	0	1	0.132	0.096	0	1	-0.105	0.149	0	0	0.000	0.000	0.000	0.000
RMH26	10:33:43	-27:14:58	-5	15.08	0	3	2286	28	2.018	0.006	0	1	0.240	0.005	0	3	0.201	0.010	0	1	0.890	0.252	20.270	0.365
501G30	10:33:51	-26:54:12	-5	14.14	1	4	3978	31	2.353	0.006	1	1	0.323	0.013	2	5	0.615	0.009	2	2	0.983	0.013	19.123	0.099
D80	10:33:52	-27:25:44	-2	15.59	0	1	4196	43	1.920	0.011	0	2	0.000	0.000	0	1	-0.023	0.123	0	0	0.000	0.000	0.000	0.000
D190	10:33:59	-26:54:25	-2	16.53	0	1	3687	39	1.863	0.011	0	2	0.000	0.000	1	1	-0.071	0.005	1	0	0.850	0.276	20.790	0.365
D107	10:33:58	-27:27:42	-2	15.49	0	1	3551	38	1.910	0.011	0	0	0.000	0.000	0	1	0.010	0.114	0	0	0.000	0.000	0.000	0.000
501G34	10:34:01	-27:10:42	-2	13.55	1	5	3674	29	2.275	0.005	1	2	0.302	0.002	2	5	0.610	0.013	2	2	1.345	0.108	20.255	0.423
RMH28	10:34:02	-27:05:41	-2	15.19	1	4	3006	34	2.101	0.020	0	1	0.273	0.023	0	3	0.261	0.010	0	1	0.790	0.317	19.750	0.365
D66	10:34:04	-27:19:20	-3	15.46	0	1	2816	32	1.961	0.011	0	1	0.000	0.000	0	1	0.081	0.097	0	0	0.000	0.000	0.000	0.000
RMH29	10:34:06	-27:03:33	-2	14.93	1	3	3441	37	2.275	0.034	1	1	0.282	0.010	0	3	0.421	0.005	0	1	0.610	0.479	18.430	0.365
D46	10:34:08	-27:13:28	-2	15.00	0	2	4776	48	2.029	0.008	0	1	0.000	0.000	1	2	0.132	0.010	1	0	1.270	0.105	21.440	0.365
D154	10:34:14	-27:12:37	-5	15.91	0	2	3193	35	2.080	0.008	0	1	0.000	0.000	0	2	0.114	0.006	0	0	0.000	0.000	0.000	0.000
501G36	10:34:15	-27:15:30	-5	12.24	1	5	4058	33	2.409	0.016	1	2	0.329	0.006	0	3	0.752	0.007	0	1	1.340	0.089	20.000	0.365
D37	10:34:20	-27:18:04	-5	14.97	0	3	4739	47	2.070	0.006	0	1	0.283	0.005	0	3	0.294	0.004	0	1	0.800	0.310	19.620	0.365
501G38	10:34:22	-27:16:06	-2	12.19	1	6	3593	28	2.260	0.018	1	2	0.312	0.011	0	5	0.542	0.013	0	2	2.105	0.045	22.665	0.135
D61	10:34:24	-27:12:35	-5	15.13	0	2	2703	31	2.314	0.008	0	3	0.000	0.000	0	2	0.372	0.006	0	0	0.000	0.000	0.000	0.000
D195	10:34:28	-27:07:44	-5	16.03	1	1	4478	45	1.997	0.059	1	0	0.248	0.097	0	1	-0.031	0.125	0	0	0.000	0.000	0.000	0.000
437G11	10:34:30	-27:39:35	-2	14.22	0	1	4938	49	2.265	0.011	0	1	0.285	0.005	0	1	0.509	0.036	0	1	0.920	0.235	19.330	0.365
437G13	10:34:33	-27:39:28	-2	14.58	0	1	3499	37	2.210	0.011	0	1	0.249	0.005	0	1	0.479	0.039	0	1	0.800	0.310	19.000	0.365
437G15	10:34:37	-27:55:06	-2	13.81	1	0	2753	22	2.191	0.031	1	0	0.176	0.035	1	0	0.664	0.025	1	0	0.800	0.310	17.990	0.365
D23	10:34:43	-27:08:24	-2	14.60	0	2	2710	31	2.065	0.008	0	2	0.000	0.000	0	2	0.234	0.006	0	0	0.000	0.000	0.000	0.000
D135	10:34:48	-27:23:52	-5	15.60	0	2	4115	42	2.049	0.008	0	2	0.000	0.000	0	2	0.206	0.006	0	0	0.000	0.000	0.000	0.000
501G47	10:34:56	-27:12:31	-2	14.18	0	3	4820	48	2.093	0.023	0	1	0.287	0.021	0	2	0.368	0.006	0	0	0.000	0.000	0.000	0.000
501G48	10:34:58	-26:55:54	-2	14.12	0	3	3840	30	2.232	0.006	0	1	0.249	0.005	0	2	0.538	0.006	0	0	0.000	0.000	0.000	0.000
501G49	10:34:59	-27:17:57	-2	15.05	0	3	4014	42	2.031	0.006	0	1	0.237	0.006	0	2	0.211	0.006	0	0	0.000	0.000	0.000	0.000
501G54	10:35:16	-27:20:00	-2	13.92	2	3	4213	33	2.256	0.015	1	1	0.279	0.004	2	2	0.542	0.010	2	0	1.075	0.015	19.450	0.100
RMH50	10:35:20	-26:47:02	-2	0.00	0	1	3075	34	1.957	0.011	0	1	0.244	0.005	1	1	0.059	0.102	1	1	0.820	0.296	20.620	0.365
501G56	10:35:23	-26:22:12	-2	14.05	1	0	3456	27	2.313	0.031	1	0	0.255	0.035	1	0	0.604	0.029	1	0	1.050	0.174	19.190	0.365
501G58	10:35:26	-26:49:18	-2	13.01	0	2	2940	23	2.339	0.093	0	1	0.318	0.062	1	1	0.749	0.021	1	1	1.360	0.085	20.070	0.365
D119	10:35:40	-27:11:27	-2	15.87	0	2	5247	51	2.017	0.008	0	1	0.000	0.000	0	2	0.190	0.006	0	0	0.000	0.000	0.000	0.000
437G21	10:35:50	-28:31:24	-2	14.26	2	1	3953	31	2.221	0.016	2	1	0.284	0.002	1	1	0.519	0.035	1	1	1.060	0.170	19.840	0.365

TABLE 5.5—*Continued*

Name	α (1950)	δ (1950)	T	m_B	N_s^o	N_s^t	cz_{hel}	$\epsilon_{cz_{hel}}$	$\log\sigma$	$\epsilon_{\log\sigma}$	N_M^o	N_M^t	Mg_2	ϵ_{Mg_2}	N_d^o	N_d^t	$logd_n$	ϵ_{logd_n}	N_F^o	N_F^t	$log\, r_e$	ϵ_{r_e}	$\bar{\mu}_e$	$\epsilon_{\bar{\mu}_e}$
(1)	(2)	(3)	(4)	(5)	(6)	(7)	(8)	(9)	(10)	(11)	(12)	(13)	(14)	(15)	(16)	(17)	(18)	(19)	(20)	(21)	(22)	(23)	(24)	(25)
R466	10:38:11	-27:36:00	-2	14.62	1	0	3992	41	1.988	0.011	1	0	0.183	0.014	0	1	0.209	0.072	0	1	1.230	0.115	21.260	0.365
437G38	10:38:29	-27:42:10	-2	14.47	1	0	4510	46	2.296	0.011	1	0	0.236	0.014	0	1	0.449	0.041	0	1	0.960	0.214	19.720	0.365
437G45	10:39:38	-28:30:54	-2	14.26	3	1	3786	30	2.151	0.021	2	1	0.271	0.004	1	1	0.447	0.002	1	1	1.130	0.040	20.180	0.258
Centaurus																								
322G38	12:35:35	-41:13:36	-2	13.94	0	2	3165	27	2.307	0.008	0	1	0.316	0.006	0	2	0.654	0.018	0	0	0.000	0.000	0.000	0.000
322G51	12:38:10	-41:19:54	-2	14.22	0	2	3263	26	2.240	0.008	0	1	0.318	0.006	0	2	0.624	0.020	0	0	0.000	0.000	0.000	0.000
322G59	12:40:21	-41:05:06	-2	13.71	0	2	3178	25	2.359	0.008	0	1	0.312	0.006	0	2	0.504	0.026	0	0	0.000	0.000	0.000	0.000
322G60	12:40:47	-41:05:18	-2	13.68	0	2	2559	20	2.210	0.008	0	1	0.313	0.006	0	2	0.764	0.014	0	0	0.000	0.000	0.000	0.000
322G66	12:41:25	-41:28:36	-5	13.08	0	3	2652	21	2.272	0.008	0	2	0.281	0.014	0	3	0.844	0.012	0	0	0.000	0.000	0.000	0.000
N4661	12:42:19	-40:44:24	-5	14.74	0	2	2566	31	2.164	0.011	0	1	0.264	0.006	0	2	0.387	0.048	0	0	0.000	0.000	0.000	0.000
322G81	12:44:36	-40:57:54	-2	14.10	0	3	2993	23	2.372	0.019	0	1	0.284	0.018	0	3	0.698	0.002	0	0	0.000	0.000	0.000	0.000
322G88	12:45:36	-41:26:30	-2	14.28	0	2	2650	21	2.204	0.008	0	1	0.277	0.006	0	2	0.664	0.018	0	0	0.000	0.000	0.000	0.000
D56	12:45:37	-40:51:03	-5	0.00	0	2	3685	39	2.133	0.008	0	1	0.000	0.000	0	2	0.376	0.006	0	0	0.000	0.000	0.000	0.000
D40	12:45:45	-41:02:03	-5	16.62	0	1	3001	34	1.920	0.011	0	1	0.000	0.000	0	1	0.082	0.097	0	0	0.000	0.000	0.000	0.000
322G91	12:46:04	-41:02:18	-2	11.47	0	4	3008	25	2.404	0.021	0	2	0.283	0.006	0	4	0.924	0.005	0	0	0.000	0.000	0.000	0.000
D36	12:46:33	-41:03:48	-5	0.00	0	1	3134	35	1.905	0.011	0	2	0.000	0.000	0	1	0.107	0.091	0	0	0.000	0.000	0.000	0.000
322G101	12:46:48	-40:47:00	-5	14.16	0	3	2040	27	2.200	0.008	0	1	0.306	0.006	0	3	0.500	0.019	0	0	0.000	0.000	0.000	0.000
D29	12:46:52	-41:06:59	-2	14.58	1	2	3672	39	2.011	0.008	1	0	0.237	0.085	0	2	0.476	0.006	0	0	0.000	0.000	0.000	0.000
J357	12:47:06	-40:57:16	-5	15.18	1	3	2176	27	2.087	0.008	0	1	0.254	0.006	0	2	0.381	0.006	0	0	0.000	0.000	0.000	0.000
323G1	12:47:08	-41:00:30	-2	14.26	0	3	3678	29	2.335	0.023	0	1	0.320	0.021	0	3	0.646	0.002	0	0	0.000	0.000	0.000	0.000
D49	12:47:25	-40:56:57	-5	15.72	1	3	2939	33	2.075	0.008	0	1	0.290	0.006	0	2	0.339	0.006	0	0	0.000	0.000	0.000	0.000
D35	12:47:26	-41:01:38	-5	0.00	0	1	4172	43	1.834	0.011	0	1	0.000	0.000	0	1	-0.015	0.121	0	0	0.000	0.000	0.000	0.000
323G5	12:47:26	-41:14:36	-2	14.25	0	2	2644	21	2.294	0.008	0	1	0.000	0.000	0	2	0.656	0.006	0	0	0.000	0.000	0.000	0.000
J347	12:47:57	-41:09:31	-2	14.96	0	2	2385	29	2.087	0.008	0	2	0.000	0.000	0	2	0.444	0.006	0	0	0.000	0.000	0.000	0.000
323G15	12:48:59	-38:33:30	-2	14.16	0	2	3140	27	2.156	0.008	0	1	0.246	0.006	0	2	0.474	0.028	0	0	0.000	0.000	0.000	0.000
323G16	12:49:00	-40:51:36	-3	13.75	0	3	2268	18	2.192	0.008	0	2	0.270	0.018	0	3	0.669	0.005	0	0	0.000	0.000	0.000	0.000
323G19	12:49:17	-41:11:18	-3	14.36	0	2	3739	29	2.093	0.008	0	1	0.254	0.006	0	2	0.594	0.021	0	0	0.000	0.000	0.000	0.000
323G21	12:49:29	-41:07:06	-2	14.26	0	2	3014	24	2.082	0.008	0	1	0.263	0.006	0	2	0.604	0.021	0	0	0.000	0.000	0.000	0.000
323G36	12:51:07	-39:26:36	-5	12.88	0	3	2976	23	2.318	0.008	0	2	0.289	0.009	0	3	0.864	0.011	0	0	0.000	0.000	0.000	0.000
Klemola27																								
-5-32-74	13:42:31	-29:46:04	-2	14.39	3	0	4381	35	2.252	0.016	3	0	0.288	0.003	1	1	0.391	0.008	1	1	0.695	0.025	18.790	0.040
445G28	13:44:27	-29:33:36	-5	14.30	1	1	4515	36	2.364	0.033	1	1	0.302	0.006	1	1	0.546	0.002	1	1	0.925	0.035	19.075	0.015
445G40	13:45:48	-30:33:48	-2	14.45	1	1	5235	41	2.116	0.053	1	1	0.255	0.004	1	1	0.377	0.002	1	1	1.540	0.020	21.580	0.170
445G42	13:45:57	-30:54:26	-2	14.35	2	0	5201	41	2.052	0.037	2	0	0.225	0.009	1	0	0.414	0.045	1	0	0.890	0.252	19.290	0.365
445G46	13:46:14	-30:02:54	-3	12.22	4	4	4576	37	2.447	0.011	4	3	0.322	0.004	1	3	0.662	0.039	1	1	1.590	0.050	20.880	0.365
445G52	13:47:10	-30:19:48	-2	13.85	0	3	3779	31	2.327	0.006	0	2	0.272	0.011	1	4	0.558	0.005	1	1	1.350	0.080	20.515	0.125
445G54	13:47:41	-29:48:03	-2	14.97	0	1	5275	42	1.936	0.011	0	1	0.170	0.006	0	1	0.319	0.056	0	1	0.950	0.219	22.120	0.365
1347-2945	13:47:54	-29:45:04	-2	14.77	0	1	4301	34	2.319	0.011	0	1	0.299	0.006	0	1	0.419	0.044	0	1	0.720	0.372	18.940	0.365
445G59	13:48:47	-30:14:31	-2	13.65	1	1	4531	36	2.271	0.010	1	1	0.293	0.004	1	1	0.521	0.002	1	1	1.145	0.055	20.005	0.035
445G62	13:49:16	-30:12:18	-2	15.43	1	0	4705	37	1.973	0.056	1	0	0.216	0.075	0	1	0.169	0.079	0	1	0.960	0.214	20.600	0.365
445G78	13:53:07	-30:05:48	-2	13.35	0	3	4975	39	2.318	0.038	0	2	0.251	0.006	0	3	0.709	0.005	0	0	0.000	0.000	0.000	0.000
Abell S753																								
384G13	13:52:47	-33:28:54	-2	14.23	1	1	3805	31	1.958	0.036	1	1	0.197	0.001	0	1	0.464	0.040	0	0	0.000	0.000	0.000	0.000
384G19	13:54:44	-33:58:30	-2	13.92	1	2	4282	35	2.166	0.007	1	1	0.268	0.011	2	2	0.591	0.005	2	0	0.965	0.035	18.915	0.095
384G21	13:55:02	-33:45:55	-2	14.40	1	0	4333	34	2.040	0.067	1	0	0.269	0.085	1	0	0.424	0.044	1	0	1.020	0.187	19.750	0.365
384G23	13:55:34	-33:59:58	-2	14.48	1	1	3989	31	2.055	0.011	1	1	0.225	0.009	1	1	0.399	0.047	1	1	1.560	0.054	21.680	0.365
1355-3313	13:55:45	-33:13:32	-2	15.29	0	1	3986	31	2.097	0.011	0	1	0.226	0.006	0	1	0.359	0.051	0	1	0.620	0.468	18.740	0.365
1355-3314	13:55:56	-33:14:52	-2	14.84	0	1	4166	33	2.202	0.011	0	1	0.282	0.006	0	1	0.399	0.047	0	1	0.800	0.310	19.290	0.365
1356-3404	13:56:55	-34:04:31	-5	15.17	1	1	4224	33	1.994	0.011	0	1	0.197	0.006	0	1	0.289	0.060	0	1	0.740	0.355	19.530	0.365
384G29	13:57:51	-33:59:00	-2	14.16	2	1	3460	28	2.150	0.009	2	1	0.218	0.015	1	1	0.479	0.039	1	1	1.110	0.152	20.130	0.365
384G31	13:58:14	-33:42:12	-2	14.05	1	3	4174	34	2.405	0.010	1	2	0.305	0.004	1	3	0.578	0.008	1	1	1.085	0.015	19.500	0.100
1359-3332	13:59:14	-33:32:59	-2	14.93	0	1	3883	31	2.219	0.011	0	1	0.298	0.006	0	1	0.409	0.045	0	1	0.690	0.399	18.850	0.365
1359-3400	13:59:57	-34:00:56	-2	15.05	0	1	4190	33	2.066	0.011	0	1	0.249	0.006	0	1	0.369	0.050	0	1	0.770	0.332	19.310	0.365
1400-3347	14:00:10	-33:47:30	-2	14.57	0	1	5214	41	2.389	0.011	0	1	0.302	0.006	0	1	0.499	0.037	0	1	0.460	0.677	17.550	0.365
1400-3351	14:00:11	-33:51:30	-5	14.67	0	1	3978	31	2.170	0.011	0	1	0.247	0.006	0	1	0.339	0.053	0	1	0.910	0.240	19.950	0.365
384G39	14:00:42	-33:44:18	-2	12.03	3	5	4172	34	2.523	0.008	2	3	0.338	0.004	2	4	0.894	0.009	2	1	1.610	0.048	20.360	0.365
1401-3343	14:01:36	-33:43:17	-2	14.01	0	1	3855	30	2.259	0.011	0	1	0.301	0.006	1	1	0.516	0.002	1	1	0.990	0.060	19.430	0.360
1403-3404	14:03:07	-34:04:20	-2	14.76	1	0	4526	36	1.975	0.090	0	1	0.000	0.000	0	1	0.279	0.061	0	1	1.230	0.115	21.160	0.365
384G49	14:03:10	-33:41:05	-2	14.16	0	3	4441	35	2.282	0.038	0	2	0.287	0.007	1	3	0.522	0.004	1	1	0.840	0.020	18.855	0.195

TABLE 5.5—*Continued*

Name	α (1950)	δ (1950)	T	m_B	N_s^o	N_s^l	cz_{hel}	$\epsilon_{cz_{hel}}$	$\log\sigma$	$\epsilon_{\log\sigma}$	N_M^o	N_M^l	Mg_2	ϵ_{Mg_2}	N_d^o	N_d^l	$logd_n$	ϵ_{logd_n}	N_F^o	N_F^l	$log\, r_e$	ϵ_{r_e}	$\bar{\mu}_e$	$\epsilon_{\bar{\mu}_e}$
				mag			km/s	km/s															mag/$''^2$	mag/$''^2$
(1)	(2)	(3)	(4)	(5)	(6)	(7)	(8)	(9)	(10)	(11)	(12)	(13)	(14)	(15)	(16)	(17)	(18)	(19)	(20)	(21)	(22)	(23)	(24)	(25)
1403-3415	14:03:52	-34:15:13	-5	14.90	0	1	4701	37	2.110	0.011	0	1	0.259	0.006	0	1	0.349	0.052	0	1	0.910	0.240	19.900	0.365
Klemola44																								
2344-2831	23:44:02	-28:31:51	-5	16.86	0	1	8005	74	1.969	0.011	0	1	0.000	0.000	0	1	-0.025	0.124	0	0	0.000	0.000	0.000	0.000
2344-2812	23:44:36	-28:12:28	-2	16.14	1	1	8784	80	2.048	0.036	1	0	0.279	0.058	2	1	0.101	0.003	2	1	0.820	0.010	20.290	0.220
471G14	23:44:39	-28:14:06	-5	14.20	0	3	8427	67	2.329	0.034	0	1	0.288	0.025	2	3	0.378	0.006	2	1	0.867	0.007	19.447	0.129
2344-2824	23:44:40	-28:24:07	-5	16.35	1	3	8301	66	2.142	0.030	1	1	0.261	0.017	2	4	0.108	0.002	2	1	1.015	0.415	21.055	1.415
2344-2820	23:44:44	-28:20:26	-2	17.23	0	1	8338	66	1.989	0.011	0	1	0.000	0.000	3	1	-0.140	0.098	2	1	0.773	0.116	21.017	0.447
2344-2815	23:44:46	-28:15:12	-2	16.70	0	1	7454	69	2.127	0.011	0	1	0.000	0.000	2	1	0.019	0.003	2	1	0.620	0.023	19.810	0.122
2344-2823	23:44:47	-28:23:49	-2	14.88	1	2	8299	68	2.216	0.007	1	0	0.338	0.022	2	1	0.076	0.002	2	1	0.740	0.010	20.110	0.100
2344-2824a	23:44:52	-28:24:50	-5	14.76	0	3	8302	66	2.401	0.008	0	1	0.286	0.006	1	4	0.370	0.005	1	1	0.830	0.289	19.520	0.365
2344-2823b	23:44:52	-28:23:13	-5	14.20	1	3	8231	65	2.424	0.011	1	1	0.326	0.022	2	3	0.438	0.004	2	1	1.250	0.050	20.560	0.020
2344-2819a	23:44:54	-28:19:16	-2	0.00	0	1	8219	75	2.005	0.011	0	2	0.000	0.000	1	1	-0.109	0.013	1	1	0.515	0.005	19.940	0.170
2344-2823a	23:44:55	-28:23:06	-5	14.05	1	3	8423	68	2.218	0.007	1	1	0.328	0.030	2	4	0.179	0.002	1	1	0.830	0.310	20.105	1.055
2344-2824b	23:44:59	-28:24:11	-5	16.47	0	3	8332	66	2.059	0.008	0	1	0.279	0.006	3	3	0.056	0.026	3	0	0.390	0.796	19.020	0.365
2345-2825	23:45:07	-28:25:18	-2	15.61	0	1	7320	58	2.256	0.011	0	1	0.000	0.000	3	1	0.236	0.002	3	1	0.875	0.085	20.035	0.425
2345-2825a	23:45:08	-28:25:01	-2	13.78	0	3	8726	70	2.326	0.015	0	1	0.357	0.012	3	4	0.334	0.004	3	1	1.320	0.093	21.250	0.365
2345-2826	23:45:09	-28:26:30	-5	17.21	0	3	9529	76	2.196	0.008	0	1	0.286	0.006	3	4	0.043	0.003	0	0	0.000	0.000	0.000	0.000
2345-2823	23:45:09	-28:23:08	-2	0.00	0	1	8152	65	1.784	0.011	0	1	0.000	0.000	2	1	-0.271	0.218	1	1	0.270	1.049	19.680	0.365
2345-2825b	23:45:23	-28:25:11	-2	16.27	0	1	7434	59	2.139	0.011	0	2	0.000	0.000	4	0	0.107	0.003	4	0	0.693	0.033	19.653	0.119
2345-2828a	23:45:50	-28:28:03	-2	16.26	0	2	8964	81	2.133	0.061	0	1	0.000	0.000	2	1	0.162	0.002	2	1	0.497	0.024	18.877	0.153
2345-2833	23:45:50	-28:33:24	-2	15.85	1	1	8117	64	2.182	0.010	1	0	0.298	0.022	1	0	0.174	0.078	1	0	0.880	0.257	20.160	0.365
2345-2823a	23:45:51	-28:23:18	-2	15.46	0	1	8923	71	2.073	0.011	0	2	0.000	0.000	0	1	-0.041	0.128	0	1	0.440	0.709	19.620	0.365
2345-2825c	23:45:51	-28:25:40	-2	16.81	0	1	9274	84	1.921	0.011	0	1	0.000	0.000	0	1	-0.141	0.161	0	1	0.690	0.399	20.670	0.365
I5362	23:49:01	-28:14:06	-2	13.75	0	2	8137	76	2.343	0.011	0	1	0.309	0.006	0	2	0.414	0.045	0	0	0.000	0.000	0.000	0.000
7S21																								
CGCG457-008	00:18:16	+21:15:33	-2	15.18	0	1	5926	60	2.053	0.030	0	1	0.259	0.009	0	1	0.277	0.025	0	1	0.827	0.028	19.470	0.325
N79	00:18:27	+22:17:21	-5	14.80	0	1	5479	56	2.280	0.030	0	1	0.312	0.009	0	1	0.354	0.025	0	1	1.053	0.028	20.000	0.325
S06	00:18:45	+21:42:22	-2	15.99	0	1	5646	58	2.103	0.021	0	1	0.211	0.009	0	1	0.018	0.025	0	1	0.827	0.028	20.340	0.325
N83	00:18:48	+22:09:00	-5	14.21	0	3	6304	56	2.394	0.027	0	1	0.326	0.024	0	3	0.538	0.034	0	1	1.360	0.085	20.430	0.365
N85A	00:18:49	+22:14:04	-2	15.27	0	1	6189	62	2.025	0.030	0	1	0.244	0.009	0	1	0.175	0.025	0	1	1.201	0.028	20.990	0.325
I1548	00:19:19	+21:43:45	-2	15.15	0	1	5775	59	2.165	0.030	0	1	0.202	0.009	0	1	0.294	0.025	0	1	0.691	0.028	18.910	0.325
HMS0122+33																								
I1673	01:17:58	+32:46:59	-5	14.92	0	1	5090	53	2.268	0.030	0	1	0.277	0.009	0	1	0.361	0.025	0	1	0.555	0.028	18.140	0.325
CGCG502-043	01:18:17	+33:07:02	-5	15.19	0	1	5237	54	2.097	0.024	0	1	0.268	0.009	0	1	0.270	0.025	0	1	0.799	0.028	19.410	0.325
I1680	01:18:58	+33:01:27	-2	15.14	0	1	4438	48	2.122	0.030	0	1	0.269	0.009	0	1	0.295	0.025	0	1	0.734	0.028	19.050	0.325
0120+3313	01:20:24	+33:13:00	-2	13.00	0	3	4375	35	2.405	0.011	0	2	0.329	0.006	0	3	0.701	0.023	0	1	1.250	0.110	19.440	0.365
N501	01:20:36	+33:11:06	-5	15.64	0	2	4887	50	2.201	0.011	0	2	0.306	0.006	0	2	0.261	0.064	0	1	0.730	0.364	19.160	0.365
N507	01:20:50	+32:59:42	-3	11.89	0	3	4917	50	2.458	0.011	0	2	0.299	0.006	0	3	0.732	0.022	0	1	1.370	0.083	19.700	0.365
N508	01:20:52	+33:01:13	-5	14.54	0	1	5517	57	2.343	0.024	0	1	0.312	0.009	0	1	0.446	0.025	0	1	1.144	0.028	19.960	0.325
0122+3325	01:22:42	+33:25:00	-2	13.70	1	1	4879	39	2.384	0.005	1	0	0.275	0.006	1	1	0.571	0.013	1	1	0.865	0.165	18.615	0.585
N529	01:22:50	+34:27:12	-5	13.75	0	1	4796	51	2.363	0.024	0	1	0.297	0.009	0	1	0.670	0.025	0	1	1.123	0.028	19.140	0.325
Abell 347																								
U1859	02:21:35	+42:23:51	-5	14.31	0	1	5917	60	2.550	0.030	0	1	0.354	0.009	0	1	0.543	0.025	0	1	0.881	0.028	18.680	0.325
CGCG538-065	02:21:43	+43:05:57	-2	14.77	0	1	5301	55	2.308	0.030	0	1	0.314	0.009	0	1	0.425	0.025	0	1	0.899	0.028	19.200	0.325
N909	02:22:14	+41:48:37	-5	14.59	0	1	4978	52	2.273	0.030	0	1	0.276	0.009	0	1	0.457	0.025	0	1	0.983	0.028	19.360	0.325
N911	02:22:33	+41:43:51	-2	14.32	0	1	5766	59	2.400	0.030	0	1	0.328	0.009	0	1	0.534	0.025	0	1	0.905	0.028	18.810	0.325
N912	02:22:34	+41:33:08	-5	14.92	0	1	4418	48	2.235	0.030	0	1	0.295	0.009	0	1	0.360	0.025	0	1	0.918	0.028	19.520	0.325
CGCG539-042	02:29:18	+41:43:27	-5	14.99	0	1	4885	52	2.185	0.030	0	1	0.272	0.009	0	1	0.342	0.025	0	1	1.035	0.028	19.940	0.325
Abell 1367																								
N3805	11:38:12	+20:37:00	-3	13.80	1	0	6472	53	2.465	0.067	1	0	0.326	0.085	1	0	0.604	0.029	1	0	1.380	0.081	20.240	0.365
N3837	11:41:18	+20:10:00	-5	14.20	1	2	6248	55	2.378	0.039	1	1	0.315	0.012	0	2	0.374	0.049	0	0	0.000	0.000	0.000	0.000
N3841	11:41:18	+20:16:00	-5	14.95	0	1	6363	61	2.326	0.011	0	1	0.305	0.005	0	1	0.294	0.059	0	0	0.000	0.000	0.000	0.000
N3842	11:41:30	+20:14:00	-5	13.30	0	2	6237	55	2.454	0.011	0	1	0.333	0.006	0	2	0.544	0.033	0	0	0.000	0.000	0.000	0.000
N3862	11:42:29	+19:53:02	-5	14.00	0	2	6462	57	2.422	0.011	0	1	0.292	0.006	0	2	0.474	0.039	0	0	0.000	0.000	0.000	0.000
I2955	11:42:31	+19:53:00	-5	14.93	0	1	6345	61	2.278	0.011	0	1	0.283	0.005	0	1	0.214	0.071	0	0	0.000	0.000	0.000	0.000

TABLE 5.5—*Continued*

Name	α (1950)	δ (1950)	T	m_B mag	N_s^o	N_s^l	cz_{hel} km/s	$\epsilon_{cz_{hel}}$ km/s	$\log\sigma$	$\epsilon_{\log\sigma}$	N_M^o	N_M^l	Mg_2	ϵ_{Mg_2}	N_d^o	N_d^l	$logd_n$	ϵ_{logd_n}	N_F^o	N_F^l	$log\,r_e$	ϵ_{r_e}	$\bar{\mu}_e$ mag/″^{2}	$\epsilon_{\bar{\mu}_e}$ mag/″^{2}
(1)	(2)	(3)	(4)	(5)	(6)	(7)	(8)	(9)	(10)	(11)	(12)	(13)	(14)	(15)	(16)	(17)	(18)	(19)	(20)	(21)	(22)	(23)	(24)	(25)
N3873	11:43:06	+20:03:00	-5	14.20	0	2	5438	49	2.391	0.011	0	1	0.296	0.006	0	2	0.464	0.040	0	0	0.000	0.000	0.000	0.000
N3886	11:44:30	+20:07:00	-3	14.30	1	0	5767	52	2.417	0.067	1	0	0.321	0.085	1	0	0.534	0.034	1	0	1.180	0.129	19.780	0.365
HG50																								
N5813	14:58:42	+01:54:00	-5	12.09	4	3	1963	21	2.374	0.014	1	1	0.312	0.004	0	2	0.914	0.014	0	0	0.000	0.000	0.000	0.000
N5831	15:01:36	+01:25:00	-5	13.05	0	2	1683	19	2.223	0.011	0	1	0.289	0.006	1	2	0.799	0.015	1	0	1.270	0.105	19.250	0.365
N5845	15:03:28	+01:49:36	-5	13.51	1	1	1446	17	2.388	0.013	1	1	0.294	0.010	1	1	0.754	0.010	1	0	0.680	0.408	16.990	0.365
N5846	15:03:56	+01:47:48	-5	11.76	1	3	1709	19	2.410	0.020	1	1	0.321	0.000	1	2	1.004	0.012	0	0	0.000	0.000	0.000	0.000
Pegasus																								
N7617	23:17:36	+07:53:00	-2	14.64	0	2	4072	43	2.150	0.011	0	1	0.223	0.006	0	2	0.254	0.065	0	0	0.000	0.000	0.000	0.000
N7619	23:17:42	+07:55:57	-5	12.78	1	3	3747	35	2.513	0.018	1	2	0.335	0.004	0	2	0.844	0.017	0	0	0.000	0.000	0.000	0.000
N7623	23:17:58	+08:07:20	-2	14.17	1	0	3674	35	2.261	0.034	1	0	0.283	0.022	1	0	0.594	0.030	1	0	1.310	0.096	20.200	0.365
N7626	23:18:10	+07:56:36	-5	12.90	1	3	3450	33	2.404	0.014	1	2	0.332	0.009	2	2	0.829	0.025	1	0	1.360	0.085	19.410	0.365
Doradus																								
249G11	03:37:04	-44:15:42	-2	11.96	0	1	998	20	2.075	0.011	0	1	0.213	0.006	0	1	0.889	0.015	0	1	1.240	0.112	19.080	0.365
201G20	04:06:56	-48:01:42	-2	11.96	0	1	1174	11	2.176	0.011	0	1	0.260	0.006	0	1	0.949	0.013	0	1	1.450	0.069	19.650	0.365
250G7	04:07:28	-45:38:54	-5	12.44	1	0	1503	13	2.002	0.011	1	0	0.142	0.010	0	1	0.924	0.014	0	0	0.000	0.000	0.000	0.000
157G3	04:08:46	-56:15:00	-2	12.14	0	1	823	20	2.238	0.011	0	1	0.282	0.006	0	1	0.909	0.014	0	1	1.360	0.085	19.410	0.365
118G10	04:11:44	-57:51:48	-2	11.83	0	1	1088	20	2.134	0.011	0	1	0.277	0.006	1	1	0.982	0.013	1	1	1.645	0.195	20.170	0.570
157G16	04:14:39	-55:42:54	-3	11.13	0	3	1238	11	2.291	0.021	0	2	0.305	0.041	2	3	1.160	0.009	2	0	1.570	0.070	18.975	0.255
157G17	04:15:05	-55:54:12	-2	10.73	0	1	1270	12	2.216	0.011	0	1	0.264	0.006	2	1	1.269	0.006	0	0	0.000	0.000	0.000	0.000
157G22	04:20:59	-57:05:24	-2	11.56	0	1	1050	10	2.314	0.011	0	1	0.287	0.006	1	1	1.059	0.010	1	1	1.320	0.093	18.760	0.365
157G31	04:26:32	-55:08:12	-2	12.16	0	1	1533	14	2.201	0.011	0	1	0.271	0.006	0	1	0.919	0.014	0	1	1.320	0.093	19.290	0.365
Abell 3381																								
0608-3334	06:08:05	-33:34:53	-2	15.06	0	1	11557	51	2.324	0.011	0	1	0.322	0.005	0	1	0.179	0.077	0	1	1.200	0.123	21.370	0.365
0608-3332	06:08:08	-33:32:29	-5	17.07	0	1	11335	50	2.196	0.011	0	1	0.283	0.006	0	1	0.049	0.104	0	1	0.680	0.408	20.170	0.365
0609-3317	06:09:17	-33:17:38	-2	15.44	0	1	11488	50	2.311	0.011	0	1	0.284	0.006	0	1	0.209	0.072	0	1	0.800	0.310	19.970	0.365
0609-3306	06:09:50	-33:06:39	-3	15.12	0	1	11059	98	2.348	0.011	0	1	0.288	0.006	0	1	0.259	0.064	0	1	1.070	0.166	20.730	0.365
Abell S639																								
264G23	10:36:59	-46:14:40	-2	14.46	0	1	5658	55	2.327	0.011	0	1	0.292	0.005	0	1	0.459	0.041	0	1	1.240	0.112	20.620	0.365
1037-4552	10:37:02	-45:52:48	-3	14.12	0	1	6099	58	2.352	0.011	0	1	0.273	0.006	0	1	0.669	0.025	0	1	0.970	0.209	18.920	0.365
1037-4555	10:37:49	-45:55:46	-5	14.71	0	1	6627	63	2.277	0.011	0	1	0.263	0.005	0	1	0.519	0.035	0	1	0.830	0.289	18.980	0.365
1037-4607	10:37:52	-46:07:24	-5	16.14	0	1	5854	56	2.090	0.011	0	1	0.207	0.005	0	1	0.259	0.064	0	1	0.470	0.662	18.630	0.365
264G300	10:38:05	-46:05:00	-2	0.00	0	1	6140	59	2.450	0.011	0	1	0.315	0.006	0	1	0.589	0.030	0	1	1.120	0.148	19.780	0.365
264G301	10:38:06	-46:03:59	-2	13.94	0	2	5358	52	2.226	0.043	0	1	0.280	0.039	0	1	0.379	0.049	0	1	0.680	0.408	18.920	0.365
264G31	10:38:23	-45:55:46	-3	13.35	0	3	6694	63	2.389	0.008	0	2	0.286	0.003	0	3	0.566	0.032	0	1	1.270	0.105	20.280	0.365
Centaurus																								
322G56	12:39:33	-40:22:06	-2	14.41	0	2	4580	36	2.234	0.011	0	1	0.264	0.006	0	2	0.544	0.033	0	0	0.000	0.000	0.000	0.000
322G75	12:43:41	-40:28:48	-2	14.11	0	2	4538	38	2.165	0.008	0	1	0.268	0.006	0	2	0.624	0.020	0	0	0.000	0.000	0.000	0.000
D20	12:46:40	-41:13:02	-2	14.74	0	2	4277	44	2.060	0.008	0	1	0.000	0.000	0	2	0.497	0.006	0	0	0.000	0.000	0.000	0.000
D24	12:46:41	-41:11:27	-2	14.62	0	2	4831	48	2.015	0.008	0	1	0.000	0.000	0	2	0.397	0.006	0	0	0.000	0.000	0.000	0.000
323G3	12:47:18	-41:06:36	-2	12.74	0	4	4624	36	2.401	0.012	0	2	0.333	0.009	0	4	0.815	0.004	0	0	0.000	0.000	0.000	0.000
D27	12:47:21	-41:07:31	-5	14.40	0	3	4957	49	2.012	0.008	0	1	0.261	0.006	0	3	0.399	0.006	0	0	0.000	0.000	0.000	0.000
1247-4111	12:47:48	-41:11:57	-2	14.83	0	2	5312	52	2.109	0.008	0	2	0.000	0.000	0	2	0.467	0.006	0	0	0.000	0.000	0.000	0.000
323G23	12:49:40	-40:26:12	-2	14.45	0	2	4230	35	2.168	0.008	0	1	0.298	0.006	0	2	0.514	0.025	0	0	0.000	0.000	0.000	0.000
323G24	12:49:44	-38:52:30	-5	13.12	0	1	4277	36	2.383	0.011	0	1	0.302	0.006	0	1	0.824	0.017	0	0	0.000	0.000	0.000	0.000
323G34	12:50:39	-40:56:00	-5	13.28	0	2	4230	35	2.385	0.011	0	1	0.293	0.006	0	2	0.814	0.018	0	0	0.000	0.000	0.000	0.000
Abell S714																								
507G14	12:45:40	-26:11:30	-2	13.92	1	0	3361	27	2.165	0.067	1	0	0.266	0.085	1	0	0.624	0.028	1	0	1.070	0.166	19.200	0.365
507G21	12:47:48	-26:34:12	-2	13.51	1	0	3157	26	2.309	0.067	1	0	0.326	0.085	1	0	0.654	0.026	1	0	1.290	0.100	19.700	0.365
507G24	12:48:46	-26:32:06	-2	13.96	2	0	3407	28	2.030	0.019	2	0	0.222	0.008	1	0	0.504	0.037	1	0	1.030	0.182	19.460	0.365
507G25	12:48:51	-26:10:48	-2	12.73	0	3	3239	26	2.388	0.008	0	2	0.298	0.000	0	3	0.854	0.012	0	0	0.000	0.000	0.000	0.000

TABLE 5.5—*Continued*

Name	α (1950)	δ (1950)	T	m_B mag	N_s^o	N_s^l	cz_{hel} km/s	$\epsilon_{cz_{hel}}$ km/s	$\log\sigma$	$\epsilon_{\log\sigma}$	N_M^o	N_M^l	Mg_2	ϵ_{Mg_2}	N_d^o	N_d^l	$logd_n$	ϵ_{logd_n}	N_F^o	N_F^l	$log\,r_e$	ϵ_{r_e}	$\bar{\mu}_e$ mag/″²	ϵ_{μ_e} mag/″²
(1)	(2)	(3)	(4)	(5)	(6)	(7)	(8)	(9)	(10)	(11)	(12)	(13)	(14)	(15)	(16)	(17)	(18)	(19)	(20)	(21)	(22)	(23)	(24)	(25)
507G55	12:54:55	-27:01:18	-2	13.65	0	2	3320	27	2.186	0.008	0	1	0.286	0.006	1	2	0.621	0.003	1	0	1.230	0.115	19.770	0.365
Pavo2																								
1820-6316	18:20:22	-63:16:30	-3	13.80	2	0	4520	36	2.358	0.030	2	0	0.313	0.012	1	0	0.624	0.028	1	0	1.210	0.120	19.700	0.365
1833-6244	18:33:15	-62:44:36	-3	14.06	1	0	4410	35	2.336	0.014	1	0	0.308	0.015	1	0	0.584	0.030	1	0	1.520	0.059	20.800	0.365
1838-6209	18:38:42	-62:09:42	-2	14.08	1	0	4531	36	2.100	0.011	1	0	0.193	0.010	1	0	0.544	0.033	1	0	0.870	0.263	18.770	0.365
1842-6324a	18:42:09	-63:24:53	-2	15.03	1	2	4206	43	2.076	0.008	1	0	0.274	0.085	0	2	0.245	0.006	0	0	0.000	0.000	0.000	0.000
1842-6324	18:42:34	-63:24:54	-5	13.79	0	2	3874	30	2.336	0.008	0	2	0.000	0.000	0	2	0.600	0.006	0	0	0.000	0.000	0.000	0.000
1842-6323	18:42:34	-63:23:12	-3	12.33	0	3	4498	35	2.464	0.006	0	1	0.337	0.006	0	4	0.673	0.005	0	0	0.000	0.000	0.000	0.000

Chapter 6

The $D_n - \sigma$ Relation

The cluster sample of 446 elliptical and S0 galaxies in 28 clusters defined in Chapter 5 is used to derive an accurate $D_n - \sigma$ relation for our early-type galaxies. The slope of this relation is obtained by combining galaxies in all clusters, under the assumption that the distance relation is "universal". Parameters for the direct and inverse relations, suitably corrected for biases associated with the completeness of our sample, are presented. We find that $\log d_n = 1.18 \log \sigma + 1.39$, where the zero-point has been set by requiring that the distant clusters be at rest relative to the CMB. When used as a distance indicator, this relation implies a peculiar velocity of about 200 kms^{-1} for the Coma cluster. The scatter in the distance relation is about 0.08 dex, corresponding to a distance error of about 19%, comparable to what is obtained for the Fundamental Plane relation. No correlation between the residuals and other parameters that characterize the stellar population was found.

6.1 Deriving the distance relation

Present-day elliptical galaxies appear to constitute a remarkable homogeneous class of objects which obey scaling relations involving their structural and dynamical properties such as the $L - \sigma$ relation found by Faber & Jackson (1976). In fact, elliptical galaxies are better represented by a well-defined plane, the so-called fundamental plane (FP, Djorgovski & Davis 1987; Dressler et al. 1987a), in a three-dimensional space defined by the surface brightness, luminosity and internal velocity dispersionl the Faber-Jackson relation is a projection of this plane. Therefore, by choosing an appropriate combination of the parameters, a tight relation between distance–dependent and independent quantities can be found: the $D_n - \sigma$ is such a relation. The existence of such scaling relations provides an important tool for studying the properties of the stellar population and the evolution of ellipticals (e.g., Jørgensen et al. 1996; Franx et al. 1997), and for constraining models of spheroidal formation (e.g., Bressan et al. 1994; Baugh et al. 1996). Furthermore, these relations provide the means for measuring relative distances to early-type galaxies, the primary goal of this work, although there are some concerns about how they relate to distances measured by the TF relation (Scodeggio et al. 1998). In addition, if they depend on the environment (e.g., Gibbons et al. 1998), then using these relations to map the peculiar velocity field of galaxies may be more difficult.

While the FP relation is usually used for detailed cluster studies, in large galaxy samples, the $D_n - \sigma$ relation is much easier to measure. It has been claimed that the FP

leads to significantly smaller scatter, and thus yields more reliable distance measurements (e.g., Jørgensen et al. 1993). However, more recent work has found no evidence of this difference (e.g., Jørgensen et al. 1996; D'Onofrio et al. 1997). Furthermore, analysis of our photometric data shows that the parameters involved in computing FP distances are more sensitive to seeing effects, and to the procedure used in fitting the surface brightness profile. Therefore, we will first use our data to determine the $D_n - \sigma$ relation, instead of the FP relation, because we have a larger number of galaxies ($\sim 30\%$) with available d_n measurements. We hope to use our data to determine the FP as well, sometime in the near future.

6.1.1 The method

Since the angular size of a galaxy varies as $1/r$, if d_n is the measured scale of a galaxy, then $1/d_n$ is a measure of its distance. Empirically it has been determined that $d_n \sim \sigma^a$ and thus the basic distance indicator takes the form

$$\log R = a \log \sigma - \log d_n + b, \tag{6.1}$$

where R is the estimated distance of the galaxy, σ is the central velocity dispersion, and d_n is a measure of the angular size of the galaxy. The quantities R and σ are in units of kms^{-1}, and d_n is expressed in units of 0.1 arcmin. For what follows, we define the quantities $y \equiv \log D_n + \log h$ with $D_n = d_n \times R$ and $x \equiv \log \sigma$. So the distance relation is

$$y = ax + b, \tag{6.2}$$

where $h = H_o/(100 \text{ kms}^{-1} \text{ Mpc}^{-1})$.

The slope of the distance relation is usually determined by using galaxies in clusters. Because the peculiar velocity field is unknown, combining galaxies spanning a broad range of velocities, should improve the statistical accuracy with which the slope is determined. This is because, in the case of clusters, all galaxies are known to be at essentially the same distance, thus allowing for a more accurate determination of their distances. As long as the distance relation can be assumed to be universal, independent of other cluster properties, the distance relation can be determined by combining the data from all available clusters and producing a template relation. By examining different morphologies, stellar populations and environments, we will argue that the assumption that such a universal relation exists is reasonably accurate (see section 6.2.2). In what follows, the parameters which describe the template relation, such as the zero point, the slope and the motion correction of each cluster, are determined simultaneously. Such a procedure has recently been adopted by a number of authors (Baggley 1996; Giovanelli et al. 1997b (G97b)) in determining the $D_n - \sigma$, FP and TF relations. Below we follow the notation of G97b. The distance relation can be described by either a direct (forward) or inverse fit, depending on whether the slope is obtained by regressing on the distance-dependent or distance-independent parameter. The case of the direct relation is studied first; the inverse case is studied in Section 6.1.3.

For a set of N galaxies with data points (x_i, y_i) a direct fit to

$$y = a_d x + b_d \tag{6.3}$$

leads to the determination of the coefficients a_d and b_d. This is done by minimizing

$$\chi^2 = \sum_{i,k}^{N} \Big[\frac{y^c_{i,k} - y(x_i; a_d, b_d)}{\sigma_i} \Big]^2, \tag{6.4}$$

with respect to the zero-point b_d, the slope a_d and the relative offsets Δy_k. Here σ_i is related to the measurement error in D_n, and, for the k-th cluster,

$$y^c_{i,k} = y_{i,k} - \Delta y_k. \tag{6.5}$$

The quantity Δy_k allows for relative motions of the clusters relative to the Hubble flow, as measured by the individual zero-points of the cluster: $b_k = b_d + \Delta y_k$. Other conditions can be imposed to set the overall zero-point of the distance relation. As shown in the next section we may require an external condition, for instance that "distant" clusters are at rest relative to the CMB, or that the Coma cluster is at rest, in which case an additional condition can be imposed. In the former case we may require that the number-weighted offsets satisfy the constraint

$$\sum_k N_k \Delta y_k / \sum N_k = 0. \tag{6.6}$$

Formally, the equations above fully describe the procedure adopted in the next section for determining the fitting parameters which describe the linear distance relation. However, when applying them to real data, one must also consider possible sources of bias. In the case of the direct relations, i.e., when regressing on the distance-dependent parameter, the most pernicious bias is that due to incompleteness. This bias is particularly difficult to handle in the case of a cluster sample in which the completeness varies from cluster to cluster. It is well-known the bias leads to a shallower slope, a brighter zero-point, and an underestimate of the scatter. Although analytic bias-correction schemes have been proposed (Willick 1994), they usually make sufficiently restrictive assumptions that they cannot usually be applied to real data. Instead, we follow most recent work in resorting to a Monte-Carlo approach for estimating the bias correction. In this approach, one assumes that a universal distance relation exists. Then the scatter about this relation, which depends on the assumed slope, is computed empirically and iteratively.

6.1.2 Monte-Carlo bias correction

A number of recipes have been derived for correcting distances inferred using the TF and $D_n - \sigma$ (or FP) relations for the effect of incompleteness bias (for a review, see Strauss & Willick 1995 and references therein). However, as mentioned above, analytical formulations all assume that the sample is rigorously magnitude-limited and that errors and scatter in the relation are uniform and constant for all values of the parameters involved. This is almost never the case for real data-sets. Monte Carlo simulations of the bias effects on the TF and FP relation were obtained by G97b and Scodeggio (1997), respectively, and here we follow their approach.

The procedure is as follows. Using an estimate for the slope and the zero-point, the distances to the clusters are estimated. New coefficients a_d and b_d are found by minimizing χ^2 in equation 6.4. A new scatter, as a function of the velocity dispersion,

$\epsilon(x)$, is computed and for the $i-$th galaxy in the $k-$th cluster a bias correction $b_{i,k}$ is obtained and the values $y_{i,k}$ corrected. The bias correction is estimated by generating 500 Monte-Carlo realizations: for each galaxy i in the k-th cluster a new value of $y_{i,k}$ is obtained by adding a Gaussian deviate (gas, which is a number in the interval 0 - 1) of rms equal to $\epsilon(x)$: $y_{i,k} = a_d x_{i,k} + b_d + gas * \epsilon(x_{i,k})$. By applying the appropriate selection function to the simulated data, the final distribution of $y^s_{i,k}$ will reflect the incompleteness of the real sample. It thus allows a direct estimate of the bias:

$$b_{i,k} = \bar{y}^s_{i,k} - y_{i,k} \tag{6.7}$$

where $\bar{y}^s_{i,k}$ is the mean value of the simulated data at $x_{i,k}$.

The simulated values $y^s_{i,k}$, satisfying the selection function of the $k-$th cluster are produced as follows. For each value of $y^s_{i,k}$ a random number between 0 and 1 is generated and compared to the value of the selection function for the given cluster. The generated point is kept only if it is smaller than the selection function for that value of $y^s_{i,k}$. After the bias is estimated, all data points are corrected, and new values

$$y^c_{i,k} = y_{i,k} - b_{i,k} \tag{6.8}$$

are obtained. At this point, new coefficients for the fit, relative offsets Δy_k, and scatter $\epsilon(x)$ are computed, and the process repeated. When applied to our data, this iterative process converges after about 5 iterations, after which the slope is larger and the zero-point smaller, as expected.

To estimate the incompleteness in D_n for each cluster, knowledge of the D_n distribution function, the counterpart of the luminosity function, is required. Since this function is not directly available, two possible approaches are 1) to assume that a fair representation of this distribution is given by the observations of a nearby cluster spanning a broad range of measurements; 2) to examine the correlation of D_n with other measures of the angular size of the galaxy, such as the angular diameter Θ^B_{25}, enclosing an integrated surface brightness of 25 mag arcsec^{-2}, and to then use the diameter function

$$\Phi(D)\, dD \propto \exp\left(\frac{-D}{D_\star}\right) \frac{dD}{D_\star} \tag{6.9}$$

with $D_\star = 2610$ kms^{-1}, as determined by Sodré & Lahav (1993) for galaxies in the ESO-LV catalog (Lauberts & Valentjin 1989). For most of the following we take the second approach, as a clear correlation between these measures exists. However, it is important to point out that the results which follow are insensitive to the details of the diameter function. As demonstrated by G97b, the bias correction depends primarily in the nature and the amplitude of the scatter of the distance relation.

6.1.3 The template distance relation: Fitting parameters

In this section we use the procedure described above to analyze the cluster data sample described in Chapter 5. Our starting point is to assume that the clusters are at rest relative to the Hubble flow and that their distances are given by the mean cluster redshift as computed, whenever available, from the group catalog (see Chapter 5).

Figure 6.1 shows the individual uncorrected cluster data at the start of the iterative process. The solid line represents the best fit after minimizing the $\chi 2$ (equation 6.4) for

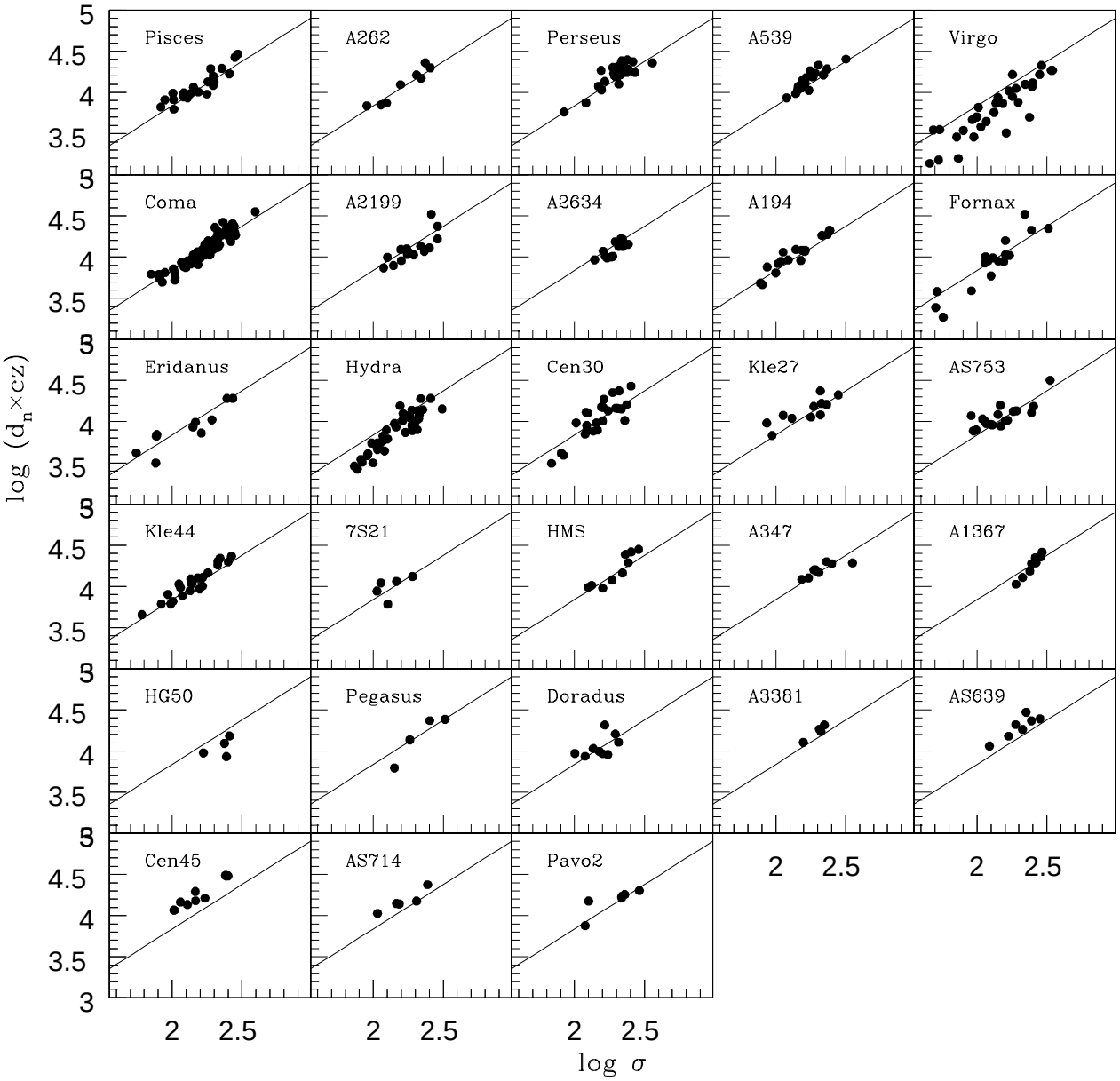

Figure 6.1 The product of d_n (in 0.1 arcmin) and the redshift (in km/s) of each cluster galaxy is plotted versus its velocity dispersion. The solid line represents the best fit after minimizing the χ^2 defined in Equation (6.4) for the first time.

the first time. Note that the number of galaxies in each cluster varies dramatically; we tend to sample the more luminous galaxies with large velocity dispersions. Therefore, if a selection bias correction is not applied a significant bias will be introduced in the global template constructed by combining all clusters. The relative offsets between those data points and the distance relation reflect the cluster motions.

To proceed we must compute the selection function required for the bias correction. Using the diameter-function of Sodré & Lahav (1993) we obtain the results shown in Figure 6.2. The histograms show the selection function for each cluster computed from the ratio of the number of objects observed in the cluster to the number predicted by the fitted diameter-distribution function in $\Delta y = 0.2$ bins. In practice, this is done after convolving with a [0.25,0.50,0.25] function to partly reduce the effects of small number statistics. The solid curve is a fit to the histograms using the function (G97b)

$$c(y) = \frac{1}{1 + \mathrm{e}^{(y-y_f)/\eta}} \tag{6.10}$$

to represent the completeness function, thereby further reducing the effects of small number statistics in the Monte-Carlo simulation. Table 6.1 gives the parameters y_f and η for each cluster. At the bright end (large values of y) the completeness was normalized to unity, based on the observation that in all clusters the brightest galaxies are always included in the cluster sample. We note that comparison of the predicted and observed diameter-functions for the nearby Virgo cluster are in good agreement down to small values of D_n, indicating that we could have use it to estimate the completeness of the other clusters.

Using this function as input, we have estimated the bias correction $b_{i,k}$ for the i-th galaxy in the k-th cluster. The results after the last iteration are shown in Figure 6.3. For nearby clusters, such as Virgo and Fornax, the incompleteness bias correction is small, while for more distant clusters the correction can be quite significant, with $\Delta y \sim 0.1$ (this is about $\Delta m \sim 0.5$ mag).

After the iterative procedure, final values for the distance relation coefficients are determined. Requiring that "distant" clusters, with a mean redshift of 6000 kms^{-1} are at rest, leads to the following final relation:

$$\log D_n = 1.180(\pm 0.036)\ \log \sigma_0\ +\ 1.391(\pm 0.018), \tag{6.11}$$

where the error of the slope is derived by bootstrap re-sampling. The bootstrap error analysis is based on the distribution of the slopes derived from a large number of data sets constructed by random sampling of the observed data set with replacement. The error on the zero-point is discussed below.

Figure 6.4 shows the initial and final fits of the the distance relation together with the distribution of the observed rms scatter (solid line), and the intrinsic scatter (dashed line), as a function of σ. The intrinsic scatter was derived by subtracting the measurement uncertainties in quadrature from the rms scatter of the fit. The mean scatter ϵ is about 0.08 dex, yielding a distance error $\Delta \sim 19\%$ comparable to the errors obtained using FP relations (e.g., Hudson et al. 1997). For some special clusters, this value is smaller.

Note that here we use galaxies that are likely to be cluster members, on the basis of their redshift and sky coordinates, including the "peripheral" objects as defined in

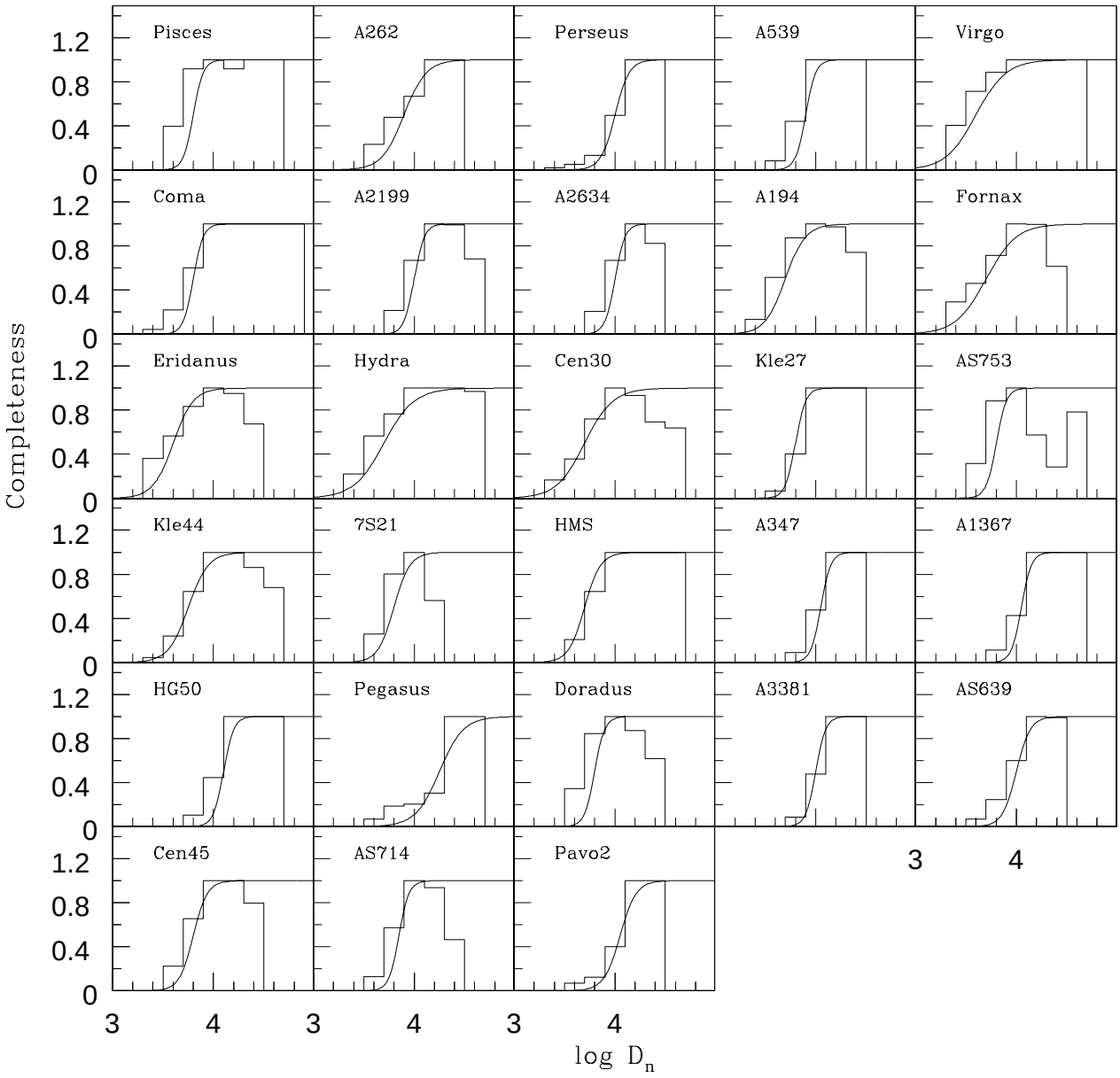

Figure 6.2 Histograms show the selection function for each cluster, computed from the ratio of the number of objects observed in the cluster, to the number predicted by the fitted diameter distribution function. Solid curves show fits to the histograms of the form given by Equation 6.10.

Table 6.1 Completeness function coefficients

Cluster Name (1)	y_f (2)	η (3)
Pisces	3.70	0.05
A262	3.90	0.10
Perseus	3.90	0.07
A539	3.90	0.05
Virgo	3.50	0.15
Coma	3.70	0.10
A2199	3.90	0.05
A2634	3.90	0.05
A194	3.60	0.10
Fornax	3.60	0.15
Eridanus	3.60	0.10
Hydra	3.60	0.15
Cen30	3.60	0.14
Kle27	3.80	0.05
AS753	3.75	0.05
Kle44	3.70	0.10
7S21	3.70	0.08
HMS	3.90	0.05
A347	4.00	0.05
A1367	4.15	0.05
HG50	4.10	0.05
Pegasus	4.15	0.15
Doradus	3.80	0.05
A3381	3.95	0.05
AS639	3.95	0.07
Cen45	3.80	0.07
AS714	3.80	0.05
Pavo2	3.95	0.08

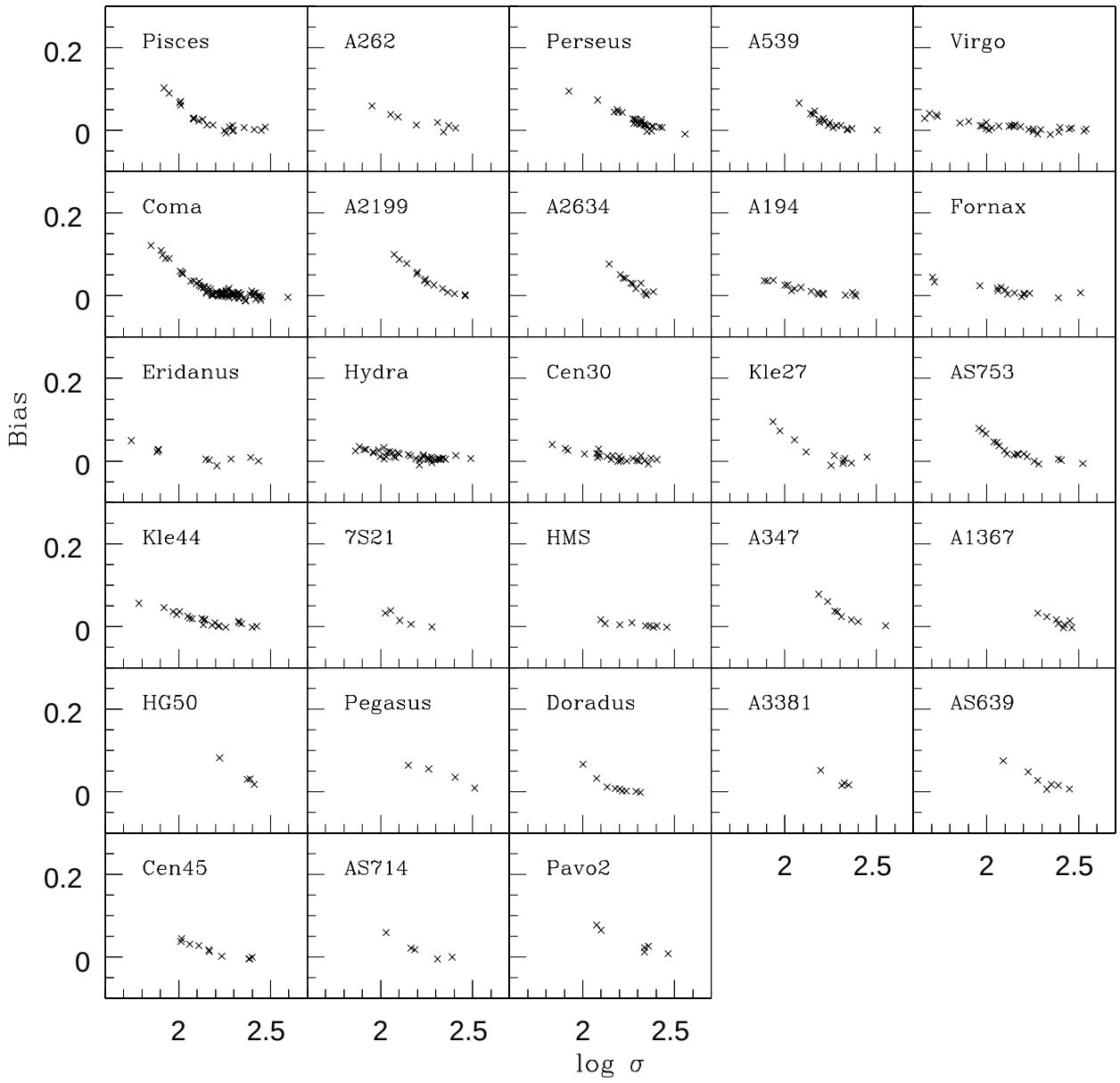

Figure 6.3 The incompleteness bias corrections that were applied to the individual measurements.

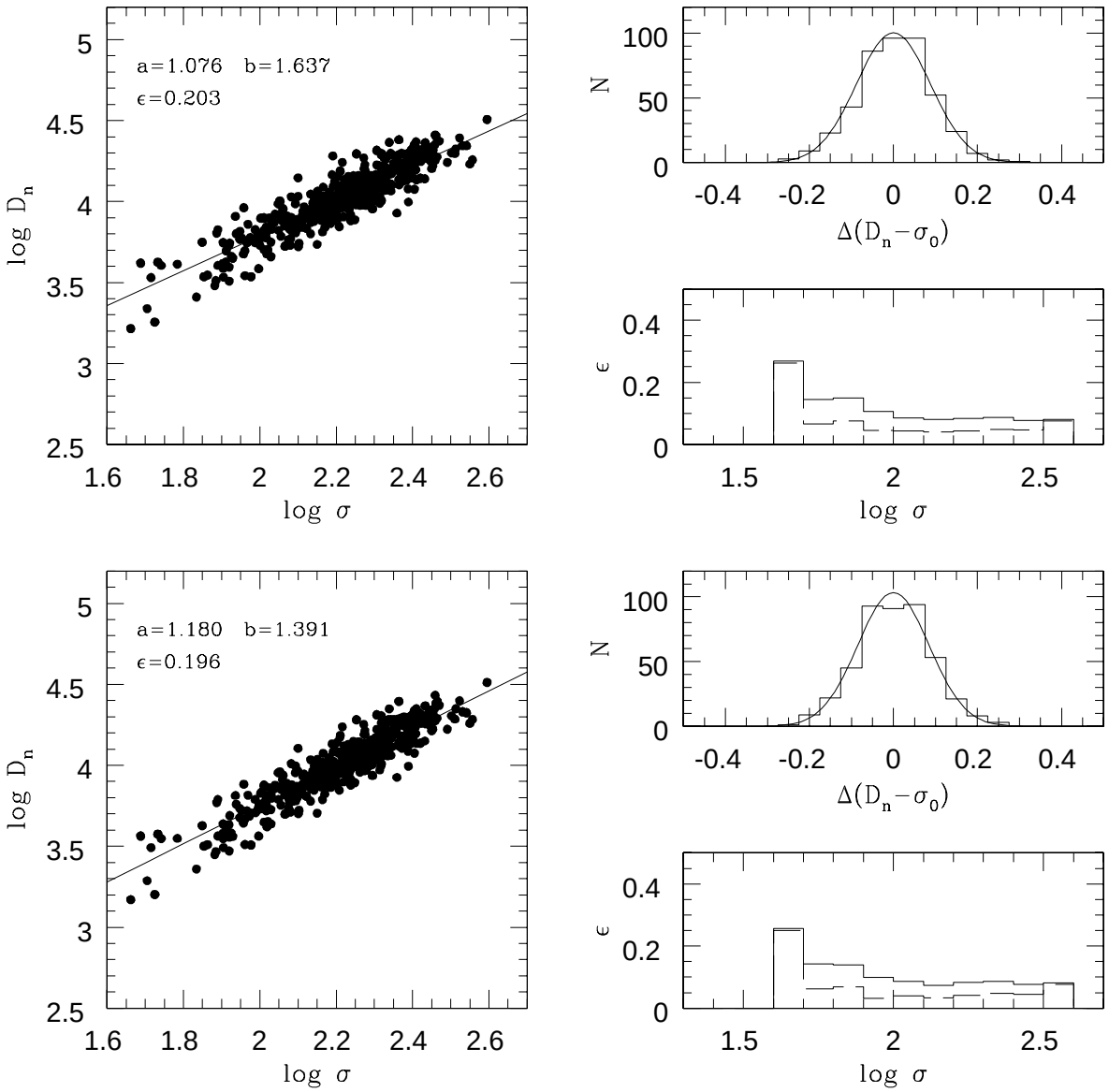

Figure 6.4 Panels on the left show measurements before the bias correction is applied (upper), and the final corrected values derived from the iterative process (lower) as a function of σ. The line shows the derived distance relation. The values of the slope (a), zero-point (b), and *rms* scatter (ϵ) are also shown. Panels on the right show the distribution of the residuals relative to the $D_n - \sigma$ relation, as well as the distribution of the corresponding observed *rms* (solid line) and intrinsic scatter (dashed line) as a function of σ.

Chapter 5. Note also that the scatter increases significantly for low values of σ; this variation has been modelled in our Monte-Carlo simulations. The mean intrinsic scatter is $\sim$ 5%. This scatter implies the existence of unknown physical effects which could affect the determination of the derived distances. One possibility is that this scatter reflects differences in the stellar population of the cluster member galaxies, as discussed in Section 6.2.2.

Figure 6.5 shows the bias-corrected data points for all clusters superposing the final fit. A number of interesting cases are evident. For instance, Cen45 and Coma exhibit clear evidence for the presence of either spatial sub-structure or distinct galaxy populations, while for Hydra and Pavo2, the cluster galaxies do not strictly follow the template relation: the individual $D_n - \sigma$ exhibit a tilt relative to the former. We will return to these points below.

To evaluate the robustness of our results, we have derived the distance relation by: 1) excluding the peripheral objects; 2) removing specific clusters, such as those mentioned above; 3) removing those clusters in which none of the galaxies were measured by us; 4) evaluating the *rms* variation of the slope by excluding each individual cluster from the sample. The results are summarized in Table 6.2. Based on these tests we estimate that the variation of the slope of the distance relation is in good agreement (0.033) with the formal error computed from the bootstrap re-sampling.

We have also computed the direct relation using orthogonal fits, allowing for errors in both $\log D_n$ and $\log \sigma$, and for the inverse relation, ignoring any bias correction. The results are shown in the upper panel of Figure 6.6. The corresponding coefficients and scatter in $\log D_n$ are given in Table 6.3. We point out that the inverse relation is insensitive to the photometric selection and is, in principle, bias-free, if no a priori cut is made in that variable (see Strauss & Willick 1995). However, since we are also using data from the literature, which, in some cases is limited to galaxies with $\sigma \gtrsim 100$ kms^{-1}, this may not hold. If so, a similar treatement to that carried out for the distance-dependent parameter should be considered.

The coefficients determined from the various fits obtained with our sample are compared with those of other authors in Table 6.4. The Table shows that our coefficients as well as the scatter are in general in good agreement with previous determinations, except for those of Baggley (1996) and Lucey et al. (1997). The former result has recently been reviewed by Saglia et al. (1999) (private communication) giving slope and zero-point comparable to our estimated values. The latter was obtained from two distant clusters, A2199 and A2634. Our analysis shows that these clusters have individual $D_n - \sigma$ relations which differ significantly from Eq. 6.11 (Table 6.5; see also Section 6.1.4).

6.1.4 Peculiar velocities of clusters

Distances to galaxies in clusters are computed using the "direct" template relation derived in the previous section, yielding the distance distributions displayed in Figure 6.7, which show the difference between the individual galaxy distances and the error-weighted mean of the distributions, which we assigned as the cluster distance. For most clusters, the distance distributions have a well-defined peak and relatively small scatter, resulting in well-defined mean distances. On the other hand, there are a few more complex cases such as: 1) systems that exhibit sub-structure (Coma, Cen30 and A1367); 2) systems with very large scatter and poorly defined peaks (A2199, A2634); 3) systems with very

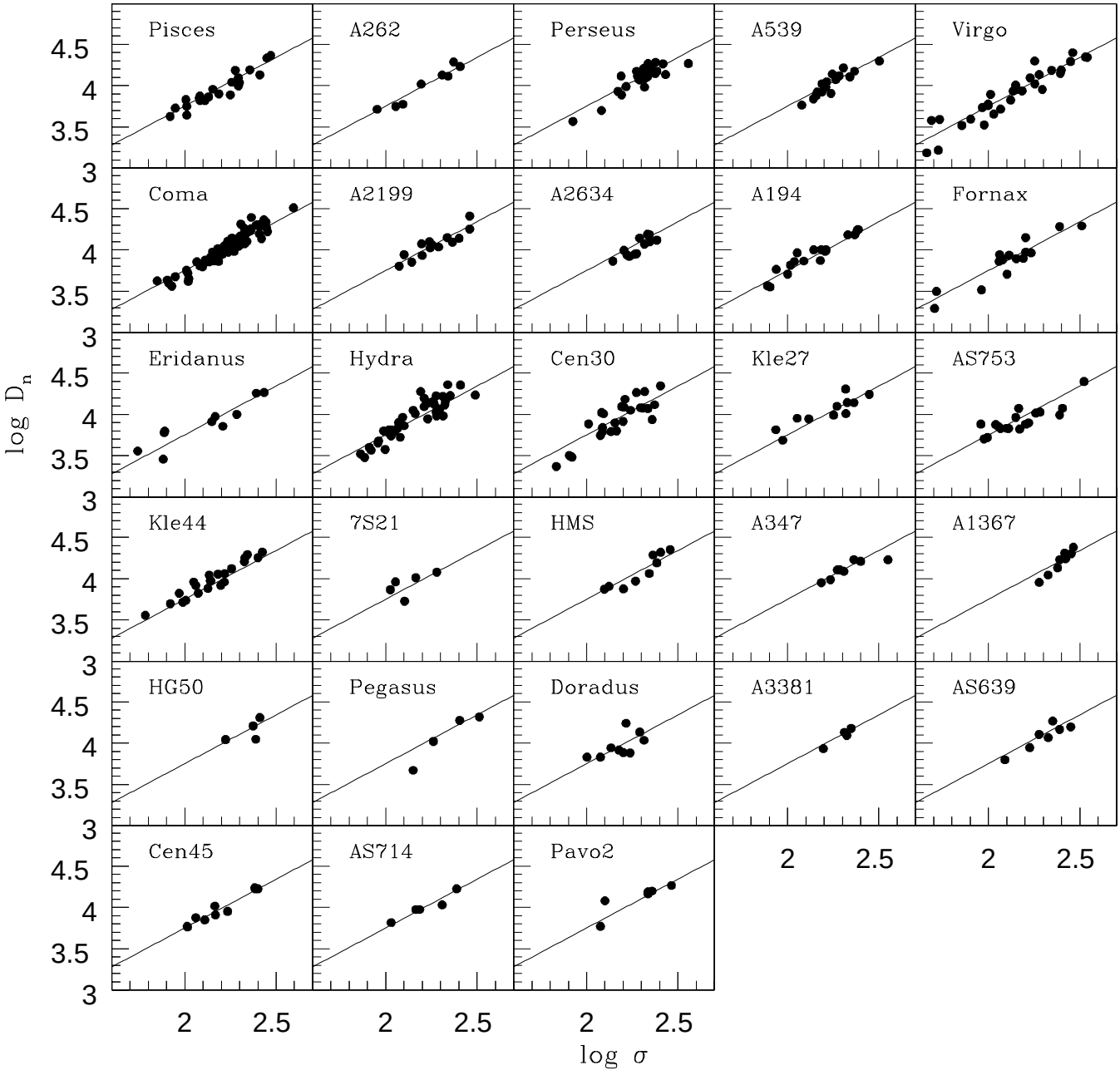

Figure 6.5 Bias-corrected D_n of each cluster member galaxy versus its velocity dispersion. Solid line shows the derived distance relation (Equation 6.11).

Table 6.2 Tests of the $D_n - \sigma$ relation

Objects removed (1)	N_{gal} (2)	b (3)	a (4)	ϵ (5)
A[1]	385	1.183	1.373	0.076
B[2]	302	1.205	1.340	0.082
C[3]	369	1.188	1.363	0.090
Pisces	424	1.176	1.400	0.086
A262	439	1.177	1.399	0.086
Perseus	420	1.182	1.389	0.086
A539	431	1.177	1.397	0.086
Virgo	413	1.187	1.375	0.082
Coma	371	1.037	1.720	0.096
A2199	431	1.184	1.375	0.086
A2634	434	1.177	1.399	0.086
A194	429	1.169	1.413	0.086
Fornax	429	1.201	1.347	0.084
Eridanus	436	1.167	1.422	0.085
Hydra	405	1.182	1.385	0.084
Cen30	421	1.197	1.359	0.082
Kle27	435	1.188	1.370	0.084
AS753	428	1.180	1.393	0.085
Kle44	424	1.221	1.289	0.086
7S21	440	1.178	1.397	0.085
HMS	437	1.177	1.398	0.086
A347	440	1.177	1.398	0.086
A1367	438	1.177	1.398	0.086
HG50	442	1.180	1.391	0.085
Pegasus	442	1.178	1.397	0.085
Doradus	437	1.179	1.393	0.085
A3381	442	1.177	1.398	0.086
AS639	439	1.177	1.398	0.086
Cen45	436	1.178	1.395	0.086
AS714	441	1.178	1.396	0.086
Pavo2	440	1.175	1.404	0.085

Notes: (1) peripheral cluster galaxies; (2) clusters whose individual $D_n - \sigma$ relations differ significantly from Eq. 6.11: A2199, A2634, Cen30, AS753, 7S21, A0347, and A1367; (3) clusters for which we have no measurement: A539, A2199, A2634, 7S21, A0347, A3381, AS639, and Cen45.

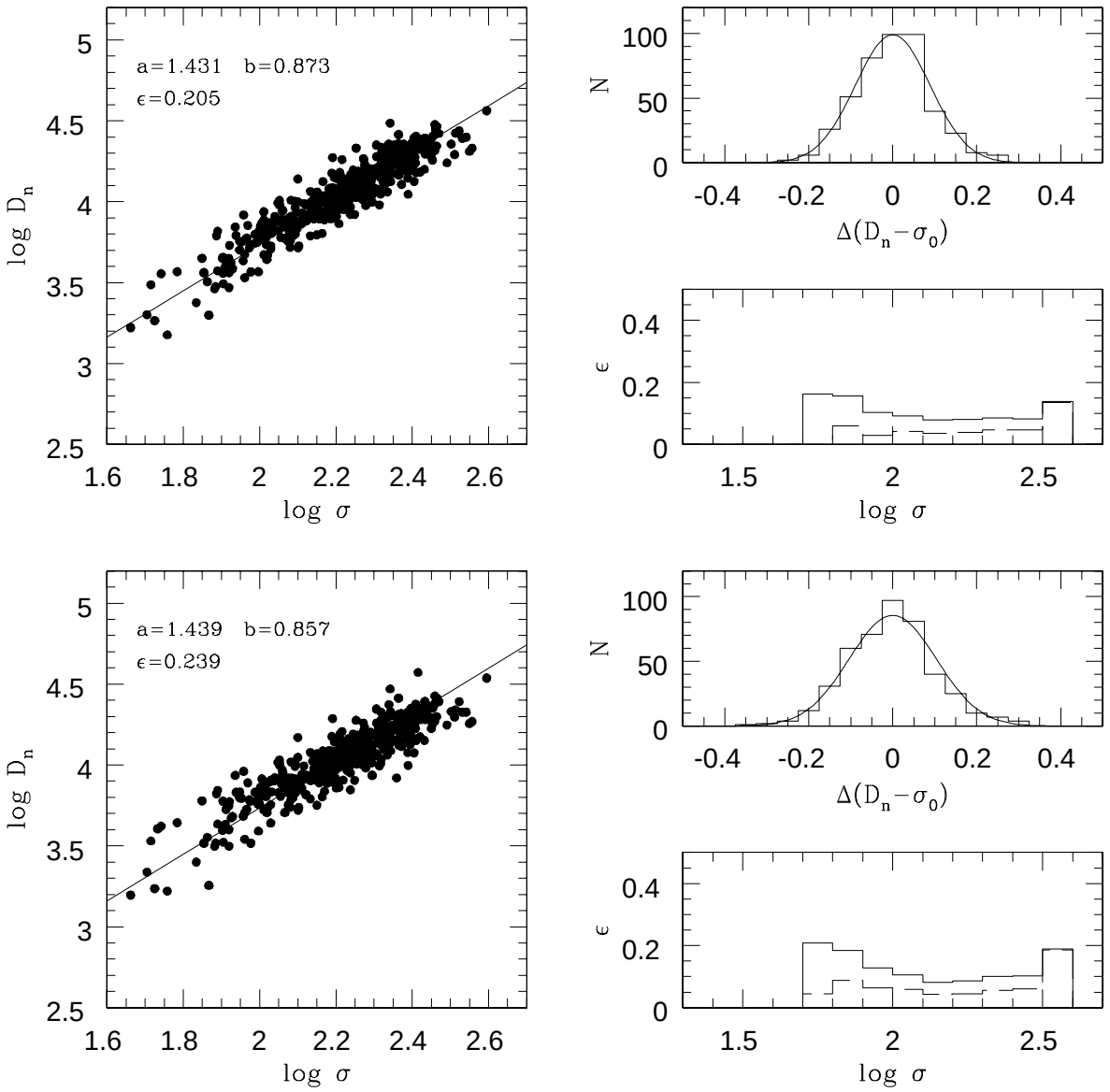

Figure 6.6 Symbols in the panels on the left show the bias corrected measurements; straight lines show the derived bivariate distance relation (upper) and the inverse relation (lower). The values of the slope (a), zero-point (b), and *rms* scatter (ϵ) are also shown. Panels on the right show the distribution of residuals relative to the $D_n - \sigma$ relation, together with the distribution of the corresponding observed *rms* (solid line) and intrinsic scatter (dashed line), as a function of σ.

Table 6.3 Our determinations of the $D_n - \sigma$ relation

Type (1)	a (2)	b (3)	ϵ (4)	note (5)
direct	1.180±0.036	1.391	0.085	
direct orthogonal fit	1.426±0.040	0.890	0.088	
inverse	1.439±0.038	0.870	0.072	1

Notes: (1) the uncertainty in the distances determined using the inverse relation is $(a \times \epsilon)$.

Table 6.4 Other determinations of the $D_n - \sigma$ relation

Source (1)	Type (2)	a (3)	b (4)	ϵ (5)	note (6)
LC	direct	1.200±	-1.679	0.090	1
7S	direct	1.200±	1.411	0.090	
D	direct	1.330±	-1.967	0.110	1
B96	direct	0.938 ± 0.072	-	0.071	
JFK96	orthogonal	1.320 ± 0.070	-	0.088	
Lc	direct	0.913 ± 0.090	-1.019	0.075	1
DCZC97	direct	1.240 ± 0.060	-1.080	0.080	2
HLSS97	inverse	1.419 ± 0.044	-	0.065	3
GFB	inverse	1.420 ± 0.040	-	0.059	3

Notes: The references are: LC: Lucey & Carter (1988); 7S: Lynden-Bell et al. (1988); D: Dressler et al. (1991); B96: Baggley (1996); JFK96 : Jorgensen et al. (1996); Lc: Lucey et al. (1997); DCZC97: D'Onofrio et al. (1997); HLSS97 : Hudson et al. (1997); GFB: Gibbons et al. (1998).
(1) they used $\log D_n = a \log \sigma + b$ with D_n in arcsec. Using $D_n = \log (d_n \times R)$, where d_n is in arcmin/0.1, one must add $\log R_{\rm Coma} - 0.778$ to their zero point.
(2) as in (1), but substitute $R_{\rm Coma}$ for $R_{\rm Virgo}$.
(3) the uncertainty in the distances determined using the inverse relation is $(a \times \epsilon)$.

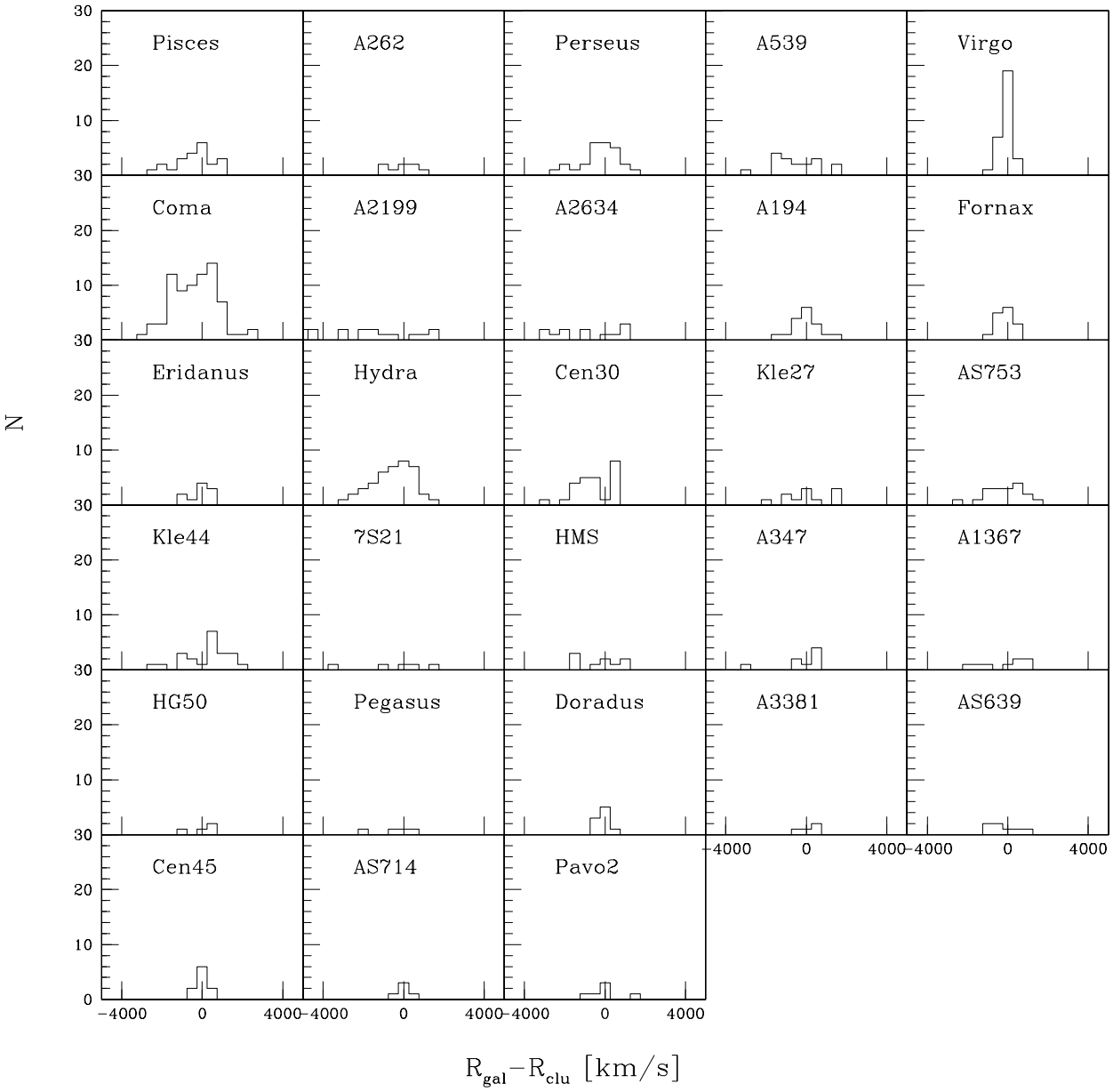

Figure 6.7 The distribution of the difference between the individual galaxy distances derived from Equation 6.11, and the error-weighted mean of the distribution, which is used as the cluster distance.

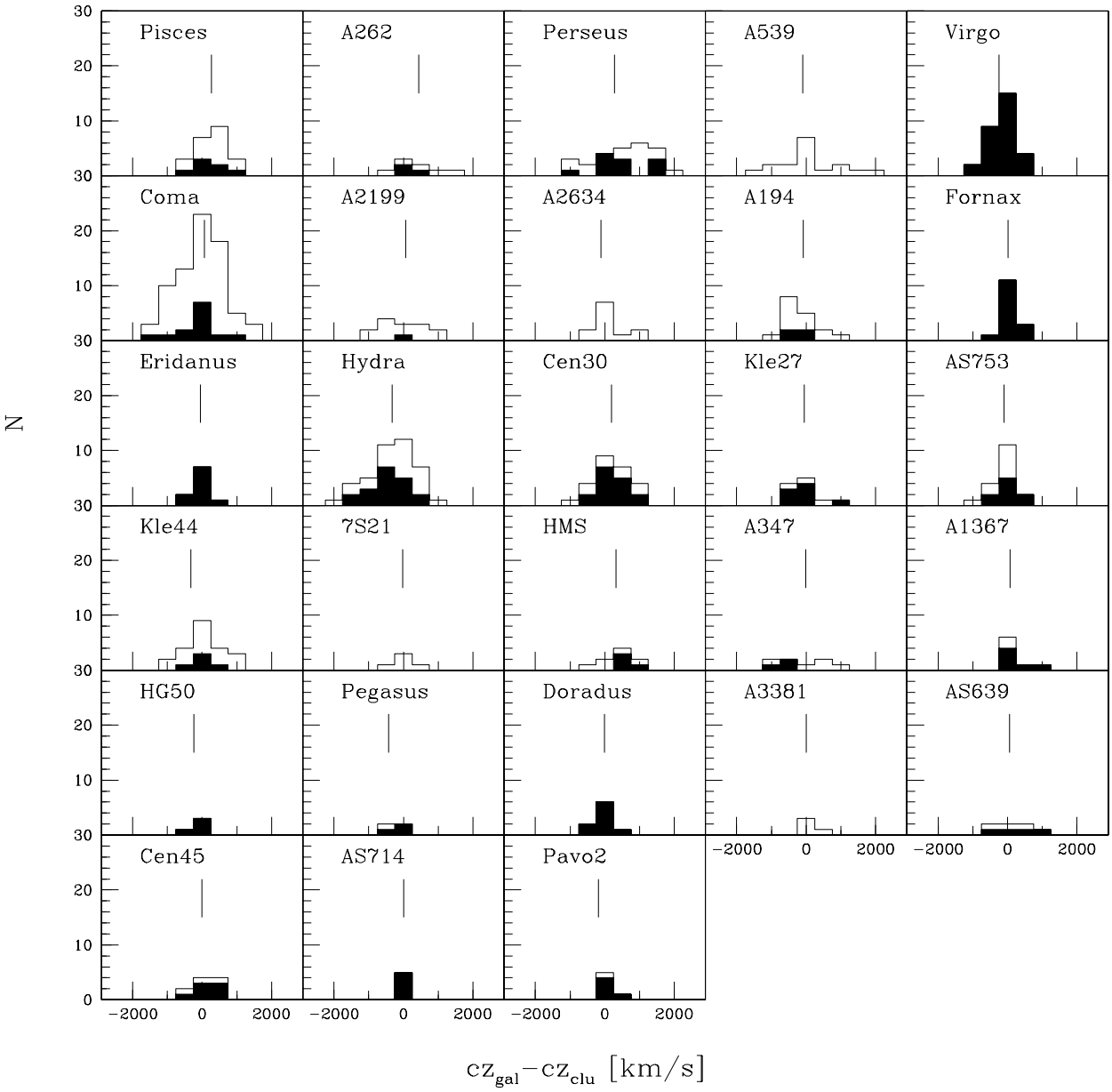

Figure 6.8 The redshift distribution of galaxies in each of the clusters considered. Empty histograms show the distribution of the difference between a galaxy's redshift and the redshift assigned to the parent cluster, for all galaxies in the cluster, regardless of their magnitude. Solid histograms show the redshift distribution of galaxies which were identified as members of groups by the group assignment procedure.

few objects, which, while useful for the calculation of the $D_n - \sigma$ relation, are usually either in nearby small groups (e.g., HG50, Pavo2, 7S21, AS714) or in very distant clusters (e.g., A3381), leading to large distance uncertainties.

The cluster distances computed in this way were corrected for homogeneous Malmquist bias. That is, the clusters are assumed to be distributed uniformly in space, and so the estimated distance is multiplied by $exp(3.5\epsilon^2/N_g)$, where N_g is the number of galaxies in each cluster (e.g., Lynden-Bell et al. 1988). This correction is in general small, amounting to less than $\sim 3\%$ of the distance, for the smallest group considered.

The radial component of the peculiar velocities $v_p = cz_{cor} - R$ of each cluster was computed using the Malmquist corrected distance R and the mean cluster redshift cz listed in Chapter 5 corrected for the cosmological effect (Lynden-Bell et al. 1988):

$$cz_{cor} = cz - \log\left(\frac{1 + 7/4 * cz/c}{1 + 7/4 * cz_{Coma}/c}\right) \tag{6.12}$$

where cz_{Coma} is the redshift of the Coma cluster and c is the speed of light. Baggley (1996) computed a more accurate relation for the cosmological correction, but for nearby galaxies Equation 6.12 is a good approximation.

Figure 6.8 shows the redshift distribution of galaxies in each of the clusters considered. The open histogram shows the distribution of the difference between the individual galaxy redshift and the assigned cluster redshift for all galaxies assigned to the cluster, regardless of their magnitude. The solid histogram represents the redshift distribution of galaxies which were identified as members of groups by the group assignment procedure. In principle, the latter method should minimize the number of interlopers which may affect the calculation of the mean redshift of the cluster. The difference relative to other sources of cluster redshifts, as reported from recent work (JFK96, Hudson et al. 1997; Giovanelli et al. 1997b; Lucey et al. 1997) as well as some older references is also shown. Notice that the redshift differences can be significant, sometimes as large as 400 kms^{-1}! The most deviant cases ($> 3\sigma$) are Virgo, Hydra, Klem44, HMS and Pegasus. At least in some cases, the differences can be partly explained by including only observed ellipticals, rather than the galaxy population as a whole, when computing the mean. This potential systematic error has been largely ignored in the past and may account for some disparities in the measurements of the peculiar velocity.

The upper panel in Figure 6.9 shows the distribution of cluster peculiar velocities and the lower panel shows that these velocities do not depend on the estimated distance. The filled symbols indicate the "distant" clusters used for the final calibration of the $D_n - \sigma$ relation (by requiring that they are at the rest relative to the CMB). The open symbols are either clusters nearby (circles) or which were not observed by us (triangles) so they were not been considered for the calibration. The 1σ error bars are computed by adding, in quadrature, the distance and the cluster mean redshift errors. The error in the distances is given by $\Delta R/\sqrt{(N)}$, where Δ is the fractional distance error derived from the scatter of the composite distance relation, and N is the number of observed galaxies in the cluster. The error in the cluster redshift is estimated to be $\sigma_{\rm cl}/\sqrt{N'}$, where $\sigma_{\rm cl}$ is the velocity dispersion of the cluster and N' is the number of galaxies in the group catalog that were used in the calculating this dispersion.

From the cluster peculiar velocity distribution shown in the upper panel we find an error-weighted mean of 130 ± 91 kms^{-1} with an rms of 484 ± 53 kms^{-1}, when all

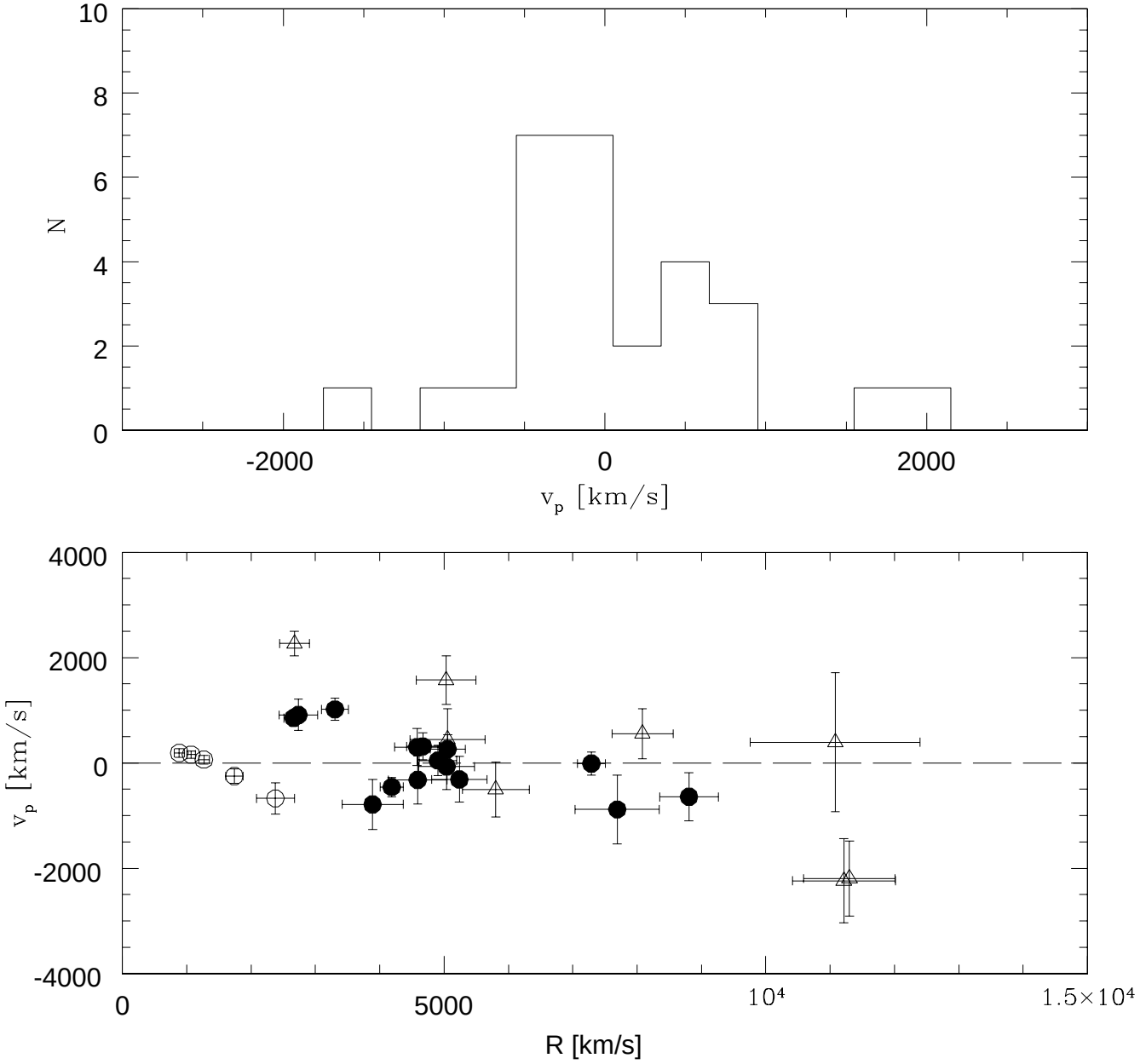

Figure 6.9 Distribution of cluster peculiar velocities (upper panel). Cluster peculiar velocities versus the estimated distances (lower panel). Filled symbols represent the "distant" clusters used for the final calibration of the $D_n - \sigma$ relation; open symbols represent either nearby clusters (circles) or clusters that were not observed by us (triangles), so they were not used for the calibration.

clusters are included. There are four obvious outliers, Cen45, AS639, A2199 and A2634, none of which were observed by us, (although the data for these objects have been coverted to our standard system). Furthermore, there are three additional clusters, Cen30 (601 ± 167 kms^{-1}), AS753 (995 ± 176 kms^{-1}) and A714 (987 ± 249 kms^{-1} which also have suspisciously large peculiar velocities. If these clusters are removed from the sample, then the mean peculiar velocity of the remaining 21 clusters is 32 ± 46 and a *rms* one-dimensional cluster velocity of 340 ± 43 kms^{-1}. This is comparable to that measured from the SCI sample which used TF data and yielded 266 ± 30 kms^{-1}. This small one-dimensional *rms* cluster velocity by itself has important implications for the cosmolgical parameters (e.g., Giovanelli 1998; Borgani et al. 1999). The cases of large peculiar velocity occur both at small and large distances (see the lower panel of Figure 6.9).

The large peculiar velocities measured for Cen30 and Cen45 can be partially explained by the fact that they are along the same direction and are part of a complex structure. In fact, from Figure 6.7 one finds that Cen30 shows a bi-modal distance distribution due to the difficulty of assigning galaxies to the different clumps. While this can be clearly seen in the distance distribution, it is not evident in the redshift distribution shown in Figure 6.8. On the other hand, the large positive peculiar velocity of Cen45 is likely caused by its infall towards the more massive component of the system (e.g., Lucey & Carter 1988). Given the complexity of the Centaurus system one should be cautious using Cen30 and Cen45 in quantitative analyses.

The cluster AS639, located at low galactic latitude ($b \sim 10^o$), was originally studied by Jørgensen et al. (1996) who found this cluster to be outflowing with an amplitude of 1295 ± 359 kms^{-1}. Using these original measurements, corrected to our standard system, we find an amplitude of 1968 ± 359 kms^{-1}, where the difference possibly reflects differences in the distance relations used by Jørgensen et al. and us. However, Jørgensen et al. argued that this large amplitude was partially due to a difference in the stellar populations (section 6.2.2). By using the correlation between the Mg_2 line index and the central velocity dispersion, they argued that the amplitude of the motion was smaller than $\sim 879 \pm 392$ kms^{-1}. Recently, Jørgensen & Jønch-Sørensen (1998), using additional data, find a peculiar velocity of 838 ± 350 kms^{-1}. They argue that this is also an overestimate, because of evidence for an apparently younger stellar population. On the other hand, since this cluster lies so close to the galactic plane, uncertainties in absorption correction may be large, and these may lead to artificially high values of the peculiar velocity.

Another cluster/group with a suspiciously large amplitude is AS714. This only has a few members, close the minimum number of galaxies required for it to be included in the cluster sample. Although the group has 19 members, as identified by the group-finding algorithm, only 7 are early-types, of which 5, all lenticulars, have new measurements obtained by us. The measured peculiar velocity of 987 ± 249 kms^{-1} is high. However, the group is located in the general direction of the Great Attractor (GA), which may account for its amplitude, comparable to that of Cen30. On the other hand, because of the complexity of the region, the large peculiar velocity can also arise from small-scale dynamical effects, such as those in Cen45.

Also, in the region of the GA, we have another example of large outflow, namely AS753. It has a velocity of 955 ± 176 kms^{-1}, which is significantly larger than the 279 ± 182 kms^{-1} obtained by Jørgensen et al. (1996) using a different distance relation. As we will show in the next section, this is one of the cases where the individual fit de-

parts significantly from the template relation. The difference between the value reported by Jørgensen et al. and us is solely due to our procedure of assigning an error-weighted, rather than a simple, mean distance to a cluster. This illustrates how systematic rather than random errors can sometimes be responsible for significant differences in the measured peculiar velocity of individual clusters.

Finally, the two most distant clusters in our sample, A2199 and A2634, with redshifts $cz \sim 9000$ kms^{-1}, also have the largest peculiar velocities. Again, we have no measurements of our own for the galaxies in these clusters. Recently, Lucey et al. (1997) have re-observed some of the galaxies in these two clusters. They concluded that the original values for the central velocity dispersions for galaxies in A2634 were underestimated; this partially accounts for the large infall velocity of this cluster. Here the peculiar velocities for these clusters were determined using the same data that was presented by Lucey et al. (1997), adjusted to our standard system using our template relation. Even though the values we obtain are smaller compared to those originally reported by Faber et al. (1989) and Lucey et al. (1991) (~ -1500 kms^{-1}), they are still in marked disagreement with more recent results of Lucey et al. (1997) that are based on early-type galaxies and the SCI sample of cluster spiral galaxies (G97b). For instance, the Lucey et al. (1997) values are significantly smaller ($\lesssim -600$ kms^{-1}), with the actual value varying considerably, depending on the distance relation used (FP or $D_n - \sigma$). In the SCI survey these clusters are found to be nearly at rest relative to the Hubble flow. It is intersting to point out that Hudson et al. (1997), using a sub-sample of the new Lucey et al. (1997) data set and the FP relation derived in their paper, also find a low amplitude for the infall of these two clusters. However, if one uses the slope of their $D_n - \sigma$ relation, together with a zero-point derived from the peculiar velocities of the other two clusters we have in common, A347 and 7S2 (since the zero-point of the $D_n - \sigma$ relation is not reported in that paper), then one finds the peculiar velocity of A2199 to be -1956 ± 490 kms^{-1} and -1982 ± 635 kms^{-1} for A2634, comparable to our values. We also note that both A2199 and A2634 have nearby companions (A2197 and A2166), at approximately the same redshift, which may affect the membership assignment and explain the large variations in their measured peculiar velocities.

Since our cluster sample overlaps with those of others, it is interesting to compare the measured peculiar velocities globally. Figure 6.10 shows our cluster v_p, computed using the direct $D_n - \sigma$ relation, for the clusters we have in common with Jørgensen et al. (1996) (10 clusters), SCI (11 clusters), Hudson et al. (1997) (15 clusters), and Gibbons et al. (1998) (14 clusters). Apart from A2199 and A2634, which are not shown in the figure, the comparison is excellent when the errors in the measurements are taken into account. We find mean differences of 21 ± 153 kms^{-1} (Jørgensen et al.), 116 ± 110 kms^{-1} (SCI), -57 ± 135 kms^{-1} (Hudson et al.) and -138 ± 131 kms^{-1} (Gibbons et al.). All clusters are in the same rest frame to within 2σ. This agreeement shows not only consistency between different determinations of cluster distances (e.g., those based on the $D_n - \sigma$ and/or FP relation) but, more importantly, with the TF relation for spiral galaxies. Previous work had suggested inconsistency with the TF results, thus casting doubt on the accuracy of this way of measuring distances. Similar results have also been found by Scodeggio (1997) for a largely independent set of clusters.

Finally, we point out that the peculiar velocities of the clusters are largely insensitive to how one weights the fit to the template relation and to whether we use the direct or inverse relations. Figure 6.11 compares the peculiar velocities computed by the bivariate

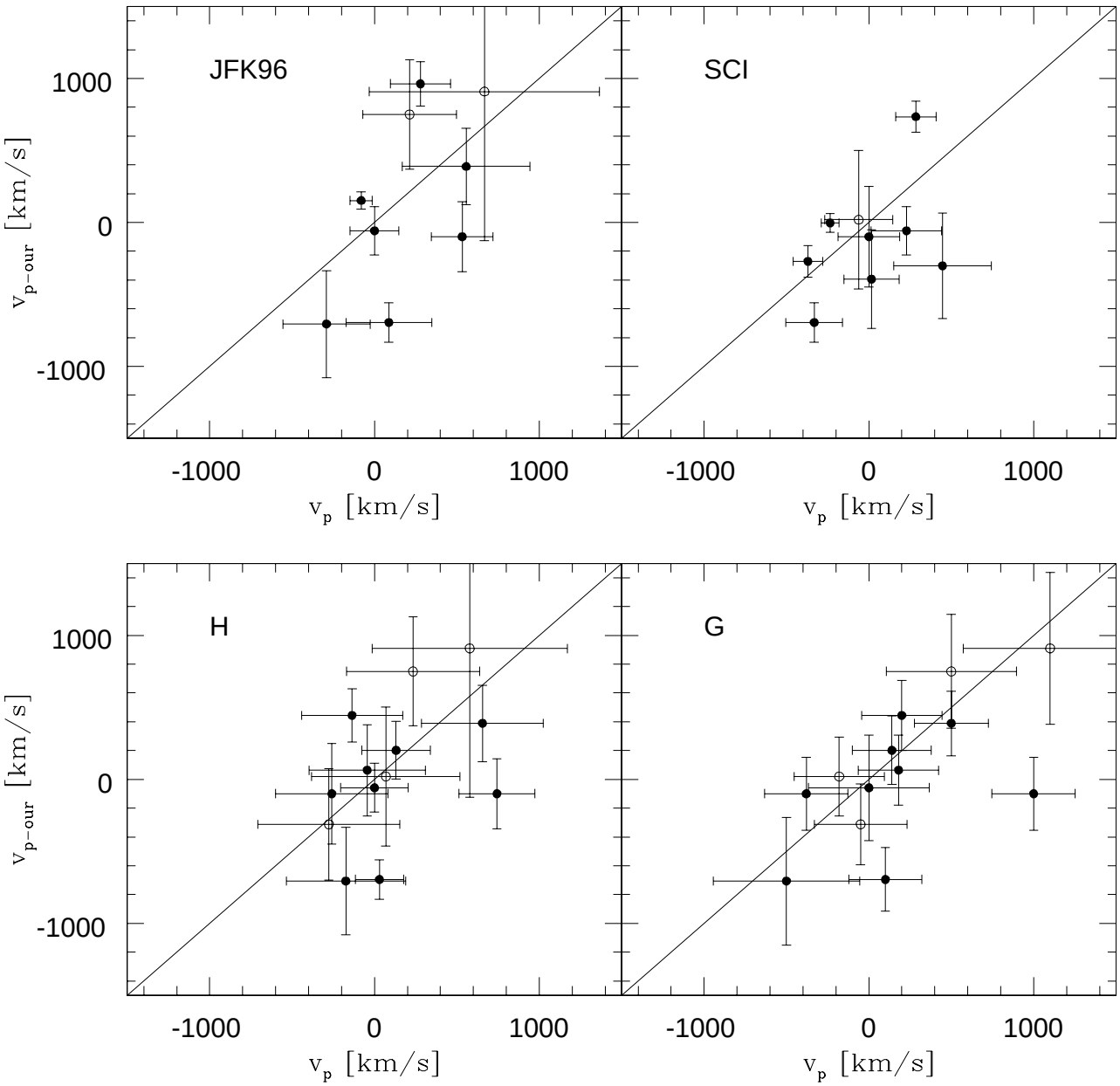

Figure 6.10 Cluster peculiar velocities obtained using Equation 6.11 versus the values computed by Jørgensen et al. (1996) (JFK96), SCI, Hudson et al. (1997) (H), and Gibbons et al. (1998) (G).

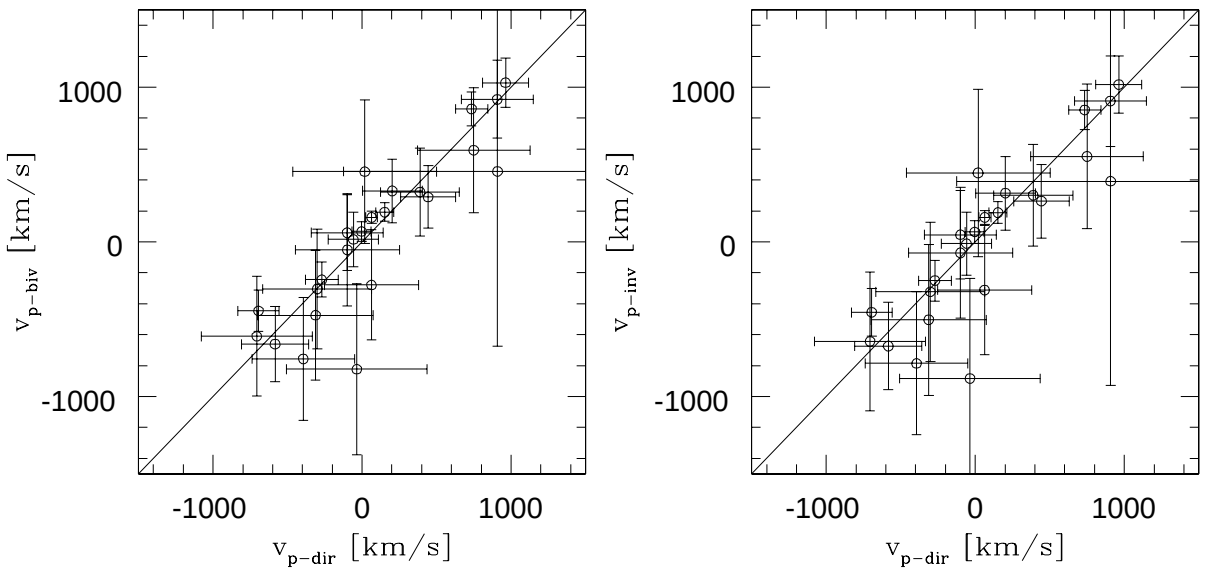

Figure 6.11 Cluster peculiar velocities obtained using the direct $D_n - \sigma$ relation (Equation 6.11) versus the values computed using the bivariate (left) and the inverse relations (right).

(right panel; this relation was corrected for selection bias effects) and the inverse (left panel) with those determined using the direct relation. The mean differences are -38 ± 65 kms^{-1} with a scatter of 252 kms^{-1}, and -59 ± 58 kms^{-1} with a scatter of 266 kms^{-1} for the bivariate and inverse relations, respectively.

As mentioned above, the zero-point of our template relation was determined by requiring that the "distant" clusters, those with $cz \gtrsim 3000$ kms^{-1} exhibit no net inflow or outflow in the CMB rest-frame (see Figure 6.9). This is achieved by shifting the zero-point after running the iterative process. We find that the final error-weighted mean of the radial peculiar velocity of the clusters is 72 ± 83 kms^{-1}. We have also to consider the random error in the zero-point; this has been estimated as follows. We simulated a large number of data sets by randomly sampling the observed data set with replacement. For each cluster the same fraction of data points were replaced. We varied the percentage of replacements from 5% to 25%, except for clusters with few members ($\lesssim$10). In these cases, we have left out one or two observations in sequence. We fixed the slope of the $D_n - \sigma$ relation, and derived the zero-point from each simulated data set. The random uncertainty in the zero-point is given by the standard deviation of a Gaussian fitted to the distribution of these zero-points. Based on this method we have estimated an error of 0.018; this corresponds to an error of $\sim 4\%$ in distance.

In addition to the random errors, there are other sources of systematic errors. For instance, the mean redshift of clusters may differ significantly between different sources. Comparing our cluster redshifts to values given in the literature we find that these differences can be as large as 400 kms^{-1}. Other sources of systematic errors are possible if the coefficients of the template relation show any correlation with either the stellar populations of the member galaxies or other physical properties of the clusters as discussed below.

6.2 The universality of the distance relation

To use the derived $D_n - \sigma$ relation as a distance indicator one must test that the assumption that it is truly universal. This requires systematic cluster-to-cluster differences to be small; that is, the computed cluster distances should not be affected by possible differences in the morphological mix of the galaxy population, different stellar populations or any other cluster property. Furthermore, one must investigate if the measured peculiar velocities are free of any other systematic effects such as extinction, and contamination by interlopers. Such tests can be conducted by examining variations of the residuals of the distance relation which, for our data, are larger than the estimated measurement errors of the $D_n - \sigma$ parameters.

In addition, it is interesting to investigate the source of the scatter in the distance relation, since this scatter is not fully accounted by measurement errors. If identified, these could be corrected for, thus leading to still more accurate distance estimates.

6.2.1 Results for individual clusters

Figure 6.12 shows the data points for each cluster, compared to individual incompleteness bias-corrected fits (dashed line), and the composite template relation (solid line). The parameters for the individual fits are in Table 6.5 where column (1) gives the cluster name; column (2) the number of cluster galaxies; column (3) the slope; column (4) the zero-point offset between the individual and the template relations; column (5) the mean scatter in $\log D_n$ of the data points relative to the individual fit; column (6) the scatter relative to fits obtained with the same slope of the composite template relation; column (7) the intrinsic scatter; and column (8) gives the fraction of the cluster galaxies that were ellipticals in the observed sample.

Figure 6.12 shows that for most clusters the individual fits have nearly the same slope as the template. The figure also shows the benefit of combining all the data because the slope for the poorer systems in the sample is poorly determined. Significant departures are seen for A2634, A1367, A2199, AS753, the first two with very steep slopes and the latter with shallow slopes. As discussed above, with the exception of A1367, all these clusters show large amplitude motions. Also, recall that A2634 and A2199 are parts of two-component systems. Notice that the tilt of the individual $D_n - \sigma$ does not seem to correlate with the fraction of ellipticals in the cluster, but one should be aware that some morphological classification problems may still be present.

The Table shows that, in general, the individual fit does not significantly improve the scatter and that the variations of the slope are likely due to poor statistics. E.g., in AS753, the bright end of high-velocity dispersion galaxies is, essentially, unconstrained.

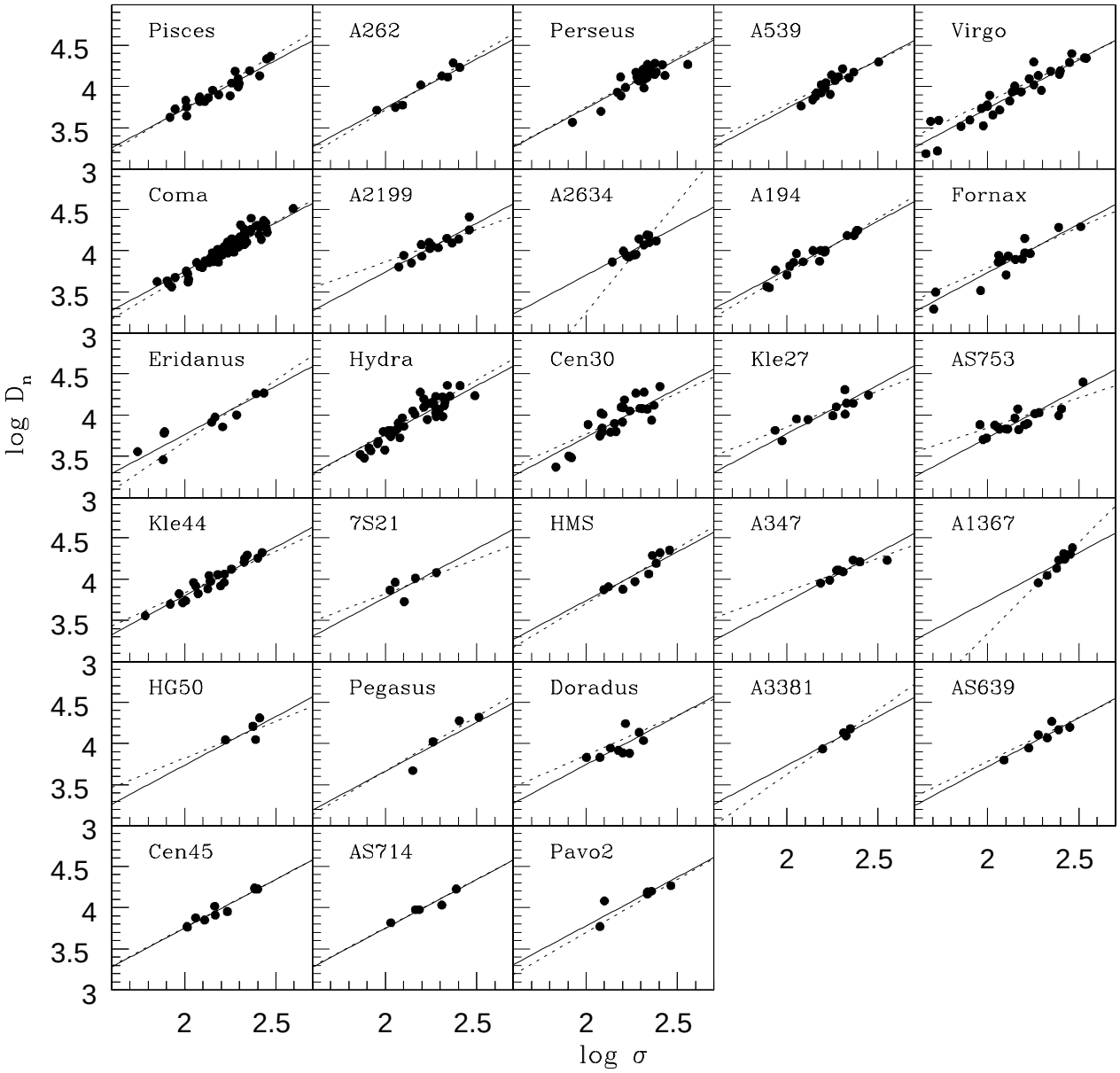

Figure 6.12 The individual cluster $D_n - \sigma$ relations obtained by fitting the bias-corrected data points of the cluster (dashed line). The solid line which is the same in all panels shows the derived distance relation (Equation 6.11).

Table 6.5 Individual cluster $D_n - \sigma$ relations

Cluster (1)	N_{gal} (2)	a (3)	Δb (4)	ϵ_{ind} (5)	ϵ (6)	ϵ_{intr} (7)	F_e (8)
Pisces	22	1.309±0.032	-0.022	0.075	0.066	0.053	0.59
A262	7	1.321±0.060	-0.008	0.052	0.056	0.042	0.75
Perseus	26	1.198±0.042	-0.014	0.083	0.081	0.070	0.62
A539	17	1.073±0.145	-0.017	0.067	0.061	–	0.18
Virgo	33	1.052±0.006	-0.016	0.128	0.109	0.080	0.80
Coma	75	1.309±0.003	-0.002	0.068	0.068	0.008	0.67
A2199	15	0.788±0.011	-0.008	0.079	0.065	–	0.79
A2634	12	2.668±0.269	-0.047	0.112	0.059	–	0.50
A194	17	1.338±0.010	0.019	0.070	0.062	0.030	0.38
Fornax	17	0.982±0.010	-0.017	0.113	0.099	0.085	0.60
Eridanus	10	1.491±0.015	0.011	0.161	0.110	0.100	0.50
Hydra	41	1.279±0.010	0.013	0.102	0.103	0.084	0.32
CenA	25	0.989±0.010	-0.020	0.137	0.128	0.121	0.48
Kle27	11	0.873±0.011	0.022	0.083	0.090	0.074	0.18
AS753	18	0.734±0.024	-0.027	0.094	0.097	0.080	0.17
Kle44	22	1.006±0.009	0.050	0.069	0.060	–	0.36
7S21	6	0.842±0.123	0.027	0.096	0.100	0.091	0.20
HMS	9	1.336±0.066	-0.010	0.073	0.078	0.067	0.67
A347	6	0.807±0.083	-0.021	0.051	0.064	0.047	0.75
A1367	8	2.209±0.298	-0.018	0.031	0.069	0.027	1.00
HG50	4	0.893±0.096	-0.015	0.091	0.090	0.087	1.00
Pegasus	4	1.321±0.115	-0.087	0.104	0.113	0.103	0.50
Doradus	9	0.970±0.043	-0.007	0.126	0.109	0.107	0.22
A3381	4	1.558±0.794	-0.018	0.022	0.030	–	0.50
AS639	7	1.069±0.158	-0.033	0.070	0.063	0.042	0.57
Cen45	10	1.165±0.014	0.002	0.042	0.042	0.037	0.30
AS714	5	1.173±0.057	-0.001	0.043	0.043	–	0.00
Pavo2	6	1.283±0.020	0.029	0.109	0.089	0.084	0.67

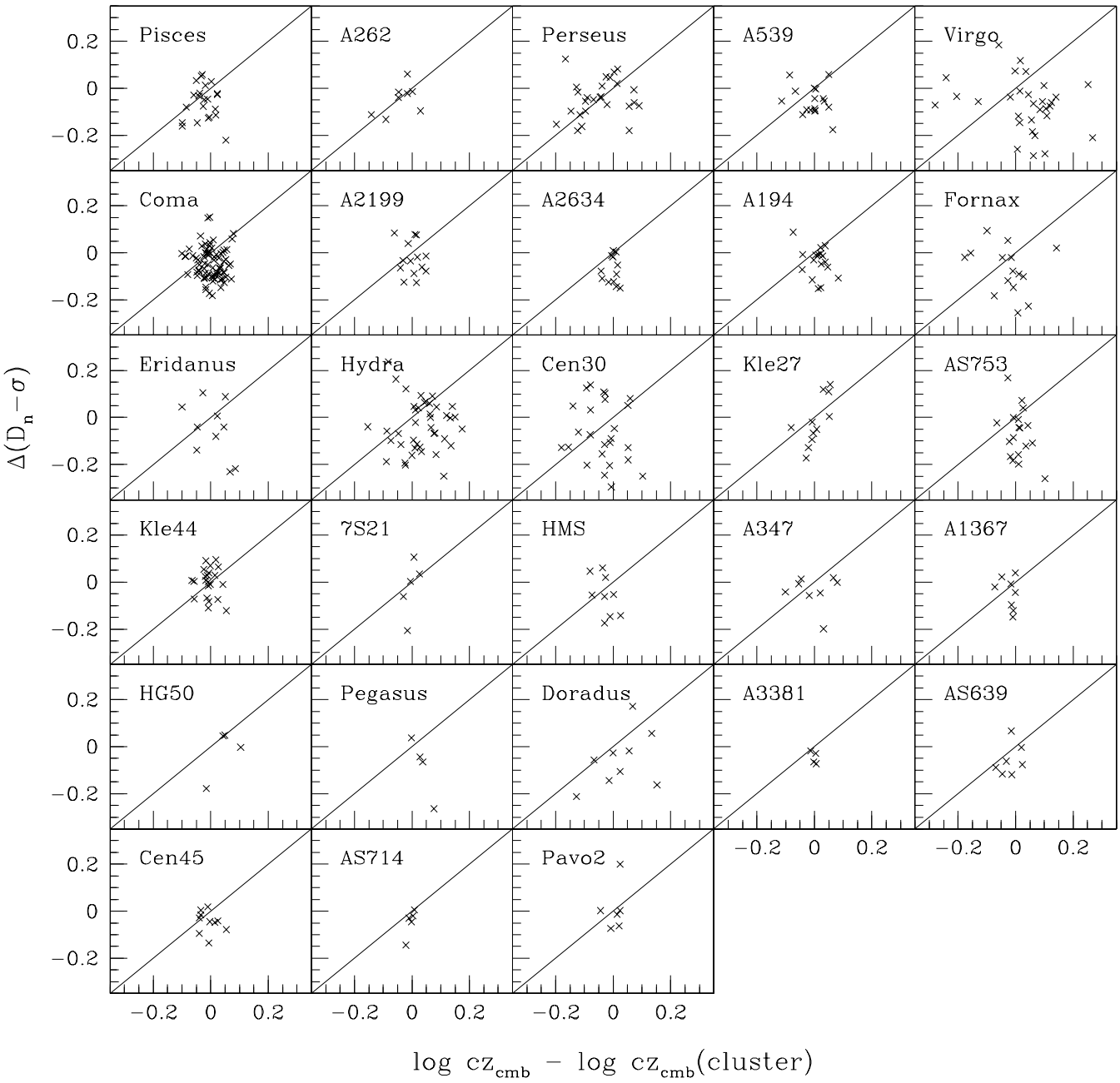

Figure 6.13 The residual, relative to the distance relation, of each galaxy, as a function of the difference between the galaxy's redshift and that adopted for its cluster.

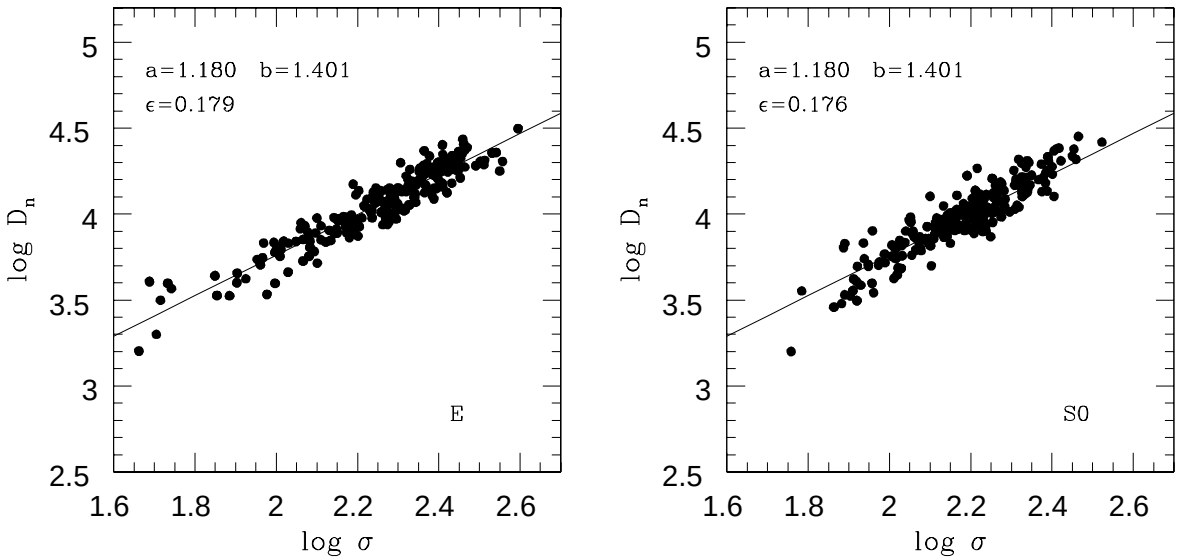

Figure 6.14 The $D_n - \sigma$ relation obtained from ellipticals (left panel) and S0s (right panel). The derived slopes (a), zero-points (b), and rms scatters (ϵ) are also shown.

To examine the impact of interlopers, Figure 6.13 shows the residual of each galaxy relative to the distance relation as a function of the difference between the galaxy's redshift and that of the parent cluster. If field galaxies were contaminating the sample, they would lie preferentially along the 45^o line shown in each panel. No such effect is seen. This is a consequence of our careful membership assignment and the fact that early-types are more likely to reside at the central regions of the clusters (this test may be more important for spirals).

To investigate the effects of morphological type, we split the sample into ellipticals (T ≤ -3) and S0s (T = -2), using the morphological classification given in Chapter 3, and determined the relative shift in the composite template relation by fitting a linear relation with fixed slope, separately for each class. Figure 6.14 shows these relations for the ellipticals (left panel) and S0s (right panel); the intercept and the scatter of the distance relations in the two panels are comparable. This justifies our neglect of any morphological bias (Section 6.1.1). However, our photometric analysis in Section 3.3.3 of Chapter 3 showed that the classification available from the original catalog is not sufficiently reliable to allow one to define sub-types of the early-type population. Therefore, one could, instead, consider the residuals in the $D_n - \sigma$ relation as a function of the D/B ratio. Unfortunately, this ratio is available only for our data (other authors used a one-component model to derive global photometric parameters), so we have not

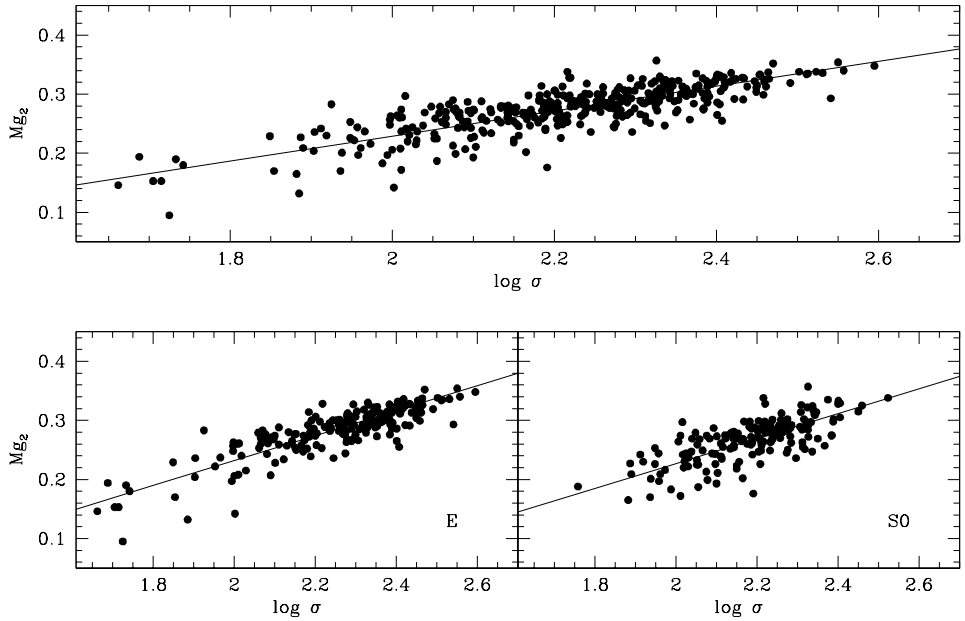

Figure 6.15 (Upper panel) Measurements of the Mg_2 index versus the velocity dispersion for the whole cluster sample. The solid line is the $Mg_2 - \sigma$ relation derived from the bivariate fit. (Lower panels) As in the upper panel, but here the sample is split into ellipticals (left) and S0s (right).

done this yet. Recently we have obtained new data for 135 cluster galaxies which have not yet been included in this work. Once they have been included, we will be able to construct a sample of 265 cluster galaxies with available D/B ratio to do this test.

6.2.2 Stellar populations

As pointed out earlier, the observed intrinsic scatter of galaxies relative to the template distance relation is roughly a factor of 2 larger than can be accounted for by measurements errors. The additional scatter has been attributed by several authors to differences in stellar populations. In the context of distance measurements, we must worry if these differences can lead to systematic errors in the distance and so to spurious peculiar velocities.

To study the effect of different stellar populations, the $Mg_2 - \sigma$ relation, which is supposed to be distance independent, was computed for all galaxies in the sample, and again after sorting the galaxies according to their morphological types (as shown in Figure 6.15). The parameters of orthogonal fits are given in Table 6.6. Column (1) of the Table gives the sample; column (2) the number of galaxies considered; columns (3) and (4) the slope and zero-point, and their respective errors; and column (4) the scatter relative to the relation. Note that the coefficients for the linear fit obtained here for the total samples differ slightly ($< 2\sigma$) from those of Bernardi et al. (1998) because we have added Mg_2 from other authors, adequately scaled to our system. Note that the fit obtained for the S0s is slightly steeper than that obtained for the ellipticals. This is partly due to the fact that we have measured more ellipticals with small velocity

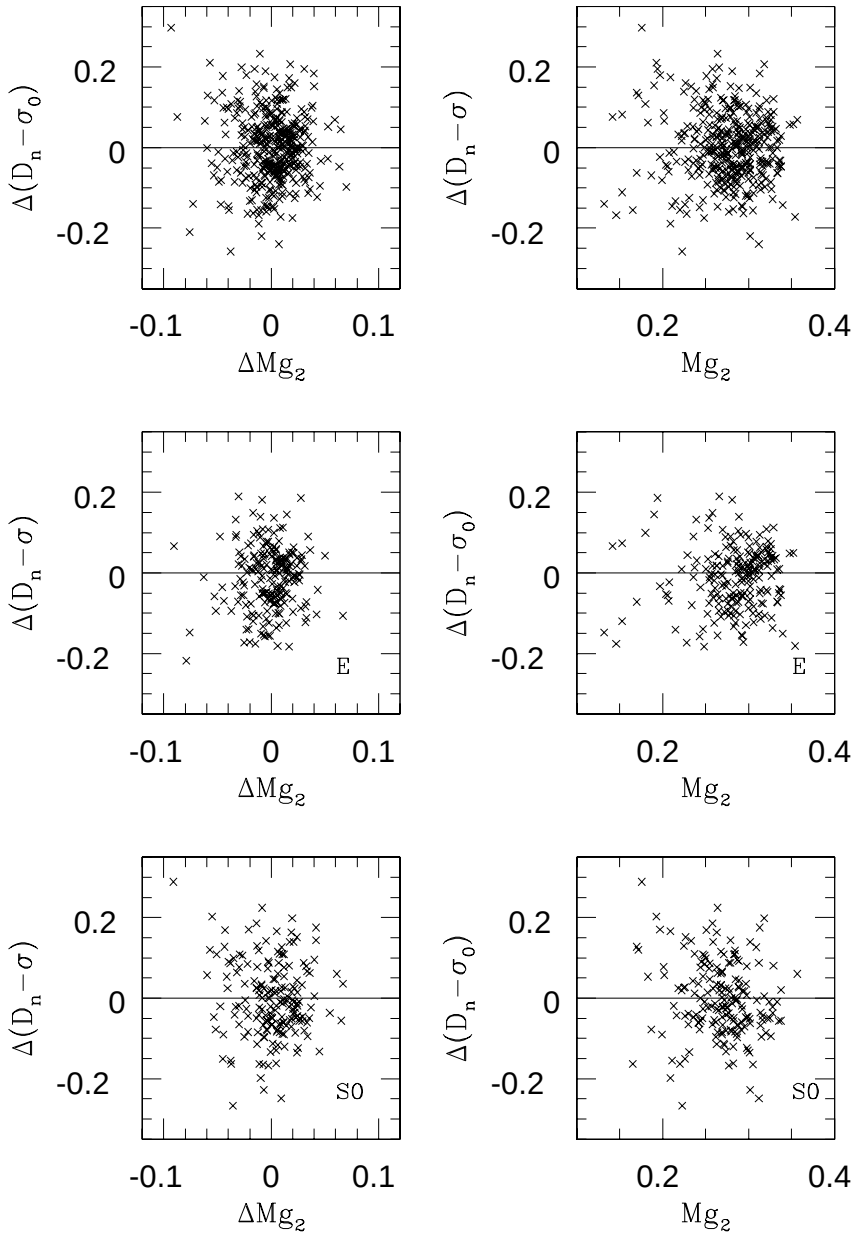

Figure 6.16 (Left panels) Residuals with respect to the mean $D_n - \sigma$ relation versus residuals with respect to the mean $Mg_2 - \sigma$ relation for the cluster sample as a whole (upper panel), for the ellipticals (middle panel), and for S0s (lower panel). (Right panels) As on the left, but now for the residuals of the $D_n - \sigma$ relation versus the measured Mg_2 index.

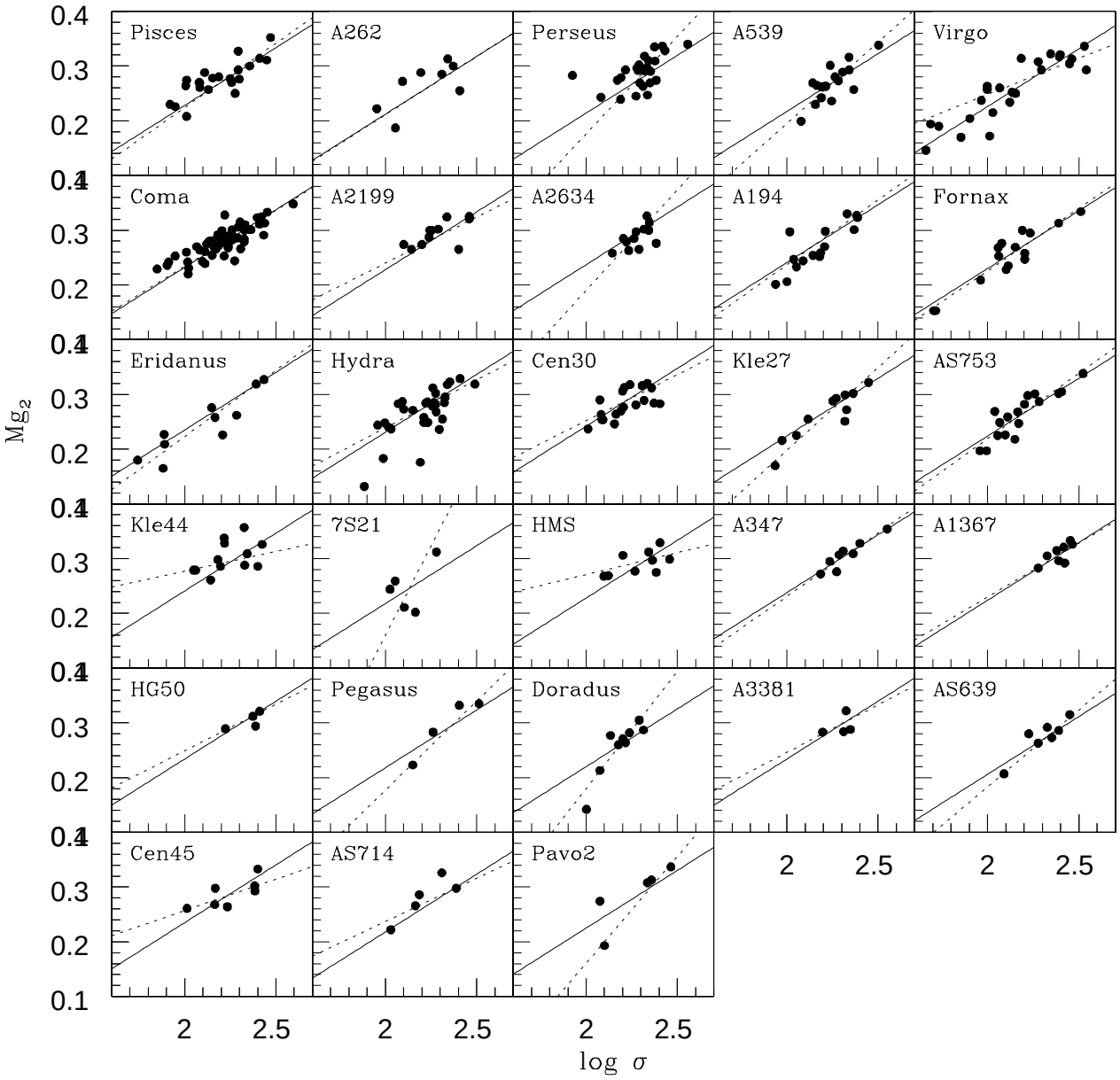

Figure 6.17 The individual cluster $Mg_2 - \sigma$ relation measured in each cluster. Dashed line shows the fit to the individual cluster, solid line (the same in all panels) shows the global $Mg_2 - \sigma$ relation derived from the entire sample.

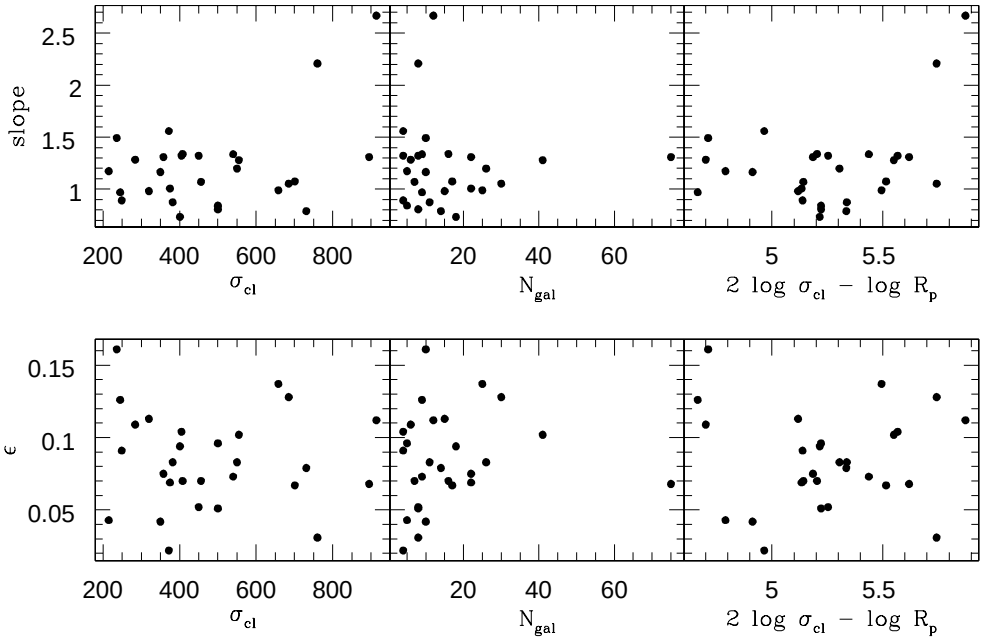

Figure 6.18 (Upper panels) The slope of the individual cluster $D_n - \sigma$ relations versus the measured velocity dispersion of the cluster σ_{cl}, the number of observed galaxies in the cluster, and the logarithm of the ratio $\sigma_{\rm cl}^2/R_p$, where R_p is the pair radius defined in Chapter 5. (Lower panels) The *rms* scatter of the individual cluster fits as function of the same cluster parameters as in the upper panels.

dispersions than for the sample of S0s.

If differences in stellar populations were important in estimating distances, one would expect correlations between the $D_n - \sigma$ and $\mathrm{Mg}_2 - \sigma$ residuals, Δ_{D_n} and Δ_{Mg_2}, respectively, since the latter should reflect either age or metallicity differences. The left panels of Figure 6.16 show Δ_{D_n} versus Δ_{Mg_2} for the cluster galaxies as a whole (upper panel); for the ellipticals (middle panel); and for S0s (lower panel). From the figures we find no evidence for any significant correlation. However, it is also clear that ellipticals form a more homogeneous population than S0s, which have a significantly larger scatter. The

Table 6.6 Our determination of the $\mathrm{Mg}_2 - \sigma$ relation

Sample (1)	$N_{\rm gal}$ (2)	a (3)	b (4)	ϵ (5)
All	384	0.211±0.014	-0.193±0.036	0.024
E	205	0.211±0.014	-0.190±0.036	0.043
S0	179	0.211±0.014	-0.195±0.037	0.054

panels on the right of figure 6.16 show Δ_{D_n} as a function of the Mg_2 line index: no strong correlation is seen. These results, using larger samples and new observations, are in agreement with the conclusions of previous studies (e.g., JFK96).

Finally, Figure 6.17 compares $Mg_2 - \sigma$ relations for the individual clusters with the one for the population as a whole. Apart from a few, most galaxies lie along the globally derived relation. The only exception is AS639 for which all points seem to lie below the relation. Note, however, that all data points for this cluster come from JFK96, and, in any case, it has been eliminated from the sample because of it is at low galactic latitude.

Our results suggest that that differences in stellar populations do not influence the distance relation sufficiently to mimic peculiar motions. Furthermore, none of the most discrepant peculiar velocities discussed in the previous section show evidence that their velocities are caused by stellar population effects.

6.2.3 Environment

There is some concern that there may be systematic environmental differences from cluster to cluster. To examine this possible source of systematic effect Figure 6.18 shows the dependence of the slope and the *rms* (ϵ) of the fit on the measured velocity dispersion of the cluster $\sigma_{\rm cl}$, the number of observed galaxies, and on the logarithm of the ratio $\sigma_{\rm cl}^2/R_p$, where R_p is the pair radius defined in Chapter 5. This last is intended to be a rough measure of the central density of the cluster where early-type galaxies are likely to be located. The Spearman rank test confirms that there is no obvious correlation.

Recently, Gibbons et al. (1998) used 20 clusters, of which 14 are in common with our sample, to argue that the amplitude of the measured peculiar velocity correlates with the *rms* scatter of the distance relation. Figure 6.19 shows the cluster peculiar velocities

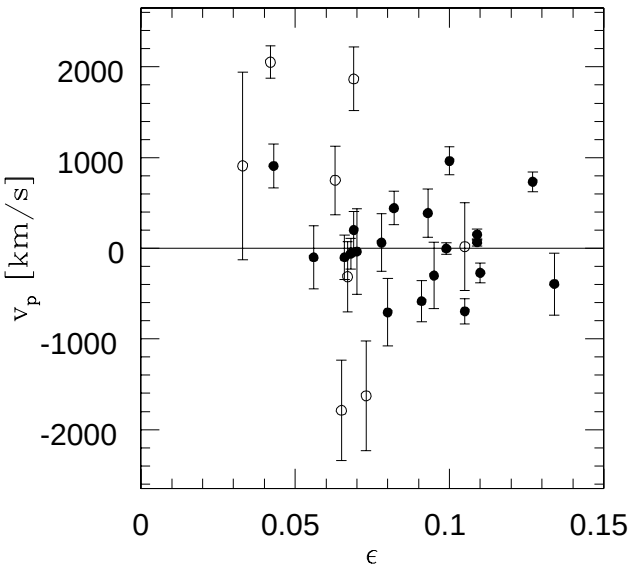

Figure 6.19 Peculiar velocities of the 28 clusters as a function of the amplitude of the scatter of the individual $D_n - \sigma$ relations of each cluster.

and their respective errors as a function of the amplitude of the scatter in $\log D_n$. This is similar to the plot shown by Gibbons et al. (1998): if the discrepant cases discussed in the previous section are discarded, no correlation is found.

We believe that cases of bad fits are more likely to be due to observational problems rather than more profound reasons. In conclusion, we find no compelling evidence that the peculiar velocities are spurious artifacts. Rather, we believe our quoted velocites are a true measure of the cluster motions relative to the Hubble flow.

Chapter 7

The velocity field

In the ENEAR database, 1694 galaxies have measured d_n and velocity dispersions. Of these, 1238 galaxies in 849 independent objects come from the ENEARf sample. The $D_n - \sigma$ relation of Chapter 6 is used to determine distances to the ENEARf objects. These are then used to compute the corresponding peculiar velocities.

These velocities are used to compute the dipole out to $\sim$ 7000 kms^{-1} , as sampled by the 28 clusters and 500 field "objects" (including individual galaxies as well as small loose groups) in the ENEAR dataset. The cluster sample shows a bulk flow of 354 kms^{-1} towards $l = 284^o \pm 10$ and $b = 39^o \pm 5$. This agrees remarkably well with that determined for the "field", which has a flow of 333 ± 52 kms^{-1} towards $l = 263^o \pm 10$ and $b = 32^o \pm 8$. Moreover, the direction of the motion nearly coincides with the direction of the Local Group relative to the Cosmic Microwave Background. These results are relatively insensitive to the weighting scheme used when doing the calculation, indicating that the clusters fairly sample the velocity field.

We discuss how our results compare with measurements based on field spiral galaxies and clusters. The velocity field sampled by the ENEARf and ENEARc early-type galaxies is remarkably similar to that of TF surveys of spirals. This demonstrates, unequivocally, that these motions are real—they are not artifacts of, e.g., systematic variations in the scaling relations from which distances were derived. The agreement between these fields, and the agreement between $D_n - \sigma$ and TF distances to clusters, suggest that the samples can be safely combined for future analyses of the nearby peculiar velocity field.

Finally, we present the velocity and density fields reconstructed from the ENEARf+ENEARc sample using the Wiener-Filter technique, and we compare our result with those obtained from the Mark III catalog and the $IRAS$ data set. The results of this Chapter represent the first results of an analysis of the local velocity and density fields probed by the ENEARf and ENEARc catalogs.

7.1 The ENEARf catalog of galaxy peculiar velocities

In the present analysis the ENEARc cluster sample is supplemented by the ENEARf homogeneous all-sky sample of early-type galaxies. Chapter 2 showed that this sample consists of 1238 galaxies with $D_n - \sigma$ distances extracted from a $m_B = 14.5$ magnitude-limited sample of early-type galaxies within $cz \leq 7000$ kms^{-1}. The sample is nearly

complete for ellipticals and about 70% complete for lenticular galaxies with $D/B < 2$.

By using galaxies assigned to clusters, we derived a template $D_n - \sigma$ distance relation with a scatter corresponding to a fractional distance error of $\sim 19\%$, which is free of systematic biases which depend on environment, morphological type or stellar population (Chapter 6). In particular, we obtained coefficients for the incompleteness corrected direct (forward) $D_n - \sigma$ relation. This relation is used to derive distances and peculiar velocities for the objects in the ENEARf sample, as described below. Distances derived from the direct $D_n - \sigma$ relation are corrected for homogeneous Malmquist bias assuming a distance error of 19% per galaxy, as estimated from the scatter of the distance relation. The correction was applied after assigning galaxies to clusters/groups. Galaxies assigned to any one of the 28 clusters were eliminated from the "group" sample, while the others were assigned to groups identified by the group-finding algorithm as described in Chapter 5.

The redshifts of early-type galaxies in groups/clusters were replaced by the mean group redshift. Redshifts and distances of groups in which there was more than one early-type galaxy were computed as follows. The mean redshift of all the galaxies of all morphological types in the group, was used as the group redshift, and the error-weighted mean of the individual distances was used for the distance to the group. The ENEARf sample consists of 608 isolated galaxies, 274 galaxies in clusters and 356 in groups within 7000 kms^{-1}. The groups can have from one up to 4 members. For clusters and groups the homogeneous Malmquist bias is reduced by a factor of $\sqrt{N}$.

7.1.1 Measuring distances and peculiar velocities

For each galaxy an estimate of the distance R was computed using the forward $D_n - \sigma$ relation:

$$\log R = 1.180 \times \log \sigma - \log d_n + 1.391, \tag{7.1}$$

where the zero-point of the relation was set by requiring that "distant" clusters show no net infall and outflow. The validity of this assumption depends on whether or not we are within a local Hubble bubble (e.g., Giovanell et al. 1999). Because these distances suffer from Malmquist bias, we have also computed corrected distances

$$R^c = R \times \exp\left(3.5\epsilon^2\right), \tag{7.2}$$

where ϵ is the *rms* scatter of the distance relation. This correction assumes that the underlying galaxy distribution is uniformly distributed.

As discussed in Chapter 6, for clusters and groups the distance is given by

$$\log R_g = \overline{\log R} \tag{7.3}$$

where $\overline{\log R}$ is the median of the logarithm of the distances to the galaxies in the group/cluster. These distances have also been corrected for the homogeneous Malmquist bias, yielding corrected distances

$$R_g^c = R_g \times \exp\left(3.5\frac{\epsilon^2}{N_g}\right), \tag{7.4}$$

where N_g is the number of early-type galaxies with estimated distances in the group/cluster. Distances should also be corrected for inhomogeneous Malmquist bias. This bias arises

from small-scale clustering of the galaxy distribution, but is relatively small for our sample because of our grouping procedure.

The radial component of the peculiar velocity of a galaxy in the CMB restframe is then $v_p = cz_{cor} - R^c$ where cz_{cor} is the CMB redshift of the galaxy corrected for the cosmological effect (Equation 6.12). For groups/clusters, cz_{cor} is the median value of the individual redshifts corrected for the cosmological effect and R^c is replaced by R^c_g.

Figure 7.1 shows the peculiar velocities of galaxies, groups and clusters as a function of estimated distance (upper panel) and measured redshift (lower panel). First, notice that the mean of the peculiar velocities is close to zero for all the populations (see also Chapter 6). Second, at large estimated distances, there is a systematic trend for the peculiar velocities of galaxies to be negative. This is due to the redshift cutoff adopted which, at a given distance, excludes those galaxies with peculiar velocities $v_p > cz_{lim} - R$. This effect is only gradual, and for $R = 6000$ kms^{-1} we expect galaxies to scatter within ± 1200 kms^{-1}. Therefore, only a small fraction of galaxies will be removed. Third, in the nearby volume we see a number of galaxies with very large positive and negative peculiar velocities. While some reflect real large peculiar velocities induced by large structures like the Great Attractor and Perseus-Pisces, others seem to be unreasonably large for their location. We re-examined these galaxies (106 entries), and found that most of them were either misclassified (e.g., with $D/B > 10$ or showing shells, arms, dust lane, large bar) or are contaminated by the light of nearby objects (see Chapter 3). Furthermore, a large part of these galaxies were observed by the literature (e.g., Faber et al. 1989). Therefore we removed these 106 galaxies from the sample. Of these, 16 were the only observed early-type member of their group; this means that we removed 16 "objects" from the ENEARf dataset.

Figure 7.2 compares the normalized distribution of peculiar velocities obtained from the ENEARf sample with the distribution derived from the SFI (left panel) and the 7S (Mark II; right panel) samples. The distributions are normalized to have the same maximum value to allow comparison of the dispersions of the different data sets. The ENEARf sample has an *rms* scatter of ~ 500 kms^{-1}, which comparable to that found by 7S, but is smaller than the value obtained from SFI.

7.1.2 The catalog

Table 7.1 lists the peculiar velocities of galaxies in the ENEARf sample (1132 entries). Column (1) gives the name of the galaxy; column (2) an internal number identifying the group/cluster to which the galaxy belongs; columns (3) and (4) the Galactic latitude and longitude; columns (5)and (6) the heliocentric and Local Group radial velocities where, for galaxies in groups/clusters, the adopted group/cluster velocity is used; column (7) the predicted peculiar velocity assuming a malmquist bias correction, and referred to the velocity of the galaxy with respect to the CMB; column (8) the predicted distance of the galaxy, in km/s, corrected for homogeneous Malmquist bias assuming an error of 19%; column (9) the predicted distance of the galaxy without any Malmquist bias correction; and column (10) gives the error in the distance.

Table 7.2, comprising 810 entries, provides the same information as the previous table, except that it lists the relevant parameters for individual objects which consists of "isolated" galaxies and groups. Objects in the ENEARf sample which belong to the clusters presented in Chapter 5 (23 entries) are excluded from this table to ease the

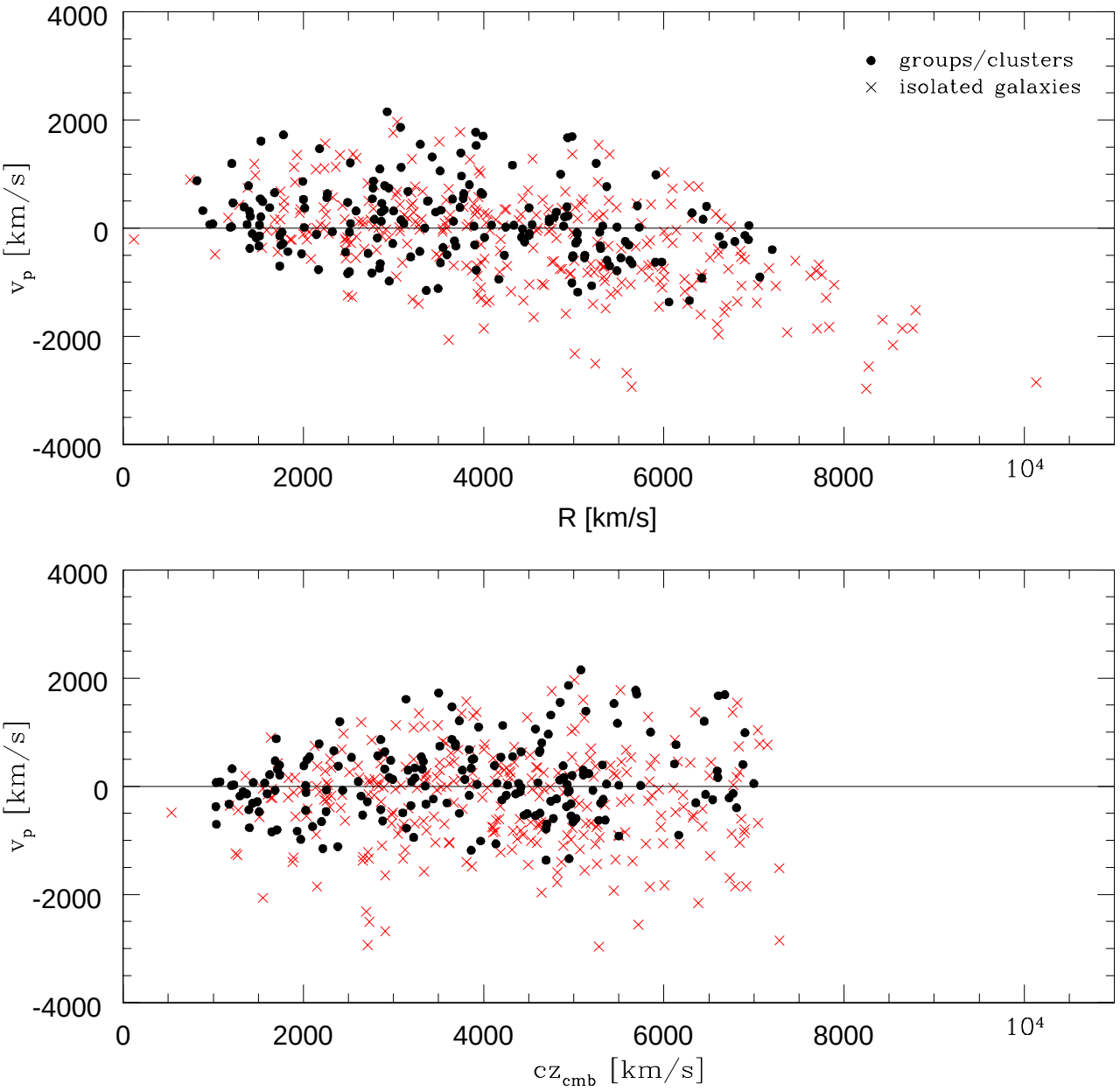

Figure 7.1 Peculiar velocities of the ENEARf galaxies versus estimated distances (upper panel) and redshifts (lower panel). Crosses indicate isolated galaxies, dots are for group/cluster galaxies.

Table 7.1 Peculiar velocities of galaxies in the ENEARf+ENEARc sample

Name	ID_{gr}	l	b	cz_{hel} km/s	cz_{LG} km/s	v_p km/s	R_c km/s	R km/s	δR km/s
(1)	(2)	(3)	(4)	(5)	(6)	(7)	(8)	(9)	(10)
409G12	3002	12.025	-79.233	8325	8357	754	6948	6074	1361
-0101033	0	98.077	-62.441	6204	6376	377	5474	4785	1073
0004+4646	0	115.200	-15.166	5277	5577	-586	5588	4885	1095
N43	2060	113.291	-31.223	4794	5071	-914	5373	5024	1053
0011+3037	2060	113.508	-31.289	4794	5071	146	4263	3986	835
-0101058	3004	98.700	-67.222	5478	5623	894	4256	3721	834
N63	0	109.842	-50.567	1179	1400	-302	1129	987	221
N68	0	114.457	-32.248	5711	5985	1077	4308	4888	844
N78A	0	106.756	-61.062	5481	5660	1026	4105	4658	804
N80	2063	113.798	-39.974	5704	5958	-730	6088	5322	1193
N83	908	113.871	-39.915	5840	6094	-736	6700	5857	1313
N108	0	116.268	-33.331	4737	5007	705	3706	3240	726
-0102016	0	109.246	-63.166	4346	4516	679	3321	2903	650
N125	0	111.758	-59.555	5354	5539	1965	3041	2658	596
N128	2067	111.963	-59.539	4290	4475	621	3259	2849	638
0031+0659A	2070	115.302	-55.354	5456	5656	1020	4082	4632	800
-0202055	0	108.547	-73.159	6155	6278	-270	6098	5330	1195
N160	0	118.417	-38.778	5327	5581	-652	5648	4937	1107
-0202066	0	110.159	-72.597	5981	6106	-1379	7032	6147	1378
540G7	0	103.462	-80.201	6027	6114	1143	4573	5189	896
N183	203	119.557	-33.262	5252	5518	-577	5660	5292	1109
N194	2074	116.906	-59.688	4962	5144	577	4267	3990	836
N193	2074	116.959	-59.406	4962	5144	-137	4135	3866	810
0036+2522	2075	119.542	-37.152	4580	4837	-768	5056	4420	991
0037+4125	0	120.709	-21.133	857	1144	360	212	185	41
N223	0	118.105	-61.946	5355	5527	1088	3927	3433	769
0039+4036	0	121.138	-21.967	200	486	-206	120	105	23
N227	2076	118.141	-62.716	5442	5603	-540	5500	4808	1078
-0103001	3027	117.184	-70.035	6023	6150	1192	4517	3949	885
N233	203	120.958	-32.252	5252	5518	-59	5175	4839	1014
N252	2079	121.994	-35.243	5037	5297	376	4295	3755	841
-0103018	0	122.187	-68.473	5820	5960	-909	6402	5597	1254
-0103019	0	122.434	-69.449	4753	4889	624	3802	3324	745
-0203028	0	122.928	-69.750	4228	4362	780	3122	3543	612
N312	7019	301.242	-64.329	7621	7525	857	7056	6597	1383
N323	7019	301.120	-64.133	7621	7525	-1066	8655	8092	1696
-0103049	0	127.797	-70.039	4619	4749	251	4047	3538	793
0056+2335	2083	125.152	-38.986	5104	5351	989	3749	3277	734
295G26	0	296.007	-76.683	6983	6948	1365	5398	4719	1058
-0103081	0	130.795	-67.805	2406	2543	-577	2663	2328	522

Table 7.2 Peculiar velocities of "objects" in the ENEARf+ENEARc sample

Name	ID_{gr}	l	b	cz_{hel} km/s	cz_{LG} km/s	v_p km/s	R_c km/s	R km/s	δR km/s
(1)	(2)	(3)	(4)	(5)	(6)	(7)	(8)	(9)	(10)
409G12	3002	12.025	-79.233	8325	8357	754	6948	6074	1361
-0101033	0	98.077	-62.441	6204	6376	377	5474	4785	1073
0004+4646	0	115.200	-15.166	5277	5577	-586	5588	4885	1095
N43	2060	113.291	-31.223	4794	5071	-914	5373	5024	1053
-0101058	3004	98.700	-67.222	5478	5623	894	4256	3721	834
N63	0	109.842	-50.567	1179	1400	-302	1129	987	221
N68	0	114.457	-32.248	5711	5985	1077	4308	4888	844
N78A	0	106.756	-61.062	5481	5660	1026	4105	4658	804
N80	2063	113.798	-39.974	5704	5958	-730	6088	5322	1193
N108	0	116.268	-33.331	4737	5007	705	3706	3240	726
-0102016	0	109.246	-63.166	4346	4516	679	3321	2903	650
N125	0	111.758	-59.555	5354	5539	1965	3041	2658	596
N128	2067	111.963	-59.539	4290	4475	621	3259	2849	638
0031+0659A	2070	115.302	-55.354	5456	5656	1020	4082	4632	800
-0202055	0	108.547	-73.159	6155	6278	-270	6098	5330	1195
N160	0	118.417	-38.778	5327	5581	-652	5648	4937	1107
-0202066	0	110.159	-72.597	5981	6106	-1379	7032	6147	1378
540G7	0	103.462	-80.201	6027	6114	1143	4573	5189	896
N194	2074	116.906	-59.688	4962	5144	577	4267	3990	836
0036+2522	2075	119.542	-37.152	4580	4837	-768	5056	4420	991
0037+4125	0	120.709	-21.133	857	1144	360	212	185	41
N223	0	118.105	-61.946	5355	5527	1088	3927	3433	769
0039+4036	0	121.138	-21.967	200	486	-206	120	105	23
N227	2076	118.141	-62.716	5442	5603	-540	5500	4808	1078
-0103001	3027	117.184	-70.035	6023	6150	1192	4517	3949	885
N252	2079	121.994	-35.243	5037	5297	376	4295	3755	841
-0103018	0	122.187	-68.473	5820	5960	-909	6402	5597	1254
-0103019	0	122.434	-69.449	4753	4889	624	3802	3324	745
-0203028	0	122.928	-69.750	4228	4362	780	3122	3543	612
N312	7019	301.242	-64.329	7621	7525	857	7056	6597	1383
-0103049	0	127.797	-70.039	4619	4749	251	4047	3538	793
0056+2335	2083	125.152	-38.986	5104	5351	989	3749	3277	734
295G26	0	296.007	-76.683	6983	6948	1365	5398	4719	1058
-0103081	0	130.795	-67.805	2406	2543	-577	2663	2328	522
N380	5150	126.804	-30.269	4414	4677	823	3293	3737	645
243G33	7033	294.803	-69.964	6957	6890	1305	5222	5925	1023
0105+3923	0	126.528	-23.102	6149	6425	924	4947	4324	969
412G7	0	234.699	-85.900	5447	5468	708	4478	3915	877
0106+3527	0	127.045	-27.011	36	305	-463	211	184	41
0111+3327	0	128.314	-28.920	6297	6560	-315	6322	5527	1239

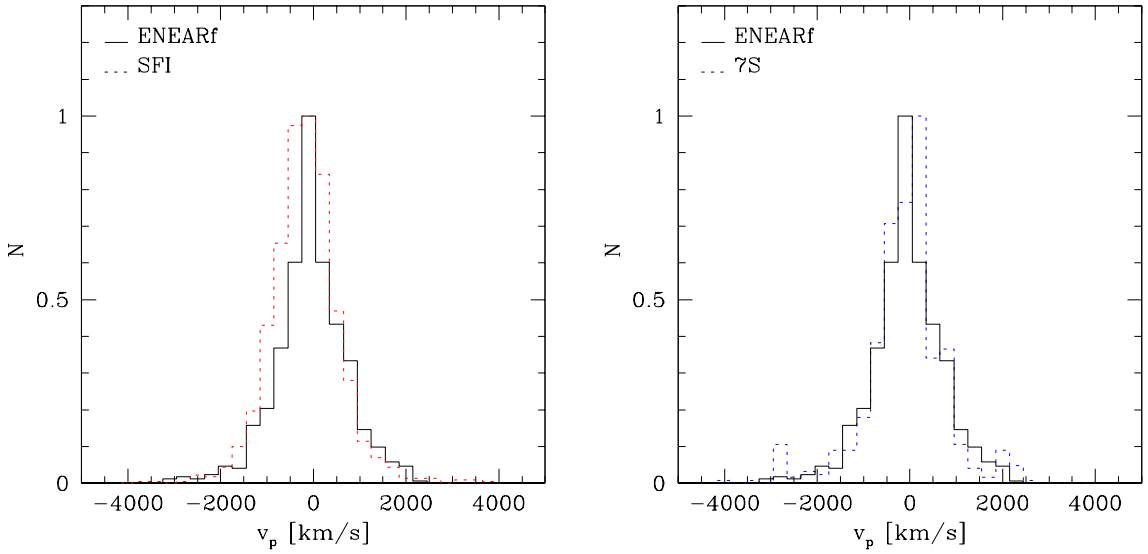

Figure 7.2 Normalized peculiar velocity distributions. The panel on the left compares the ENEARf and SFI samples, and the panel on the right compares ENEARf with the 7S (right panel) sample.

combination of the different samples for analysis.

7.1.3 The peculiar velocity field

To illustrate the current status of redshift-distance surveys, Figure 7.3 shows the peculiar velocities derived for the 833 "objects" in the ENEARf sample, in supergalactic coordinates (X, Y). The two dominant concentrations of galaxies, the Great Atractor (GA) and the Perseus-Pisces (PP) superclusters, are easily identified.

Figure 7.4 compares the peculiar velocity field of the "objects" in the ENEARf sample and that in the 7S sample (Mark II), showing different slices in redshift. One finds comparable results in the region of the GA, although it is sampled better by ENEARf; the lack of 7S observations in the PP supercluster region is also obvious.

Following the same procedure, Figure 7.5 compares the peculiar velocity field traced by the 1132 early-types in ENEARf and by the spirals of the SFI TF survey, in different redshift slices. The general features of the two velocity fields are remarkably similar. Since the distances are based on different scaling relations, and the galaxies tend to reside in regions with quite different densities, the similarities in the two velocity fields strongly and directly support the claim that the peculiar velocities we measure are real, rather

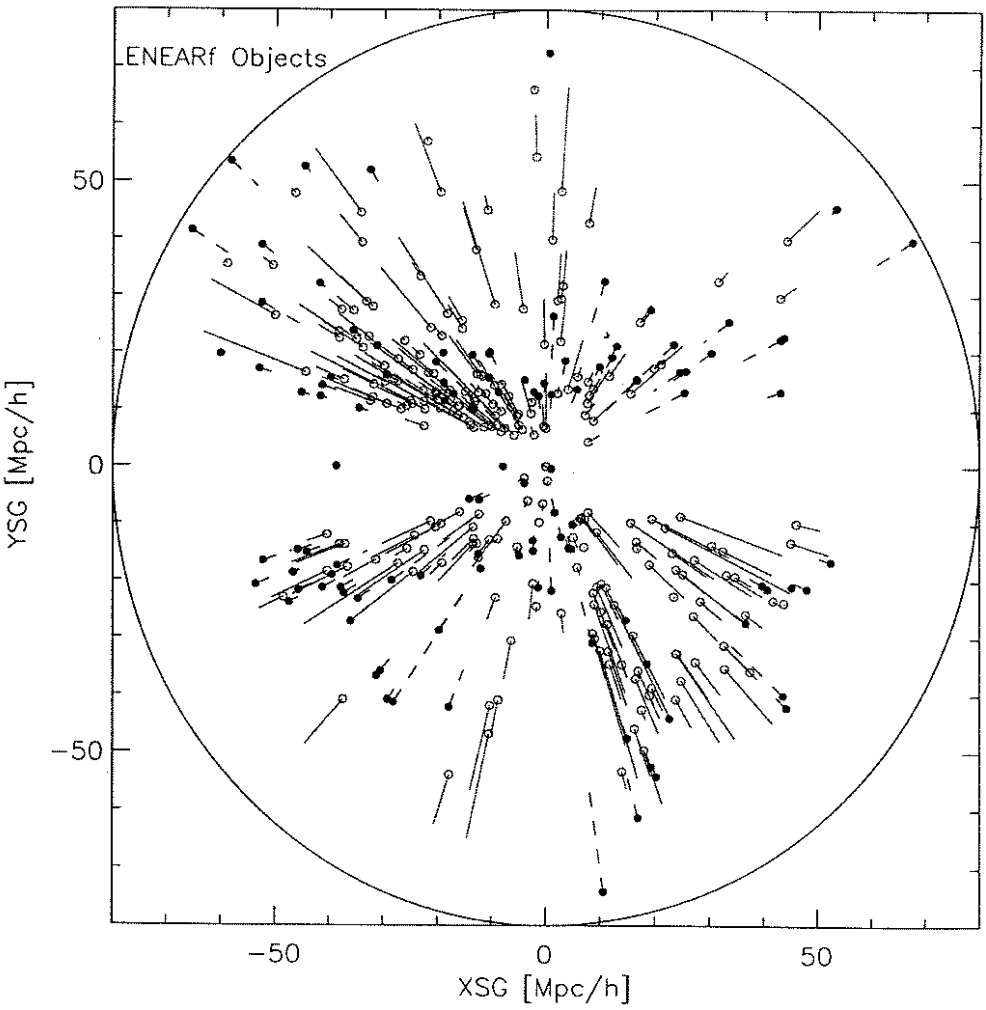

Figure 7.3 The peculiar velocity of the ENEARf "objects", in Cartesian supergalactic coordinates (X, Y), expressed in Mpc/h ($h \equiv H_0/100$ kms^{-1} Mpc^{-1}) with reference to the CMB reference frame. Open circles represent positive peculiar velocities, with amplitude reltaed to the length of the solid line; filled circles and dashed lines show negative peculiar velocities.

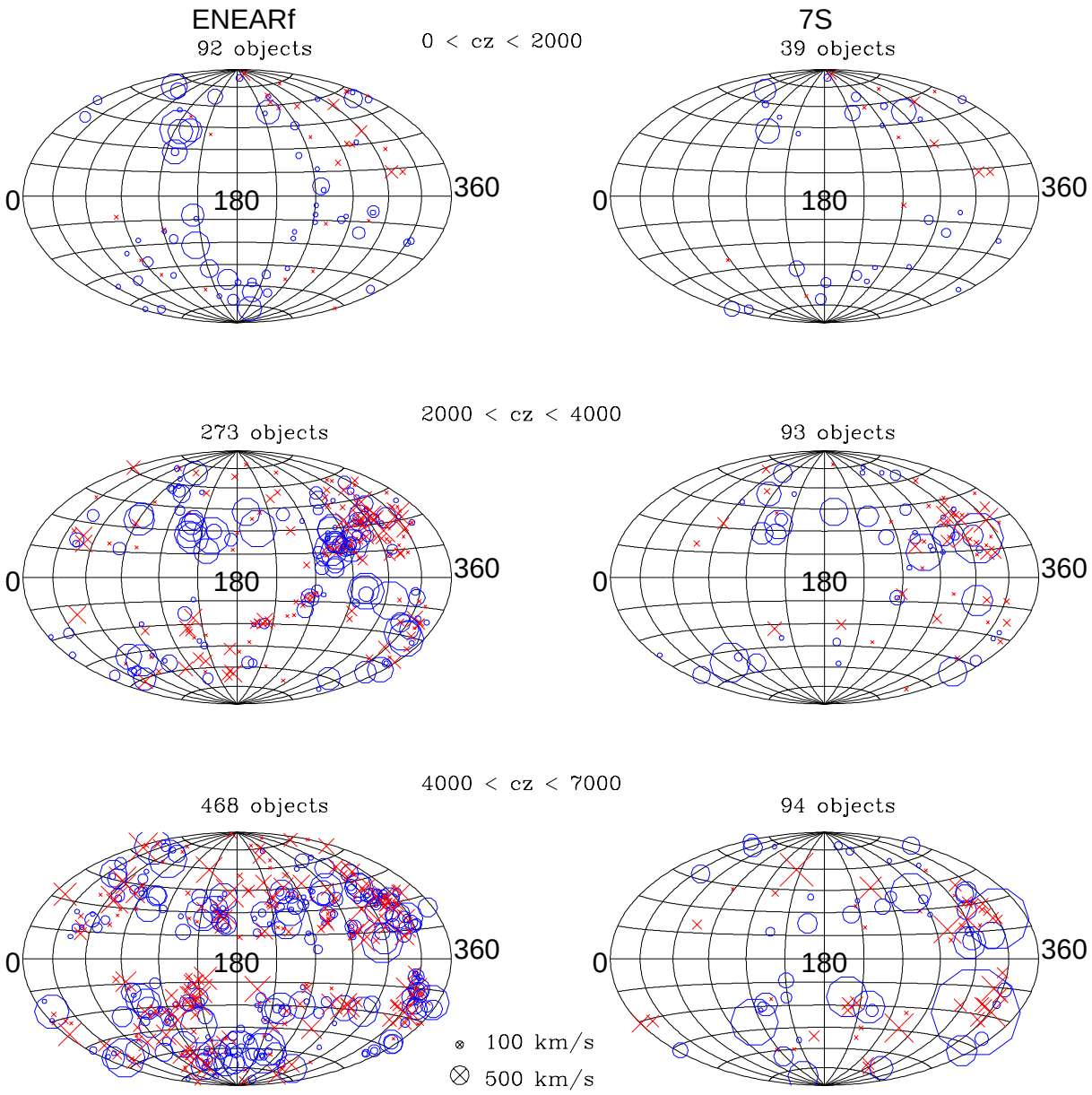

Figure 7.4 Comparison of the peculiar velocities of the "objects" in the ENEARf (left panels) and 7S samples (right panels) projected in different redshift slices. Crosses indicate positive peculiar velocities, open circles negative; the size of the symbols is proportional to the amplitude of the velocity dispersion.

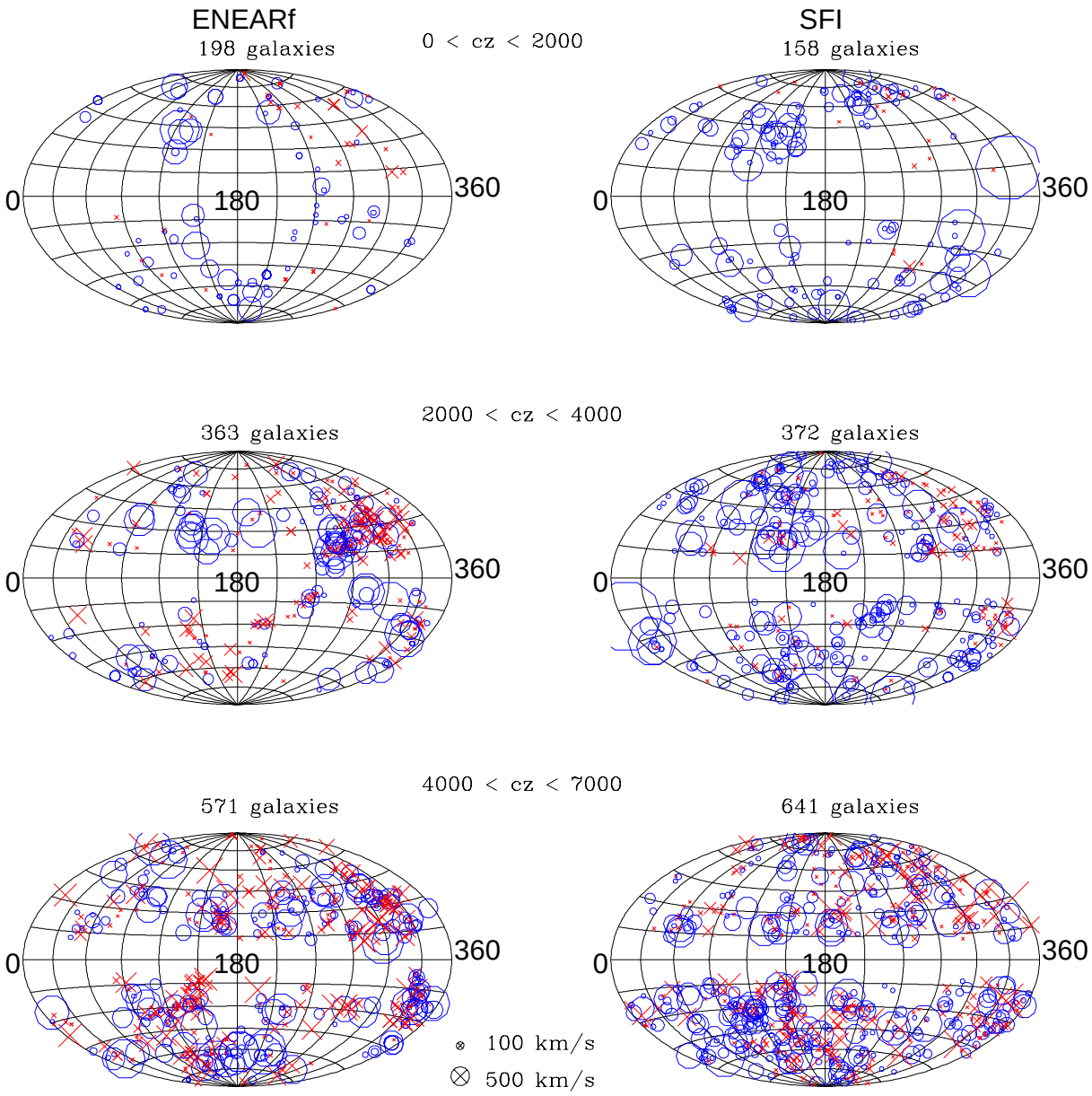

Figure 7.5 Comparison of the peculiar velocities of the early-type galaxies in ENEARf (left panels) and the spirals in the SFI samples (right panels) projected in different redshift slices. Crosses indicate positive peculiar velocities, open circles negative, and the size of the symbols is proportional to the amplitude of the velocity dispersion.

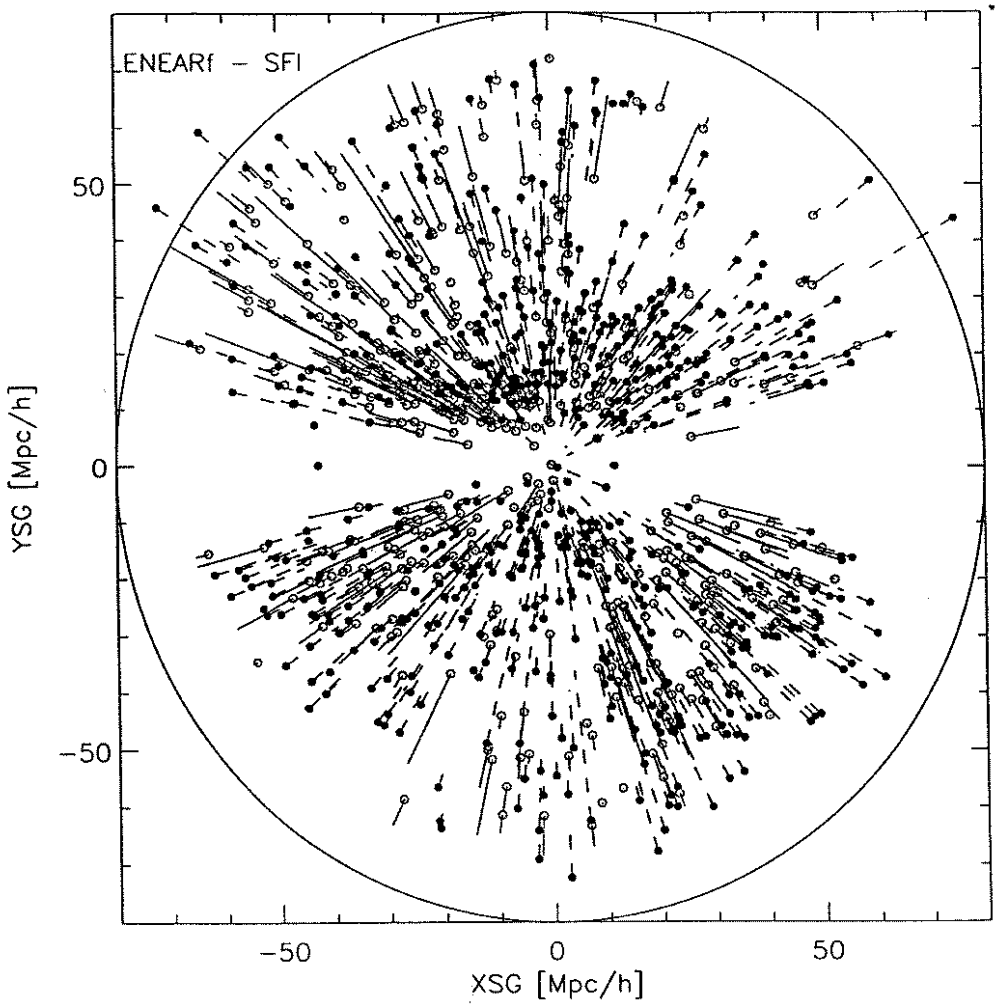

Figure 7.6 Combined ENEARf early-type and SFI spiral peculiar velocities. The galaxy positions are projected in Cartesian supergalactic coordinates (X, Y), expressed in Mpc/h ($h \equiv H_0/100$ kms^{-1} Mpc^{-1}) with reference to the CMB reference frame. Open circles have a positive peculiar velocity, with amplitude is given by the solid line, while filled circles and dashed lines are for negative peculiar velocities.

than artifacts arising from variations in the distance relation that may be correlated with stellar population and environmental effects. This fully justifies continued use of these data for estimating cosmological paramaters based on dynamical measurements. Furthermore, the good agreement of these velocity fields and the good agreement in the cluster distances obtained using $D_n - \sigma$ and TF relations show that the samples can be safely combined in future analyses of the peculiar velocity field of the nearby universe. Figure 7.6 shows the result of combining the ENEARf early-type sample with the SFI spirals: a total of 2303 galaxies are shown—together they are an impressive sample!

7.2 Dipoles of the velocity field

In hierarchical clustering scenario, the peculiar velocity field of galaxies and clusters is a direct probe of the underlying total mass distribution. Among the many ways of characterizing the local velocity field, the bulk flow component or dipole motion is interesting because it is relatively simple to measure, and can directly provide information about the scale of primordial perturbations. Furthermore, by investigating its dependence on the volume, the coherence length of the velocity field in the local Universe can be measured.

Over the past two decades several attempts to measure these quantities have been made: different techniques have been applied to various galaxy and cluster samples, spanning different volumes. Despite these efforts, the results are controversial and sometimes contradictory. In the local Universe the original claim of a large amplitude bulk motion (Mathewson et al. 1992a; Courteau 1992, Courteau et al. 1993; Lauer & Postman 1994) was revised to incorporate a large concentration of mass in the putative Great Attractor. Claims of a large coherent flow involving all of the major observed structures have been reviewed and, based on different methods and peculiar velocity data, are now thought to have significantly smaller amplitude and smaller coherence length (da Costa et al. 1996; Dekel et al. 1998; Giovanelli et al. 1998; Giovanelli et al. 1999).

In this Section, we use the set of ENEARf distances obtained in Section 7.1.2 and those estimated in Chapter 6 for the ENEARc sample to study the dipole motion of "field" objects (galaxies and small groups) and cluster of galaxies within a common volume of 7000 kms^{-1} in radius.

7.2.1 The dipole motion of field galaxies and clusters

The simplest model for the peculiar velocity field is that of a bulk flow which can be computed minimizing

$$\chi^2 = \sum w_i \left(v_i - \hat{\mathbf{v}}_b \hat{\mathbf{r}}_i\right)^2 \tag{7.5}$$

(e.g., Lynden-Bell et al. 1988), where v_i is the radial component of the peculiar velocity of the $i-$th object in the CMB rest-frame, located in the direction $\hat{\mathbf{r}}_i$, $\hat{\mathbf{v}}_b$ is the bulk flow and w_i is the weight given to the i^{th} object in the sample. In our calculations we use either uniform weigths $w_i = 1$ or

$$w_i = \frac{1}{\epsilon_i^2 + \sigma^2}, \tag{7.6}$$

where ϵ_i is the quadrature sum of the distance error and redshift errors (neglected in the case of field objects), and σ is the one-dimensional velocity dispersion due to true velocity

Table 7.3 Dipole solutions

Shell km/s (1)	$\|\hat{\mathbf{v}}_b\|$(uniform) km/s (2)	l (3)	b (4)	$\|\hat{\mathbf{v}}_b\|$(weighted) km/s (5)	l (6)	b (7)
Clusters						
0-2000	1005 ±144	300±18	27±10	987±111	297±12	28±7
2000-4000	1293 ±216	292±11	-20± 9	1293±177	292±11	-24±9
4000-6000	552±149	240±24	6±16	502±127	25± 7	65±5
All	629±123	250± 6	32± 5	771± 56	261± 7	40±3
< 4000	639± 95	284±11	29± 5	892± 88	285± 5	33±4
< 6000	442± 88	284±10	39± 5	714± 57	264± 7	40±4
Field Objects						
0-2000	696±124	273±13	39± 7	722±103	272±12	42±8
2000-4000	413± 94	275±12	7±10	489± 98	277±11	9±6
4000-6000	412±103	252±17	54±17	438±101	257±11	52±7
All	418± 54	266±15	35±11	614± 60	268± 8	39±6
< 4000	472± 69	271± 8	22± 7	640± 68	269± 9	37±6
< 6000	425± 52	263±10	32± 8	619± 61	267± 8	38±6

noise generated on small scales. The small scale velocity dispersion can either be given or be determined iteratively (e.g., Strauss, Cen & Ostriker 1993). The error-weigthing gives more weight to nearby clusters, reducing the effective depth of the sample. Uniform weighting increases the effective depth of the sample and allows for a more significant contribution of distant clusters, at the expense of larger uncertainties in the resulting bulk flow.

Table 7.2.1 summarizes the bulk flow results for different sub-samples. The upper part of the table gives results computed for the cluster sample and the lower part is for the "field" objects defined above. The table lists the amplitude of the bulk flow for different sub-samples and weighting schemes, in the CMB rest frame, and its direction, the galactic longitude and latitude, and their respective errors. These uncertainties were estimated from Monte-Carlo simulations. These were generated by adding random Gaussian deviates of the distance errors to the original peculiar velocities, from which the dipole is computed and the dispersion calculated. For clusters we also used bootstrap re-sampling to assess the impact on the solution of any of the individual clusters.

The bulk flow varies significantly from shell to shell; this is probably because different structures being probed at different distances. The amplitude of the bulk velocity

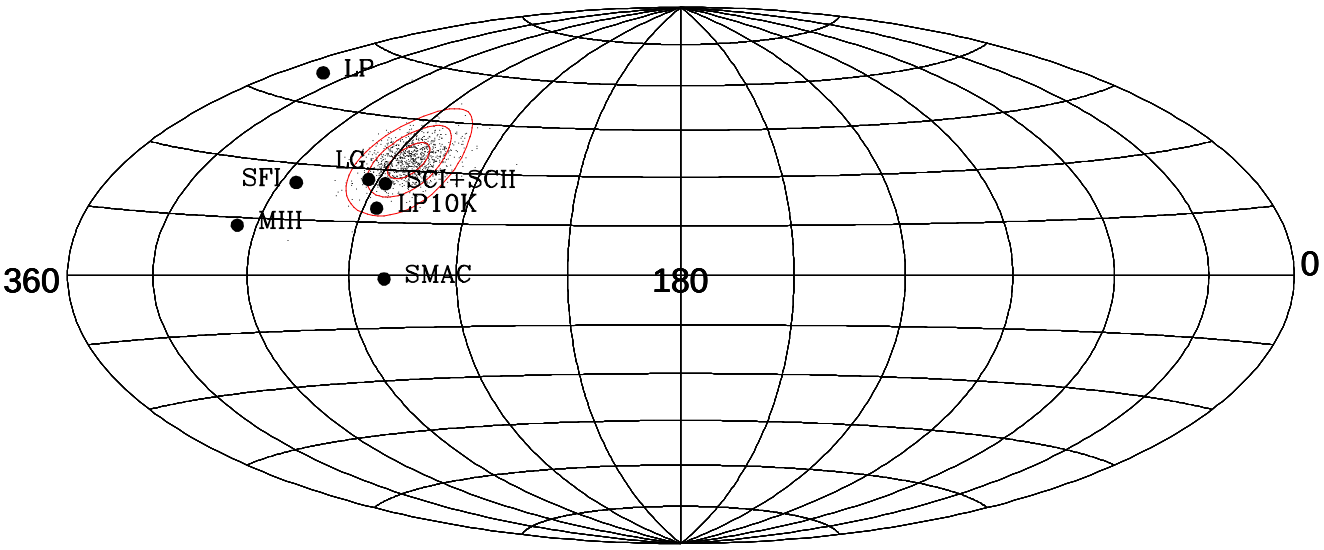

Figure 7.7 The bulk flow direction in Galactic coordinates and the 1000 simulated directions (small dots) drawn from the bulk flow error ellipsoid. The solid lines indicate the 1, 2, and 3σ levels. Other results from the literature are also shown: (LP) the bulk flow of Lauer & Postman (1994); (MIII) the motion derived from the Mark III catalog (Dekel et al. 1998); (SFI) the bulk flow of the sample of spirals in the field (Giovanelli et al. 1998); (LP10K) the dipole solutions derived from Willick (1998); (SCI+SCII) the motion of the cluster sample of spiral galaxies (Dale et al. 1998); and (SMAC) the bulk flow of the SMAC sample of early-type galaxies (Hudson et al. 1999).

decreases to $\sim$ 412 kms^{-1} for the field objects and $\sim$ 552 kms^{-1} for the clusters in the last shell considered. It is interesting that, if limited to 6000 kms^{-1} the bulk flow determined for the cluster and "field" samples is in good agreement, both in amplitude and direction, regardless of the weighting schemes. Differences in the weighting schemes primarily affect the amplitude of the solution (it is 100-300 kms^{-1} larger in the error-weighted solution, possibly due to the influence of nearby structures). Using uniform weights we find that the bulk motion computed for the clusters is 442 ± 88 kms^{-1} towards $(l = 284 \pm 10, b = 39 \pm 5)$ compared to 425 ± 52 kms^{-1} towards $(l = 263 \pm 10, b = 32 \pm 8)$ in both samples. One has also to take into account the "error-bias" which inflates the dipole amplitude (Lauer & Postman 1994), e.g., $|\hat{\mathbf{v}}_b|^2 = v_x^2 + v_y^2 + v_z^2 - e_x^2 - e_y^2 - e_z^2$, where $|\hat{\mathbf{v}}_b|$ is the amplitude and e_x^2, e_y^2, and e_z^2 are the uncertainties on the Cartesian coordinates of the dipole. Correcting the amplitudes for this "error-bias" we get the $|\hat{\mathbf{v}}_b| = 354 \pm 88$ for the clusters and $|\hat{\mathbf{v}}_b| = 333 \pm 52$ for the field objects.

The fact that the dipole measured using the clusters is in agreement with that using the field galaxies strongly suggests that both are equivalent representations of the same

Table 7.4 Comparison with other authors

Source	$\lvert\hat{\mathbf{v}}_b\rvert$ km/s	l	b
(1)	(2)	(3)	(4)
ENEARC	354 ± 88	284 ± 10	39 ± 5
ENEARF	333 ± 52	263 ± 10	32 ± 8
LP	689 ± 178	343 ± 23	52 ± 23
MIII	370 ± 110	305	14
SFI	200 ± 65	295 ± 20	25 ± 20
SCI	$\lesssim 350$	~ 273	~ 27
SCI+SCII	$\lesssim 200$	267 ± 22	26 ± 10
LP10K	720 ± 280	266 ± 38	19 ± 38
SMAC	630 ± 200	260 ± 15	-1 ± 12
LG	611 ± 22	273 ± 3	27 ± 3

underlying velocity field. Therefore, we combine the clusters and field galaxies which yields our final bulk flow estimate: 343 ± 53 kms^{-1} towards $(l = 264 \pm 8, b = 33 \pm 5)$, where the amplitude has already been corrected for the bias-error.

Figure 7.7 shows an Aitoff projection, in galactic coordinates, indicating the direction of the ENEAR bulk flow (large filled circle) and the directions measured from the Monte-carlo simulations. The contours encompass 68%, 95% and 99.7% of the simulated points, representing the 1σ, 2σ and 3σ confidence regions. The directions of other recent determinations are also shown. These include the measurements of Lauer & Postman (1994) based on the brightest cluster galaxy (LP); the result derived from the Mark III catalog (Dekel et al. 1998), which is a compilation of spiral and elliptical/S0 galaxies (MIII); and those based on TF distances of spiral galaxies in the field (Giovanelli et al. 1998) (SFI). Recent determinations derived from samples that extend to much larger volumes than probed by our sample are the LP10K spirals data set (Willick 1998); the SCI+SCII cluster sample of spiral galaxies (Dale et al. 1998); and the SMAC sample of early-type galaxies (Hudson et al. 1999). The direction of the Local Group motion (LG) towards the CMB is also shown. Note that Giovanelli et al. (1998) present many solutions for the bulk motion derived from the SCI sample of spiral galaxies in 24 clusters. Here we simply report their main conclusion: the bulk flow of a sphere of 6000 kms^{-1} radius in the CMB reference frame is smaller than 350 kms^{-1} at the 95% confidence level or better, and it agrees with the apex direction of the LG. The dipole solutions obtained by all the above mentioned works are also presented in Table 7.2.1.

From these results one finds that:

1. the bulk flow derived for the cluster sample is in remarkable agreement with that computed for the field objects. This indicates that the clusters fairly sample the underlying velocity field

2. the direction of the bulk motion of the combined cluster+object sample nearly coincides with that of the Local Group motion, and it is consistent with that found by most other authors, with the exception of LP and SMAC

3. the SFI and SCI samples, which occupy a similar volume to ours, give results which are comparable to ours. This is important, because it means that these samples can be safely combined in future peculiar velocity analyses

4. our result of the bulk flow is also in good agreement with the value obtained by combining the SCI and SCII cluster samples

5. the amplitude of the dipole derived from our sample disagrees, at more than the 3σ level, with the determinations by LP, LP10K and SMAC surveys.

7.3 Reconstructing structure on large scales

On large scales, where the dynamics is supposed to be dominated by gravity and deviations from homogeneity are small, the observed velocity field reflects the dynamical evolution of the total underlying distribution of mass, both dark and luminous. Under the assumption of structure evolution via linear gravitational instability, the observed velocity distribution is simply related to the underlying mass-density fluctuations. From this, one may be able to measure cosmological parameters such as the mean mass density, Ω; comparison with the distribution of luminous matter can shed light on "biasing", the relation between galaxies and mass ($\beta = \Omega^{0.6}/b$, where b is the biasing parameter) and thus on the process of galaxy formation. When compared to the fluctuations in the CMB, they allow a unique test of the hypothesis that gravitational instability is the primary source for fluctuation growth, and they provide constraints on the initial amplitude of fluctuations on scales that are intermediate between the small scales probed by galaxy surveys, and the much larger scales probed by the CMB.

One way to achieve these goals is by *reconstruction* of the full dynamical structure in the local cosmological neighborhood from observed peculiar velocities. Several methods have been developed for this purpose: e.g., the POTENT method (Dekel et al. 1998 and references therein); inverse Tully-Fisher based methods (Davis et al. 1996); the VELMOD method (Willick et al. 1997b); and the Wiener Filter technique (Zaroubi et al. 1999).

The basic assumptions common to all these methods are the following. Any initial vorticity in the velocity field would have disappeared as the universe expanded. If structure evolved by gravitational instability, then the peculiar velocity field, smoothed on large scales, is espected to be irrotational, $\nabla \times \hat{\mathbf{v}} = 0$. Thereafter, the flow remains irrotational even in the weakly non-linear regime, as long as no orbit crossing has occurred. Since orbits of galaxies in a deep potential well (e.g., cluster) have probably crossed, one must consider regions at least, say, five times larger than the typical size of a currently collapsed region. Therefore, it is crucial to group all the galaxies in a cluster together, and to use the velocity of this grouped "object" in the subsequent analysis.

Some methods overcome this problem by simply smoothing all regions on scales of a few Mpc or more.

The POTENT method works as follows. Irrotationality implies that the velocity field can be derived from a scalar potential, $\hat{\mathbf{v}}(\hat{\mathbf{x}}) = -\nabla\Phi(\hat{\mathbf{x}})$, and thus the radial velocity field $v_r(\hat{\mathbf{x}})$, should contain enough information for a full reconstruction. The velocity potential is computed by integration along the line-of-sight,

$$\Phi(\hat{\mathbf{x}}) = -\int_o^r v_r(r^{'}, \theta, \phi)dr^{'}. \tag{7.7}$$

The two transverse velocity components along θ and ϕ are then computed by differentation. Finally, the mass-density fluctuation field in a sphere of radius R can be computed

$$\hat{\mathbf{v}}(R) = \frac{H_0\Omega_0^{0.6}}{4\pi}\int \delta_{mass}(\hat{\mathbf{r}})\frac{\hat{\mathbf{r}}}{r^3}W(r,R)d^3\hat{\mathbf{r}} \tag{7.8}$$

where $W(r,R)$ is a window function of with R, $H_0\hat{\mathbf{r}}$ is the distance in kms^{-1}, and δ_{mass} is the mass overdensity at $\hat{\mathbf{r}}$.

A major effort in the POTENT approach is directed towards minimizing various biases in the smoothed velocity field. However, the current treatment of random errors in POTENT is not optimal (Zaroubi et al. 1999). Therefore, we will consider an alternative, the Wiener Filter technique (WF). The WF provides an optimal estimator of the underlying field in the sense of a minimum-variance solution given the noisy data and an assumed prior model (Wiener 1949; Press et al. 1992; Zaroubi et al. 1995). In the case where the data is drawn from a random Gaussian field, the WF estimator coincides with the conditional mean field and with the most probable configuration given the data. Since we will be assuming that the underlying velocity field is Gaussian, this WF method includes a rigorous treatment of the random errors and allows powerful extrapolation into poorly sampled regions; this is one of the advantages of WF with respect to POTENT.

Zaroubi et al. (1995) have described how such a method can be used for the general case of noisy and sparse observations of Gaussian fields. It is useful to sketch how the method works. The measured velocity (d for data) is a combination of the true velocity (s for signal) plus noise (n). The method asserts that the best estimate of s is a linear function of d

$$\hat{s} \equiv Wd \tag{7.9}$$

where W, the Wiener Filter is

$$W \equiv \frac{\sigma_s^2}{\sigma_s^2 + \sigma_n^2}. \tag{7.10}$$

Here, σ_s and σ_n are the *rms* standard deviation of the true velocity and of the noise. Notice that when σ_n is small then W is almost unity, in which case the true velocity is the same of the measured one (as it should with the noise is negligible). In the other limit, the case of noisy data, one finds that W is almost zero. As a consequence the reconstructed mean field turns out to be statistically inhomogeneous. To recover statistical homogeneity constrained realizations are produced, in which random realizations of the residual from the mean field are generated such that they are statistically consistent both with the data and the assumed theoretical model.

Whereas σ_n can be measured from the data, it is evident that σ_s must be known a priory. Therefore the technique is Bayesian. In our case, the prior assumption is

that the small-amplitude early fluctuations were Gaussian. The statistical properties of a Gaussian field are completely determined by the two-point correlation function or its Fourier conjugate, the power spectrum. Because we will use the ENEAR peculiar velocities as the data, we require, a priori, the velocity power spectrum, denoted Ψ. In linear theory Ψ is just an integral over the power spectrum $P(k)$ of the density fluctuations (Górski 1988). So, if $P(k)$ is known, then we can proceed. We will use the $P(k)$ determined by Zaroubi et al. (1997); it was determined by a Maximum Likelihood fit to previous data.

Maps of the velocity and density fields in our local Universe, obtained by applying the WF to the ENEAR data, are shown in Figures 7.8 and 7.9. The maps are in the Supergalactic plane, with Gaussian smoothing of radius $R = 1200$ kms^{-1}. This reconstruction recovers the main features of our local cosmography quite well, including the Great Attractor (GA) on the left, the Perseus-Pisces supercluster (PP) on the right, and the Local Void in between. The GA region at the left of the map is made of a broad peak centered roughly at $(X, Y) \approx (-5000, 0)$, extending towards Pavo-Indus-Telescopium across the galactic plane to the south $(X < 0, Y < 0)$, and branching out, with a moderate slope through the Hydra and Centaurus clusters towards Virgo $(-300, 1300)$, the Local Group $(0, 0)$, Coma $(0, 7000)$, and the Shapley concentration $(X < 0, Y > 0)$. The density peak of the PP supercluster, on the opposite side of the sky with a peak at $(X, Y) \approx (4000, -1500)$, shows an overdensity of comparable amplitude.

We can qualitatively compare this map with those reconstructed from the Mark III catalog (Dekel et al. 1998; Zaroubi et al. 1999) and from *IRAS* 1.2Jy data (Branchini et al. 1999; Zaroubi et al. 1999). The main differences are the following: the density peak of the PP supercluster shows somewhat lower values for the Mark III catalog, reflecting the differences in sampling in this region between the ENEAR and the Mark III catalogs, whereas our result agrees well with the *IRAS* reconstruction; on the other hand the amplitude and position of the density peak in the GA region in our map is more like what is found in the Mark III catalog, $(X, Y) \approx (-4000, 0)$, than from the *IRAS* data, for which $(X, Y) \approx (-3000, 1000)$.

The results reported here are limited to maps of low resolution in the supergalactic plane; reconstruction of maps of higher resolution is still ongoing. These higher resolution maps will allow us to resolve small-scale structures, which are not clearly identified in the raw data.

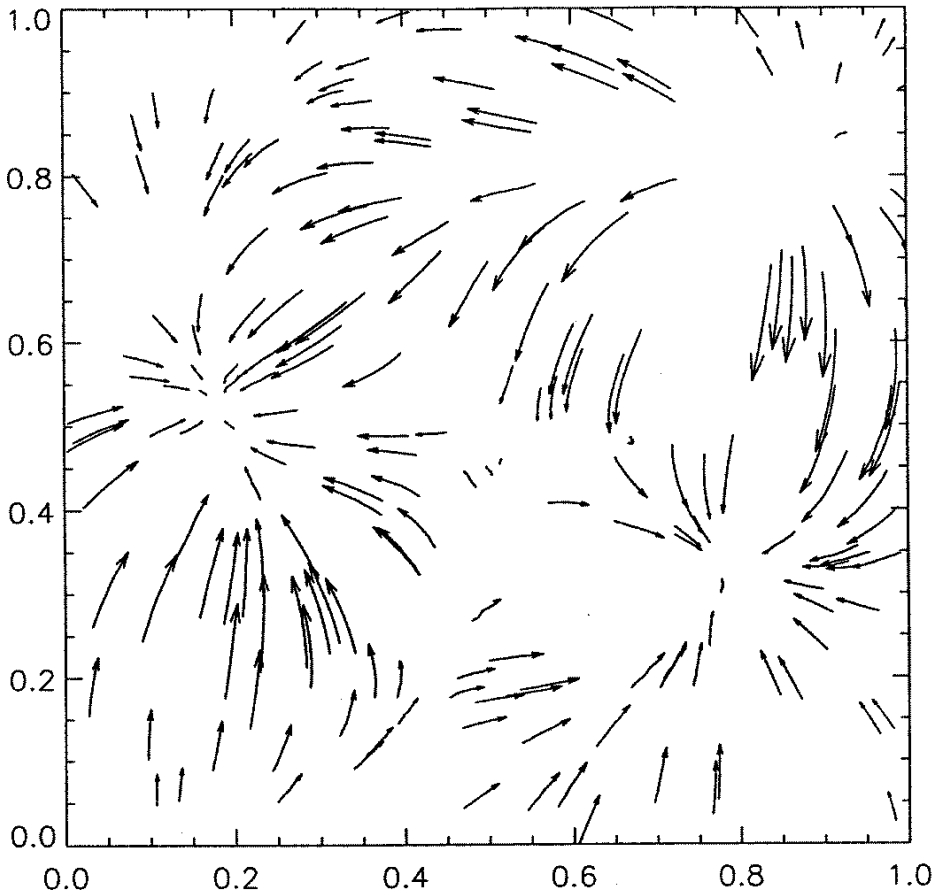

Figure 7.8 Map of the velocity field in the supergalactic plane (the coordinates are as in Figure 7.9), obtained from the ENEARf+ENEARc data using the Wiener Filter technique. The standard CDM model has been assumed ($\Omega_0 = 1$, $\Lambda = 0$, $H_0 = 50$ $\mathrm{kms^{-1}Mpc^{-1}}$). The smoothing window is a Gaussian of radius 1200 $\mathrm{kms^{-1}}$. The velocity field is presented by arrows with arbitrary scaling.

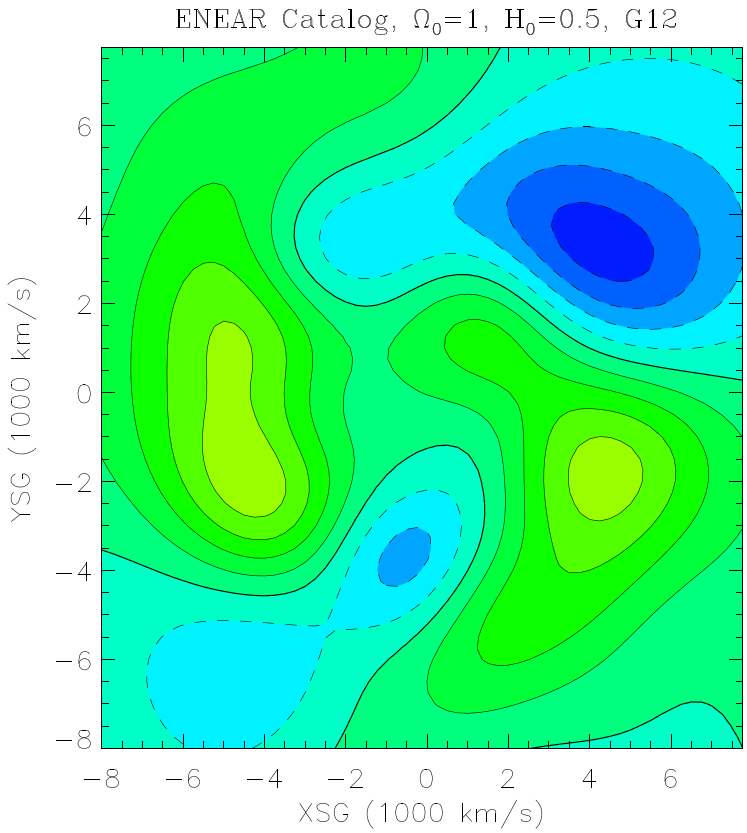

Figure 7.9 Map of the density filed in the supergalactic plane reconstructed from the ENEARf+ENEARc data using the Wiener Filter technique. The standard CDM model has been assumed, and the smoothing window is a Gaussian of radius 1200 kms^{-1}. Density contour spacing is 0.2, positive contours are solid and negative contours are dashed.

Chapter 8

Cluster vs. field ellipticals and clues on their formation

We investigate whether the Mg_2–σ relation shows any dependence on the local environment using our observations of 931 early-type galaxies.[1] Complete magnitude limited redshift surveys were used to assign the galaxies to three local-density environments: clusters, groups, and the field. We find that cluster, group and field early-type galaxies follow almost identical Mg_2–σ relations, with the largest Mg_2 zero-point difference (clusters minus field) being only 0.006 ± 0.003 mag. The small zero-point difference implies a luminosity-weighted age difference of only ~ 1 Gyr between the corresponding stellar populations, with field galaxies being younger. The mass-weighted age difference could be significantly smaller, if minor events of late star formation took place preferentially in field galaxies. We combine these results with the existing evidence for the bulk of stars in cluster early-type galaxies having formed at very high redshift, and conclude that the bulk of stars in galactic spheroids had to form at high redshifts ($z \gtrsim 3$), no matter whether such spheroids now reside in low or high density regions. The cosmological implications of these findings are briefly discussed.

8.1 Background

Great progress has been made in recent years towards charting and modeling galaxy formation and evolution. Yet, the origin of the galaxy morphologies, as illustrated by the Hubble classification, has so far defied a generally accepted explanation. This is especially the case for elliptical galaxies, with two quite different scenarios still confronting each other. One scenario is motivated by hierarchical clustering cosmologies: ellipticals form through a series of merging events that occur over a major fraction of cosmological time (e.g. Baugh et al. 1996; Kauffmann 1996). The other scenario assumes, instead, that the whole baryonic mass of the galaxy was already assembled at early times in gaseous form; for this reason it is sometimes qualified as *monolithic*. Early examples of this latter scenario (Larson 1974; Arimoto & Yoshii 1987) stemmed from the Milky

[1]This Chapter is based on "Cluster vs. Field Ellipticals and Clues on their Formation", by Bernardi et al. (1998), ApJL, 508, 143. When that paper was published, no groups at low galactic latitude were available. The group catalog described in Chapter 5 includes these low b groups. So, in this Chapter, we have used the same dataset as in Bernardi et al.., but with the more complete groups catalog. We find that the new results are consistent with those of our earlier work.

Way collapse model of Eggen et al. (1962); more recent incarnations include models by Bressan et al. (1994) and Matteucci (1994).

Through the 1980's much of the debate focused on the age of ellipticals as derived from the integrated spectrum of their stellar populations. In general, advocates of the merger model favored an intermediate age for the bulk of the stars in ellipticals, but the matter remained controversial (for opposite views see O'Connell 1986, and Renzini 1986). A first breakthrough came from noting the very tight color-σ relation followed by ellipticals in the Virgo and Coma clusters (Bower et al. 1992). This demostrated that at least *cluster* ellipticals are made of very old stars, with the bulk of them having formed at $z \gtrsim 2$. Evidence in support of this conclusion has greatly expanded over the last few years. This came from the tightness of the fundamental plane relation for ellipticals in local clusters (Renzini & Ciotti 1993), from the tightness of the color-magnitude relation for ellipticals in clusters up to $z \sim 1$ (e.g., Aragon-Salamanca et al. 1993; Stanford et al. 1998), and from the modest shift with increasing redshift in the zero-point of the fundamental plane, $\mathrm{Mg}_2 - \sigma$, and color-magnitude relations of cluster ellipticals (e.g., Bender et al. 1997; Dickinson 1995; Ellis et al. 1997; van Dokkum et al. 1998; Pahre et al. 1997; Stanford et al. 1998; Kodama et al. 1998). All these studies agree in concluding that most stars in ellipticals formed at $z \gtrsim 3$.

However, much of this evidence is restricted to cluster ellipticals. In hierarchical models, clusters form from the highest peaks in the primordial density fluctuations, and cluster ellipticals completing most of their star formation at high redshifts could be accommodated in the model (e.g. Kauffmann 1996; Kauffmann & Charlot 1998). However, in lower density, *field* environments, both star formation and merging are appreciably delayed to later times (Kauffmann 1996). This offers the opportunity for an observational test of the hierarchical merger model.

The notion of field ellipticals being a less homogeneous sample compared to their cluster counterparts has been widely entertained, though the direct evidence has been only rarely discussed. Visvanathan & Sandage (1977) found cluster and field ellipticals to follow the same color-magnitude relation, but Larson et al. (1980) – using the same database – concluded that the scatter about the mean relation is larger in the field than in clusters (see also Burstein 1977). More recently, a larger scatter in field versus cluster ellipticals was also found for the fundamental plane (FP) relations by de Carvalho & Djorgovski (1992). However, at least part of the larger scatter for the field ellipticals can simply be a manifestation of the distances being more uncertain, which will also affect the FP relations. Moreover, the database analyzed by de Carvalho & Djorgovki includes only ~ 60 cluster galaxies and about the same number of field galaxies. Pahre (1998) argues that most of the effect is due to reddening errors.

The lack of conclusive evidence for or against systematic differences between clusters and field ellipticals prompted us to take advantage of the large ENEAR database. In addition to redshift, the measured quantities in this database include the central velocity dispersion σ, the magnesium index Mg_2, and the photometric parameters D_n, R_e and μ_e. Analysis of other absorption lines (Hβ, Fe, NaD) is currently underway. Since both σ and Mg_2 are distance and reddening independent quantities, the comparison of the Mg_2-σ relations for cluster and field ellipticals offers the best available way of establishing whether intrinsic differences exist between the two populations.

8.2 The $Mg_2 - \sigma$ relation in clusters and in the field

In the present analysis we restrict ourselves to the sample of 931 galaxies used in the published paper (Bernardi et al. 1998). There, at low galactic latitudes, the assignment to groups was based only on early-type galaxies. The assigment to groups described in Chapter 5 has allowed us to improve the grouping of these galaxies at $-15 < b < 15$. From the new assignment, 258 and 146 galaxies have been assigned to clusters and groups, respectively; all remaining early-types were assigned to the field (527 galaxies).

The resulting Mg_2-σ relations are shown in Figure 8.1, for the whole sample, as well as separately for the field, group, and cluster samples. Also shown are linear least squares fits to the data ($Mg_2 = a\log\sigma + b$), where a is the slope and b the zero-point. For each subsample the slope obtained for the whole sample was retained, and only the zero-point was derived. As is evident from the figure, field, group, and cluster ellipticals all follow basically the same relation. The zero-point offset between cluster and field galaxies is 0.006 ± 0.003 mag, with field galaxies having lower values of Mg_2, a statistically significant, yet very small difference. This is in excellent agreement with the offset of 0.009 ± 0.002 mag, obtained by Jørgensen (1997) using 100 field and 143 cluster galaxies from the *old* 7S sample (Faber et al. 1989). Our own redetermination using the revised 7S sample (Burstein 1998) yields a marginally lower value, i.e., 0.005 ± 0.002 mag. Figure 8.2 shows a histogram of the residuals for the ENEAR sample. The rms of the field sample is 0.031 mag, virtually identical to that of the cluster sample (0.033 mag). This is appreciably larger than our estimated internal errors, indicating that most of the scatter is indeed intrinsic (cf. Colless et al. 1999).

Subsamples of the cluster and field galaxies have been analyzed for possible correlations. No significant correlations of the residuals were found with morphology or disk-to-bulge ratio (D/B). In practice we recover here the result that ellipticals and spiral bulges are alike (Jablonka et al. 1996). Marginally significant differences are instead found when dividing about the median each of the samples into high and low velocity dispersion subsamples (at $\log\sigma = 2.15$), and high and low luminosity subsamples (at $M_{B_0} = -18.5$). (The subsamples are highly correlated given the Faber-Jackson relation.) When keeping the slope constant, the zero point difference between the high velocity/high luminosity cluster and field subsamples is 0.005 ± 0.004 mag. The difference between the low luminosity/low velocity subsamples is instead 0.011 ± 0.006 mag. If anything, it appears that bright/massive galaxies form a more homogeneous population, with a smaller difference in their Mg_2-σ relation between cluster and field objects, compared to subsamples of intrinsically smaller galaxies. Finally, it is worth noting that no correlation seems to exist between the zero-point of the Mg_2–σ relation for cluster ellipticals in the EFAR sample and cluster richness as measured by cluster X-ray luminosity, temperature of the ICM, or σ_{cl} (Colless et al. 1999). The present study extends this (lack of) trend to the lowest density regions inhabited by early-type galaxies.

8.3 Discussion and conclusions

As is well known, the Mg_2 index of a stellar population depends on both age and metallicity. When dealing with real galaxies, it will also depend on the detailed *distribution* of stellar ages and metallicities within a given galaxy (Greggio 1997). Here we let this

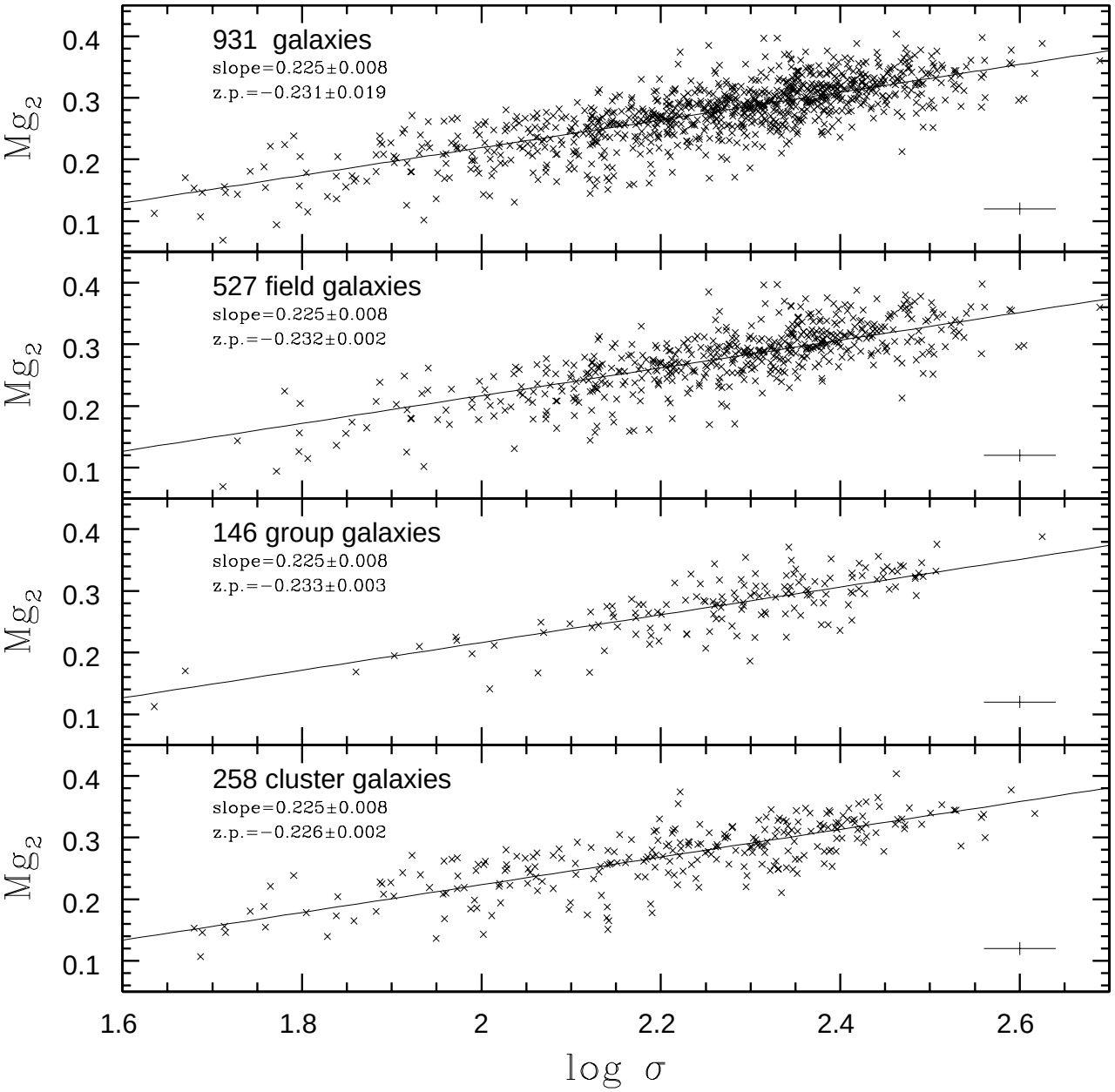

Figure 8.1 The $Mg_2 - \sigma$ relation for the total sample of early-type galaxies (upper panel), and for the field, group and cluster subsamples (lower panels). Lines show least squares fits to the $Mg_2 - \sigma$ relation. For the three subsamples the slope as derived for the total sample was retained, and only the zero-point was re-determined. The number of objects, the slope, and the zero-point are shown in the upper left corner of each panel. Error bars are shown in the lower right corner.

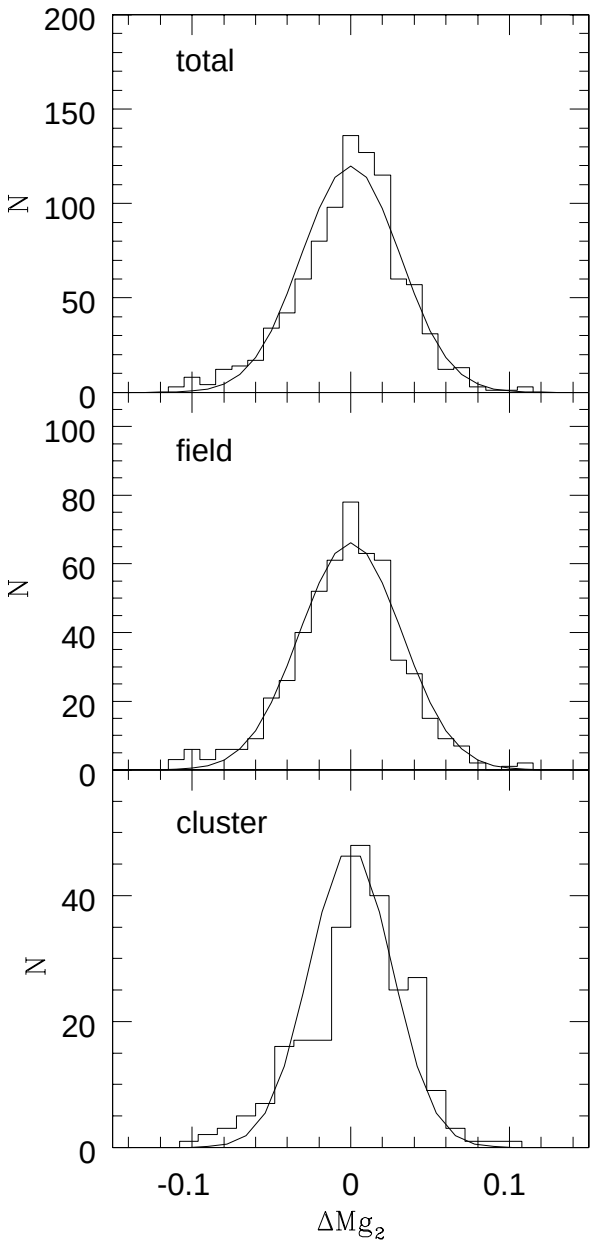

Figure 8.2 The distribution of the Mg_2 residuals relative to the least squares fit obtained for the total sample in Figure 8.1 are shown for the total, field and cluster data sets. The Gaussian bestfitting the residuals for the total sample is overplotted in each panel.

complication aside (though it may help explaining the intrinsic scatter of the Mg_2-σ relation), and use simple stellar population models to set constraints on an indicative *age difference* between cluster and field ellipticals. For solar composition and an age in excess of 10 Gyr, the time derivative $(\partial \mathrm{Mg}_2 / \partial t)$ is 0.0060, 0.0034, and 0.0077 mag/Gyr, in the models of Buzzoni et al. (1992), Worthey (1994), and Weiss et al. (1995), respectively. A straight average gives $(\partial \mathrm{Mg}_2 / \partial t) \simeq 0.0057$ mag/Gyr, or $\Delta t(\mathrm{Gyr}) \simeq 175\,\Delta \mathrm{Mg}_2$. Therefore, the zero-point offset between cluster and field galaxies suggests an average age difference between the two samples of $\sim 1.2 \pm 0.35$ Gyr. This roughly corresponds to a luminosity-weighted age, while the actual, mass-weighted age difference can be substantially smaller. To produce the observed offset it is indeed sufficient that some galaxies have undergone a minor star formation event a few Gyr ago, and that this has taken place preferentially among field galaxies (this effect may have been already detected among HDF ellipticals, see Abraham et al. 1998). Therefore, this ~ 1 Gyr age difference should be regarded as an upper limit to the intrinsic, mass averaged age of stars in field and cluster ellipticals. Of course, given the age/metallicity degeneracy affecting spectroscopic indices such as Mg_2, one can claim that the age difference may be larger than the above limit, but is almost precisely compensated by field galaxies being more metal rich at any given value of σ. We find this alternative interpretation very contrived, hence unattractive.

We are now in a position to compare with theoretical simulations. In the hierarchical merger model of Kauffmann (1996) the luminosity-weighted age of stars in bright ellipticals that reside in low-density environments is about 4 Gyr less than that of cluster galaxies of similar luminosity. This would correspond to a difference $\Delta \mathrm{Mg}_2 \simeq 0.023$ mag, which our data exclude at the 4.6σ level. Indeed, in the hierarchical merger model, the brightest field ellipticals form last (as expected) while smaller ones are instead more coeval to cluster galaxies. The evidence presented in Section 2 suggests the opposite: brighter field galaxies appear to be more similar to their cluster counterparts than the fainter ones. We should warn that the specific model with which we are comparing refers to a standard CDM model, i.e. $\Omega = 1$. Hierarchical models for low Ω (and even more so Λ models) should produce more homogeneous populations of ellipticals and spheroids. It remains to be seen whether such models can meet the age constraint established in this paper.

The present results do not necessarily invalidate the hierarchical merging paradigm, but tend to push the action back to an earlier cosmological epoch, favoring a scenario in which merging takes place at high redshifts, among still mostly gaseous components in which the merging itself promotes widespread starburst activity. The natural observational counterparts of these events is represented by the Lyman-break galaxies at $z \gtrsim 3$ (Steidel et al. 1996), where star formation rates can reach values as high as $\sim 1000\ M_\odot \mathrm{yr}^{-1}$ (Dickinson 1998).

Combining the evidence mentioned in Section 1 of this paper, with the close similarity of cluster and field early-type galaxies documented here, one can conclude that the bulk of stellar populations in galactic spheroids formed at high redshift ($z \gtrsim 3$), no matter whether such spheroids now reside in high or low density regions. Additional direct evidence supporting this conclusion also come from stellar color-magnitude diagrams of globular clusters and fields in the bulge of our own Galaxy, that indicate a uniform old age for the Galactic spheroid (Ortolani et al. 1995). With spheroids containing at least 30% of all stars in the local universe (Schechter & Dressler 1987; Persic & Salucci 1992)

or even more (Fukujita et al. 1998), one can conclude that at least 30% of all stars and metal have formed at $z \gtrsim 3$ (Renzini 1998; see also Dressler & Gunn 1990). This is several times more than suggested by a conservative interpretation of the early attempt at tracing the cosmic history of star formation, either empirically (Madau et al. 1996) or from theoretical simulations (e.g. Baugh et al. 1996). Yet, it is is more in line with recent direct estimates from the spectroscopy of Lyman-break galaxies (Steidel et al. 1998).

Chapter 9

Conclusions and further work

The main results of this thesis are summarized. They concern the construction of, and some of the first results from the recently completed redshift-distance survey of early-type galaxies in the nearby universe (ENEAR). The ENEAR database is extremely useful for mapping the peculiar velocity and density fields in our local Universe, as well for studying many different aspects of early-type galaxies. We also describe ongoing analyses, which will be completed in the near future.

9.1 Results

We have drawn 1694 galaxies from selected nearby clusters and magnitude-limited ($m_{\rm B} = 14.5$ mag) redshift surveys. All the objects have measured $D_n - \sigma$ distances; most of these are based on new spectroscopic and $R-$band imaging observations, others were combined with data from the literature, after scaling everything to a common homogeneous system. Two databases were constructed:

- the ENEARc cluster sample, which consists of 446 galaxies in 28 clusters/groups, and
- the ENEARf sample, which consists of 1238 galaxies in 849 objects representing groups and isolated galaxies.

The ENEARf is an all-sky magnitude and redshift limited sample: it includes objects brighter than 14.5 mag and extends out to 7000 kms^{-1}. Galaxies in the sample were assigned to groups based on groups found, using an objective algorithm, from complete redshift surveys. The sample is about 70% complete, is unbiased in redshift and magnitude, and is uniform across the sky. It is currently the largest homogeneous sample of peculiar velocities of early-type galaxies. It extends far beyond the limit of the 7S data, and samples the most prominent structures in the nearby universe well. The ENEARf catalog complements other, recently completed, TF surveys of spiral galaxies.

Chapter 3 presented new surface photometry results for 1294 early-type galaxies obtained from analysis of 1636 images, of which 946 had no previous photometric measurements. The present sample is the start of a continuing effort to complete a wide-angle photometric survey of early-type galaxies brighter than $m_{\rm B} = 14.5$. The data presented in Chapter 3 demonstrate the quality that can be expected from such a survey. We have carefully examined the observational parameters which enter in measurements of

the $D_n - \sigma$ and FP scaling relations. The images also provide additional information which can be used to probe the nature of the scatter in the distance relations that are used to estimate distances to early-type galaxies.

Observations, reduction and analysis for 1679 spectra of 1146 galaxies, of which 914 had no previously measured velocity dispersions were presented in Chapter 4. About 65% of the galaxies were observed with a resolution ($\lesssim$2.5 Å) that is a factor of two better than in previous large surveys. In addition to measuring 1103 new redshifts and velocity dispersions, we also measured the Mg_2 line index for 1036 galaxies. A total of 43 of our galaxies show strong emission lines; the spectroscopic parameters of these galaxies have not yet been derived.

Although our photometric and spectroscopic observations span a number of years, repeated observations allowed us to bring all of the measurements into a common system which is both internally consistent and compares well with published data. Furthermore, because we observed many objects that were previously observed by others, we were able to derive statistical corrections which, when applied to these earlier measurements, allowed us to combine most existing data into a uniform, homogeneous catalog of about 2000 early-type galaxies with measured velocity dispersions and about 1900 with photometric parameters.

We have also presented a homogeneous set of data for 446 galaxies located in 28 groups or clusters (the ENEARc sample), which can be used to estimate distances using the $D_n - \sigma$ relation. Of these, 310, spanning a wide range of characteristics, can also be used to derive a Fundamental Plane relation. Assignment of galaxies to groups and clusters was done using objectively identified group catalogs derived from complete redshift surveys. Roughly 7% of the galaxy population previously assigned to clusters and groups were found to be misassigned, and 14% were found to be "peripheral" cluster objects. The data for the ENEARc sample are a combination of new measurements and those available in the literature, all scaled to the same reference system. This was possible because there are many galaxies in common between the various data sets.

We used the ENEARc sample to derive a bias-corrected $D_n - \sigma$ relation. This relation was used to measure relative distances to galaxies in the recently completed survey of early-type galaxies, and to map the peculiar velocity field. Our final results are:

1. The slope of the $D_n - \sigma$ relation, obtained by combining data for all cluster/groups, does not differ significantly from previous determinations.

2. The scatter in the relation is 0.08 dex, implying a distance error of about 19% per galaxy, comparable to the error of FP relations. Since $D_n - \sigma$ does not require fits to light profiles it is, in general, both less sensitive to seeing effects and easier to compute. Therefore, it is the relation of choice when dealing with large samples of galaxies.

3. Our cluster peculiar velocities are in good agreement with other determinations, in particular, with those based on spiral TF distances, further supporting the validity of the distance indicators.

4. We find no evidence that systematic effects contaminate our computed peculiar velocities; our quoted velocities are fair estimates of motions relative to the Hubble flow.

5. Of the 28 clusters in the sample, seven show suspiciously large peculiar velocities (both infall and outflow). Of these, five are likely to be due to small-scale dynamical effects, or to contamination by other components, and one may be affected by absorption effects, because it lies at low galacitic latitude.

6. If these clusters are eliminated, we find that the cluster one-dimensional *rms* velocity is relatively small, 340 ± 43 kms^{-1} . This is consistent with what is obtained from TF data, and suggests that the velocity field is rather quiescent.

The distance relation derived here was used to estimate distances to 1132 ENEARf galaxies. Of these, 106 galaxies were found to be either misclassified (e.g., they had $D/B > 10$, or had shells, arms, dust lanes, a large bar, etc.) or contaminated by the light of nearby objects. These objects also showed unreasonably large peculiar velocities, and were removed from the ENEARf sample. The sample was then used to map the peculiar velocity field in the nearby universe.

This sample is comparable in size to the SFI sample of field spirals. Since it uses a different distance relation, and it probes different density regimes, it allows an independent analysis of the characteristics of the local velocity field. The ENEARf-ENEARc sample of early-types and the SFI-SCI sample of spirals agree well. Therefore, it should be possible to merge these two data bases to provide the largest, most homogeneous sample currently available for cosmic flow studies.

The ENEAR catalog is invaluable for studies of the properties of early-type galaxies and their peculiar motions. Our main findings about the bulk flow of ENEAR clusters and "field" objects within $cz = 6000$ kms^{-1} are:

1. the bulk flow derived for the cluster sample is in remarkable agreement with that computed for the field objects. This indicates that the clusters fairly sample the underlying velocity field

2. the direction of the bulk motion of the combined cluster+object sample nearly coincides with that of the Local Group with respect to the CMB; it is consistent with that found by most other authors, with the exceptions of LP and SMAC

3. the SFI, SCI, and SCI+SCII samples of spiral galaxies give comparable results. Since the SFI and SCI samples occupy a similar volume to ours they can be safely combined with the ENEARf and ENEARc samples in future peculiar velocity analyses

4. the amplitude of the dipole derived from our sample disagrees, at more than the 3σ level, with the determinations by LP, LP10K and SMAC surveys.

We have applied the Wiener Fielter technique to the ENEARf+ENEARc sample to study the velocity and density fields of galaxies in a volume of 7000 kms^{-1}. There are two major concentrations in the nearby Universe: the Perseus-Pisces and the Great Attractor; between them there is the Local Void. These findings are consistent with predictions from the *IRAS* survey, results obtained from the SFI sample (da Costa et al. (1996); Haynes et al. 1999a,b), and with the mass distribution recovered by Dekel et al. (1998) using the MARK III database.

Finally, we have confirmed the result of Bernardi et al. (1998): the $Mg_2 - \sigma$ relation does not show any dependence on environment. This results favours the *monolithic*

scenario of formation and evolution of early-type galaxies in which merging takes place at high redshifts. Furthermore, the lack of environment effects also supports the assumption that the empirical distance indicators such as the $D_n - \sigma$ relation, are universal; this is a crucial assumption for peculiar velocity field analyses.

9.2 Future work

The results described above come from the first applications of the ENEAR catalog. Certainly, in the future, a large amount of information will be extracted from this database. ENEAR is an ongoing project: we intend to update all the available measurements derived from the observed data in the near future. About 400 images and 500 spectra are still being analyzed. Furthermore, all the light profiles were analyzed by imposing a conservative cutoff (an error of $\sim$3% of the sky) on the maximum extent of the profile. We hope to re-analyze all the available profiles after relaxing this condition.

Galaxies with spectra showing strong emission lines deserve more study. Some of these objects were obvious misclassifications in the original catalog, while others may indicate the presence of residual star-formation. A direct inspection of our images shows galaxies with features such as shells, arms, dust lanes, large bars or with other peculiarities. A detailed analysis of these objects could lead to interesting results on the stellar population topics.

An additional 232 galaxies have been found to satisfy our membership assignment criteria, so they can be added to the ENEARc cluster sample. Spectroscopic and photometric data for 135 of these is already available. It is our intention to include them in the ENEARc sample in the near future.

A total of 58 clusters have been identified using our criteria, e.g., a cluster must have more than 15 cluster members and more than 5 early-type galaxies (see Chapter 5); most of these objects are in the Abell or the ACO cluster catalogs. However, since our main effort was directed at completing the observations of the field galaxies, we used only 28 of them, for which a substantial number of observations were already available in the literature. We hope to observe all 58 clusters in the future. This will increase the number of galaxies that are used for testing the accuracy of the derived $D_n - \sigma$ distance indicator, and it will allow us to determine the FP from a sample comparable in size to that used here when deriving the $D_n - \sigma$ relation.

At the moment the all-sky magnitude-distance sub-sample of the ENEAR database, is 70% complete and extends out to 7000 kms^{-1}. Galaxies were selected only out to 7000 kms^{-1} in order to have a depth comparable to the SFI and make the sample more manageable. We have since realized that this was a poor decision; it is our intention to extend the present sample and make it truly magnitude-limited.

Note that in the ENEARf sample of peculiar velocities we have removed galaxies which are either misclassified or are contaminated by the light of nearby objects. The pruning of the parent sample is still ongoing.

The velocity field sampled by the ENEARf and ENEARc early-type galaxies is remarkably similar to that of TF surveys of spirals. This demonstrates, unequivocally, that these motions are real—they are not artifacts of, e.g., systematic variations in the scaling relations from which distances were derived. Furthermore, as expected, the ENEARf early-types delineate the structures more sharply than do the more spread out

spirals. For these reasons, combining samples of $D_n - \sigma$ and TF distances is highly desirable, and is the subject of future analyses of the nearby peculiar velocity field.

We have reconstracted the velocity and density fields using the Wiener Filter technique. Our reconstruction recovers the main structures, GA and PP, found by other works. However, the results reported here are limited to maps of low resolution in the supergalactic plane; reconstruction of maps of higher resolution is still ongoing. The reconstruction of the mass power spectrum and estimates of the parameter β will also follow.

The higher resolution maps of the density field will allow us to resolve small-scale structures, which are not clearly identified in the raw data. Combining these maps with the available spectroscopic and photometric data will provide the perfect condition for investigating the dependence of the scaling relations on the environment.

It is important to point out that the total number of galaxies in the ENEAR database with photometric information could increase significantly if the frames already available were analyzed more carefully. This is because, in several frames, other early-type galaxies which did not satisfy our strict selection criteria (see Chapter 1) are present, especially in the vicinity of groups/clusters. For many of these objects, light profiles were not derived. We intend to re-analyze the available frames to search for other early-type galaxies, especially those that are brighter than 14.5 but with redhisfts $cz > 7000$ kms^{-1}, or that are in clusters.

The ENEAR database may, in the future, be enriched by spin-offs of this project. New photometric measurements derived from near-IR CCD images in the K and H bands of ~ 200 cluster galaxies (observed for a project in collaboration with Roberto Saglia and Ralf Bender). Furthermore, other ~ 180 galaxies have been observed in the B-band. These data will be used to determine the distance indicators in the near-IR (which may provide a smaller scatter than the relations in the optical bands), to analyze colour profiles, to investigate possible correlations between global parameters in different bands, and to analyze, in more detail, the sub-components of the early-type galaxies.

In this thesis we have only presented measurements of the Mg_2 line index. An accurate analysis of 10 other absorption lines is still ongoing. Line indeces are useful tools for investigating the stellar populations of early-type galaxies, revealing evidence of correlations between linestrengths and other structural and dynamical properties of galaxies, and understanding the formation and evolution of spheroidal systems.